Neutron Scattering Investigations on $3d$ and $4f$ Frustrated Magnetic Insulators

vorgelegt von
Master of Physics
Diana Lucía Quintero Castro
aus Manizales

von der Fakultät II - Mathematik und Naturwissenschaften
der Technischen Universität Berlin
zur Erlangung des akademischen Grades
Doktorin der Naturwissensschaften
Dr. rer. nat.

genehmigte Dissertation

a mi luz, Lucía

Abstract

This thesis deals with the investigation of two different types of magnetic insulating frustrated systems, $Sr_3Cr_2O_8$ and $SrYb_2O_4$. In the case of $Sr_3Cr_2O_8$, the magnetic ion is a transition metal, the spin orbit coupling is weak while the crystal field effect is big and the orbital moment is quenched. For the case of $SrYb_2O_4$, the magnetic ion is a rare earth, the spin orbit coupling is strong, whereas the crystal field is weak and the orbital moment is unquenched, satisfying Hund's rules. Consequently, the physical behavior of two very different strongly correlated systems is investigated. $Sr_3Cr_2O_8$ consists of a three dimensional arrangement of spin-1/2 Cr^{5+} ions, which are paired into dimers by a dominant antiferromagnetic coupling J_0. The configuration of the Cr ions makes it a frustrated triangular lattice above room temperature. A Jahn-Teller distortion lifts the frustration and leads to spatially anisotropic exchange interactions. Single crystals of this compound have been grown. The magnetic properties have been studied by the analysis of DC susceptibility, high field magnetization and inelastic neutron scattering data. The experiments reveal three singlet to triplet magnon modes. The dispersion relation could be modeled by using a random phase approximation. The competition between quantum and thermal fluctuations is studied by the measurement of the temperature dependence of the linewidth of the excitations. The second compound, $SrYb_2O_4$, is a geometrically frustrated magnet which presents a variety of interrelated magnetic phenomena. The nuclear structure has been investigated by means of powder and single crystal neutron diffraction. The magnetic Yb^{3+} ions (J=7/2) form zig-zag chains which consists of edge sharing distorted octahedra containing only one of the two crystallographic independent Yb^{3+} ions. Low temperature heat capacity measurements reveal a magnetic phase transition at $T_N = 0.9\,K$. Neutron diffraction studies allow the determination of the antiferromagnetic structure. Powder inelastic scattering experiments at different temperatures have been performed with the aim of understanding the crystal field scheme for this compound. These data have been fitted simultaneously to determine the crystal field parameters. Single crystal inelastic neutron experiments reveal low energy magnetic excitations below T_N, while diffuse magnetic scattering above T_N suggest the presence of short range magnetic order. Heat capacity and magnetocaloric effect measurements have been performed to map out the magnetic phase diagram, the results imply substantial magnetic anisotropy. Both compounds exhibit a variety of interrelated magnetic phenomena which provide a fertile ground for the investigation of critical behavior and unconventional states of matter.

Zusammenfassung

Diese Dissertation behandelt die Untersuchung von zwei verschiedenen, magnetisch frustrierten Systemen, $Sr_3Cr_2O_8$ and $SrYb_2O_4$. Beide sind elektrische Isolatoren. Im Fall des $Sr_3Cr_2O_8$ stammt der Magnetismus von dem magnetischen Übergangsmetallion Cr^{5+}. Charakteristisch für das Material ist eine schwache Spin-Bahn Kopplung, ein starkes Kristallfeld und ein unterdrücktes Bahnmoment. Im Fall des $SrYb_2O_4$ ist das magnetische Ion das Selten Erden Element Yb, wobei hier die Spin-Bahn Kopplung stark ist und das Bahnmoment im Rahmen der Hundt'schen Regeln zum Gesamtmoment beiträgt. Dementsprechend wird hier das Verhalten von zwei verschiedenen Systemen untersucht, die magnetisch hochkorreliert sind.

$Sr_3Cr_2O_8$ besteht aus einer dreidimensionalen Anordnung von Cr^{5+} Ionen mit Spin $-1/2$, diese sind als Dimere mit dominanter antiferromagnetischer Wechselwirkung J_0 gepaart. Oberhalb der Raumtemperatur bilden die Cr - Ionen ein frustriertes Dreiecksgitter. Die Frustration wird durch eine Jahn-Teller-Verzerrung aufgehoben, was zu einer anisotropen Austauschwechselwirkung führt. Von diesem Material konnten Einkristalle hergestellt werden und die magnetischen Eigenschaften wurden mit Messungen der Suszeptibilität, der Hochfeld-Magnetisierung und der inelastischen Neutronenstreuung untersucht und analysiert. Die Experimente ermöglichten die Detektion von drei Magnonenmoden, die alle als Singlet -Triplet Anregungen identifiziert werden konnten. Die Dispersion konnte mit Hilfe des Heißenbergmodells und einer 'Random Phase' Näherung erklärt werden. Die Konkurrenz zwischen Quanten- und thermischen Fluktuationen wurde schließlich mit einer temperaturabhängigen Messung der Linienbreiten der Anregungen untersucht.

Die zweite Verbindung, $SrYb_2O_4$, ist ein geometrisch frustriertes magnetisches System, das eine Reihe eng zusammenhängender magnetischer Eigenschaften aufweist. Die Kristallstruktur wurde mit Neutronenstreuexperimenten an Pulver- und Einkristallproben untersucht. Die magnetischen Yb^{3+} Ionen ($J = 7/2$) bilden Zickzack-Ketten, welche aus kantenteilenden Oktaedern gebildet werden. Nur eines der beiden unabhängigen Yb Ionen gehört zu jeweils einer Kette. Messungen der spezifischen Wärme zeigen einen magnetischen Phasenübergang bei $T_N = 0.9\,K$. Untersuchungen mittels Neutronenstreuung erlaubten die Bestimmung der antiferromagnetischen Struktur. Um die Kristallfeldparameter zu identifizieren, wurden zusätzlich inelastische Neutronenstreuexperimente an Pulverproben bei verschiedenen Temperaturen durchgeführt. Die erhaltenen Daten wurden theoretisch analysiert und mittels einer Fit-Software konnten die entsprechenden Kristallfeldparameter bestimmt werden. Inelastische Neutronenstreuexperimente an Einkristallen zeigten niederenergetische magnetische Anregungen unterhalb T_N; oberhalb T_N führen kurzreichweitige Korrelationen zu diffuser Streuung. Mit Messungen der spezifischen Wärme und des magnetokalorischen Effekts wurde das magnetische Phasendiagramm bestimmt, die dabei gewonnenen Ergebnisse deuten auf ein beträchtliches anisotropes Verhalten hin.

An beiden Substanzen wird hier eine Vielzahl komplexer magnetischer Eigenschaften beschrieben. Die gewonnenen Resultate bilden eine gute Grundlage für weitere Untersuchungen, z.B. des kritischen Verhaltens und neuer magnetischer Zustände.

Acknowledgments

Contents

1 Introduction

The study of cooperative phenomena in condensed matter offers the perfect scenario for the application and improvement of theories of interacting many-body systems. Magnetic condensed matter systems can have a variety of different geometrical connectivity between the atoms, different spatial dimensions, sign and strength of interactions, anisotropy, and therefore, they provide many interacting degrees of freedom that can be explored and controlled. Furthermore, under certain conditions the competition between interactions can be modified by restrictions in the connectivity between the atoms, such as frustration. This can lead to quantum fluctuations that reduce significantly the critical temperature where the system could develop long range magnetic correlations. Another possibility is to reinforce the interaction between pairs of atoms, creating dimerization, this, would lead to the formation of a non-magnetic singlet ground state and to excitations which can be treated as pseudo-particles that follow quasi Bosonic statistics. The competition between interactions presents enormous opportunities for the discovery and exploration of exotic magnetic states.

All of these competing interactions, frustration, dimerization and exotic phases are present in the compounds investigated here; the dimerized antiferromagnet $Sr_3Cr_2O_8$ and the highly frustrated rare earth system $SrYb_2O_4$.

$\mathbf{Sr_3Cr_2O_8}$ is an insulating three dimensional antiferromagnet. The magnetic ion, Cr^{5+}, is a transition metal in which the spin orbit coupling is weak and the crystal field is strong, quenching the orbital moment. The Cr^{5+} ions lie on hexagonal bilayers where the dominant intrabilayer interaction is antiferromagnetic and gives rise to the dimerization, as a result it has a singlet ground state and magnon excitations to the triplet excited state. At room temperature the compound is geometrically frustrated, but a structural distortion makes the interdimer exchange interactions spatially anisotropic. Applying a magnetic field, drives the magnons into the ground state, this condensation could be described as Bose Einstein condensation. At finite temperature, the dimers are thermally excited and there exist intersite interactions, the magnons them behave as a strongly correlated gas of hardcore bosons.

$\mathbf{SrYb_2O_4}$ is a geometrically frustrated insulator which presents a variety of interrelated

magnetic phenomena. The magnetic Yb^{3+} is a rare earth ion in which the spin orbit coupling is strong and the crystal field is weak, obeying Hund's rules. These ions are arranged in zig-zags chains that run parallel to the c-axis, and form honeycombs in the $a - b$ plane. This geometrical arrangement is frustrated. The exchange interactions compete with the anisotropy and magnetic order is suppressed to $0.92\,\mathrm{K}$. The complex competition between magnetic frustration and anisotropy gives rise to a large number of potentially unusual magnetic states and the coexistence of long range and short range magnetic correlations.

Studies on $SrYb_2O_4$ and $Sr_3Cr_2O_8$ are important because they then enhance current understanding of competing interactions in highly correlated materials.

The thesis is structured as follows. Chapter 2 provides an introduction to the theory of magnetism. The main interactions in a magnetic system are explained, such as free ion interactions, the interactions of an ion with the surrounding crystal field, and the magnetic exchange interactions that would lead to the development of long range order. The differences between the properties of rare earth and transition metal ions are explained. The principal experimental technique used in this thesis is neutron scattering, the neutron has a magnetic moment but no charge, this allows the spin degrees of freedom in a material to be investigated without having to account for the Coulomb interaction. Many different neutron scattering methods were used, the theoretical basis of this technique is explained in Chapter 3 and the results are shown in Chapters 5, 6 and 7. Other experimental techniques such as magnetization, DC susceptibility, heat capacity and magnetocaloric effect are explained as well in Chapter 3.

Chapter 4 explains the general properties of $Sr_3Cr_2O_8$, the sample preparation and single crystal growth is described and heat capacity, magnetization and magnetic susceptibility data are shown. The bulk properties of $Sr_3Cr_2O_8$ give the overview needed to understand the inelastic neutron scattering data which are shown in the Chapter 5, where the dispersion relation of the magnetic excitations are measured and modeled using a random phase approximation. The temperature dependence of the magnetic excitations is also investigated. In Chapter 6, the properties of the insulating frustrated rare earth antiferromagnet $SrYb_2O_4$ are described with an exhaustive study of the nuclear and magnetic structure. In Chapter 7, the effect of the local crystal field on the Yb^{3+} ions and its magnetic properties are studied. Together with a description of the low energy dispersive modes and diffuse magnetic scattering.

Finally, the main results of the investigations on both, $Sr_3Cr_2O_8$ and $SrYb_2O_4$ are reviewed in Chapter 8 and some suggestions for possible future experimental and theoretical work are given.

2 Introduction to Magnetism: from the Free Ion to the Long Range Order

2.1 Introduction

The magnetism in most atoms is determined by the electrons in unfilled shells. Each electron possesses a spin s and orbital angular momentum l. In the *Russell-Saunders scheme*, relevant to the $3d$ and $4f$ shells investigated here, the individual electronic contributions are added, taking into account interactions between electrons and the Pauli exclusion principle, this gives rise to the total orbital momentum $\boldsymbol{L} = \sum_i \boldsymbol{L}_i$ and the total spin is $\boldsymbol{S} = \sum_i \boldsymbol{S}_i$.

In this thesis, the magnetic behavior of two compounds $Sr_3Cr_2O_8$ and $SrYb_2O_4$ is investigated. In the first one, the magnetic ion is the transition metal Cr^{5+} which posses one unpaired electron in the $3d$ shell and in the second compound, the magnetic ion is the rare earth Yb^{3+} which posses 13 outer electrons in the $4f$ shell. Even though, these two compounds are insulating oxides, they have very different electronic configurations and therefore are expected to display very different magnetic behavior.

As stated by J. H. Van Vleck in his Nobel lecture in 1977, 'Quantum mechanics is the key to understanding magnetism. When one enters the first room with this key there are unexpected rooms beyond, but it is always the master key that unlocks each door' [1]. But these quantum mechanical theories and our concepts of magnetism need to be tested by experiments. Therefore, experimental techniques are the "eyes that see the rooms" are the "hands that turn the key". In the last years, technical developments have created and improved experimental techniques and only now it is possible to performed experiments under extreme conditions such as very low temperatures and high magnetic fields with very high sensitivity. These new conditions allow exotic phases of condensed matter to be investigated.

Performing a measurement involves perturbing a system and detecting its response. One of the properties that can be investigated is magnetization which is the measurement of the magnetic moment of a sample when applying a magnetic field. This measurement was
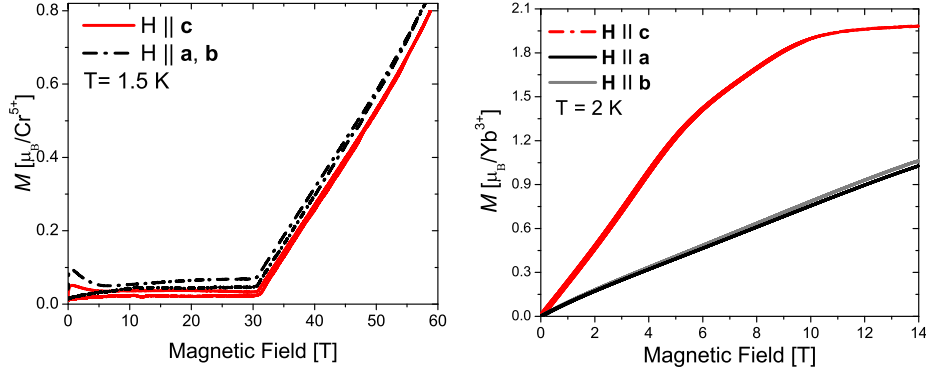
Figure 2.1: (left) Magnetization of $Sr_3Cr_2O_8$. (Right) Magnetization of $SrYb_2O_4$.

done on the two compounds $Sr_3Cr_2O_8$ and $SrYb_2O_4$, the results are shown in Figure 2.1. A magnetic field was applied along the principal crystallographic axes of both samples and the magnetization was measured. The most remarkable difference between the two results is that for $SrYb_2O_4$ the magnetization along the c axis is very different from the magnetization along the a and b axes, while for $Sr_3Cr_2O_8$ the magnetization along a, b and c axes is almost equal. The orientational dependence of the magnetization provides information about a very important property, the *magnetic anisotropy* which is directly related to a key problem in magnetism which is the origin, size and orientation of the magnetic moment. The questions that arise are; why are the responses of these two compounds to a magnetic field so different? how do they respond to other kind of perturbations? what are the electronic configurations in these compounds? what are the magnetic ground states and what are the excitations? this thesis is intended to solve these questions and to formulate others. This first chapter gives the fundamental physical concepts needed to understand the magnetic behavior in these samples, explaining the differences between the properties of rare earth and transition metal ions. The single ion interactions are explained with a special emphasis on the spin-orbit coupling in the next section. The magnetic ions in these compounds are not free but are embedded in a crystal lattice, therefore the interactions with the crystal lattice are considered in the third section. In the fourth section, the interaction between magnetic ions is explained, which gives rise to long-range magnetic order and collective excitations. For a more detailed description of these concepts, the following references are suggested [2, 3, 4, 5, 6, 7].

2.2 Free Ion Interactions

The Coulomb and spin-orbit interactions arise as a result of the forces between the electrons in a single atom or between the electrons and the nucleus. Thus they are present regardless of the environment in which the atom is located, that is whether the atom is embedded in a crystal or left free in a gas. They are thus called free ion interactions.

In a simple picture, the spin-orbit coupling, (SO), is the dipole interaction between the spin $\boldsymbol{S}$ and the magnetic field created by the electrons from their orbital motion. This coupling is ubiquitous in physical systems and is crucial in many condensed matter systems. The effect of this interaction is to couple $\boldsymbol{L}$ and $\boldsymbol{S}$ to yield the total momentum $\boldsymbol{J} = \boldsymbol{L} + \boldsymbol{S}$ that can have the values $(L+S)$, $(L+S-1)$, $(L+S-2)$,...,$|L-S|$ and the multiplicity of terms corresponding to a given J is $2J+1$. The degeneracy of these multiplets is removed by the SO interaction of the magnetic moment associated with the angular momentum L and spin S. The moments obey the matrix operator rules $S^2 = S(S+1)$, $L^2 = L(L+1)$ and $J^2 = J(J+1)$ and the states are characterized by these quantum numbers and also by the z-component of J, denoted m_J. In the Russell-Saunder scheme, these spin-orbit interactions are relatively weak and therefore can be considered as perturbation terms to the single ion description. This means that the energy differences between multiplet levels (different J, same L and S) are small compared to those between levels having different L and/or S values.

SO interactions tend to be much smaller than the leading electrostatic interactions, but the higher effective nuclear charge experienced by unfilled inner shell of electrons is enhanced compared to outer electrons thus intensifying the SO. Being close to the nucleus also helps to reduce the interaction with external charges which compete with SO as the leading perturbation. That is the case for the rare earth ions, where although the coulomb interaction is much stronger than SO the ground state is defined by the total angular momentum $\boldsymbol{J}$. The resulting multiplet of levels which are each $(2J+1)$ degenerate is the starting point of most theoretical considerations for these kind of ions. $\boldsymbol{L}$ and $\boldsymbol{S}$ are still good quantum numbers since the overall multiplet splitting due to SO is usually much less than the energy separation of the terms. Conversely, the effects of SO in transition metal systems are not as strong as for RE systems, however the $3d$ orbitals are extended in space and therefore are more susceptible to having strong interactions with charges outside the atom, this case will be shown in the next section.

The ground state of an ion can be defined by the combination of angular momentum quantum numbers which are found to minimize the energy. Hund's rules are a set of rules which can estimate the ground state configuration of a single ion. These are a conse-

quence of the Pauli principle plus electrostatic interactions between the electrons. Since any dual occupation of a spatial orbital must involve large electrostatic electron-electron repulsions, the energy of the multielectron state is lowered if such dual occupations can be minimized. The first rule is to maximize S, in this way the Coulomb energy is minimized because the Pauli exclusion principle forces the electrons to occupy different orbitals, thus reducing the coulomb repulsion between electrons. The second rule is to maximize L which can be understood in a semi classical way as the electrons in orbits rotating in the same direction can avoid each other more effectively and therefore reduce Coulomb repulsion. The third states that multiplets formed from equivalent electrons are regular when less than half the shell is occupied, but inverted when more than half the shell is occupied. This is to choose J when the shell is less than half full as $J = |L - S|$ and when the shell is more than half full $J = |L + S|$; this arises from an attempt to minimize the spin orbit energy and is only applicable in certain circumstances [8]. Hund's rules lead to a prediction of the ground state but do not predict the excited states or how close they are to the ground state. They allow the magnetic moment of an ion to be estimated assuming that only this ground state is populated.

The ground state of rare earth ions in general obey Hund's rules, for example in the case of Yb^{3+}, the electronic configuration is $[Xe]4f^{13}6s^2$, this leaves 13 electrons in the unfilled shell $4f$. f electrons have $l = 3$, to satisfy Hund's first rule, $2l + 1 = 7$ of the electrons are spin-up, 6 electrons are spin down. This gives the value of S as $S = 7 \times \frac{1}{2} - 6 \times \frac{1}{2} = \frac{1}{2}$, which implies that the spin degeneracy is $2S + 1 = 2$. The spin up electrons give no net orbital angular momentum, since they occupy all m_l levels of the f orbital, there is only the orbital contribution from 6 spin down electrons and it is this which must be maximized. This implies that $L = 3$. The shell is more than half full so $J = |3 + 1/2| = 7/2$. The term symbol for this ion is: $^2F_{7/2}$, which summarizes the quantum numbers which define the ground state. Total spin degeneracy is 2, total orbital moment is 3 (symbolized by F) and total angular moment is 7/2.

2.3 Crystal Field

In condensed matter physics, the bulk properties of magnetic materials are of special interest because they are the principle basis to understand microscopic phenomena. Consequently, research deals with non-isolated ions that are embedded in crystalline solids. Crystals can be regarded as assemblies of free ions, bound together in several possible ways. Ionic crystals are held together by a balance between long range electrostatic attractive forces and short-range repulsions, the latter being largely attributable to the

exclusion principle acting between the outer electrons on neighboring ions. Therefore, these magnetic systems are subject to, at first approximation, electrostatic interactions with the surrounding atoms. The potential is known as the crystal field (CF).

The crystal field can therefore be thought of as a perturbation acting on 'free' magnetic ions. The site symmetry of magnetic ions is often lowered from the spherical distribution of the free ion, which breaks the degeneracy of the J or L multiplets. The effect of the CF is therefore to lift the $(2J+1)$ degeneracy of the orbital level creating small splittings. The splitting and energy level scheme are totally defined by the site symmetry of the ion. To first approximation, the surrounding charges can be treated as point charges and the electrostatic potential can be defined at a position $\mathbf{r}$ away from a particular ion due to a charge density $\rho(\mathbf{R})$ caused by neighboring ions at $\mathbf{R}$ as:

$$V_{CF} = \int \frac{\rho(R)}{|r-R|} dR. \tag{2.1}$$

This model gives a qualitative idea of the kind of splitting the CF creates but it rarely gives the quantitative values of the multiplet splittings. It was initially thought that the neighboring ions may be treated solely as point sources of electric field, and that only the magnetic properties of the ion of interest needed to be taken into account, these models are referred as *point charge models* and discount the angular momentum properties of the open shell electrons of neighboring ions and only deal with their charge. The potential in Equation 2.1 can be written in spherical coordinates in terms of a sum of spherical harmonics Y_{kq},

$$V_{CF}(r,\theta,\phi) = \sum_{k,q} C_{kq} r^k Y_{kq}(\theta,\phi), \tag{2.2}$$

where k specifies the rank and q the components. The possible values for the rank are: $k = 0, 1, 2, 3, 4, 5, 6$, and C_{kq} is the charge density and can be written as:

$$C_{kq} = (-1)^q \frac{4\pi}{2k+1} \int \frac{\rho(R)}{R^{k+1}} Y_{k,-q}(\hat{R}) dR. \tag{2.3}$$

This is called the multipole expansion of the charge density. As said earlier, this model considers the ions as point charges. Nevertheless, because the spherical harmonic functions form a complete orthonormal set, the expansion of any crystal field potential in them is still valid. However, the coefficients in this expansion are now not proportional to r^k and the parameters C_{kq} are not given by Equation 2.3. As the expansion is not restricted to electrostatic potentials, it can take into account the full range of mecha-

nisms that contribute to the CF. The phenomenological model, replaces the spherical harmonic function by a tesseral harmonic Z_{kq}. The charge distribution is replaced by a collection of point charges q_j.

$$A_{kq} = \frac{4\pi}{2k+1} \sum_i \frac{q_j}{R_j^{k+1}} Z_{kq}(\theta_j, \phi_j). \tag{2.4}$$

This expression, converted back into Cartesian coordinates, forms the starting point of the Steven's operator equivalents $\bar{O}_{k,q}(\mathbf{J})$ [9]. Additionally, there is a proportionality constant θ_k, called the Steven's operator equivalent factor between $\bar{O}_{k,q}(\mathbf{J})$ and Z_{kq}. The phenomenological crystal field Hamiltonian is:

$$\mathcal{H}_{CF} = e \sum_{k=2,4,6} \sum_{q=-k}^{k} \theta_k A_{kq} \langle r^n \rangle \bar{O}_{k,q}(\mathbf{J}). \tag{2.5}$$

The crystal field parameters are phenomenological variables and are given by:

$$B_q^k \equiv |e| \, \theta_k A_{kq} \langle r^n \rangle, \tag{2.6}$$

writing the CF Hamiltonian in terms of the CF parameters, one obtains:

$$\mathcal{H}_{CF} = \sum_{kq} B_k^q O_k^q(J_x, J_y, J_z). \tag{2.7}$$

The potential function describing the CF must be invariant under the operations of the point group of the ion which the crystal field affects. This limits the allowed harmonics and hence the nonzero crystal field parameters. The particular allowed set k and q for an ion is affected by the definition of the coordinate axes. Hermicity and time reversal invariance of the CF Hamiltonian ensure that only CF parameters with k even are nonzero [10]. $k = 0$ is an isotropic potential, it does not split the CF levels, so it is omitted and q runs from $-k$ to k. In general, if there is a center of inversion, there will be no odd-k term, and if the z-axis is a q-fold rotation axis, then the B_q^k will be nonzero [11]. The lowest number of crystal field parameters are obtained for high symmetry point groups, where the calculation axes are set to coincide with the symmetry axes. It is possible to rotate sets of crystal field parameters between one set of axes and another using rotation matrices for each Euler angle [12]. The site symmetry at a magnetic ion imposes further restrictions on the values of the components q [10]. Therefore, the qualitative form of the splitting (i.e. the effect of the crystal field on the degeneracies) can be predicted from a knowledge of the site symmetry of the magnetic ion. The symmetry of

the crystal field Hamiltonian is defined as the point group of symmetry operators which leave the crystal field Hamiltonian invariant, but it always has an inversion symmetry, so the group is always higher than the ion local symmetry.

One common approach is to take these B_k^q terms and use them as freely varying parameters to fit experimentally observed crystal field split energy levels. This is the so-called phenomenological approach and can be highly successful [13]. The most powerful spectroscopic technique to determine the positions of energy levels and matrix elements of the transitions between levels is inelastic neutron scattering. In inelastic neutron scattering experiments both energy gain and the energy loss processes can be probed. The neutron can excite the ion from a lower energy state to a higher orbital state with a corresponding loss of the neutron energy or the ion is de-excited from a higher energy level to a lower energy level and the neutron gains the corresponding energy. So the measured energy spectrum exhibits resonance peaks which can be associated with the transitions between the crystal-field-split levels. A unique identification of the observed energy levels is only possible by comparing the observed intensities of the resonance peaks with the expected neutron scattering cross-sections of different transitions among the levels. In neutron scattering investigations one is confronted with the problem of distinguishing the crystal-field excitation peaks from, say, phonon peaks. In such cases it is useful to check the Q dependence of the intensity of the inelastic peaks because the magnetic form factor reduces the intensity of crystal field transition with increasing Q. The temperature dependence of the inelastic peak intensity is also useful for such purpose: phonons obey Bose statistics whereas the population of the crystal-field levels is governed by Boltzmann statistics. These phenomenological techniques were used to determine the CF splitting and ground state wavefunction of $SrYb_2O_4$, as described in Chapter 7.

The effect of the crystal field on rare earth compounds and transition metals is very different. These differences arise due to the orbital distribution. For the RE ions, the $4f$ orbitals are shielded from perturbations due to neighboring ions by the closed shells $5s$ and $5p$, therefore, the CF effects are very small and can be treated as perturbations. The splitting due to the CF potential is much smaller than the J multiplet separations, so that the mixing of different multiplets can usually be neglected. While for the transition metal ions, the electrons in the $3d$ orbitals are not screened and take part in the bonding processes, therefore the effect of the CF is very strong. The $3d$ wave functions have aspherical charge distributions, which in the CF's have different electrostatic energies. In Figure 2.2 a simple comparison is given. To the left a $3d$ ion is placed in a tetrahedral crystal field. The orbitals are extended in space and the action of the CF is so strong
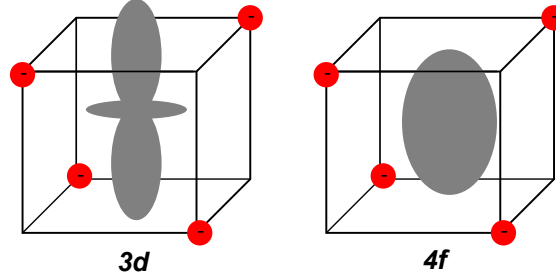
Figure 2.2: $3d$ and $4f$ ions in a tetrahedral environment.

that the ground state is not completely degenerate. The orbitals of the central ion that are directed along the axes containing ligand ions will have higher energy than those directed away from the ligands. In the case of the $4f$ orbital, the shell is almost full, so the orbital symmetry is almost spherical, the action of the tetrahedral CF is so small that the ground state degeneracy is only lifted slightly.

In both cases, the competition between the CF and SO determines the magnitude of the magnetic anisotropy. These differences in the orbital distribution and in the strength of the SO coupling can explain the different magnetization results that were shown at the beginning of this chapter in Figure 2.1. On applying a magnetic field, the spin direction in the system changes. If the SO is strong ($4f$ ions), the orbital moment and the charge cloud follow the spin, because the CF is not strong enough to break the SO coupling. As the spin direction has changed, the CF energy is modified. So, by applying a magnetic field along different crystallographic directions, the response of the system will be different as shown for $SrYb_2O_4$, where it is easier to align the spins along the c-axis with respect to the other two axes. In the case of $Sr_3Cr_2O_8$, the CF is much stronger than the SO interaction, the spin and orbital angular momentum are effectively decoupled and the magnetization is almost equal along all crystallographic directions.

In the case of $Sr_3Cr_2O_8$ the Cr^{5+} ion is in a tetrahedral environment. The electronic configuration for this ion is $[Ar]3d^1$; therefore, there is only one electron in the $3d$ shell: $S = 1/2$ and $L = 2$. Then according to Hund's rules $J = 3/2$ for the ground state multiplet which is $^2D_{3/2}$. This term has a 5-fold orbital degeneracy $2L+1 = 5$. If a tetrahedral crystal field, $V_{cryst}(r)$, is added to the spherically symmetric one-electron ion potential, the five $L = 2$ states split into a triplet T_2 and a doublet E which do not mix under the symmetry operations of a tetrahedron. Within the electrostatic approximation, in which the ligands are substituted by point charges, the lowest level is the doublet level. This process is illustrated in Figure 2.3. The Hamiltonian for a tetrahedral environment is given by a real function ($A(x^2 + y^2 - 2z^2)$) and the eigenfunctions are all real. The total
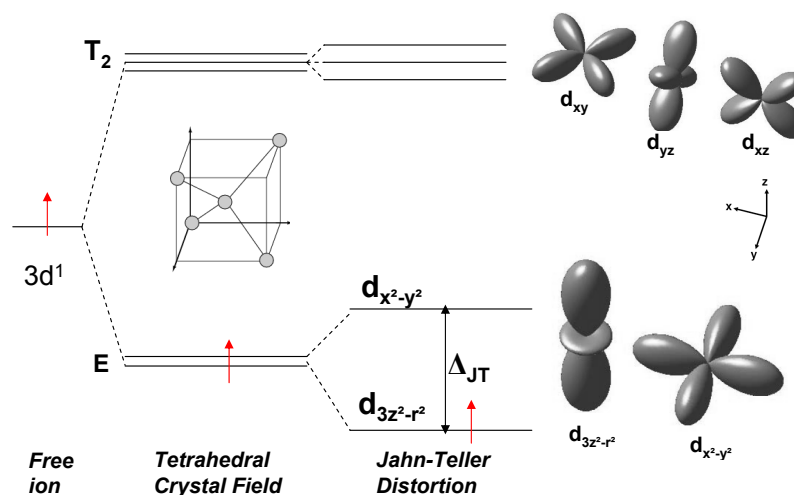
Figure 2.3: CF tetrahedron.

momentum operator L is hermitian and so has real eigenvalues but the operator is itself purely imaginary. If the ground state is non-degenerate which is realized by a strong CF splitting, this must be a real function. Therefore $\langle 0|\hat{L}|0\rangle$ must be purely imaginary but, since L is hermitian it must be purely real, this is only possible if $\langle 0|\hat{L}|0\rangle = 0$ so that all components of the orbital angular momentum of a non-degenerate state are quenched. Therefore Cr^{5+} is consider to have a spin $1/2$, $L = 0$ and $J = S$. This is the well known *orbital quenching* and it is a result of the symmetry lowering of the ionic one electron effective potential due to the charge distributions around the magnetic ion. It is very common in $3d$ ions due to the strength of the crystal field.

A general theorem of group theory which is important in understanding the lowest energy level structure, is the *Kramers theorem* which states that in the absence of an applied magnetic field the levels of an ion with an odd number of $4f$ electrons can at most be split into levels which are doubly degenerate. This applies to rare earths with half integral J ground states, for example Yb^{3+} has 13 electrons in the $4f$ orbital, $J = 7/2$ and $L = 3$, therefore, it is a so-called Kramer's ion, the degeneracy is $(2J + 1) = 8$, by this theorem, the CF would lift the 8-fold degeneracy into 4 doublets. A second theorem that defines the lowest energy level structure is the *Jahn Teller distortion* and is described in the next subsection.

2.3.1 Jahn-Teller Distortion

It has been assumed so far, that the ground state of the ion in a crystal field depends on the symmetry of the local environment. Sometimes it can be energetically favorable

for, say, an tetrahedron to spontaneously distort because the energy cost of increased elastic energy is less than a resultant electronic energy saving due to the distortion. This phenomenon is known as the *Jahn-Teller effect* [14]. This effect states that the environment of an ion with a degenerate ground state, Kramer's doublets excepted, spontaneously distorts to a lower symmetry so as to remove the orbital degeneracy. For a $3d$ ion with $L = 2$, the d-shell has five degenerate levels. The degeneracy is present due to rotational invariance within the angular momentum L. In empty space, any direction or axis is the same as any other. The situation drastically changes once the ions are part of a crystal structure, the orbitals cost different energies depending on their overlap with the neighboring ions. Full rotational invariance is lost, but a subgroup remains. In the case of the 5 $L = 2$ levels in a tetrahedral field these subgroups are the E doublet and the T_2 triplet. The ligand ions surrounding the transition metal ion under consideration can slightly readjust their locations, creating an asymmetry between the different directions that effectively removes the degeneracy. The lifting of degeneracy by a collective distortion of the whole lattice due to the orbital-lattice interaction is called the Jahn-Teller effect. This effect tends to occur spontaneously because the energy penalization of the lattice distortion grows as the square of that distortion, while the energy splitting of the otherwise degenerate orbitals is linear. Cr^{5+} is a Jahn-Teller active ion, the distortion lifts the degeneracy of the low lying E orbitals, and the single electron occupies the lower lying $d_{3z^2-r^2}$ state as depicted in Figure 2.3. The electronic energy gained by the lowering of the $d_{3z^2-r^2}$-level is larger than the loss of elastic energy necessary to distort the crystal. These distortions do not occur randomly, but they form a well defined pattern. This phenomenon is called the cooperative Jahn-Teller effect and is the most prominent example of orbital order. In Chapter 4, the details of the Jahn-Teller distortion in $Sr_3Cr_2O_8$ are described.

2.4 Magnetic Coupling

So far only the single ion interactions and the interaction of an ion in a crystal field have been discussed. But a magnetic ion in a lattice can also be coupled to neighboring magnetic ions via exchange interactions. They arise as a consequence of the overlap of the electronic shells of the ions and the Pauli exclusion principle. The total wave function of two electrons is composed of the product of the spatial and the spin wave functions, which must be antisymmetric giving rise to two different possibilities for combining the spin and the spatial part. The first one consists of a symmetric spatial and an antisymmetric spin wave function while the second one presents the opposite with an

antisymmetric spatial and a symmetric spin version. Including a coulomb interaction between the electrons lifts the degeneracy between the two possibilities resulting in an energy difference between the symmetric and the antisymmetric spatial wave functions.

The first person to point out that the Hamiltonian that describes the electrostatic interactions between magnetic ions can be replaced by an effective spin Hamiltonian was Dirac [15]. For neighboring magnetic ions with spins S^i and S^j the exchange interaction due to their overlap can be approximated by their dot product. For a magnetic material where all neighboring spins interact, the resulting exchange Hamiltonian which is known as the Heisenberg model, is given by,

$$\mathcal{H} = 2 \sum_{i>j} \boldsymbol{J}_{ij} \boldsymbol{S}_i \cdot \boldsymbol{S}_j, \qquad (2.8)$$

where $\boldsymbol{S}_i$ and $\boldsymbol{S}_j$ are the operators for the ith and j^{th} spins, and $\boldsymbol{J}_{ij}$ is the exchange constant between spins i and j. The interaction depends upon the scalar product of the spin moments and is known as the Heisenberg interaction. A negative value of J results in ferromagnetic exchange, where it is energetically favorable for S^i and S^j to be aligned in the same direction. While, a positive value of $\boldsymbol{J}$ results in antiferromagnetic exchange, which is obtained for the antisymmetric spin wave function. The Heisenberg model works best for insulating materials with well-localized wave functions where the number of electrons per atom is fixed.

Without any exchange interactions the individual magnetic moments would be disordered at any temperature in the absence of magnetic field. Introducing exchange interactions produces non-vanishing moments below a critical temperature leading to a variety of magnetic order or correlated states. The exchange interactions in magnetic compounds can be rather complex exhibiting several different values between ions. In addition to the exchange interactions between neighboring ions, couplings between next nearest neighbor ions have to be taken into account, although usually they are expected to be weaker due to a greater distance between the ions. The exact contribution of couplings strongly depends on the geometric connectivity between the ions in the compound. In situations where the electronic shells of the two magnetic ions overlap each other directly the interaction is known as direct exchange. In many materials, the crystallographic geometry prevents sufficient direct overlap of the orbitals. But the magnetic exchange interaction can be also indirect, that means, it can be mediated by a non-magnetic ion which is placed in between the magnetic ions. An important indirect exchange mechanism is the superexchange mediated by the p orbitals of for example oxygen ions [16]. Goodenough and Kanamori formulated general rules for the sign of

superexchange interactions, those rules state; that superexchange interactions are antiferromagnetic if the virtual electron transfer occurs between orbitals that are each half-filled (ferro-orbital order), while the interactions are ferromagnetic, if the virtual electron transfer occurs between an empty and a half-filled, or an filled and a half-filled orbital (antiferro-orbital order) [7]. This kind of interaction is present in both transition metal and rare earth compounds. Indeed for the compounds investigated here, the magnetic ions are well separated from each other, so it is expected that the surrounding oxygen ions mediate the exchange interaction.

Another kind of magnetic interaction is the *Dzyaloshinsky - Moriya* (DM) interaction or anisotropic exchange interaction, which is not mediated via oxygen but is produced by the spin orbit interaction in one of the magnetic ions. There is then an exchange interaction between the excited state of one ion and the ground state of the other ion.

Most materials containing magnetic ions develop long range magnetic order at sufficiently low temperatures. Magnetic compounds can have several different independent exchange interactions between neighboring magnetic ions. The number of interactions depends partly on the symmetry of the compound and on how many magnetic ions are in the structural unit cell. Coupling can occur between next nearest neighbors ions as well as nearest neighbors, although the size of the interaction is usually reduced considerably as the separation of the magnetic ions increases. Common magnetic structures include the ferromagnet which shows spontaneous magnetization even in the absence of an applied magnetic field, with all the magnetic moments lying along a single unique direction. The antiferromagnet arises if the exchange interaction is negative $J < 0$, the molecular field is oriented such that it is favorable for nearest neighbor magnetic moments to lie antiparallel to one another. It can be considered as two interpenetrating sublattices on one of which the magnetic moments point up and on the other they point down. This leads to a zero total magnetic moment, the critical temperature where the spins order is known as Néel temperature [17, 18]. Other frequently observed magnetic structures are helical structures where the direction of the ordered spin moment rotates between successive magnetic ions in the compound and sinusoidal structures where the size of the ordered moment varies sinusoidally through the crystal. A useful experimental technique that allows the determination of the type of magnetic order is neutron diffraction and it will be discuss in the next chapter.

Not all lattice structures are suitable for long range magnetic order. Frustration occurs in triangular and Kagomé lattices where the spatial arrangement of spins is such that it prevents the simultaneously minimization of all interaction energies. In such compounds, order can occur although at very low temperatures compared to the strength of

the exchange constants and the resulting magnetic structure is a compromise which only partially satisfies the different interactions. This is called *geometrical frustration* and it enhances quantum fluctuations as the ground state is highly degenerate suppressing long range order. Reduction of the order parameter by quantum fluctuations also depends on the coordination number and on the competition of non equivalent NN bonds, as occurs in the honeycomb lattice where due to the low coordination number the ordered moment is approx 10% percent smaller than expected. Both the honeycomb lattice and geometrical frustration are present in $SrYb_2O_4$. Magnetic order can also be suppressed in systems where there is a dominant antiferromagnetic exchange interaction which couples the magnetic ions into singlet pairs. This is the case for $Sr_3Cr_2O_8$ and a simplified example is given in the next section.

2.5 Magnetic Excitations

A simple example of a Heisenberg system is the coupling of two spin-1/2 particles, where the Hamiltonian 2.8 can be simplified to,

$$\mathcal{H}_{dimer} = J_0 \boldsymbol{S}^a \cdot \boldsymbol{S}^b, \tag{2.9}$$

where J_0 is the antiferromagnetic exchange constant between $\boldsymbol{S}^a$ and $\boldsymbol{S}^b$.

These two coupled spins can be considered as a joint entity, called a dimer and the total spin can also be represented by an operator $\boldsymbol{S}_{tot} = \boldsymbol{S}^a + \boldsymbol{S}^b$. The energy levels of this system can be solved exactly and consist of a spin singlet ground state $|0\rangle = |0, 0\rangle$ with total spin $S_{tot} = 0$ and energy $-3J_0/4$ and then a triplet of excited states lying at energy J_0 above the ground state. The excitations have total spin $S_{tot} = 1$ and wavefunctions are $|1\rangle = |1, 1\rangle$, $|2\rangle = |1, 0\rangle$, $|3\rangle = |1, -1\rangle$, where the notation indicates the eigenvalues of S and S^z in an arbitrary z direction. Making use of the raising and lowering operators the eigenstates and eigenvalues can be determined in the basis of the two spins: $|\uparrow\uparrow\rangle$, $|\uparrow\downarrow\rangle$, $|\downarrow\uparrow\rangle$, $|\downarrow\downarrow\rangle$. The eigenstates are linear combinations of these basis states and are listed in Table 2.1. The states $|\uparrow\uparrow\rangle$ and $|\downarrow\downarrow\rangle$ are clearly symmetric under exchange of electrons. The states $|\uparrow\downarrow\rangle$, $|\downarrow\uparrow\rangle$ are neither symmetric or antisymmetric under exchange of the two electrons and their linear combinations must be taken. If $J_0 > 0$ the lower level is a singlet with a triplet of excited states.

The energy level diagram for a dimer is shown in Figure 2.4. When applying a magnetic field, the triple degeneracy of the excited states is lifted, and for sufficiently strong field one of the triplets would merge with the ground state.

Table 2.1: The eigenfunctions and corresponding eigenvalues of an isolated dimer are given where $-J_0$ is the dimer exchange constant which is deigned as antiferromagnetic. In this notation $|\uparrow\downarrow\rangle$ is the state where the first spin in the dimer points up and the second spin points down with respect to an arbitrary z-axis.

eigenfunction	eigenvalue	spin	state
$\|0\rangle = \|0,0\rangle = \|\uparrow\downarrow\rangle - \|\downarrow\uparrow\rangle$	$-\frac{3}{4}J_0$	$S = 0,\ s^z = 0$	ground state
$\|1\rangle = \|1,1\rangle = \|\uparrow\uparrow\rangle$	$\frac{1}{4}J_0$	$S = 1,\ s^z = +1$	excited state
$\|2\rangle = \|1,0\rangle = \|\uparrow\downarrow\rangle + \|\downarrow\uparrow\rangle$	$\frac{1}{4}J_0$	$S = 1,\ s^z = 0$	excited state
$\|3\rangle = \|1,-1\rangle = \|\downarrow\downarrow\rangle$	$\frac{1}{4}J_0$	$S = 1,\ s^z = -1$	excited state
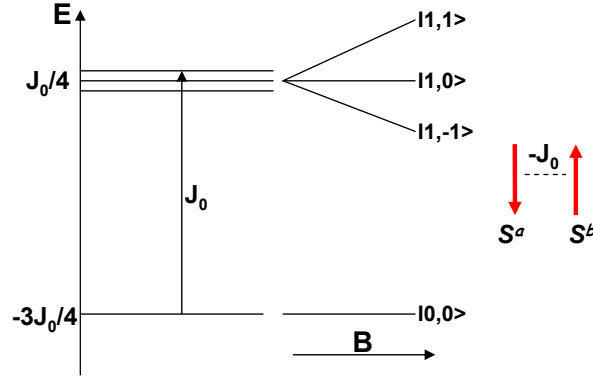
Figure 2.4: Energy level diagram for a dimer.

The magnetic susceptibility $\chi(T)$ of this kind of system can be described by using the Bleaney-Bowers equation which is defined as [19],

$$\chi = \frac{N}{2}[p(S = 0)\chi_0 + p(S = 1)\chi_1], \tag{2.10}$$

where $p(S)$ is the Boltzmann probability that the state S is occupied and is given by,

$$p(s) = \frac{e^{-E_s/k_B T}}{e^{-E_0/k_B T} + 3e^{-E_1/k_B T}}, \tag{2.11}$$

χ_0 and χ_1 can be obtain, using the following equation,

$$\chi_s = \frac{Ng^2\mu_B S(S+1)}{3k_B T}, \tag{2.12}$$

this gives, $\chi_0 = 0$ and $\chi_1 = 2C/T$, where $C = Ng^2\mu_B/(3k_B)$. Using the eigenvalues shown in Table 2.1, the dimer susceptibility can be expressed as:

$$\chi_{dimer} = \frac{(3C/T)}{3 + e^{J_0/k_B T}} \qquad (2.13)$$

Strong antiferromagnetic interactions which couple the spins into pairs can occur in real systems, called strongly *dimerized antiferromagnets*. The spins preferentially pair on the J_0 bonds as singlets, forming dimers. The dimers can then interact with their neighbors via the weaker interdimer interactions. In this case the triplet excitations have a finite bandwidth and a gap, Δ. The Hamiltonian can be solved by the use of mean field approximations, where the interaction between dimers is replaced by an effective field. One approach is the *Random Phase Approximation* (RPA) which provides a way to describe the dispersion relations of magnons in dimer systems by rewriting the Hamiltonian in terms of dimer spin operators and pseudo dimer spin operators and considering the spin operator independent of time. The magnetic excitation from the ground state singlet to the spin-1 triplet is known as a *magnon*. The origin of the gap is the energy cost associated with breaking a dimer. It is possible to follow the dispersion relation of the magnons by inelastic neutron scattering, where a neutron with an energy $\approx J_0$, breaks the dimer unit. Chapters 4 and 5 will be devoted to the analysis of the magnetic properties of the dimerized system $Sr_3Cr_2O_8$.

Magnetic excitations are also present when the ground state of the system has long-range ferromagnetic or antiferromagnetic order. These excitations can be viewed as a superposition of states where the spin component at an individual site is reduced. From a semi-classical point of view, they are coupled precessions of the moments about their equilibrium directions, with well defined frequency and the phase relations between the precessing moments on different sites.

Crystal-field excitations which are single ion rather than collective excitations have no dispersion. However, introduction of the interionic exchange interactions results in collective and weakly dispersive excitations about the crystal field energy. These excitations are linear combinations of single-ion transitions, called magnetic excitons. In the $4f$ materials, the magnetic excitations are magnetic excitons in which a transition between single-ion crystal field states is propagated through the crystal. This happens when the CF is comparable to, or greater than the exchange field between rare-earth ions.

So far, the different interactions in magnetic systems have been discussed. These interactions are present in both systems studied here. But, in each system they play a different role. For example, SO coupling is fundamental in $SrYb_2O_4$, defining the ground state, while for $Sr_3Cr_2O_8$ is weak. The CF is important in $Sr_3Cr_2O_8$, lifting the degeneracy of the orbitals and quenching the orbital momentum, but in $SrYb_2O_4$ is just a small perturbation, and the ground state stays degenerate keeping the Kramer's scheme. Therefore, the magnetic phenomena in both systems are expected to be different and a study of both compounds gives a very complete overview of condensed matter physics in insulating materials, from the quantum behavior of a geometrical frustrated spin-half system to the highly anisotropic, classical and also frustrated magnetism with unquenched orbital moment.

3 Experimental Techniques

3.1 Introduction

This chapter provides an insight into the basic theoretical concepts of the experimental techniques that have been used in this thesis with the aim of understanding the magnetic behavior of $Sr_3Cr_2O_8$ and $SrYb_2O_4$.

The samples studied here were synthesized at the Crystal Laboratory at the Helmholtz Zentrum Berlin. In both cases ($Sr_3Cr_2O_8$ and $SrYb_2O_4$) high quality large single crystals were produced for the first time specially for this work. In this chapter the basic theory of crystal growth will be explained briefly, while full details of the synthesis of each material are given in the corresponding chapters.

Bulk properties measurements were performed on these compounds. The thermodynamical properties that were investigated are DC-susceptibility, magnetization, heat capacity and magnetocaloric effect. These properties give information about the macroscopic magnetic behavior of these systems, providing important preliminary knowledge that was used to plan and develop the neutron scattering experiments.

Neutron scattering was used to investigate the crystal and magnetic structures as well as the magnetic excitations. The neutron interacts with a sample via the strong nuclear force and the dipole interaction. In a scattering experiment, the neutron perturbs the magnetic system generating spontaneous fluctuations, the response of this system is determined by the dynamical susceptibility which is related through the fluctuation-dissipation theorem to the dynamic correlation function [20, 3]. The dynamic correlation function is the Fourier transform of the spin-spin correlation function [1] which was explained in the previous chapter. Thus, there is an important and often quantitative link between theory and experiment. A wide variety of neutron scattering techniques have been employed in this thesis. Polarized and unpolarized neutron diffraction measurements have been performed in order to obtained a detailed analysis of the nuclear

---

[1]pair correlation function in terms of the total angular momentum J.

and magnetic structure of $SrYb_2O_4$. However, in this chapter only unpolarized neutron scattering will be discussed, leaving the details on polarized neutron scattering for Chapter 6. Inelastic neutron scattering has been used to study magnetic excitations and has been done in two types of instruments, the triple axis spectrometer and the time-of-flight spectrometer, both techniques will be explained here. In this chapter only the main equations and concepts are shown, for a more complete review of the technique, the following references are suggested: [20, 21, 22, 23, 24].

3.2 Powder Synthesis and Crystal Growth

The samples studied in this work were synthesized and growth in the Crystal Laboratory at the Helmholtz Zentrum Berlin für Materialien und Energie (HZB) in Berlin, Germany. The initial powders were prepared by a solid state reaction, which is a solvent-less or dry reaction. The reactants were oxides in powder forms and the reaction occurs through a thermal treatment without melting and without the presence of a solvent. Correct stoichiometric amounts of the reactants were mixed thoroughly, pressed and heated in a high temperature furnace above T= 1000°C.

When single phases of the desired compound were achieved, single crystal growth was performed using the floating zone technique.
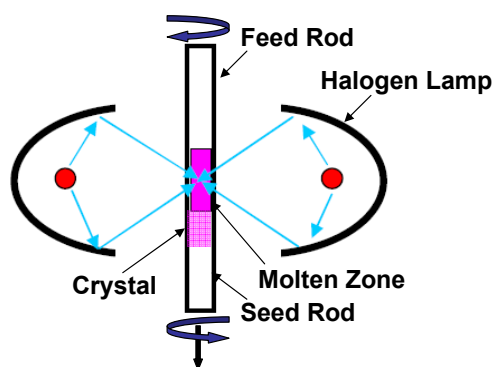
Figure 3.1: Principle of the Floating Zone crystallization method.

This technique is based on the formation of a molten zone that is held between two solid rods by its own surface tension. For the materials produced for this work a four-mirror optical floating zone furnace was used. It consists of four tungsten halide lamps focused by four ellipsoidal mirrors, the focused optical radiation provides an efficient and compact way for localizing the heat into a narrow band on the rod. Once a small

section of the rod has been melted, the molten (floating) zone is translated along the sample length by moving the material with respect to the radiation focus. Crystalline material is grown on the solidifying end of the floating zone and is often seeded by a single crystal as is shown in the Figure 3.1. This technique allows large single crystals of different materials to be grown, including transition metal and rare earth oxides. The details for the growths of each crystal will be given in the experimental details of the relevant chapters.

3.3 Thermodynamic Properties

The thermodynamic properties that were measured on $Sr_3Cr_2O_8$ and $SrYb_2O_4$ were magnetization, static susceptibility, heat capacity and magnetocaloric effect. Different techniques were employed such as a superconducting quantum interference device (SQUID), a vibrating sample magnetometer (VSM), a pulsed field induction magnetometer and calorimeters. A commercial Physical Property Measurement System (PPMS) from Quantum Design was used, for the susceptibility and high temperature (2 K-400 K) heat capacity [25]. Heat capacity and magnetocaloric effect were measured at dilution temperatures using CM14.5T which is a home made calorimeter [26]. Pulsed field induction magnetometers built at the High Magnetic Field Laboratory, in Dresden [27] were used to measure the magnetization at high magnetic fields (up to H= 100 T). The following section will discuss each type of measurement in turn.

3.3.1 Magnetization and DC Magnetic Susceptibility

Magnetization is the measurement of the magnetic moment of a sample when applying a magnetic field. It is described by the equation:

$$M(H,T) = \frac{1}{Z} \sum_n \langle \psi_n(H) | \hat{\mu} | \psi_n(H) \rangle \, e^{\left(\frac{-E_n(H)}{k_B T}\right)}, \tag{3.1}$$

where T is the temperature, Z is the partition function $Z = \sum e^{\frac{-E_n}{k_B T}}$, $\beta = 1/k_B T$, $|\psi_n(H)\rangle$ are the wavefunctions and $E_n(H)$ are the energies obtained by solving the full Hamiltonian of the system which includes a Zeeman term due to a magnetic field H. This Hamiltonian can be defined in different ways as explained in the previous chapter. The property that describes the response of a magnetic system to an external magnetic field is the magnetic susceptibility χ. This property is independent of the applied field for small magnetic fields and high temperatures, therefore when $g\mu_B H \ll k_B T$. In this

limit, the static magnetic susceptibility χ is:

$$\chi = \frac{M}{H}. \tag{3.2}$$

As mentioned previously different methods were used to measured the magnetization and static magnetic susceptibility (DC susceptibility) in $Sr_3Cr_2O_8$ and $SrYb_2O_4$. These are SQUID, VSM and induction magnetometry.

The standard method for measuring the magnetic moment of a sample is the inductive detection of the magnetic signal, where the sample is magnetized by a homogeneous magnetic field. The magnetometer is based on the measurement of the voltage in a pick-up coil produced by a time-varying magnetic flux following Faraday's law. The pickup coils are in general sensitive to the signal from the magnetized sample and also the magnetic field acting on it, so it is necessary to use specially designed coils (compensated coils) that consist of two or more loops wound in opposite directions, thus making them sensitive only to the gradient of the magnetic field. An example of a pick up coil is illustrated in Figure 3.2. The sample is moved through the coil's loops and the difference between the measured voltages in each loop is proportional to the magnetization of the sample.
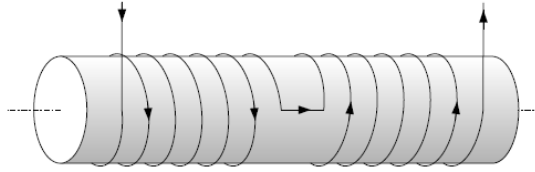
Figure 3.2: Compensated pick up coils for the inductive magnetometer.

The time derivative of the enclosed flux in the pick up coil is:

$$U_{ind}(t) = -\frac{d\Phi}{dt} = \tilde{\alpha}\frac{dB(t)}{dt} = \tilde{\beta}\frac{dM(t)}{dt} + \tilde{\gamma}\frac{dH(t)}{dt}, \tag{3.3}$$

where U_{ind} is the induced voltage. To find the magnetization it is necessary to know the coefficients $\tilde{\beta}$ and $\tilde{\gamma}$.

The most sensitive magnetometers available nowadays is the SQUID, where the induced current is not directly measured, but the coils are inductively coupled to a superconducting ring in which a tunneling barrier is implemented. The barrier can be tunneled by Cooper pairs, thus providing a good way to detect the field-dependent change of the ring current. Due to the laws of quantum mechanics the magnetic flux through the superconducting ring has to be a multiple of the magnetic flux quantum

$\Phi_0 = h/2e = 2.07 \times 10^{-15} Vs$ [2]. This effect makes the SQUID the most sensitive detector of magnetic flux. This superconducting device must be operated at liquid Helium temperatures and must be shielded from external magnetic fields, therefore it is usually designed to measure the magnetization at low fields and temperatures. For higher fields and temperatures a VSM is used.

In a VSM the sample is mounted on a stick which is positioned in the middle of a first order gradiometer pick-up coil pair (counter wound). The sample stick is moved in a sinusoidal way within the coils and the time-varying magnetic flux from the sample induces a current, which is amplified and lock-in detected [25]

For the high field magnetization measured on $Sr_3Cr_2O_8$, pulsed magnets made of ordinary copper wire isolated with Kapton film were used [27]. The compensation circuit in this magnetometer must be calibrated before each measurement at the current temperature by making a pulse at low voltage and changing the resistance value, this process leads to perfectly compensated field gradients. $\tilde{\gamma}$ is assumed to be zero, and $\tilde{\beta}$ can be approximated to 110 by assuming that the sample has a spherical geometry [28]. It is often necessary to compare and adjust the size of the magnetization measured using pulsed magnets to the results at lower fields from VSM or SQUID.

3.3.2 Heat Capacity and Magnetocaloric Effect (MCE)

The heat capacity is the derivative of the internal energy with respect to temperature:

$$C_p = \frac{\partial U}{\partial T},$$
(3.4)

where the magnetic internal energy U is given by:

$$U = -\frac{\partial lnZ}{\partial \beta} = \frac{1}{Z} \sum_n E_n e^{\frac{-E_n}{K_B T}}.$$
(3.5)

A Zeeman term can be added to the Hamiltonian and the heat capacity can be calculated at different fields applied along different crystallographic directions.

The heat capacity was measured using two systems, the CM14.5T calorimeter built in-house [26] and the adiabatic relaxation method in a Quantum Design Physical Property Measurement System (PPMS). In both cases, the sample is mounted on a microcalorimeter platform which is suspended by eight thin wires to a 'puck', which is a removable sample insert. The eight wires provide electrical and thermal connections to the embedded heater and thermometer on the microcalorimeter platform, and also ensure a degree

---

[2]http://www.qdusa.com/

of thermal isolation. The puck has a thermometer and thermal shield, and is mounted in high vacuum.

The measurement process consists of stabilizing the system at a particular temperature, then power is applied to a platform heater for a specified time, the temperature of the combined sample and platform is measured after the heater is switched off as the system relaxes adiabatically back to the initial temperature [29]. An addenda measurement is done in order to subtract the contributions from other parts of the system (puck, glue, connections etc).

The magnetocaloric effect has its origin in the coupling of the magnetic system of the solid to an applied external magnetic field H, resulting in a change of the magnetic contribution to the entropy of the system. This change can be measured by applying a homogeneous magnetic field on a thermally insulated solid while detecting changes in the sample temperature. The change of the magnetic entropy can lead for example to a change in the lattice vibration and therefore it can induce a temperature change of the solid. The infinitesimal adiabatic temperature change $\Delta T_{ad}(T_0, H_1 - H_0) = T_1 - T_0$ can be calculated using:

$$\Delta T_{ad}(T, \Delta H) = \int_{H_1}^{H_2} \left(\frac{T}{C(T,H)}\right)_H \left(\frac{\partial M(T,H)}{\partial T}\right)_H dH, \tag{3.6}$$

where C is the heat capacity. The direct measurement of the MCE includes the determination of the initial temperature T_0 and the temperature T_1 of the sample, when the applied magnetic field changes from an initial value H_0 to the final value H_1. In order to measure the temperature difference, a fast changing magnetic field is needed. The sample can be either moved out of a constant magnetic field or is fixed and the applied magnetic field is changed rapidly. This measurement was performed on $SrYb_2O_4$ using CM14.5T [26], further details will be given in Chapter 6.

3.4 Neutron Scattering Theory

The technique of neutron scattering can be used to determine crystal and magnetic structures as well as investigate phonons and magnetic excitations. The theory of this technique is outlined below.

3.4.1 Neutron Scattering Cross Section

In a neutron scattering process, a collimated beam of neutrons with well defined momentum $\hbar \boldsymbol{k}_i$ and energy E_i scatters from a sample at an angle θ with a wave vector $\hbar \boldsymbol{k}_f$

and a final energy E_f. Since the total energy and momentum are conserved quantities, the scattering event can be expressed by the following equations:

$$\boldsymbol{Q} \quad = \quad \boldsymbol{k}_i - \boldsymbol{k}_f, \quad Q^2 = k_i^2 + k_f^2 - 2k_i k_f \cos(2\theta), \tag{3.7}$$

$$\hbar\omega \quad = \quad E_i - E_f = \frac{\hbar^2 k_i^2}{2m} - \frac{\hbar^2 k_f^2}{2m} = \frac{\hbar^2(k_i^2 - k_f^2)}{2m}, \tag{3.8}$$

where m is the mass of the neutron, $\hbar$ Planck's constant, $\boldsymbol{Q}$ is the *wave vector transfer*, and $\hbar\omega$ denotes the *energy transferred* to the sample. The scattering process is explained in terms of the scattering triangle which is shown in Figure 3.3.

For elastic scattering no energy is transferred from the neutron to the sample, therefore $\hbar\omega = 0$, $|\boldsymbol{k}_i| = |\boldsymbol{k}_f|$ and the wavevector transfer is $Q = 2|\boldsymbol{k}|sin\theta$. In an inelastic scattering process both energy and momentum are transferred from the neutron to the sample, in that process $\hbar\omega \neq 0$ and $|\boldsymbol{k}_i| \neq |\boldsymbol{k}_f|$; a range of Q values are achieved by varying the scattering angle.
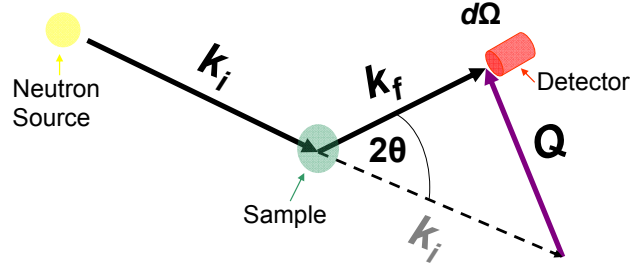
Figure 3.3: Diagram of the neutron scattering triangle, showing the principle components for an experiment.

The quantity detected in a scattering experiment is the flux of scattered neutrons, σ, within a particular range of energies $[E_f, E_f + dE_f]$ if an analyzer is used, that are detected in the solid angle range $[\Omega, \Omega + d\Omega]$ that the detector subtends with the sample. This quantity is referred to as the *partial differential cross section*. For neutrons scattered by a potential V, the partial differential cross section is given by [22]:

$$\frac{d^2\sigma}{d\Omega dE_f} = \frac{k_f}{k_i} \left(\frac{m}{2\pi\hbar^2}\right)^2 \sum_{\lambda_i, s_i} p_{\lambda_i} p_{s_i} \sum_{\lambda_f, s_f} |\langle \boldsymbol{k}_f s_f \lambda_f | \hat{V} | \boldsymbol{k}_i s_i \lambda_i \rangle|^2 \delta(E_{\lambda_i} - E_{\lambda_f} + \hbar\omega), \quad (3.9)$$

where s_i is the incident neutron spin state, λ_i is the state of the sample before the scattering process and E_{λ_i} is the energy of the state λ_i. p_λ, p_s are statistical weight

factors (assuming Boltzmann distribution) for the initial states $|\lambda_i s_i\rangle$. $\hat{V}$ is the operator corresponding to the scattering potential V. The subscript f indicates the states of the neutron and sample after the scattering process.

All the equations and discussions in this chapter correspond to unpolarized neutron scattering, in Chapter 6, the description of a polarized experiment is given.

3.4.2 Interaction Potentials

The neutron is a neutral spin-1/2 particle with a magnetic moment $\mu_n = -1.04\mu_N$. It interacts with the nuclei via the strong force and with the spin degrees of freedom in a material via an electromagnetic interaction or dipolar interaction. Since it has no charge it does not interact via the Coulomb interaction. The neutron-matter interaction is weak, unlike for X-ray and electron scattering and can be approximated by the first-order perturbation theory of the Born approximation, which assumes the incident and scattered neutron beams are plane waves. This simplifies the expressions for the cross-section and makes comparison between theory and experiment relatively simple. Both nuclear and magnetic neutron scattering are described here.

3.4.2.1 Nuclear Scattering

Nuclear scattering is the main component of the scattering cross section. The interaction between an incident neutron at position $\boldsymbol{r}$ and the lth atomic nucleus positioned at $\boldsymbol{R}_l$ can be described by a Fermi pseudo potential [22]:

$$V_l(\boldsymbol{r}) = \frac{2\pi\hbar^2}{m}b_l\delta(\boldsymbol{r} - \boldsymbol{R}_l). \tag{3.10}$$

where b_l is the scattering length of the atomic nucleus l and depends on the type of nucleus, the isotope and the relative orientation of the nuclear and neutron spins. The δ-function arises from the fact, that the strong nuclear force has a very short range and it is approximately spherically symmetrical.

The calculation of the scattering cross section using the potential in Eq. 3.10 and summing over all nuclei gives two terms, a coherent and an incoherent part:

$$\frac{d^2\sigma}{d\Omega dE_f} = \frac{d^2\sigma_{\text{coh}}}{d\Omega dE_f} + \frac{d^2\sigma_{\text{inc}}}{d\Omega dE_f} = \frac{k_f}{k_i}(S_{\text{coh}}(\boldsymbol{Q},\omega) + S_{\text{inc}}(\boldsymbol{Q},\omega)), \tag{3.11}$$

where $S_{coh}(\boldsymbol{Q}, \omega)$ and $S_{inc}(\boldsymbol{Q}, \omega)$ are the *dynamic correlation functions* and are given by:

$$S_{\text{coh}}(\boldsymbol{Q}, \omega) = \frac{1}{2\pi\hbar} \sum_{l,l'} b_l b_{l'} \int_{-\infty}^{+\infty} \langle e^{-i\boldsymbol{Q}\cdot\boldsymbol{R}_{l'}(0)} e^{i\boldsymbol{Q}\cdot\boldsymbol{R}_l(t)} \rangle e^{-i\omega t} dt, \qquad (3.12)$$

$$S_{\text{inc}}(\boldsymbol{Q}, \omega) = \frac{1}{2\pi\hbar} \sum_{l} \int_{-\infty}^{+\infty} \langle e^{-i\boldsymbol{Q}\cdot\boldsymbol{R}_l(0)} e^{i\boldsymbol{Q}\cdot\boldsymbol{R}_l(t)} \rangle e^{-i\omega t} dt. \qquad (3.13)$$

The coherent scattering manifested in the principal correlation function $S_{\text{coh}}(\boldsymbol{Q}, \omega)$, arises from the coherent interference between the same nucleus at different times, as well as from interference between different nuclei at different times. Therefore, coherent scattering provides information about the crystal structure and lattice excitations. In contrast, incoherent scattering arises only from interference effects of the same nucleus at different times. It is proportional to the variance in the neutron scattering lengths and causes an isotropic background in neutron experiments. The incoherent cross section is $\sigma_{inc} = 4\pi(\bar{b^2} - (\bar{b})^2)$

The major contribution to coherent nuclear scattering from a crystalline sample is the elastic contribution and this is caused by the periodic atomic planes, which produce peaks in the scattering pattern. These peaks, Bragg peaks, are seen at scattered wave vectors that satisfy the Bragg condition, so they are equal to a reciprocal lattice vector perpendicular to the crystal planes. The partial differential cross-section under this condition is:

$$\left(\frac{d^2\sigma}{d\Omega dE_f} \right)_{\text{nuc. elast.}} = \frac{N(2\pi)^3}{V_0} |F_N(\boldsymbol{Q})|^2 \delta(\boldsymbol{Q} - \boldsymbol{\tau}) \delta(\hbar\omega), \qquad (3.14)$$

here the crystal reciprocal lattice vector is τ, $\delta(\boldsymbol{Q} - \boldsymbol{\tau})$ reflects the periodicity of the crystal lattice and N is the number of unit cells included in the volume V_0. The *nuclear structure factor* is:

$$F_N(\boldsymbol{Q}) = \sum_l b_l \exp(i\boldsymbol{Q} \cdot \boldsymbol{R}_l) e^{(-W_l(\boldsymbol{Q}, T))}, \qquad (3.15)$$

the sum in l is over the atoms in the unit cell, located at positions $\boldsymbol{R}_l$. The factor $\exp(-W_l(\boldsymbol{Q}, T))$ is the (temperature dependent) Debye-Waller factor which indicates the probability that an atom is at position $\boldsymbol{R}_l$ at temperature T. This factor describes the thermal fluctuations of the atoms about their equilibrium positions.

3.4.2.2 Magnetic Scattering

Magnetic scattering results from the interaction of the magnetic moment of the neutron with magnetic fields arising from the spin and orbital momentum of the unpaired electrons of the ions in the sample. The magnetic dipole moment of the neutron, $\boldsymbol{\sigma}$, interacts with this electromagnetic field. In this case the potential is:

$$\hat{V}_m(\boldsymbol{Q}) = r_0 \boldsymbol{\sigma} \cdot \hat{\boldsymbol{M}}_\perp, \tag{3.16}$$

$$\hat{\boldsymbol{M}}_\perp = \tilde{\boldsymbol{Q}} \times \left(-\frac{1}{2\mu_B}\hat{\boldsymbol{M}}(\boldsymbol{Q}) \times \tilde{\boldsymbol{Q}}\right). \tag{3.17}$$

$\hat{M}(\boldsymbol{Q})$ is the Fourier transform of the magnetic field distribution in the sample, $\tilde{\boldsymbol{Q}}$ is the unit vector along the direction of the scattering vector $\boldsymbol{Q}$, r_0 is the classical electron radius. For magnetic scattering to occur only the component of $\hat{M}(Q)$ perpendicular to the scattering vector $\boldsymbol{Q}$ is observable this is denoted by $\hat{M}_\perp(Q)$, the scattering vector $\boldsymbol{Q}$, must be perpendicular to the magnetic field distribution of the sample.

Scattering due to Spin Only

The partial differential cross-section for a sample with one type of magnetic ion that has quenched orbital angular momentum as commonly found in transition metal oxides is:

$$\left(\frac{d^2\sigma}{d\Omega dE_f}\right)_{\text{mag}} = (\gamma r_0)^2 \frac{k_f}{k_i} \left(\frac{g}{2}f(\boldsymbol{Q})\right)^2 e^{(-2W(\boldsymbol{Q},T))} \sum_{\alpha\beta}(\delta_{\alpha\beta} - \frac{Q_\alpha Q_\beta}{Q^2})S^{\alpha\beta}(\boldsymbol{Q},\omega),$$
$$\tag{3.18}$$

where $f(\boldsymbol{Q})$ is the magnetic form-factor, γ is the gyromagnetic ratio and g is the Landé splitting-factor, which for spin only scattering is 2. The term $(\delta_{\alpha\beta} - \frac{Q_\alpha Q_\beta}{Q^2})$ ensures, that only spin components perpendicular to $\boldsymbol{Q}$ contribute to the cross-section. The magnetic form-factor is given by:

$$f(\boldsymbol{Q}) = \int s_d(\boldsymbol{r})e^{i\boldsymbol{Q}\cdot\boldsymbol{r}}d\boldsymbol{r}, \tag{3.19}$$

where s_d is the normalized density of the unpaired electrons in the ion d. The form factor arises because of the finite spatial extent of the scattering object (electron cloud of unpaired electrons), which cannot be approximated by a δ-function, as it is the case for nuclear scattering. Since $f(\boldsymbol{Q})$ decreases rapidly with $\boldsymbol{Q}$, it limits the range in which

magnetic scattering can be observed to the low-$\boldsymbol{Q}$ region.

The dynamic correlation function $S^{\alpha\beta}(\boldsymbol{Q},\omega)$, which is the space and time Fourier transform of the time-dependent spin correlation function $\langle s_i^\alpha(t)s_j^\beta(0)\rangle$, is defined as:

$$S^{\alpha\beta}(\boldsymbol{Q},\omega) = \frac{1}{2\pi\hbar}\int_\infty^\infty \frac{1}{N}\sum_{i,j} e^{(\mathrm{i}\boldsymbol{Q}\cdot(\boldsymbol{R}_j-\boldsymbol{R}_i))}\langle s_i^\alpha(t)s_j^\beta(0)\rangle e^{(\mathrm{i}\omega t)}dt, \qquad (3.20)$$

where $s_j^\beta(t)$ is the angular momentum operator in the Heisenberg picture: $s_j^\beta(t) = e^{i\mathcal{H}t/\hbar}s_j^\beta e^{-i\mathcal{H}t/\hbar}$. If $\langle s_j^\alpha\rangle\langle s_{j'}^\beta\rangle$ is added and subtracted, the scattering function may be written as the sum of a static (elastic) and dynamic (inelastic) contribution:

$$S^{\alpha\beta}(\boldsymbol{Q},\omega) = S^{\alpha\beta}(\boldsymbol{Q}) + S_d^{\alpha\beta}(\boldsymbol{Q},\omega), \qquad (3.21)$$

$$S^{\alpha\beta}(\boldsymbol{Q}) = \delta(\hbar\omega)\frac{1}{N}\sum_{jj'}\langle s_j^\alpha\rangle\langle s_{j'}^\beta\rangle e^{(\mathrm{i}\boldsymbol{Q}\cdot(\boldsymbol{R}_j-\boldsymbol{R}_i))}, \qquad (3.22)$$

$$S_d^{\alpha\beta}(\boldsymbol{Q},\omega) = \frac{1}{2\pi\hbar}S^{\alpha\beta}(\boldsymbol{Q},\omega) = \frac{1}{\pi}\frac{1}{1-e^{-\beta\hbar\omega}}\chi_{\alpha\beta}''(\boldsymbol{Q},\omega), \qquad (3.23)$$

where $\chi_{\alpha\beta}''(\boldsymbol{Q},\omega)$ is the corresponding susceptibility function, defined in the previous chapter, that is related to the correlation function by the fluctuation-dissipation theorem [20].

The correlation function contains all the information about the magnetic structure and dynamics of the system under investigation, giving the information of the response of the sample to the magnetic field created by the neutron. Each neutron imparts energy $\hbar\omega$ and momentum $\hbar\boldsymbol{Q}$ to the sample, so an scattering peak is interpreted as due to the creation or annihilation of quasi-particles (e.g. magnons) or elementary excitations in the system, with energy $|\hbar\omega|$ and crystal momentum $\hbar\boldsymbol{Q} = \hbar(\delta_k - \tau)$, where τ is a reciprocal lattice vector.

Scattering by Ions with Spin and Orbital Momentum

As explained in the previous chapter the effect of the crystal field on a rare earth ion is to partially or totally remove the $2J+1$ degeneracy of the ground state however it is not usually strong enough to quench the orbital angular momentum. The contributions from the interaction of the neutron with the orbital moment of the sample can be included in the neutron cross section given in Equation 3.18 by generalizing the spin correlation function (Eq. 3.20) to the pair correlation function, where the spin operator S is replaced by the total angular momentum J. Another change is necessary in the cross section expression and it is the modification of the magnetic form factor. For the generalized

case, this is:

$$f(\boldsymbol{Q}) = \frac{g_s}{g}\mathcal{J}_0 + \frac{g_L}{g}(\mathcal{J}_0 + \mathcal{J}_2), \tag{3.24}$$

$$\mathcal{J}_n = 4\pi \int_0^\infty j_n(Qr)s(r)r^2 dr, \tag{3.25}$$

where $j_n(Qr)$ is a spherical Bessel function of order n, g_s and g_L are the spin and orbital Landé factors.

All these equations have been obtained for the case where $|(Q)|^{-1}$ is large compared to the mean radius of the orbital wavefunctions of the unpaired electrons. This is called the dipole approximation.

Long Range Magnetic Order

When $M(\boldsymbol{Q})$ is a periodic function long range magnetic order occurs in the crystal and the magnetic scattering displays interference elastic peaks or magnetic Bragg peaks. Those peaks can be detected if the neutron wave vector transfer $\boldsymbol{Q}$ has a component perpendicular to the direction of the ordered spins and equals a magnetic reciprocal lattice vector $\boldsymbol{\tau}_M = \boldsymbol{\tau} + \boldsymbol{K}$. The quantity $\boldsymbol{K}$ is called the magnetic propagation vector. In the case of magnetic coherent scattering, the partial differential cross-section is:

$$\left(\frac{d^2\sigma}{d\Omega d\hbar\omega}\right)_{\text{mag. coh. elast.}} = \frac{(2\pi)^3 N_m}{V_0}\left(\frac{\gamma r_0}{2}\right)^2 \sum_{\alpha\beta}(\delta_{\alpha\beta} - \frac{Q_\alpha Q_\beta}{Q^2})F_M^\alpha(\boldsymbol{Q})F_M^\beta(\boldsymbol{Q})$$
$$\times\delta(\boldsymbol{Q} - \boldsymbol{\tau}_M)\delta(\hbar\omega), \tag{3.26}$$

where N_M is the number of magnetic unit cells contained in the volume V_0. Here, the magnetic structure factor $F_M^{\boldsymbol{\alpha}}(\boldsymbol{Q})$ is defined as:

$$F_M^{\boldsymbol{\alpha}}(\boldsymbol{Q}) = f(\boldsymbol{Q})\exp(-W(\boldsymbol{Q},T))\sum_l \mu_l^\alpha \exp(\mathrm{i}\boldsymbol{Q}\cdot\boldsymbol{R}_l), \tag{3.27}$$

where, μ_l^α is the α component of the magnetic moment of the lth atom located at position $\boldsymbol{R}_l$ in the magnetic unit cell.

The collection of a suitable set of magnetic Bragg peaks intensity and their comparison to the theoretical expression (3.27) enable a precise determination of the magnetic structure of a given system. Chapter 6 gives a practical example of the analysis of magnetic elastic scattering on $SrYb_2O_4$.

The Detailed Balance Factor

The sample can be probed by observing either neutron energy loss or neutron energy gain. In the case of neutron energy gain the temperature becomes an important factor in determining the occupation number of a particular energy state. As the probability of a transition depends on the thermal population of the initial state. The differences between the probabilities of the neutron gaining or losing energy is accounted through the detailed balance factor. The correlation function for neutron energy loss becomes:

$$S(-\boldsymbol{Q}, -\omega) = e^{(-\hbar\omega/k_B T)} S(\boldsymbol{Q}, \omega), \tag{3.28}$$

the term $e^{(-\hbar\omega/k_B T)}$ is known as the detailed balance factor. For a neutron energy gain transition (defined as $\omega < 0$), the initial state of the sample is an excited state, and has a thermal occupation given by the Boltzmann factor.

3.5 Neutron Scattering Experiments

There are two types of modern research facilities which provide neutron flux for scattering experiments; the nuclear reactor and the spallation or pulsed source. In the first one, a steady flux of neutrons is produced in a controlled fission process. The neutrons are thermalized to a particular temperature in a moderator and the energy distribution is Maxwell-Boltzmann. In a spallation source pulses of neutrons are produced by bombarding heavy targets such as W, Ta, Pb, or Hg with high-energy protons. The energy ranges of the neutrons are broad and have a larger proportion of neutrons at higher energies than the Maxwell-Boltzmann distribution.

In this work a variety of experiments were done using different instruments to measure elastic and inelastic neutron cross-sections on the two different samples $Sr_3Cr_2O_8$ and $SrYb_2O_4$. Measurements were made using the reactor sources at the Institute Laue Langevin (ILL), France, and at the Helmholtz Zentrum Berlin (HZB), Germany and the spallation source, ISIS at the Rutherford Appleton Laboratory, UK. This section is devoted to the description of the scattering techniques rather than the specifications for each instrument used. Those specifications can be found in the experimental details section of each chapter and in the web pages of each facility [30, 31, 32].

3.5.1 The Neutron Diffractometer

The aim of a neutron diffraction experiment is to gain insights into the nuclear and/or magnetic structure of a given sample. The partial differential nuclear and/or magnetic

coherent elastic cross section are measured for a broad range of wave vector transfer Q. Peaks in intensity appear in the detector that fulfill Bragg's law $n\lambda = 2dsin\theta$, where λ is the incident wave length, d is the inter-planar spacing and 2θ is the angle between the incident and diffracted beam.
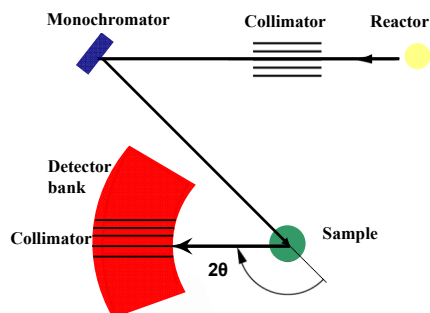

Figure 3.4: The layout of the neutron diffractometer.

Figure 3.4 shows the layout of a neutron diffractometer at a reactor source. An incident neutron beam is collimated and its wavelength is selected by the monochromator. The monochromated neutron beam is scattered by the sample and the neutrons are diffracted into an array of detectors. No energy analysis is made.

In this work four different diffractometers were used, a fine resolution powder diffractometer (E9, HZB) with a wide angle detector bank, a focusing powder diffractometer (E6, HZB) with a 2D detector, a two-axis diffractometer (E4, HZB) with a 2D detector and a multidetector diffractometer with full **XYZ** polarization analysis (D7, ILL). Using these instruments both, powder and single crystal samples were measured.

Powder diffraction is a very powerful and unique tool for characterizing materials in terms of the types and quantities of phases present in them, the crystal structure and unit cell parameters, and is also a successful tool to solve magnetic structures of materials. The final powder pattern is obtained by step scanning a detector on a circular path around the sample with small increments $\Delta(2\theta)$

A very powerful and successful method of extracting structural information from a powder pattern was developed by Rietveld [33]. His method is based on a least-squares refinement of the entire powder pattern until the best fit between a calculated and the measured data set is reached. The calculated pattern is obtained by simultaneously refining the model the crystal structure as well as the instrumental factors and other characteristics of the investigated specimen. This method was used to obtain the nuclear and magnetic structure of $SrYb_2O_4$, the details will be given in Chapter 6.

3.5.2 The Triple Axis Spectrometer, TAS

A triple axis spectrometer is designed to measure inelastic neutron scattering at a chosen point in $(\boldsymbol{Q}, \hbar\omega)$ space. Essentially it consists of a monochromator, a sample and an analyzer each sitting in a rotable axis. Figure 3.5 shows the layout of the spectrometer. The
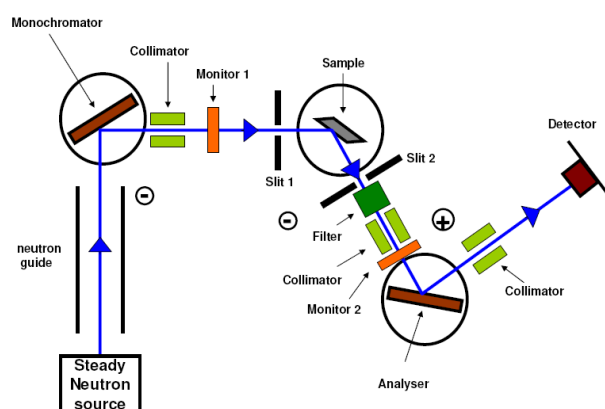

Figure 3.5: The layout of the triple axis spectrometer. Taken from reference [34].

initial energy and wave vector are selected by a Bragg reflection at the monochromator or first axis. The monochromated neutron beam is scattered by the sample which defines the second axis. The final energy of the neutrons is measured by an array of single crystals in the analyzer which is the third axis. The intensity of the scattered neutrons at the resulting energy and wave vector transfer are then measured in the detector. Several collimators are placed along the beam path in order to reduce beam divergence. Filter elements reduce the higher order scattering. The background counts can be reduced by adjusting the slits before and after the sample.

In a typical TAS experiment, the final energy of the neutrons is often fixed by the analyzer and scans are made by varying either the wave vector transfer (constant energy scans) or the energy (constant wave vector scans). In this way only the magnitude of the momentum of the incoming neutrons is varied as well as the sample and scattering angle. The advantage of this scan mode is that it provides a larger dynamic range compared to what is available with a fixed incident wavevector, nevertheless other types of scans can be performed according to the desired resolution and dynamic range. This instrument is well suited to the study of collective excitations in single crystals as it is very flexible and the resolution can be very sharp. In this work, the TAS V2-Flex at HZB was used to investigate the magnetic excitations in $Sr_3Cr_2O_8$ the results are shown in Chapter 5.

3.5.3 The Time of Flight Spectrometer, ToF

Energy analysis of the neutrons scattered at a sample can be done by measuring the neutron time of flight over known distances. This is the conceptual basis for the time of flight spectrometer (ToF). These spectrometers were originally designed to use pulsed neutrons in spallation sources but can also be implemented at nuclear reactors by creating a pseudo pulsed source by using additional choppers. There are two possible setups, the direct geometry and the inverse geometry. Both are shown in Figure 3.6.
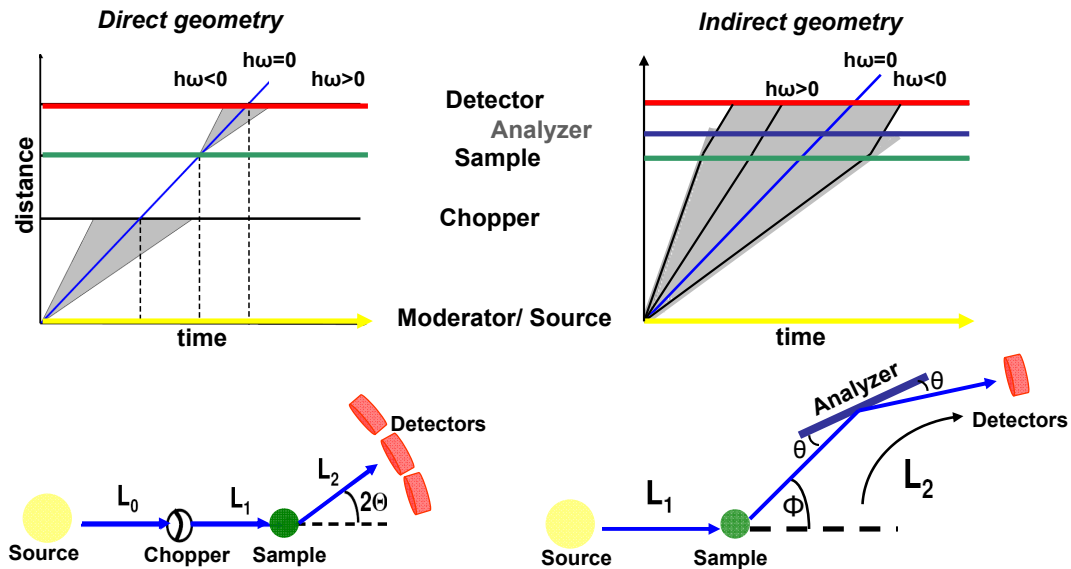
Figure 3.6: Diagrams of the direct and indirect geometry ToF spectrometers. Above, the distance vs time plots for both geometries. The gray regions represent the neutron velocity distribution in the different stages of the process.

In the direct geometry instrument, the incident beam of neutrons is monochromated by a chopper. The monochromating chopper is phased with respect to the incoming pulse so that it is open at a specific time after the pulse is created and so selects a specific initial neutron energy. The neutrons scattered by the sample are measured by an array of detectors that cover a large range of scattering angles.

The detectors record the angular position of the scattered neutrons and the time at which they are counted. The time is used to obtain the final neutron energy, while the time and detector position define the wavevector transfer Q.

In an inverted or indirect geometry spectrometer a broad wavelength band of neutrons is incident on the sample, the lower and upper limits being adjusted by a chopper. The

Wavelength band selection effectively defines the energy resolution and energy transfer range (inelastic). The scattered neutrons are energy analyzed by means of Bragg scattering from an array of analyzer crystals. The detectors measure the neutron intensity as a function of scattering angle and time. The incident energy is calculated from the time of flight of the neutrons taking into account the final neutron velocity. This type of spectrometer can offer high resolution [35].

In this work, both types of ToF spectrometers were used. The indirect geometry spectrometer IRIS at ISIS and the direct geometry spectrometer IN5 at ILL were used to measure the low energy magnetic excitations in $SrYb_2O_4$. The direct geometry spectrometer Merlin at ISIS was used to measure the crystal field excitations in $SrYb_2O_4$ and the magnon excitations in $Sr_3Cr_2O_8$. The direct geometry spectrometer NEAT at HZB was used to measure the the magnon excitations in $Sr_3Cr_2O_8$ in a powder sample. The details of these experiments will be given in Chapters 5 and 7.

Merlin and IN5 belong to a new type of ToF spectrometers as they have a large cylindrical array of pixelated position sensitive detectors (PSD) mounted inside a vacuum time-of-flight chamber. These detectors allow the measurement of the components of the scattering vector out of horizontal plane. Therefore, two spatial dimensions in addition to time of flight are measured simultaneously. For each sample position these spectrometers produce a large three dimensional cut out of the four dimensional $S(\boldsymbol{Q}, \omega)$. PSDs cover a large gapless detection surface with a spatial resolution comparable to triple-axis instruments making these spectrometers ideal for single crystal studies [36, 37, 38].

4 General Properties of the Frustrated Quantum Dimer Magnet $Sr_3Cr_2O_8$

4.1 Introduction

Dimerized antiferromagnets are systems that have a particularly strong antiferromagnetic interaction which couples the magnetic ions into pairs. These pairs of magnetic ions form units called dimers and the system can be described with a Heisenberg Hamiltonian as was explained in Chapter 2. The intradimer exchange, called J_0 is then the strongest magnetic interaction in the system. If the dimer units do not interact with each other the expected ground state is a non-magnetic singlet state with a total spin $S = 0$ and the excitations are triply degenerate with spin $S = 1$ and are gapped by an energy J_0. The triplet state can be identified by the presence of a quasiparticle called a triplon or magnon with $S = 1$. The triplons are bosons and as such, bosonic statistics can be used to describe them. An intrinsic property of these triplons is the hard core constraint that excludes states with more than one quasiparticle per dimer. Systems where dimerization occurs, maintain a singlet ground state down to absolute zero in temperature and never show long-range magnetic order in the absence of a magnetic field. Applying a magnetic field lifts the triplet degeneracy by Zeeman splitting the excited state. The energy of one of the triplet excited states is reduced by the field and when the field is large enough, the system goes through a quantum critical point (QCP) and the magnons condense into the ground state producing different kinds of magnetic order. The order which depends on the symmetry conditions can be described as a Bose Einstein condensation (BEC), Wigner crystallization or supersolidity [39, 40].

The dimers can interact with each other through interdimer exchange interactions. If these interactions are weak, the ground state continues to be singlet however the magnons become mobile, developing a dispersion, which is reflected in the appearance of an excitation bandwidth. The strength of intra and interdimer interactions are very specific to the particular compound and depend on the nuclear structure and type of magnetic bonding between ions, such as direct exchange, dipole interactions or superexchange. The interac-

tions also depend on the magnetic orbitals and orbital ordering can give rise to preferred exchange paths and reduce anisotropy. Furthermore, in some cases the interdimer interactions are frustrated and this also strongly influences the nature of the magnetism. Over the last decade, dimerized AF magnets have received a large amount of attention. Their properties are now experimentally accessible due to advances in experimental techniques such as high field magnets with fields of up to H=100 T and sophisticated inelastic neutron scattering instruments such as time of flight spectrometers with position sensitive detectors. These materials have a range of different nuclear structures, which give rise to different dimensionalities of their magnetic couplings, different energy scales of the excitations and different unusual field-induced quantum phases. Furthermore, it should be noted that in real systems the simple Heisenberg Hamiltonian is complicated by single ion anisotropy, dipolar interactions and Dzyaloshinskii-Moriya interactions, amongst others. A typical example of a quantum dimerized system is TlCuCl$_3$, which consists of spin$-1/2$ dimers coupled in a three-dimensional lattice. It has the expected spin-singlet ground state and a gapped dispersive one-magnon excited state. Application of a magnetic field causes Bose-Einstein condensation of magnons at a critical field H_c, while for higher fields magnetization increases smoothly to saturation [41, 42]. The two dimensional system, BaCuSi$_2$O$_6$ consists of Cu^{2+} ions arranged on a bilayer of square lattices with unfrustrated antiferromagnetic couplings. The intrabilayer coupling is dominant so that the system can be regarded as a square lattice of dimers. The ground state is again a singlet, the excitations are dispersive gapped magnons [43, 44] and as for TlCuCl$_3$, magnetization increases smoothly above a critical field. The spin-1/2 Shastry-Sutherland antiferromagnet SrCu$_2$(BO$_3$)$_2$ consists of spin-1/2 dimers arranged at right angles to each other so that the antiferromagnetic interdimer couplings are competing. The ground state is again a singlet and the excitations form a gapped mode whose dispersion bandwidth is suppressed by the high level of frustration [45]. Magnetization is characterized by a critical field and for higher fields a series of magnetization plateaux are found where the condensed magnons form superlattices with spontaneous breaking of translation symmetry known as Wigner crystallization [46], this happens when the effective repulsion between the triplons overwhelms their kinetic energy. In this case, magnetic field induced order is not described by BEC since the rotational symmetry around the magnetic field is broken [47, 46, 48].

The dimerized family of antiferromagnets with formula A$_3$M$_2$O$_8$ (A=Ba, Sr and M=Mn, Cr) crystallize in a hexagonal structure with space group $R\bar{3}m$ at room temperature. The magnetic ions lie on hexagonal bilayers where the dominant intrabilayer interaction
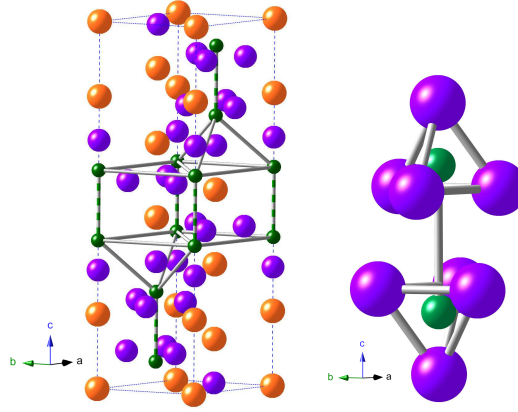
Figure 4.1: (left) $Sr_3Cr_2O_8$ unit cell. Orange atoms: Sr, purple: O, green: Cr. Grey bonds link the Cr ions. Grey plus green bonds depicted the dimer bond. (right) The two CrO_4 tetrahedra that form a dimer unit. Note that the tetrahedra are counter rotated.

is antiferromagnetic and gives rise to the dimerization. These dimers are coupled three-dimensionally, both within the bilayers and between bilayers to give a highly frustrated arrangement due to the triangular symmetry (see Fig. 4.1). It would be expected that this frustration leads to competing states and the possibility of novel magnetism. In these compounds, the magnetic ion (Mn or Cr) is in the high oxidation state of 5+. This leads to spin-1 in the case of Mn^{5+} ions. In the case of $Ba_3Cr_2O_8$ and $Sr_3Cr_2O_8$ the Cr^{5+} ions have a single electron in the $3d$ shell, leading to $S = 1/2$ on each site and the orbital moment L is quenched. In this chapter, the magnetic properties of one of the members of this family, $Sr_3Cr_2O_8$, will be explained in detail. The room temperature crystal structure of $Sr_3Cr_2O_8$ was investigated using X-ray single crystal diffraction in 1989 by Cuno and Müller and was found to be hexagonal with space group $R\bar{3}m$ [49]. In 2008 Chapon *et al.* [50] performed powder neutron diffraction at different temperatures on this system and refined the high temperature structure in $R\bar{3}m$ getting the lattice parameters $a_h = b_h = 5.57\,\text{Å}$, $c_h = 20.17\,\text{Å}$ (here the 'h' subscript denotes hexagonal structure). The atomic positions are listed in Table 4.1. Figure 4.1(left) shows the atomic unit cell in the high temperature hexagonal structure, Cr^{5+} ions are shown in green, O^{2-} in purple and Sr^{2+} in orange. There are in total 6 Cr^{5+} ions in the unit cell. The figure also shows the bonds between Cr^{5+} ions. Cr^{5+} form hexagonal layers that lie in the (a_h, b_h)-plane and are paired into bilayers in the c_h direction. These bilayers are in turn stacked along c_h in a repeated $ABCABC$ pattern, where layer B is translated with respect to A and C is translated with respect to B. Figure 4.1(right) is a close up to a pair of Cr^{5+} ions which form the basic dimer unit. The Cr^{5+} ions are in the $6c$ Wyckoff

Table 4.1: Atomic positions for both, high (275 K) and low (1.6 K) temperature crystal structures, according to Chapon *et al.* [50]. At 275 K the space group corresponds to $R\bar{3}m$ and the lattice parameters are: $a_h = b_h = 5.57$ Å, $c_h = 20.17$ Å. At low temperatures, the space group is $C2/c$, unique-axis b, and the lattice parameters are: $a_m = 9.66$ Å, $b_m = 5.5437$ Å, $c_m = 13.7882$ Å, $\beta = 103.66°$.

275K				
Site(W)	x	y	z	B(Å^2)
Sr1(3a)	0	0	0	1.17(6)
Sr2(6c)	0	0	0.20326(8)	0.73(4)
Cr(6c)	0	0	0.4058(1)	0.39(7)
O1(6c)	0	0	0.3234(9)	2.73(7)
O2(18h)	0.8321(1)	0.1679(1)	0.89852(5)	1.02(4)
1.6K				
Site(W)	x	y	z	B(Å^2)
Sr1(4e)	0	0.2850(5)	1/4	0.14(4)
Sr2(8f)	0.1002(4)	0.2479(3)	0.5545(1)	0.17(2)
Cr(8f)	0.2020(7)	0.2544(7)	0.8582(2)	0.22(5)
O1(8f)	0.1581(4)	0.3129(4)	0.7351(1)	0.35(3)
O2(8f)	0.1161(4)	0.7800(5)	0.5996(3)	0.25(3)
O3(8f)	0.8545(3)	-0.0104(5)	0.6038(2)	0.25(3)
O4(8f)	0.3744(3)	0.9858(5)	0.5894(2)	0.25(3)
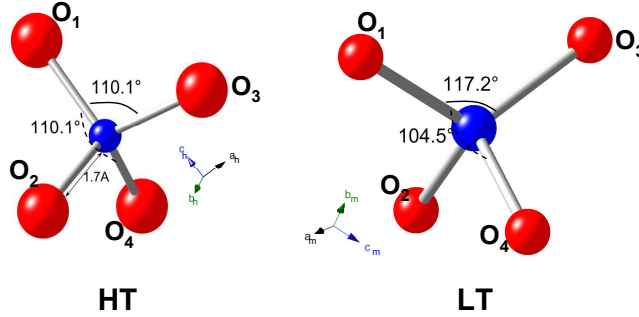
Figure 4.2: CrO$_4$ tetrahedra at high temperature (left) and low temperature (right). The tetrahedral angles (O1-Cr-O3) (O1-Cr-O4) change by 6% .

position and are surrounded by oxygen tetrahedra. These tetrahedra are counter rotated with respect to each other. The oxygen tetrahedron is undistorted and all O-Cr-O angles are 110.1° (See Figure 4.2(a)). The shortest Cr^{5+}-Cr^{5+} distance is the first neighbor intrabilayer distance (labeled d_0, in Figure 4.3) which is 3.84 Å. The distances between the Cr ions are displayed in Figure 4.3(left). For example d_1 is the interbilayer distance and d_2 is the intralayer distance. Chapon *et al.* published low-temperature powder-neutron
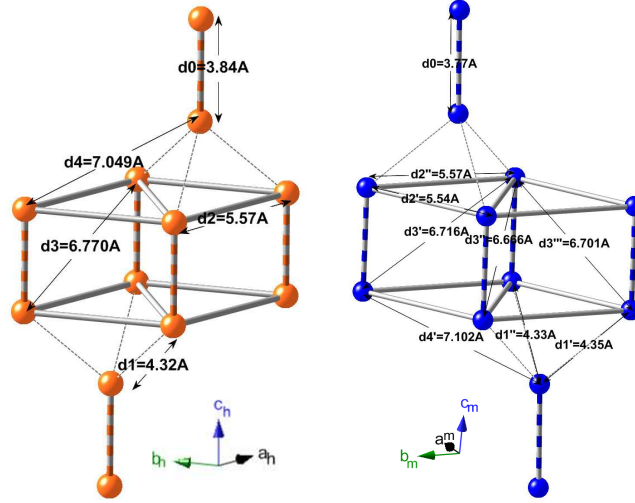
Figure 4.3: High (left) and low (right) temperature nuclear structures showing only the Cr^{5+} ions. The distances between neighboring ions are labeled on the diagram.

Table 4.2: Distances between Cr^{5+} ions for the low and high temperature structures.

d_i	Hexag. (Å)	Monocl. (Å)
d_0	3.845	3.774
d_1'	4.317	4.351
d_1''		4.330
d_2'	5.572	5.544
d_2''		5.570
d_3'	6.770	6.716
d_3''		6.666
d_3'''		6.701
d_4'	7.049	7.102
d_4''		7.035

diffraction results that showed a structural phase transition. Below 275 K, superlattice reflections were observed and fundamental peaks were split. The superlattice peaks were indexed with $\boldsymbol{k} = (0, 0, 3/2)$. The refinement of the 1.6 K pattern gives a monoclinic structure with space group $C2/c$, unique-axis b [50]. In the monoclinic phase the lattice parameters are: $a_m = 9.66$ Å, $b_m = 5.5437$ Å, $c_m = 13.7882$ Å, $\beta = 103.66°$. (The subscript 'm' denotes monoclinic structure). The atom positions are listed in Table 4.1. Below the structural distortion the hexagonal distances become unequal. For example where at high temperatures there was one interbilayer distance d_1, at low temperature there are two distances d_1' and d_1'', the intrabilayer distances also change, at low temper-
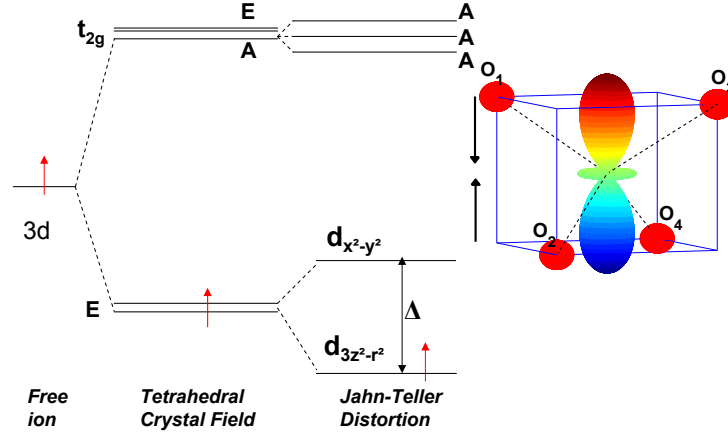
Figure 4.4: Crystal field scheme for Cr^{5+} in a tetrahedral environment. A Jahn-Teller distortion splits the low lying e orbitals. A sketch of the distorted tetrahedral is shown. A compression along the O1-Cr-O3 edge of the tetrahedral favors $3z^2 - r^2$.

ature there is only one distance d_3 and at low temperature there are three distances d_3', d_3'' and d_3''' (see Figure 4.3 and Table 4.2).

The CrO$_4$ tetrahedra also become distorted at low temperature. The tetrahedral angles (O1-Cr-O3) (O1-Cr-O4) change by 6% leading to a large modification of the structue as shown in Figure 4.2. There is an anisotropic displacement of the apical oxygen O1 that increases on cooling. This displacement is coupled to the displacement of the Sr1 ions and a slight rotation of the O2 ions in the tetrahedral basal plane. This phase transition may be considered to be a Jahn-Teller distortion. In the high temperature nuclear structure the point symmetry for the Cr ions is trigonal 3m: C$_{3v}$. The tetrahedral crystal field splits the d orbitals of the Cr ion into nonbonding E orbitals (e$_g$) and antibonding $A1 + E$ (t$_{2g}$) orbitals. The single electron of Cr^{5+} occupies the doubly degenerate low lying E state, formed by the $3z^2 - r^2$ and $x^2 - y^2$ orbitals. The Cr^{5+} ions are then clearly Jahn-Teller active and a Jahn-Teller distortion which lifts the orbital degeneracy would lower the electronic energy as indeed happens. In the low temperature structure, the site symmetry is triclinic, C_1, and there is compression along the O1-Cr-O3 edge of the tetrahedron that lifts the degeneracy of the E doublet and lowers the energy of the $3z^2 - r^2$ level (Similar to an axial compression along one of the 4-axis of a perfect tetrahedron). Figure 4.4 shows the crystal field scheme for both space groups. It should be noted that the Jahn-Teller distortion of the tetrahedral environment has not been well studied compared to the octahedral environment. Although the same orbital ($3z^2 - r^2$) is occupied by each Cr^{5+} ion the direction in which this orbital points varies. The or-
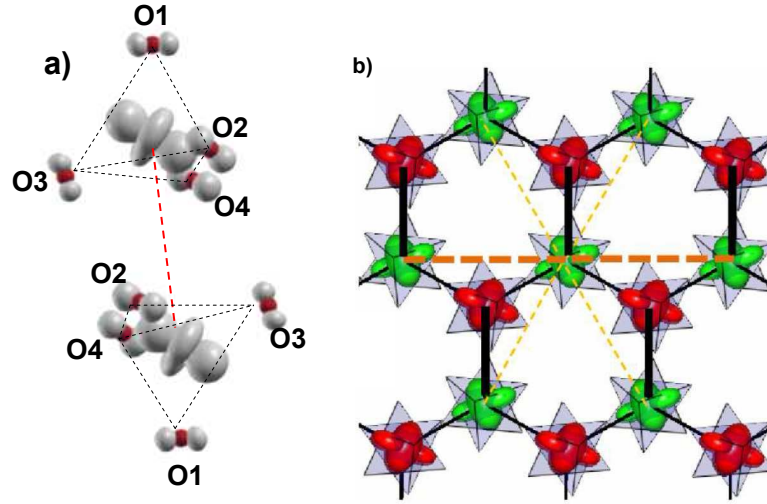
Figure 4.5: (a)Real space density map illustrating the occupied Cr^{5+} $d_{3z^2-r^2}$ orbital in the monoclinic structure of $Sr_3Cr_2O_8$ and the ferro-orbital ordering occurring within a dimer. (b) Orbital ordering superstructure in the low temperature phase of $Sr_3Cr_2O_8$, The $d_{3z^2-r^2}$ have different colors depending on their direction. There is an antiferro-orbital ordering within the bilayers [50, 51].

bital ordering pattern could be deduced simply from the positions of O1 and O3, and an antiferro-orbital ordering arrangement of the $(3z^2 - r^2)$ orbital was found. A dimer unit is ferro-orbital ordered as shown in the sketch in Figure 4.5(a) [51]. Figure 4.5(b) shows a projection of the OO superstructure onto the $a - b$ plane, where the orbitals in green all point the same way for a particular Cr^{5+} bilayer and orbitals in red which are rotated by $\approx 90°$ with respect to the green orbitals belong to the translated adjacent bilayer. This arrangement corresponds to an antiferro-orbital order. The lines connecting the Cr^{5+} ions represent possible exchange paths. The second nearest neighbors are out of the plane and are connected by solid black lines. The third nearest neighbor are within the same bilayer and are connected by orange and yellow dashed lines [50]. The strength of the intradimer and interdimer exchange interactions depend on the shape of the orbitals, therefore the OO in $Sr_3Cr_2O_8$ has important consequences on the magnetic couplings and in the magnetic properties of the compound. The distance between nearest neighbors in the low temperature structure is $d_0 = 3.77$ Å which is in fact much larger than the van der Waals distance. This means that the magnetic coupling cannot be due to direct exchange through the overlap of the Cr^{5+} orbitals but must occur via the super-super exchange interactions. The super-super exchange path Cr-O$\cdots$O-Cr is dominated by the O$\cdots$O distance and the angles $\angle$Cr-O$\cdots$O.
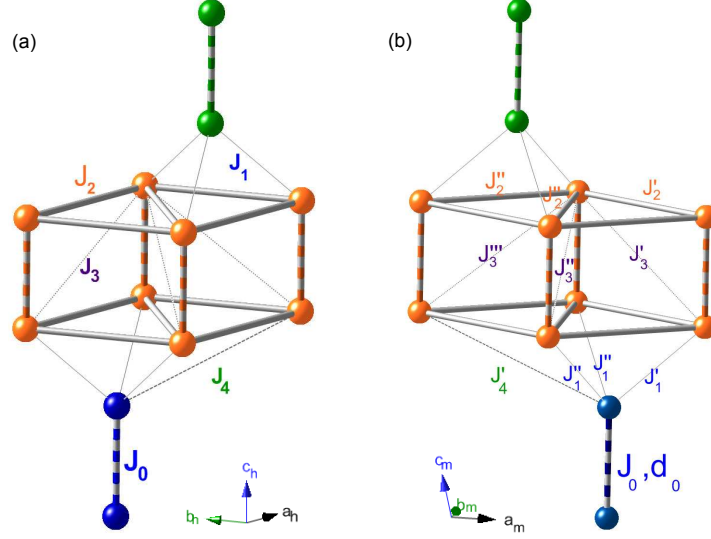
Figure 4.6: The low temperature (monoclinic) crystal structure of $Sr_3Cr_2O_8$ giving the magnetic Cr^{5+} ions only. (a) Shows the bilayer structure, (b) Shows the projection onto the 'hexagonal' plane. The exchange interactions and Cr^{5+}-Cr^{5+} distances are labeled on the diagram.

At high temperature we expect the exchange interactions J_0, J_1, J_2, J_3, J_4 corresponding to the Cr^{5+}-Cr^{5+} distances d_0, d_1, d_2, d_3, d_4, see Figure 4.6. In the low temperature phase both the distances and the exchange interactions become spatially anisotropic due to the monoclinic symmetry and whereas there was one second neighbor interaction J_1 at high temperatures there are two interactions J_1', J_1'' at low temperatures. The third nearest neighbor interactions are on the a-b plane and are represented by J_2', J_2''. The fourth nearest neighbor couplings are J_3', J_3'', J_3''' and the fifth are J_4', J_4''. The total interdimer coupling experienced by each spin can be defined as $J' = (|J_1'|+2|J_1''|)+2(|J_2'|+2|J_2''|)+2(|J_3'|+|J_3''|+|J_3'''|)+(|J_4'|+2|J_4''|)$. This definition does not take into account the possibility of frustration where if the interactions are competing they act against each other reducing the size of J'. The exchange interactions are of course affected by the orbital ordering as well as the Cr^{5+}-Cr^{5+} distances and bond angles. This has been studied in $Ba_3Cr_2O_8$ which undergoes a structural distortion as in the case of $Sr_3Cr_2O_8$ and where extended Huckel tight-binding electronic structure calculations reported by Koo *et al.* [52] concluded that the reason for a strong J_0 and weak J' coupling is that only one low lying e_g orbital is occupied. In this chapter, the single crystal growth of $Sr_3Cr_2O_8$ is described and heat capacity, magnetization and magnetic susceptibility data are shown. The results of the bulk properties of $Sr_3Cr_2O_8$ will give the overview

needed to understand inelastic neutron scattering data shown in the next chapter and shed light on the dimerization and strength of the intradimer and interdimer interactions in this compound.

4.2 Experimental Details

$Sr_3Cr_2O_8$ is a thermodynamically unstable material which makes its synthesis difficult and non-trivial. This unstable nature results from the unusual 5+ oxidation state of Cr. According to the phase diagram show in Fig 4.7, it is only stable in air above $1065°C$. In fact, at lower temperature, $Sr_3Cr_2O_8$ reacts with moisture and oxygen in the air resulting in contamination of various phases such as $SrCrO_4$ and $Sr_{10}Cr_6O_{24}(OH)_2$. With the aim of avoiding those impurities, special procedures were necessary during the synthesis, and X-ray diffraction patterns were taken after each synthesis step to check for their absence. Powder and single crystalline samples of $Sr_3Cr_2O_8$ were synthesized and grown in the Crystal Laboratory at the Helmholtz Zentrum Berlin für Materialien und Energie (HZB) in Berlin, Germany. Initial powders were synthesized by a solid state
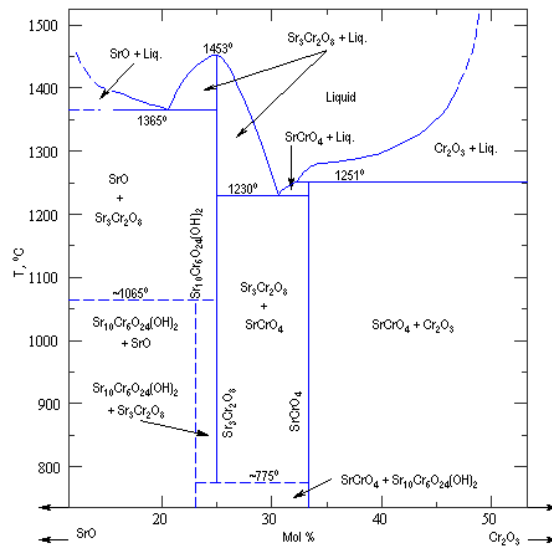
Figure 4.7: Phase diagram for $Sr_3Cr_2O_8$ compound in terms of temperature and concentration of precursors compounds. $Sr_3Cr_2O_8$ is thermodynamically stable above $1065°C$, coexisting with $SrCrO_4$ and $Sr_{10}Cr_6O_{24}(OH)_2$. Taken from reference [53].

reaction. Stoichiometric amounts of $SrCO_3$ (99.994% purity, Alfa Aesar) and Cr_2O_3 (99.97% purity, Alfa Aesar) were mixed thoroughly, pressed into a pellet and heated first

for 24 hours at 900°C and then for 24 hours at 1250°C (with intermediate grindings). The resulting powder was pulverized and packed into a cylindrical rubber tube with a diameter of about 6 mm and length of 8 cm and pressed hydrostatically up to 3000 bar in a cold isostatic pressure machine (EPSI). A cylindrical feed rod prepared by this process was then sintered in air at 1200°C for 12 h. After heating, all powders and rods were removed at high temperature from the furnace and cooled in flowing Argon. By quenching the sample in this way, reaction with atmospheric oxygen and moisture could be avoid and the formation of impurity phases below 1065° was prevented. The single crystal growth was performed by A.T.M.N. Islam [54] using the floating zone technique in a high temperature four-mirror optical floating zone furnace (Crystal Systems Inc. Model FZ-T-10000-H-VI-VPO). Equipped with four 300 W tungsten halide lamps focused by four ellipsoidal mirrors. The feed rod of stoichiometric composition was suspended from the upper shaft using nickel wire, while another small feed rod or a seed crystal from previous growths was fixed to the lower shaft to support the melt and avoid random nucleation. The typical growth rate was about 6-8 mm/h. Different atmospheres were used in order to find the best quality single crystal. Initially, air was used (6-8 liters/min), the resulting single crystal had a rough surface and contained a significant amount of the $Sr_{10}Cr_6O_{24}(OH)_2$ impurity phase. The second atmosphere used was argon (2 liters/min). The single crystal obtained was free of impurities but it was very brittle and shattered on its own after a few weeks. The surface color changed from dark green/black to light green which is a clear sign of oxidation and thus the formation of impurity phases was confirmed. Crystals grown under a lower oxygen partial pressure created oxygen deficiencies which were responsible for the eventual breaking of the crystal. The most successful growth was in synthetic air (20.5 oxygen in N_2) (6-8 liters/min). It maintained the correct level of oxygen needed for the high oxidation state of the Cr^{5+} and reduced the moisture level to prevent the growth of other phases. The resulting single crystals had smooth surfaces with a metallic luster and were typically cylindrical with diameter ≈ 6 mm and length $35 - 50$ mm. Three crystals grown under different atmospheres are shown in Fig. 4.8, further details about the crystal growth were published by A.T.M.N. Islam $et\,al.$ [54]. For the experiments described in this thesis, single phase single crystals grown in synthetic air were used. The quality of the single crystals was checked using X-ray and neutron Laue diffraction. The X-ray Laue diffractometer uses a Mo X-ray source and a commercial image plate, while for the neutron Laue patterns the Orientexpress instrument at Institute Laue Langevin was used [55]. The neutron Laue is able to observe the bulk of the crystal compared to the X-ray Laue that only measures the surface. Figure 4.9 shows the quality of one crystal oriented along the c_h-axis and showing the
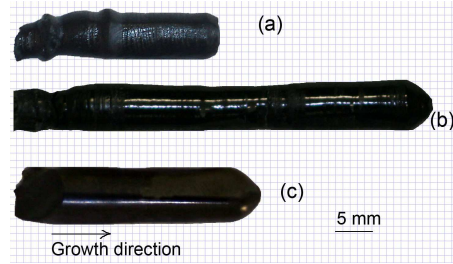
Figure 4.8: $Sr_3Cr_2O_8$ single crystals grown under different atmospheres (a) Air (6-8 liters/min), (b) Argon (2 liters/min) and (c) Synthetic air (20.5 oxygen in N_2) (6-8 liters/min). Crystal (a) has a rough surface. Crystal (b) had a good surface but was not a single crystal along the entire length. The best quality single crystal was crystal (c) having a luster surface and few impurities.
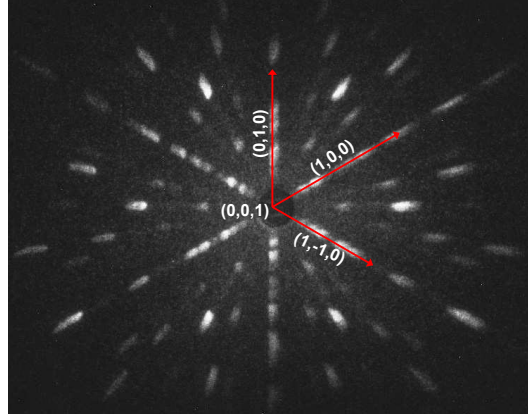
Figure 4.9: Neutron Laue pattern showing the hexagonal plane at room temperature (c_h axis is parallel to the incident beam) taken using Orientexpress at ILL, France.

hexagonal plane. The Laue reflections are broad due to the crystal twinning that happens very close to the room temperature, it was not possible to detect other big crystallites.

Heat capacity measurements were carried out using a Quantum Design Physical Property Measurement System (PPMS) at HZB with the aim of detecting the structural phase transition. A single crystal of a few milligrams was measured at zero magnetic field for a temperature range from 220 K to 350 K.

DC Susceptibility measurements were made on the three different crystals to measure the amount of magnetic impurities in the crystal. The static magnetic susceptibility and low field magnetization of $Sr_3Cr_2O_8$ were also measured using a superconducting quantum interference device (MPMS, Quantum Design) at the Laboratory for Magnetic Measurements, HZB. The samples had a volume of $3\,mm^3$ and the data were collected with a

magnetic field applied both parallel and perpendicular to the hexagonal c-axis (c_h). The susceptibility measurements were performed using a field of 3 T over a temperature range of 2-300 K. The magnetization was also measured up to ±14 T, using the VSM option in the PPMS. Hysteresis curves for magnetic field applied parallel and perpendicular to the c_h axis were obtained. These measurements were done at 2.1 K. To further explore the high field behavior of this material the very high-field magnetization of Sr$_3$Cr$_2$O$_8$ was measured using pulsed inductive magnetometers at the Institut Hochfeld-Magnetlabor Dresden, HZDR [56]. The measurements took place over a field range of $0 - 65$ T for a variety of temperatures from 1.5 to 50 K, again both field directions ($H\perp c_h$ and $H//c_h$) were measured. The samples used were single crystals aligned along the c_h-axis and the a_h-axis, with masses around 20 mg and dimensions of approximately $1.5\times1.5\times2$ mm^3. Two magnets D and E, were used in these experiments. Magnet D has a maximum field of 65 T and a pulse duration of 20 ms (Magnet bore of 20 mm), while magnet E has a maximum field of 55 T and a duration of 50 ms (Magnet bore of 24 mm).

4.3 Results and Discussion

4.3.1 Heat Capacity

Heat capacity measurements on single crystal samples have been done in zero field with the aim of identifying the exact temperature at which the structural phase transition occurs. The results are shown in Figure 4.10. The lattice contribution has not been subtracted. A lambda-type transition is seen at T=285 K denoting an order-disorder phase transition. The transition is thought to be a cooperative Jahn-Teller distortion and the transition temperature will be denoted here as T$_{JT}$. The distortion was not observed in previous specific heat measurements on powder samples by Singh $et\,al.$ [57]. Very recently detailed heat capacity measurements have been performed on our single crystals by Wang $et\,al.$ [58] for a larger temperature range. Analysis and fitting of the phonon and magnetic contribution, suggested an additional orbital contribution given by a Schottky-like anomaly caused by the excited E orbital level. More details about the crystal field will be given in the discussion section.

4.3.2 Static Susceptibility

The structural distortion discussed in the introduction of this chapter has a clear impact on the magnetic properties of Sr$_3$Cr$_2$O$_8$. It lifts the geometric frustration in the hexagonal plane and gives rise to spatially anisotropic magnetic exchange interactions. The
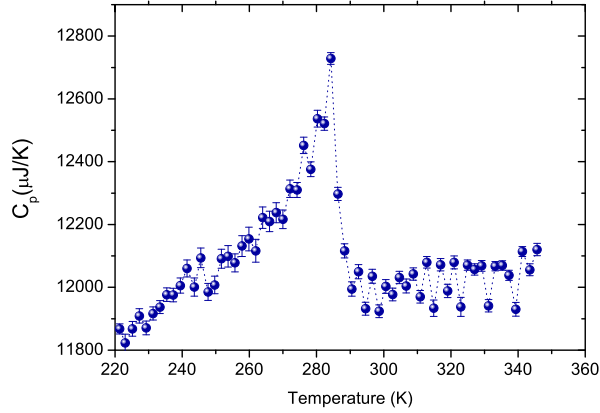
Figure 4.10: Heat capacity of $Sr_3Cr_2O_8$ at zero magnetic field shows a lambda type transition at T=285 K, that is related to the JT distortion.

spin exchange is dominated by superexchange mechanisms. The presence of OO at low temperatures modifies the different super-super exchange interactions between the Cr ions. It also enhances considerably the strength of the intradimer interaction and would favor some interdimer interactions over others. The questions of most relevance are: How strong is the dimer interaction? Do these dimers interact at all and which interdimer interactions does the orbital order favor? An experimental method that can shed light on the strength of the intra and interdimer interactions is DC magnetic susceptibility. DC susceptibility measurements were performed on aligned single crystal samples with a magnetic field applied parallel and perpendicular to c_h. This measurement also provides information about the quantity of magnetic impurities in the sample. Therefore DC susceptibility was measured in all the different single crystal samples shown in Figure 4.8 to assess their quality. Figure 4.11 shows the magnetic susceptibility for two different samples. There are two important features. The first is an upturn in the susceptibility at low temperature (< 10 K) and the second is a broad maximum at 38 K. The low temperature tail is ascribed to paramagnetic impurities and is more prominent for crystal (a) than crystal (c). The impurities are expected to give rise to Curie-like behavior that can be described by the expression:

$$\chi_{imp} = \frac{C_{imp}}{T - \theta_{imp}}, \tag{4.1}$$

where C_{imp} is the Curie constant of the impurities and θ_{imp} is their Curie-Weiss temperature. The high paramagnetic signal of crystal (a) indicates that it contains more magnetic impurities than crystal (c). Therefore, crystal (c) has been used in all the fol-

lowing experiments. Figure 4.12 shows the temperature dependence of the susceptibility
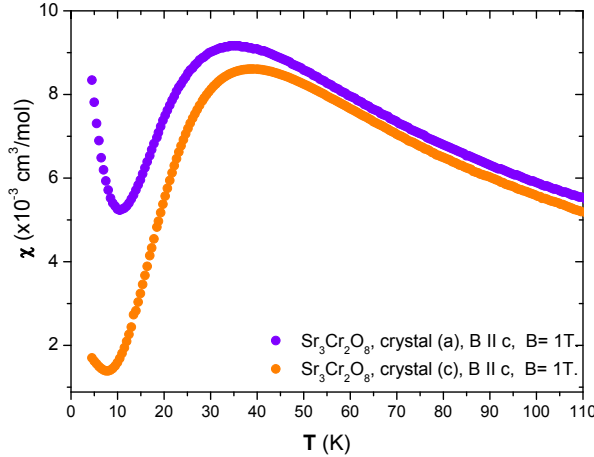
Figure 4.11: Magnetic susceptibility for two different grow crystals of $Sr_3Cr_2O_8$. The crystal (c) was used for neutron scattering experiment as it shows less magnetic impurities than crystal (a). This is clear from the increasing susceptibility at low temperatures which is due to paramagnetic impurities.

with the field applied both perpendicular and parallel to c_h, of the crystal (c) sample. The two curves are slightly different suggesting a weakly anisotropic g tensor [58, 59]. The broad peak in the susceptibility curve is characteristic of a dimerized magnet with a singlet ground state and gapped magnetic excitations, and it is in agreement with previously published susceptibility results on polycrystalline samples [57]. Altogether, three contributions to the susceptibility are expected. A term coming from the impurities χ_{imp}, a temperature independent term due to van Vleck paramagnetism and diamagnetic core susceptibility which is expected to be small $\sim 10^{-4}\,\mathrm{cm^3/mol}$ (χ_0) in addition to the susceptibility contribution from the thermal excitation of dimers. The susceptibility curve can be fit to the following expression:

$$\chi_{obs} = \chi_0 + \chi_{imp} + \chi_{interacting-dimer}. \tag{4.2}$$

The third term, $\chi_{interacting-dimer}$, is due to the coupled dimer arrangement proposed for $Sr_3Cr_2O_8$ and is modeled by

$$\chi_{interacting-dimer} = \frac{3C/T}{(3 + e^{(J_0/k_BT)} + J'/T)}. \tag{4.3}$$

This expression is described in references [57, 60]. It is derived from the Bleaney-Bowers equation for spin-1/2 dimers coupled by Heisenberg intradimer exchange constant J_0,
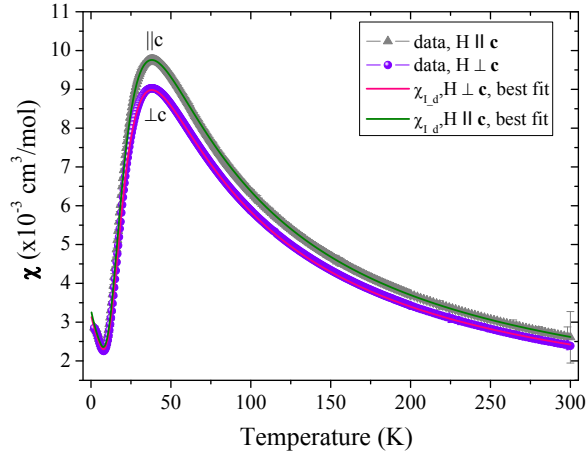
Figure 4.12: Static susceptibility data measured using the SQUID magnetometer for field applied both parallel and perpendicular to c_h displayed along with the fit interacting dimer model given by Eq. 4.2.

where J' is the effective field on each spin due to its couplings with the neighboring spins. This function has a peak at a temperature which is proportional to J_0 and a width proportional to both J_0 and J'. For $k_B T >> J_0$, it tends towards the Curie-Weiss law for a paramagnet. The constant C is the Curie constant of this system.

The measured susceptibility data were fitted to Eqn. 4.2 and good agreement was found over the full temperature range, see magenta and green lines in Fig. 4.12. The fit parameters for the data are shown in Table 4.3. The value of C corresponds to an effective moment of $1.8(1)\mu_B/\text{Cr}^{5+}$ (perpendicular to the c axis) and $\mu_{eff} = 1.9(1)\mu_B/\text{Cr}^{5+}$ parallel to the c_h-axis, which is close to the value of $1.72\mu_B$ expected for spin-1/2 Cr^{5+} ions, assuming $g \approx 2$. The impurity's Curie constant can be used to give an approximate value of the amount of impurities in the sample, which corresponds to a 6%. The values obtained for the intradimer and interdimer exchange interactions ($J_0 = 5.512(3)\,\text{meV}$ and $J' = 1.97(6)\,\text{meV}$) can be compared to the values of $J_0 = 5.17(1)\,\text{meV}$ and $J' = 0.5(2)\,\text{meV}$ found previously by Singh $et\,al.$ [57]. While the intradimer exchange constant is in good agreement, the value of the interdimer coupling is much smaller. If the values of J_0 and J' are however fixed to those of Singh $et\,al.$ [57], the fit obtained is almost as good as the one shown in Fig. 4.12, with a goodness of fit: $R^2 = 0.998937$. The extreme case of zero interdimer couplings has been tested as well and a goodness of fit of $R^2 = 0.999986$ was obtained. Figure 4.13 gives a comparison between the different parameters. It is clear that susceptibility is unable to give accurate information about

Table 4.3: DC susceptibility data along the c_h-axis and perpendicular to it were fitted to the model in Equation 4.2. The goodness of the fit along the hexagonal plane is: $R^2 = 0.99998$ and along the c_h-axis is: $R^2 = 0.999979$.

B//a$_h$						
χ_0 (cm^3/mol)	C$_{imp}$ (cm^{3}K/mol)	θ_{imp} (K)	C (cm^{3}K/mol)	J_0 (meV)	J' (meV)	μ_{eff} (μ_B/Cr^{5+})
$2.32(5) \times 10^{-4}$	0.0465(5)	$-15.7(2)$	0.875(2)	5.517(2)	1.22(5)	1.8(1)
B//c$_h$						
$1.76(5) \times 10^{-4}$	0.0481(6)	$-15.3(3)$	0.987(2)	5.512(3)	1.97(6)	1.9(1)
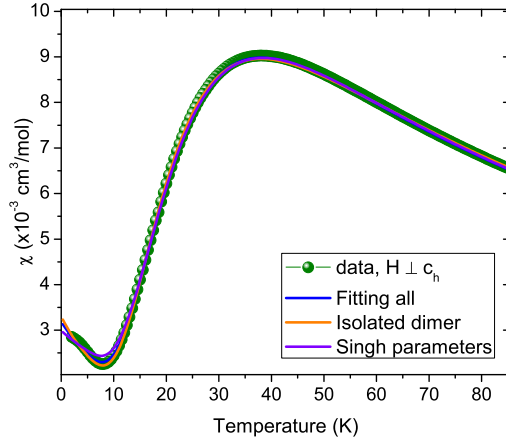
Figure 4.13: Static susceptibility data measured using the SQUID magnetometer for field applied perpendicular to the c_h-axis together with the fit to the Eq. 4.2, for three different cases, isolated dimer, interacting dimer and using the values obtained by Singh *et al.* [57]. The goodness of the fit in the three cases show that DC susceptibility does not give accurate value of the interdimer exchanges interactions.

the interdimer exchange coupling. To summarize, DC susceptibility agrees well with a model of interacting spin-1/2 dimers and gives an intradimer exchange constant of $J_0 \approx 5.5$ meV. In order to have an accurate value of the interdimer exchanges, magnetization and inelastic neutron scattering were performed and they will be described in the next section and in the next chapter respectively.
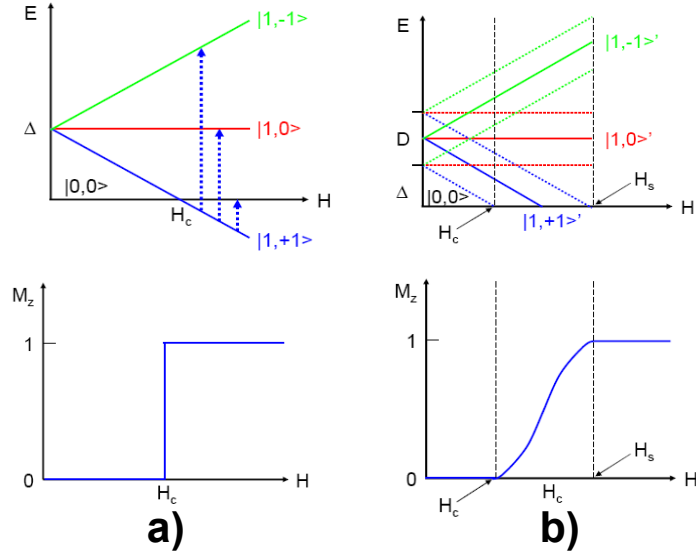
Figure 4.14: Evolution of the energy levels of the isolated (a) and interacting (b) dimer excitations (singlet and triplet) with applied magnetic field H. The resulting magnetization curves are also shown.

4.3.3 Magnetization

Magnetization measurements give a deeper insight into the details of the dimerization in $Sr_3Cr_2O_8$. In Chapter 2 the ground and excited states of two coupled spins were described. The ground state singlet is separated from the excited state, triplet, by an energy gap Δ. Applying a magnetic field would lead to a Zeeman splitting of the triplet state. This Zeeman term controls the energy of triplets or triplons and as the magnetic field is increased, the excitation energy of one of the triplon branches is lowered and crosses zero at a critical field, H_c. The magnetization would be expected to behave in two ways depending on the nature of the interdimer interactions. Firstly a step function, shown in Figure 4.14(a), is observed in the case of a non interacting dimer system. Alternatively if the dimers interact, the magnetization is as shown in Figure 4.14(b). Finite interdimer interactions allow the magnons to hop and develop a dispersion or bandwidth. Two critical fields arise, the first where the lower edge of the bandwidth is driven into the ground state and the second where the upper edge of the bandwidth goes into the ground state. To investigate the behavior of $Sr_3Cr_2O_8$, magnetization was measured using the VSM-PPMS at 2.1 K, for fields up to 14 T, at HZB. The results are shown in Figure 4.15. The magnetization seems to saturate at 13 T at $0.04\mu_B/2Cr^{5+}$, this value is very small compared to the theoretical value of $2g_s\mu_B S = 1.98\mu_B/2Cr^{5+}$. This is almost negligible and a more physical explanation is that this magnetization comes only from
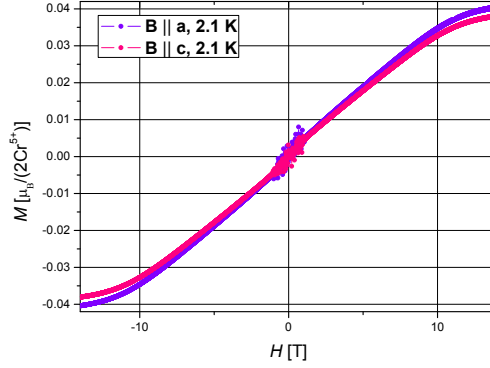
Figure 4.15: Low fields magnetization at 2.1K. Measured in the PPMS. With the magnetic field along the two different crystallographic directions. The noise at low fields is due to instrumental thresholds.

magnetic impurities in the sample. It is clear that higher fields are needed to reach the critical field that closes the gap in $Sr_3Cr_2O_8$. The high field magnetization of $Sr_3Cr_2O_8$ was measured at the institut Hochfeld-Magnetlabor Dresden, these data reveal three distinct regions, see Fig. 4.16. Below the critical field of $H_c = 30.9(4)\,T$ there is zero magnetization. The gradual increase in magnetization observed in the 65 T measurement (green line) is because this data has not been background corrected. Between $H_c = 31\,T$ and $H_s = 61.9(3)\,T$, the magnetization increases rapidly and smoothly, while above H_s a magnetization plateau is observed at $M_s = 1.97(3)\mu_B/2Cr^{5+}$. This is identified as the saturation plateau since it is very close to the value of $1.98\mu_B/2Cr^{5+}$, where all the spin moments point along the field direction. The observed magnetization can be explained within the proposed interacting dimer model of $Sr_3Cr_2O_8$. In this model, the ground state is a singlet resulting in no magnetization at low magnetic fields. The excitations would form a gapped magnon mode which disperses between an upper and lower energy. The magnetic excitations, magnons, possess a spin $S = 1$ and their triplet degeneracy is lifted by an applied magnetic field. The critical field H_c corresponds to a Zeeman energy at which the gap is just closed and the $S^z = 1$ magnons start to populate the ground state. From H_c, it can be deduced that $E_{gap} = g_s\mu_B H_c = 3.54(5)\,meV$. At the saturation field H_s, the ground state is fully occupied by excited dimers. In the case of strongly dimerized systems, the Zeeman energy is equal to the upper edge of the dispersion, thus giving $E_{upper} \approx g_s\mu_B H_s = 7.09(4)\,meV$.

The magnetization measurements have been done at different temperatures and the results are shown in Figure 4.17. Clearly, the critical field moves towards higher fields at higher temperatures. These magnetization results are however inadequate for detecting
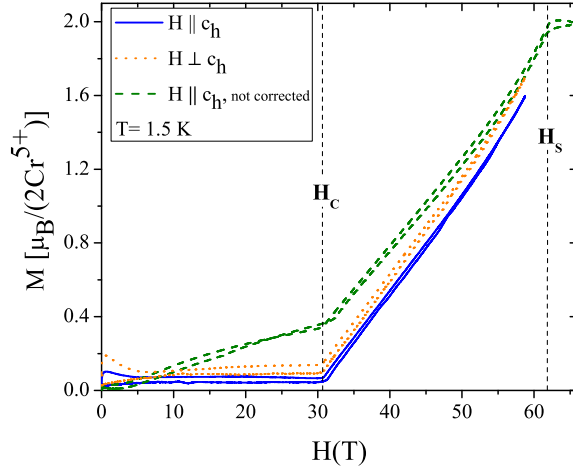
Figure 4.16: Magnetization per $2Cr^{5+}$ ions as a function of applied magnetic field. This measurement was performed using a pulsed magnet at base temperature $T = 1.5\,\text{K}$ and field applied both parallel and perpendicular to c_h. The data represented by the green line is not background corrected.
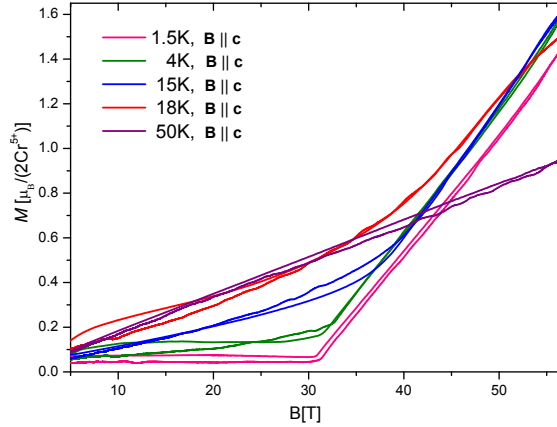
Figure 4.17: High field magnetization results with the field along c axis. At different temperatures.

phase transitions and for mapping out magnetic phase diagrams. Therefore the linear magnetization at $50\,\text{K}$ indicates a paramagnetic behavior but does not shed light onto a critical behavior. Altogether the magnetization data are consistent with the model of interacting spin-$1/2$ dimers and suggests that the excitations are centered around $\approx 5.3\,\text{meV}$ and disperse over a bandwidth of $\approx 3.55\,\text{meV}$. Since in unfrustrated dimer-

ized magnets the bandwidth is equal to J', the significant bandwidth revealed by the magnetization suggests substantial interdimer couplings with $J' \approx 3.55\,meV$.

4.4 Discussion and Conclusions

In this chapter, the general properties of $Sr_3Cr_2O_8$ were presented. Single crystal growth, DC susceptibility and high field magnetization provide a picture of $Sr_3Cr_2O_8$ as a dimerized spin-1/2 antiferromagnet. The intradimer exchange constant is identified as the intrabilayer interaction J_0 which has a value of $5.5\,meV$ according to static susceptibility data. This dimerization gives rise to a singlet ground state and gapped one-magnon excitations. According to magnetization data, there are in addition significant interdimer interactions that allow the dimer excitations to hop and develop a dispersion parameterized by $J' = 3.55\,meV$. These results can be compared to previous experimental work on $Sr_3Cr_2O_8$. Y. Singh and D.C. Johnston [57] measured the DC susceptibility and obtained a value of $J_0 = 5.17(1)\,meV$ in good agreement with the value found here. Their value for the sum of the interdimer exchange constants is $J' = 0.5(2)\,meV$, which can also fit the susceptibility data shown here. Inspection of the fitting process shows that the susceptibility data can however be well modeled by a wide range of J' values and therefore cannot give accurate values of the interdimer coupling.

The values of the exchange couplings shown here can be compared to those found in the related compounds $Ba_3Mn_2O_8$ and $Ba_3Cr_2O_8$. The values of intradimer interaction J_0 are smaller in the Ba compounds being $1.64\,meV$ for $Ba_3Mn_2O_8$ [61] and $2.38\,meV$ for $Ba_3Cr_2O_8$ [62]. The difference between $Ba_3Cr_2O_8$ and $Sr_3Cr_2O_8$ may be due to the larger distance between CrO_4 tetrahedra in $Ba_3Cr_2O_8$.

Chapon *et al.* [50] showed from diffraction measurements that $Sr_3Cr_2O_8$ undergoes a Jahn-Teller distortion resulting in a lowering of the crystal symmetry to monoclinic. The specific heat measurements shown here reveal that $T_{JT} = 285\,K$. This transition gives rise to orbital order and would produce spatially anisotropic exchange interactions which will be explained in detail in the next chapter.

In order to understand the nature of the Jahn-Teller distortion in more depth the crystals grown at HZB were oriented, cut and polished and then sent to the research groups of Peter Lemmens (TU Braunschweig) and Joachim Deisenhofer (University of Augsburg) for optical measurements. Figure 4.18(left) shows the Raman spectra at different temperatures for $Sr_3Cr_2O_8$ published by D. Wulferding *et al.* [63]. Above the structural transition, there should be 11 Raman active modes for the hexagonal structure ($R\bar{3}m$)

of which only 10 could be measured. At the lowest temperature (3 K), the nuclear struc-
ture of $Sr_3Cr_2O_8$ is C2/c and there should be 39 Raman active phonons from which
only 27 can be seen experimentally. The reason for the missing modes could be that
some phonons overlap or lack intensity. Surprisingly not all phonons appear at 285 K
(T_{JT}) where the lambda-type anomaly in the heat capacity occurs or at 275 K where the
superlattice reflections appear in the neutron diffraction pattern. Instead, there is only
a very gradual increase in phonon intensity for nearly all modes down to $\approx 120K$ which
is then followed by a rapid increase in intensity and sharpening of the phonons below
120 K, and the lattice vibration finally stabilizes below 50 K. Beside this effect noticed in
the Raman spectra, similar behavior was measured by Wang *et al* [58] in optical conduc-
tivity spectra. Here new polar phonons appear at T_{JT}, but some phonons develop only
gradually with decreasing temperature. Wang *et al.* also present ESR measurements.
They observe the triplet excitation at the Γ point at an energy of 5.14 meV which is
consistent with the results shown here because it lies within the energy band (from E_{gap}
to E_{upper}) and is close to the value of $J_0 = 5.5$ meV. When exploring the temperature
dependence they found a rapid increase in the ESR linewidth and loss of ESR signal
above 100 K. This is ascribed to a drastically increased spin-lattice relaxation rate for
$T > T^*$ as a result of strong fluctuations in the orbital and lattice degrees of freedom.
Figure 4.18(b) shows the ESR linewidth for $Sr_3Cr_2O_8$ and the solid line is a fit to
$\Delta H = \Delta H_0 + A exp(\Delta_o/kBT)$. The exponential increase of the ESR linewidth has been
attributed to the relaxation of the excited spins via an Orbach process. As shown in the
inset, an Orbach process is the absorption of a phonon with energy $\Delta_o=388$ K (35 meV)
to excite an electron to an orbital state (in this case the excited Jahn-Teller split orbital
level) and emission of a phonon with energy $\Delta_o + E_Z$, where E_Z is the Zeeman splitting
of the lower-lying E orbital. The size of the extracted Jahn-Teller splitting (≈ 35 meV)
is very small in comparison to the orbital splitting usually observed in $3d$ oxide systems.
However, the Jahn-Teller distortion in the tetrahedra environment has not been well
studied in contrast to the Jahn-Teller distortion of the octahedron, indeed the energy
gap is expected to be much smaller for the tetrahedral symmetry. The gap value Δ_o is
associated with the energy splitting of the Cr^{5+} E-orbitals in the regime $T < T^*$ where
OO is complete and is similar in size to the phonon energies. This similarity in energy
scales promotes a strong coupling of the spin, lattice and orbital sectors. The splitting
Δ_o is therefore associated with the interaction energy that drives OO and will be im-
portant for a theoretical understanding of the energy scales in this compound. Both
results (ESR and Raman) can be interpreted as a signature of strong fluctuations which
dominate the lattice dynamics and lead to a strong damping and broadening of phonons
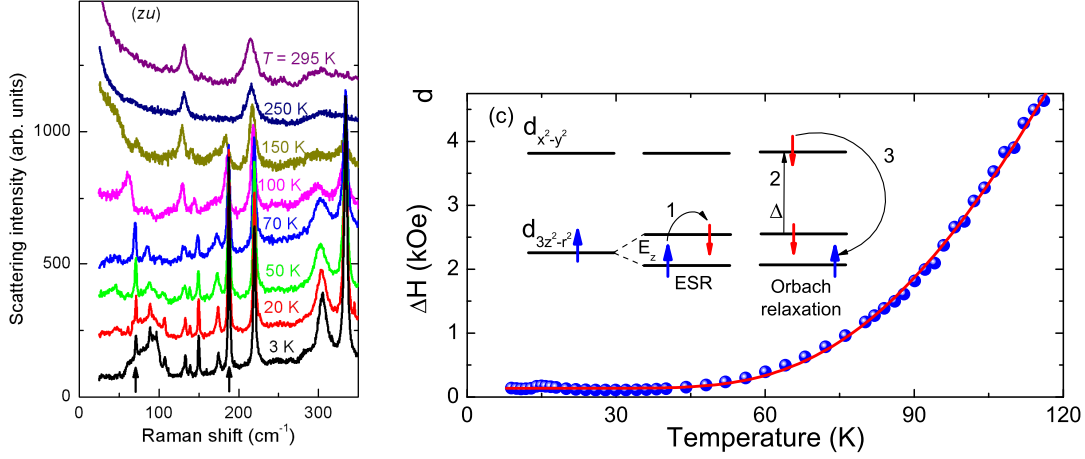
Figure 4.18: (left) Raman spectra at different temperatures in (zu) polarization; spectra are shifted in intensity for clarity. The two arrows mark the phonons at 71 and 188 cm^{-1}. (right) ESR linewidth. The solid curve is a fit described in the text. Inset:sketch of the spin relaxation via an Orbach process. Taken from references [63, 58].

in the large temperature range $T^* < T < T_{JT}$ with 100 K$< T^* <$ 150 K. This behavior is attributed to strong lattice and orbital fluctuations brought about by the Jahn-Teller distortion at 285 K, which compete with the system's new structural phase down to temperatures well below the structural transition. The observed extended fluctuation regime below the JT transition is very unusual and indicates the existence of interactions such as e.g. spin-orbit coupling, magnetoelastic coupling and electron-electron interactions which compete with electron-phonon coupling. Whether the orbital and lattice correlations develop simultaneously has to be investigated. Further powder and single crystal inelastic neutron experiments are planned to investigate both the CF scheme for Sr$_3$Cr$_2$O$_8$ and the phonon spectra as a function of temperature. Apart from these results, density functional theory calculations for Sr$_3$Cr$_2$O$_8$ [51] have also demonstrated that the strong electron correlation arising within the Cr-3d shell can clearly explain both the phase transition leading to the stabilization of its monoclinic $C2/c$ space-group symmetry by more than 140 meV/cell and the spin-singlet magnetic ground state. These calculations however predict a metallic ground state.

The behavior of Ba$_3$Cr$_2$O$_8$ is similar to that of Sr$_3$Cr$_2$O$_8$. A structural distortion has also been confirmed in Ba$_3$Cr$_2$O$_8$ by neutron powder diffraction where additional peaks corresponding to the monoclinic $C2/c$ symmetry were found [62]. Suggesting a similar Jahn-Teller distortion [62]. But this does not happen to the isostructural compound Ba$_3$Mn$_2$O$_8$ it maintains the hexagonal structure down to the lowest temperatures since

the Mn^{5+} ion is not Jahn-Teller active. Thus this compound is geometrically frustrated leading to interesting features in its magnetic behavior, such as, a small single ion uni-axial anisotropy that promotes a zero field splitting of the triplet [64].

As mentioned in the introduction of this chapter, magnons can interact and when applying a magnetic field they can condense into the ground state at a QCP. Depending on the value of the potential and kinetic energy of the magnons, the ground state can be variously described as a BEC (canted XY AFM) [65], a triplet crystal (inhomogenous Ising order) [48] or even a supersolid [40]. Close to the QCP, the phase boundary $T_c(H)$ follows a power law $T_c \propto (H - H_{c1})^\phi$ with a universal critical exponent $\phi = z/d$, which depends only on the dimensionality d and the dynamical critical exponent z, where for BEC is $z = 2$. For a 3-dimensional system $\phi = 2/3$.

BEC has been reported for dimerized compounds such as $TlCuCl_3$ [41], and $BaCuSi_2O_6$ [43]. In the case of $Ba_3Mn_2O_8$ for fields parallel to the c-axis, the critical exponent is consistent with BEC-QCP ($\phi_l = 1$ and $\phi_t = 1/2$), but quantitative differences are observed for fields perpendicular to the c-axis. This is in agreement with the expectation for the Ising like broken symmetry [66, 64]. $Ba_3Cr_2O_8$ has a weak in-plane Dzyaloshinsky-Moriya interaction (DM interactions) that should break the symmetry of the Hamiltonian but nevertheless the phase boundary of the field induced AFM state can be fit to the BEC critical exponent ($\phi = 0.49(2)$), which agrees with the Ising universality class $\phi = 1/2$ [62]. DM interactions have not been found so far in $Sr_3Cr_2O_8$ but they would be allowed by symmetry [58].

$Sr_3Cr_2O_8$ is a candidate compound for BEC, where an applied magnetic field of $H_c = 30.9(4)\,T$ is required to close the spin gap and start condensing magnons in the ground state, while full saturation is achieved at a field of $H_s = 61.9(3)\,T$. In fact the phase diagram of $Sr_3Cr_2O_8$ has recently been mapped out using heat capacity and the magnetocaloric effect measurements (see Figure 4.19) [59]. The extracted critical exponent of the ordering temperature as a function of reduced field around H_c is indeed in agreement with the universality class predicted for a three-dimensional Bose-Einstein condensate ($\phi = 0.65(2)$).

Finally, it should be noted that the absence of any intermediate magnetization plateau is in contrast to the findings for some other gapped magnets that are highly frustrated e.g. $SrCu_2(BO_3)_2$ which has steps in its magnetization [46] and $Ba_3Mn_2O_8$ [64]. This result is however in agreement with the isostructural compound $Ba_3Cr_2O_8$ [68], where the critical field is $H_c = 12.5\,T$ which is followed by a smooth increase up to saturation at
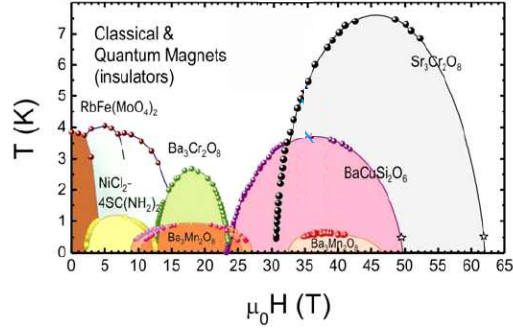
Figure 4.19: (T,H) Phase diagrams determined from Cp(T,H) and magneto caloric effect MCE experiments for RbFe(MoO$_4$)$_2$, NiCl$_2$-4SC(NH$_2$)$_2$, Ba$_3$Mn$_2$O$_8$, Ba$_3$Cr$_2$O$_8$, BaCuSi$_2$O$_6$ and Sr$_3$Cr$_2$O$_8$. Taken from reference [67].

$H_s = 23.6$ T [69, 70]. In Figure 4.19 the phase diagram of some quantum dimer systems is shown. The two phases of Ba$_3$Mn$_2$O$_8$ can be reached only below 1 K and in the case of Ba$_3$Cr$_2$O$_8$ temperatures below 3 K will be necessary to explore the long range order region. In the case of Sr$_3$Cr$_2$O$_8$ the critical temperatures are high but the critical fields are also high. The necessary fields are just below the limit of new extreme environments for neutron scattering (HZB will have an instrument supporting a magnet with maximum field of 25-34 T by 2012, just within the magnetic phase diagram of Sr$_3$Cr$_2$O$_8$). This leads to a proposal for the study of BEC in Sr$_3$Cr$_2$O$_8$ in the near future.

Details on the magnon dispersion, anisotropic exchange paths (and temperature dependence of the magnons interactions) will be given in the next chapter.

5 Magnetic Excitations of $Sr_3Cr_2O_8$

5.1 Introduction

In the previous chapter, the concept and the properties of a weakly coupled dimerized system were explained. The macroscopic properties of $Sr_3Cr_2O_8$ were investigated. High field magnetization results revealed two critical fields that are related to the Zeeman splitting of triplet excitations or magnons that disperse within a bandwidth. The upper and lower edge of these excitations are directly related to the critical fields in the magnetization. DC magnetic susceptibility was fitted to a model of interacting dimers coupled by the exchange constant J_0, an estimate of this exchange constant was acquired through the analysis of the data. As explained earlier, for an isolated dimer, the magnetic excitation from the singlet ground state to the triplet state is expected to be non-dispersive and the gap value is directly related to the intradimer exchange coupling. In the case of $Sr_3Cr_2O_8$, the excitations have a bandwidth, so the dimers are magnetically coupled to each other. The strength and sign of the magnetic coupling depends on multiple factors such, as the OO and the distances between the ions. The low temperature nuclear structure of $Sr_3Cr_2O_8$ is monoclinic, $C2/c$. This makes the distances that were equivalent at high temperatures between the Cr^{5+} ions spatially anisotropic, leading to non-equivalent magnetic coupling constants. The exchange couplings are defined as it is illustrated in Figure 5.1. There are two second neighbor interactions (or interbilayer interactions) J_1' and J_1'', two third neighbor interactions (intralayer) J_2' and J_2'', three fourth neighbor interactions (intrabilayer) J_3', J_3'' and J_3''' and two fifth neighbor interactions J_4', and J_4'' (the distances between the Cr^{5+} ions were listed in the previous chapter).

Therefore $Sr_3Cr_2O_8$ is considered as a weakly coupled dimerized system with three dimensional spatially anisotropic magnetic interactions. The macroscopic results shown in the previous chapter gave important information about the energy range of the excited states, but they do not give information about the dispersion relations of the magnons in terms of energy and wavevector which is the key information needed to obtain an estimate of the exchange couplings. The best technique to investigate the dispersion of
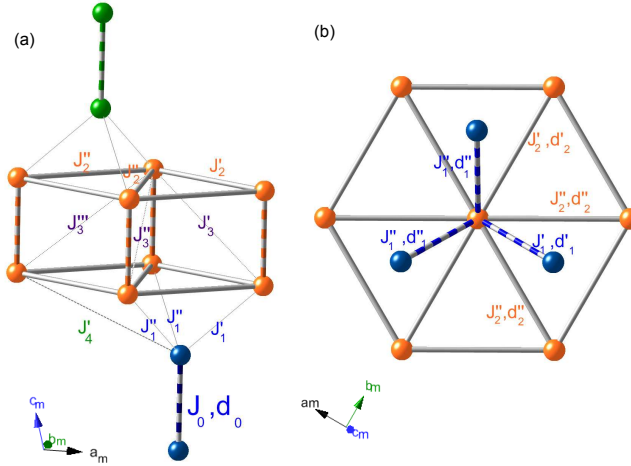
Figure 5.1: The low temperature (monoclinic) crystal structure of Sr$_3$Cr$_2$O$_8$ showing the magnetic Cr^{5+} ions only. (a) Shows the bilayer structure, (b) Shows the 'hexagonal' plane. The exchange interactions and Cr^{5+}-Cr^{5+} distances are labeled on the diagram.

magnons is inelastic neutron scattering (INS). As explained in Chapter 3, the neutron possesses a magnetic dipole moment and it can interact with the dimerized system exciting a dimer to its triplet state $S = 1$. In scattering, the total spin (neutron plus sample) is conserved, and the neutrons can exchange either zero or one unit of spin with the sample. By measuring the dynamical structure factor $S(Q, E)$, it is possible to obtain the spin dispersion (from the position in Q and energy of the excitation), as well as the intensity of the energy integrated structure factor $S(Q)$. The results of neutron studies are applicable and can be directly compared with theory and can be used to extract the exchange interactions [71, 4].

In this chapter, INS data are shown from four different spectrometers with the aim of measuring the dispersion relation of the magnons in Sr$_3$Cr$_2$O$_8$ and its temperature dependence. The first experiment was performed on a powder sample using the time of flight spectrometer (ToF), NEAT at HZB. The wavevector - intensity relation of the data could be compared directly to the first moment sum rule [72]. This comparison allowed the dominant exchange interaction in the system to be identified. High resolution INS data were acquired on a single crystal sample using the triple axis spectrometer V2-Flex at HZB. Key directions in reciprocal space were scanned and the data were fitted such that the dispersion relation was extracted. As Sr$_3$Cr$_2$O$_8$ is a 3-dimensional antiferromagnet, it was important to measure the dispersions along all directions in reciprocal space. This is possible using a novel time of flight spectrometer such as Merlin at ISIS. This spectrometer has position sensitive detectors that allowed information in the

horizontal scattering plane and in the vertical direction to be acquired simultaneously. For this experiment, the single crystal was rotated about the vertical axis and a dataset was acquired for each crystal position. All datasets were later combined using the newly developed software package called Horace [73] and the 4-dimensional $S(\mathbf{Q}, E)$ dataset was determined.

The INS data were analyzed by describing the system with a Heisenberg Hamiltonian which was then diagonalized using Green functions and making use of a random phase approximation (RPA) that decouples the Green functions matrices. RPA is only valid for low temperatures, far from critical points, where the thermal fluctuations do not play an important role.

Furthermore, since it is a mean-field approximation, it gives best agreement when many nearest neighbors are taken into account. The RPA model has also been successfully used to describe the low temperature INS data of the isostructural compounds $Ba_3Cr_2O_8$ [62] and $Ba_3Mn_2O_8$ [61]. It is important to note that the magnetic excitations in $Sr_3Cr_2O_8$ cannot be described by spin-wave theory as this requires the ground state to have long range magnetic order. It also cannot reproduce the observed spin gap, unless an unphysically large single ion anisotropy is included. The exchange constants extracted by fitting the RPA mode successfully describe the magnetic properties of $Sr_3Cr_2O_8$ such as the susceptibility and magnetization from the previous chapter as well as Raman scattering and ESR, and agree well with band structure calculations [74, 51, 63].

The temperature dependence of the magnetic excitations has also been studied by analyzing the renormalization and lineshape of the excitations at different temperatures. Two experiments were performed for this study on the TAS, Flex and on the ToF spectrometer IN5 at the ILL. The RPA is able to predict the observed renormalization but it does not take into account the increase in the linewidth which is expected due to a decrease in the lifetime of the excitations when the temperature is increased. Unusually the lineshape of $Sr_3Cr_2O_8$ was also found to broaden asymmetrically as a function of temperature. This asymmetry which has recently been predicted in one-dimensional dimer systems and has been observed in the dimer chain compound copper nitrate, is attributed to magnon-magnon interactions [75].

In this chapter the experimental details of the neutron scattering experiments are given, together with a description of the structural twinning that occurs at the Jahn-Teller distortion as well as the set of independent exchange interactions that can occur in $Sr_3Cr_2O_8$. TAS and ToF data are shown, the data are analyzed and described using a random phase approximation which enable the exchange couplings to be extracted for the system.

5.2 Experimental Details

The magnetic excitation spectrum was investigated using inelastic neutron scattering. For an overview of the excitation spectrum, powder measurements were performed on the cold multidisc-chopper neutron time-of-flight spectrometer $V3-NEAT$ at the Helmholtz Zentrum Berlin, HZB. Figure 5.2 shows a sketch of the instrument. The powder samples were prepared as described in the previous chapter. A total of 9.5 g of $Sr_3Cr_2O_8$ powder was packed into a cylindrical aluminum container and mounted inside a standard orange cryostat. Data were collected for incident wavelengths (energies) of 2 Å(20.45 meV), 2.5 Å(13.09 meV) and 3.2 Å(7.99 meV), resulting in a resolution at the elastic line (at 5.3 meV energy transfer) of 1.437 meV (1.053 meV), 0.742 meV (0.448 meV), 0.442 meV (0.187 meV) respectively. All the data were collected at 2 K and each data set was collected for approximately 20 hours. A vanadium standard measurement was used for the detector normalization and empty can measurements were used for the background subtraction.
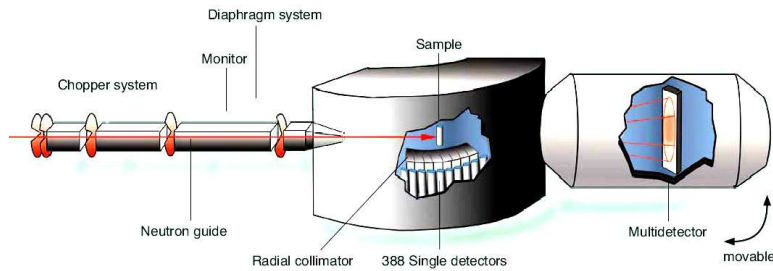
Figure 5.2: Schematic drawing of the NEAT chopper spectrometer. Taken from reference [76].

For a detailed study of the magnetic dispersion, (and its temperature dependence) single crystal inelastic neutron scattering measurements were performed on different spectrometers. The single crystal samples were grown as described in the previous chapter and were aligned using x-ray and neutron Laue diffraction, each crystal was mounted on an aluminum holder which was attached to a mini goniometer for precise alignment. As the Cr^{5+} spin moment is only $s = 1/2$ for $Sr_3Cr_2O_8$ the magnetic scattering intensity is expected to be weak, therefore for most of the experiments more than one single crystal were used, and they were co-aligned using rotation stages attached to the mini-goniometers, see Figure 5.3.

High resolution measurements were performed on a cold triple axis spectrometer, V2-Flex at HZB, for an accurate mapping of the dispersion relations along key directions in reciprocal space. Two separate experiments were performed. For the first, a single
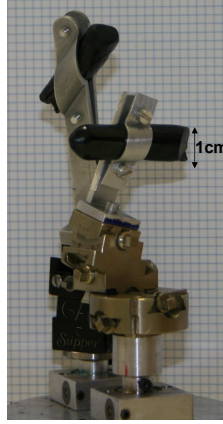
Figure 5.3: $Sr_3Cr_2O_8$ single crystals mounted on individual aluminum holders each attached to a minigoniometer and rotation stage. This set up was used for the TAS experiment.

crystal (mass $= 3.7$ g) was oriented with the $(h_h, 0_h, \ell_h)$ plane in the instrumental scattering plane. For the second experiment two single crystals of mass 3.69 g and 4.04 g respectively were co-aligned to investigate the (h_h, h_h, ℓ_h) plane. A total of 70 constant-wavevector, energy scans were performed mapping the excitations along the $(0_h, 0_h, \ell_h)$, $(1_h, 0_h, \ell_h)$, $(0.5_h, 0_h, \ell_h)$,$(h_h, 0_h, 1.5_h)$, $(h_h, 0_h, 3_h)$, $(h_h, 0_h, 4.5_h)$ and $(h_h, h_h, 3_h)$. An orange cryostat was used to cool the sample to the desired temperatures, scans were performed mostly at the base temperature of 2 K, while some scans were repeated for several temperatures up to 100 K. A vertically-focusing Pyrolitic graphite (PG) monochromator and horizontally- focusing PG analyzer selected the incident and final energies respectively. While a nitrogen-cooled beryllium filter was used between the sample and analyzer to remove $\lambda/2$ and higher order reflections from the monochromator. An sketch of the instrument is illustrated in Figure 5.4. The instrument was operated in the W-configuration $(+ - +)$ and the collimator settings were guide-60′-open-open. The measurements were performed with fixed final wavevectors of $k_f = 1.2$ Å^{-1} (2.98 meV) and $k_f = 1.55$ Å^{-1} (4.98 meV). The resolution of the instrument, determined from the full-width-half-maximum (FWHM) of the incoherent scattering was 0.09 meV for $k_f = 1.2$ Å^{-1} and 0.12 meV for a $k_f = 1.55$ Å^{-1}. Constant-wavevector scans were used to map out the magnon dispersions from $0 - 8$ meV in steps of 0.05 meV. The average counting time was 4 minutes per point.

In order to get an overview of the magnetic excitation spectrum throughout the whole Brillouin zone, the Merlin spectrometer was used [36, 37]. Merlin is a direct geometry time-of-flight spectrometer at the ISIS facility, Rutherford Appleton Laboratory, UK. Figure 5.5 is a schematic drawing of the spectrometer. Data are collected by 3 m long
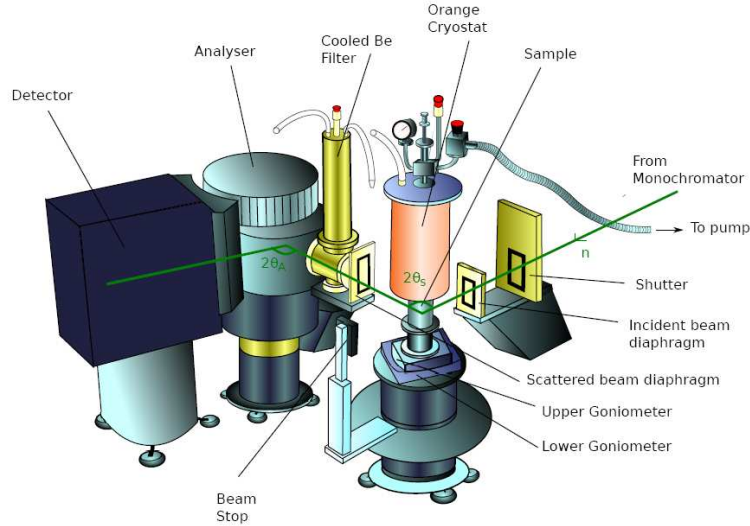
Figure 5.4: Sketch of the Flex triple-axis spectrometer in W-configuration. The neutron guide and monochromator are not shown. Taken from reference [77].

^{3}He position sensitive detectors with 2.5 cm diameter and a resolution of 21 mm along the tube covering an angular range of -45° to 135° in the horizontal plane and ±30° in the vertical direction. Such detectors make it possible to measure in two spatial dimensions in addition to time/energy; this means that each measurement on Merlin takes a large three dimensional cut out of the four dimensional $S(\mathbf{Q}, \omega)$, providing an overview of the spectrum. For this experiment three single crystals of total mass 10 g, were co-aligned with the c_h axis vertical and cooled in a closed cycle cryostat to a base temperature of 6 K. A Fermi chopper was phased to select neutrons with an incident energy of 10 meV and was spun at a frequency of 100 Hz to achieve a resolution at the elastic line of 0.37 meV and at 5.5 meV transfer of 0.19 meV. Higher energy scans were performed with incident energies 20 meV and 25 meV and chopper speeds of 100 Hz and 200 Hz, which gave a resolution at the elastic line of 0.85 meV and 0.74 meV respectively.

For a single incident energy and crystal orientation, the component of $\mathbf{Q}$ parallel to the scattered beam $(\mathbf{Q}_\parallel)$ is coupled to the time-of-flight (and so to the neutron energy transfer) for a given detector pixel. Thus as the time-of-flight changes, the measurement follows a curved path in energy and $\mathbf{Q}_\parallel$ where the actual trajectory in reciprocal space depends on the sample angle. At different orientations of the sample with respect to the incident beam, the coupling between reciprocal space and energy will be different. By making measurements at many different sample orientations and taking into account data from all the detectors, the cross-section as a function of energy and three reciprocal
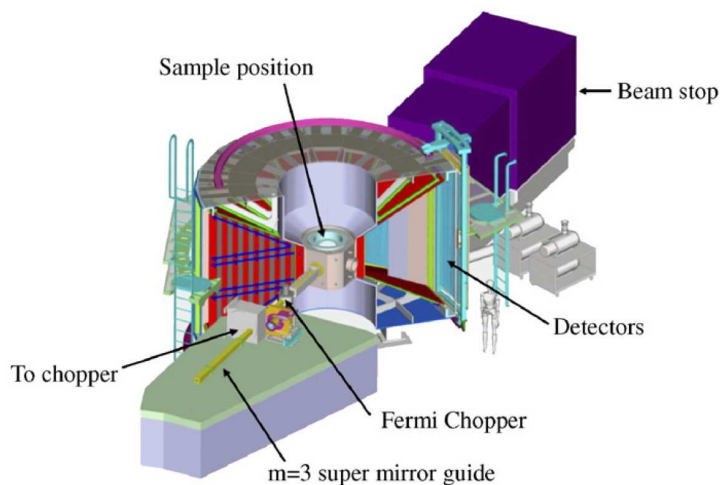
Figure 5.5: Schematic drawing of the Merlin chopper spectrometer. Taken from reference [36].

space directions can be measured [73]. This relatively new technique was used in this experiment and it will be refer to as omega (ω-) scans.

Figure 5.6 describes the method where a neutron beam with a fixed wavevector is incident on the sample which is at certain initial position, ω_0. The neutrons scatter and the spectrum is taken making use of the ^{3}He position sensitive detectors which collect the neutron in both the horizontal and the vertical plane as a function of time-of-flight. All this information is saved as a datafile. This measurement is repeated for a new sample position by rotating the crystal about the vertical axis by an angle Δ_ω and acquiring data in the same way. This procedure is repeated until a large region of reciprocal space is scanned, ideally a region of the reciprocal space larger than the magnetic Brillouin zone. The full data set can be combined and visualized using the software package Horace [73]. In this way the complete excitation spectrum over a large volume of reciprocal space and energy transfer can be collected and analyzed.

For the Merlin experiment, the samples were rotated about the vertical axis in steps of $\Delta_\omega = 1°$ covering an angular range of $70°$ with a counting time of 2 hours per step. A vanadium standard measurement was used to normalize the individual measurements for detector efficiency.

The temperature dependences of the full-width-half-maximum and lineshape of the magnon excitations were investigated in the second V2-Flex experiment and in the IN5 direct geometry time of flight spectrometer at ILL [38]. Special attention was paid to the linewidth broadening at the minimum and maximum of the dispersion. For the experiment at IN5, two single crystals of total mass 7.745 g were co-aligned with the c_h axis
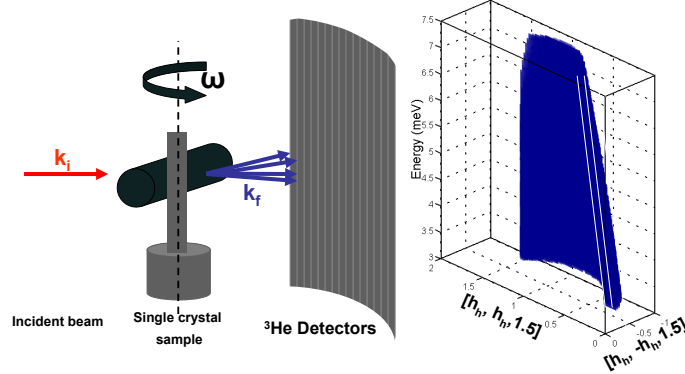
Figure 5.6: Description of an ω scan on a time of flight spectrometer with position sensitive detectors. The oriented single crystal is mounted on a rotating table, the incident neutron beam with wavevector k_i is scattered by the single crystal. The scattered neutrons are detected over a wide range of scattering angles in the horizontal and vertical directions by the position sensitive detectors. For this single crystal orientation a dataset is acquired as plotted on the right side of the figure. This measurement is repeated for a range of ω angles, thus scanning all three directions in reciprocal space.

vertical. Measurements were performed with an initial wavelength of $\lambda_0 = 2.8\,\text{Å}$ (incident energy of $10.434\,\text{meV}$), the choppers were spun at $16000\,\text{rpm}$ which gave a resolution at the elastic line of $0.5\,\text{meV}$. The crystal angle was optimized to measure at two reciprocal space points $(-1_h, -1_h, 3_h)$ and $(-1_h, -1_h, 1.5_h)$. Data have been acquired at the following temperatures: $2\,\text{K}$, $15\,\text{K}$, $20\,\text{K}$, $25\,\text{K}$, $30\,\text{K}$ and $40\,\text{K}$. No background subtraction or corrections have been done on the data.

Constant wavevector scans were performed on V2/Flex at $(0.5_h, 0.5_h, 3_h)$ and $(0_h, 0_h, 3_h)$ at 11 different temperatures: $2\,\text{K}$, $5\,\text{K}$, $10\,\text{K}$, $15\,\text{K}$, $20\,\text{K}$, $25\,\text{K}$, $30\,\text{K}$, $40\,\text{K}$, $75\,\text{K}$ and $100\,\text{K}$. The high resolution of V2/Flex (0.09meV at the elastic line) allowed small changes in the linewidth to be observed.

5.3 Crystal Twinning and Spatially Anisotropic Magnetic Interactions

As explained in the introduction and in the previous chapter, Sr$_3$Cr$_2$O$_8$ undergoes a structural phase transition to a monoclinic structure making the hexagonal Cr^{5+}-Cr^{5+} distances become unequal and the corresponding exchange interactions inequivalent. According to Chapon *et al.* [50] only four isotropy subgroups of $R\bar{3}m$ account for the necessary reflection conditions for the experimentally observed superlattice reflections.

Those four have the space groups $C2/m$ and $C2/c$ and are related to the parent space group by the same basis vectors: $(\bar{1}, 1, 0)$, $(\bar{1}, \bar{1}, 0)$, $(\frac{1}{3}, \frac{\bar{1}}{3}, \frac{2}{3})$ and with irreducible representations: T_3^+ and T_3^- [78]. From the four subgroups only two solutions with monoclinic space group $C2/c$, unique-axis b, agree with the observed reflections. Only one model, with T_3^- reproduced the observed intensities.

The monoclinic distortion can occur in three equivalent ways, each rotated by $60°$ to each other about the shared hexagonal axis. Figure 5.7(a) illustrates this rotation, by showing the original hexagonal lattice in red and 3 possible monoclinic lattices in blue, magenta and black. These equivalent distortions are known as twins and are all present at low temperature with approximately equal volume. a_h, b_h, c_h are the conventional basis vectors of the parent space group $R\bar{3}m$. They define the hexagonal coordinate system and can be written in terms of the Cartesian coordinate systems as:

$$a_h = a\hat{i}, \; b_h = -\frac{1}{2}b\hat{i} + \frac{1}{2}\sqrt{3}b\hat{j}, \; c_h = c\hat{k}. \tag{5.1}$$

The transformation from this hexagonal coordinate system to the three monoclinic coordinate systems is given in Table 5.1.

Table 5.1: The relationship between the hexagonal lattice parameters (a_h, b_h, c_h) and those of the three monoclinic twins (a_{mi}, b_{mi}, c_{mi}) are given.

Real Space			
T-1 (a_{m1}, b_{m1}, c_{m1})	$a_{m1} = a_h - b_h$	$b_{m1} = a_h + b_h$	$c_{m1} = a_h/3 - b_h/3 + 2c_h/3$
T-2 (a_{m2}, b_{m2}, c_{m2})	$a_{m2} = 2a_h + b_h$	$b_{m2} = b_h$	$c_{m2} = 2a_h/3 + b_h/3 + 2c_h/3$
T-3 (a_{m3}, b_{m3}, c_{m3})	$a_{m3} = a_h + 2b_h$	$b_{m3} = -a_h$	$c_{m3} = a_h/3 + 2b_h/3 + 2c_h/3$

The transformation from the hexagonal reciprocal space to the monoclinic reciprocal space of the three twins is given in Table 5.2 and illustrated in Figure 5.7(b), where the original hexagonal reciprocal lattice is draw in red, and the monoclinic Brillouin zone for the three twins are shown in blue, pink and black. The corners of the monoclinic Brillouin zones sit at the midpoints of the faces of the hexagonal Brillouin zone (M points). The M point at $(1/2_h, 1/2_h, 0_h)$ is at the corner of the Brillouin zone of monoclinic Twins 2 and 3, but is at the center of the Brillouin zone of Twin 1. The twins are clearly non-equivalent at this point and should give different excitations.

Even though the real low temperature space group is monoclinic, the hexagonal notation will be kept in this chapter in order to simplify the analysis and the visualization of the INS data.
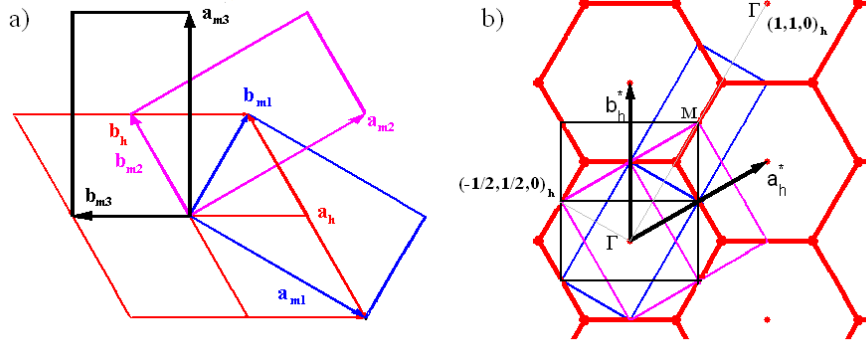
Figure 5.7: (a) Relationship between the hexagonal and monoclinic real spaces. Red: hexagonal lattice. Blue: lattice of monoclinic Twin 1. Magenta: monoclinic Twin 2. Black: monoclinic Twin 3. (b) Relationship between the hexagonal and monoclinic reciprocal spaces, projected onto the hexagonal plane, using the same color coding.

Table 5.2: Relationship between the hexagonal and monoclinic reciprocal spaces.

Reciprocal Space			
T-1 $(a_{m1}^*, b_{m1}^*, c_{m1}^*)$	$a_{m1}^* = a_h^*/2 - b_h^*/2 - c_h^*/2$	$b_{m1}^* = a_h^*/2 + b_h^*/2$	$c_{m1}^* = 3c_h^*/2$
T-2 $(a_{m2}^*, b_{m2}^*, c_{m2}^*)$	$a_{m2}^* = a_h^*/2 - c_h^*/2$	$b_{m2}^* = -a_h^*/2 + b_h^*$	$c_{m2}^* = 3c_h^*/2$
T-3 $(a_{m3}^*, b_{m3}^*, c_{m3}^*)$	$a_{m3}^* = b_h^*/2 - c_h^*/2$	$b_{m3}^* = -a_h^* + b_h^*/2$	$c_{m3}^* = 3c_h^*/2$

5.4 Powder Inelastic Neutron Scattering

Inelastic neutron scattering measurements on a powder sample were performed on the TOF spectrometer NEAT at HZB. Figure 5.8 shows two data sets collected on NEAT at 2 K plotted as a function of wavevector transfer $|Q|$ and energy transfer E with incident energies 13.08 meV and 7.989 meV respectively. The spectrum shown in Figure 5.8(a) reveals a band of gapped excitations extending between a lower and upper energy centered at ~5.5 meV. The measured neutron scattering intensity decreases with increasing $|Q|$ confirming the magnetic nature of the excitations. The figure on the right corresponds to the data set acquired using an incident energy 7.989 meV, it confirms the complete absence of magnetic scattering below 3.5 meV and reveals minima in the excitation spectrum that occur at $|Q| = 0.87\text{Å}^{-1}$ and $|Q| = 1.48\text{Å}^{-1}$ (see red arrows in Fig. 5.8(b)), suggesting that the minima of the dispersion occur at $(h_h/2, 0_h, \ell_h)$ where h_h and ℓ_h are integer, as well as symmetry equivalent positions. A higher incident energy dataset(20 meV) was used to confirm a single band of excitations.

All data shown here have been corrected for detector efficiency, vanadium normalized and background subtracted. The detectors were normalized by making a cut in the data integrating the elastic scattering as a function of detector number and then dividing
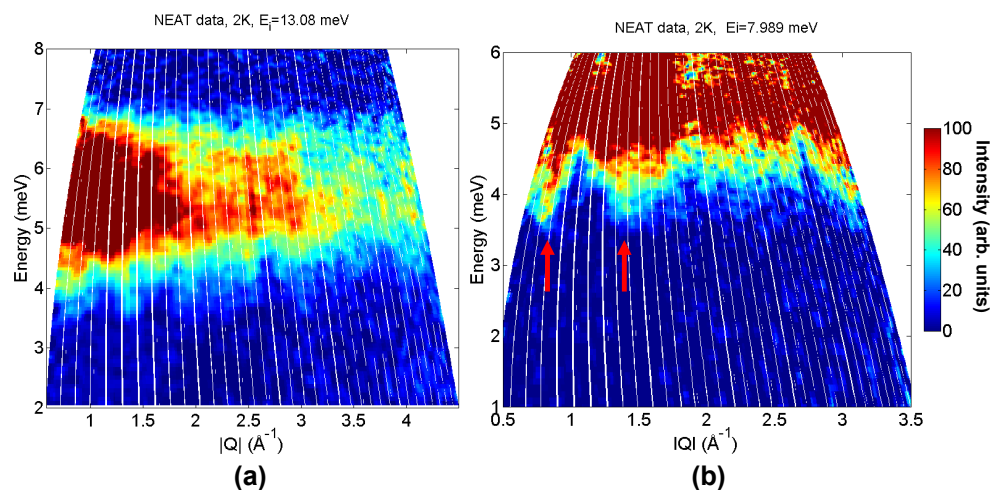
Figure 5.8: Inelastic neutron scattering data measured on a powder sample. The data were collected on NEAT at 2 K and the incident energy was 13.08 meV (left figure) and 7.9 meV (right figure). The intensity is in arbitrary units.

the dataset by this quantity. To obtain the background, the data excluding the signal region (3-7.5 meV) was used. The data were then smoothed and an extrapolation was performed between 3 and 7.5 meV to estimate the background under the signal. This was then subtracted from the data. The data correction is illustrated in Figure 5.9. The first slice is raw data and a difference in detector efficiency is clear at low wavevectors. The second is after the detector efficiency normalization and the third is the final background subtracted data.
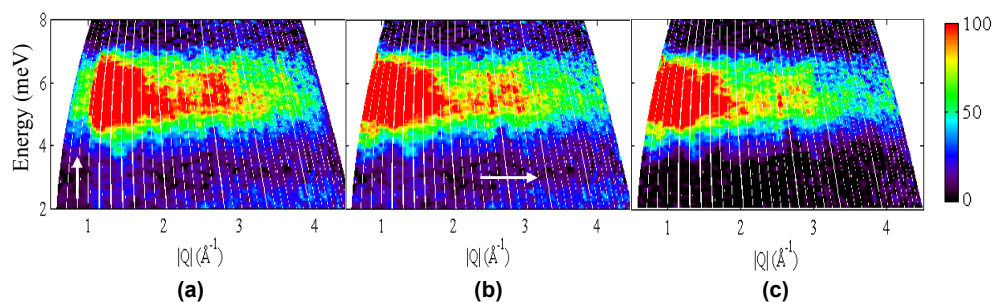
Figure 5.9: Background subtraction procedure. Figure (a) is raw data, where the white arrow shows the difference in efficiency for the detectors located at low scattering angles. Figure (b) is after the normalization, the white arrow shows the increasing background at higher wavevectors. Figure (c) shows the background corrected data.

Figure 5.10 gives the spectrum acquired on NEAT with an incident energy of 13.08 meV

integrated over the wavevector range $1.5\,\text{Å}^{-1} < |Q| < 3.5\,\text{Å}^{-1}$ and plotted as a function of energy, it shows an energy gap of $E_{gap} = 3.4(3)\,\text{meV}$ and an upper maximum of the excitation at $E_{upper} = 7.10(5)\,\text{meV}$. The inset in the figure shows a similar cut through the dataset acquired with an incident energy of $7.9\,\text{meV}$, this cut confirms a clean gap. These values of E_{gap} and E_{upper} are in agreement with the values of $3.54(5)\,\text{meV}$ and $7.09(4)\,\text{meV}$ extracted form the critical fields observed in the magnetization data in the previous chapter.
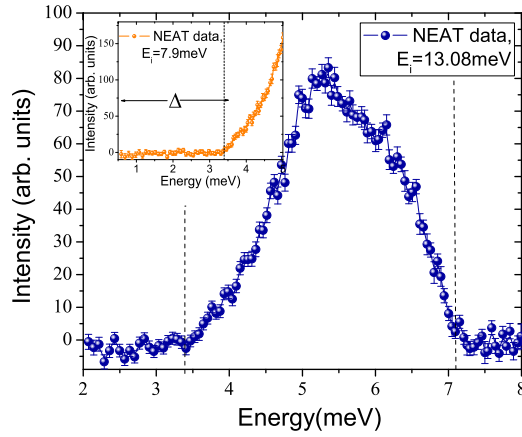
Figure 5.10: The data (blue circles) collected with an incident energy of 13.08meV, integrated over the wavevector range $1.5\,\text{Å}^{-1} < |Q| < 3.5\,\text{Å}^{-1}$ and plotted as a function of energy. The dashed lines indicate the bandwidth of the excitations. The inset shows the lower energy region and reveals the clean energy gap (Δ). These data were taken with an incident energy of $7.9\,\text{meV}$ and the cut is over the wavevector range of $0.6\,\text{Å}^{-1} < |Q| < 1.5\,\text{Å}^{-1}$.

The powder averaging prevents exact determination of the dispersion relations of the magnon excitations; however some information can be extracted from the variation of the scattered intensity with wavevector transfer. For this extraction it is necessary to understand the magnetic scattering cross section, that was described in Chapter 3 and can be written as:

$$\frac{d^2\sigma(\boldsymbol{q}, E)}{dEd\Omega} = N\frac{k_f}{k_i}r_m^2\,|F(\mathbf{q})|^2 \sum_{\alpha,\beta} \frac{g_\alpha}{2}\frac{g_\beta}{2}\left(\delta_{\alpha\beta} - \frac{q_\alpha q_\beta}{q^2}\right)S^{\alpha\beta}(\mathbf{Q}, E). \qquad (5.2)$$

where $S^{\alpha\beta}(\mathbf{q}, E)$ is the dynamical spin structure factor, given by Eq. 3.20 and is repeated here for clarification:

$$S^{\alpha\beta}(\mathbf{Q}, E) = \int_{-\infty}^{\infty} e^{iEt/\hbar}\frac{1}{N}\sum_{j,j'}\left\langle e^{-iq(\mathbf{R}_j - \mathbf{R}'_j)}S_j^\alpha S_j'^\beta(t)\right\rangle\frac{dt}{2\pi\hbar}. \qquad (5.3)$$

This factor is a fundamental characteristic of the dynamical properties of the spin system and is related to the dynamical spin susceptibility, which determines the response of the system to a perturbation that varies in space and time, in this case the incident neutron beam, therefore determining the results of the neutron scattering experiment. This relation is given by the fluctuation dissipation theorem [3, 79] which expresses the close connection between the spontaneous fluctuations in the system and the response of the system to the external perturbations. This was shown in Eq. 3.23 and shown again here for clarification:

$$S^{\alpha\beta}(\mathbf{Q}, E) = \frac{\chi''_{\alpha\beta}}{(a - e^{-\hbar\omega/k_B T})}, \tag{5.4}$$

where χ'' is the dynamical susceptibility [3]. The frequency moments of the spin structure factor generate the useful relations known as sum rules [72]. The first moment is given by:

$$\langle E \rangle = 2 \int_{-\infty}^{\infty} \frac{d\omega}{2\pi} \omega S^{\alpha\beta}(\mathbf{Q}, \omega) = \int_{-\infty}^{\infty} \frac{d\omega}{2\pi} \omega \chi''_{\alpha\beta}(\omega) = -\hbar^{-1} \left\langle [[\mathcal{H}, S^{\alpha}(\mathbf{Q})], S^{\alpha}(\mathbf{Q})^{\dagger}] \right\rangle. \tag{5.5}$$

Assuming a Heisenberg Hamiltonian: $\mathcal{H} = -\frac{1}{2} \sum_i \mathcal{J}_i S_0 \cdot S_{d_i}$, where J_i is the exchange constant coupling the ith nearest neighbor spins and d_i is their separation, the first moment sum rule gives:

$$\langle E \rangle \propto - \sum_i J_i \langle \mathbf{S}_0 \cdot \mathbf{S}_{d_i} \rangle (1 - cos(\mathbf{Q} \cdot \mathbf{d}_i)). \tag{5.6}$$

where $\langle \mathbf{S}_0 . \mathbf{S}_{d_i} \rangle$ is the two spin correlation function for this pair. From this expression it is clear that each coupling constant J_i produces a modulation in the first moment with a periodicity depending on the separation d_i of the spins. Thus by fitting this expression to the first moment of the data it should be possible to identify the dominant exchange paths.

For comparison to the powder measurement of $Sr_3Cr_2O_8$ it is necessary to take the powder average of Equation 5.6 by integrating the wavevector $\boldsymbol{Q}$ over all possible directions while keeping its modulus $|\boldsymbol{Q}|$ fixed.

$$[(1 - cos(\boldsymbol{Q} \cdot \mathbf{d}_i))]_{powder} = \frac{|\boldsymbol{Q}|^2}{4\pi |\boldsymbol{Q}|^2} \int_{\theta=0}^{2\pi} \int_{\phi=0}^{\pi} [1 - cos(|Q| |d| cos\phi)] sin\phi d\theta d\phi, \tag{5.7}$$

including the magnetic form factor for Cr^{5+} , $f_{Cr^{5+}}(|Q|)$, the first moment for the powder is:

$$\langle E \rangle \propto \sum_i J_i \langle \mathbf{S}_0 \cdot \mathbf{S}_i \rangle |f_{Cr^{5+}}(|Q|)|^2 \left(1 - \frac{sin(|Q| |d_i|)}{|Q| |d_i|} \right). \tag{5.8}$$

As explained in the introduction, the possible interactions for the monoclinic phase of $Sr_3Cr_2O_8$ are spatially anisotropic (see Figure 5.1), however since the set of distances d_i' and d_i'' (d_i''') ($i \neq 0$) are almost equal it is not possible to distinguish between them in the fitting and we therefore replace these distances by the average distance d_i ($d_0 = 3.8448$ Å, $d_1 = 4.3172$ Å, $d_2 = 5.5718$ Å, $d_3 = 6.7696$ Å). The expression then becomes

$$\langle E \rangle \propto - \sum_{i=0}^{3} A_i |f_{Cr^{5+}}(|Q|)|^2 \left(1 - \frac{sin(|Q| |d_i|)}{|Q| |d_i|} \right). \tag{5.9}$$

Where the terms A_0 and A_i are

$$A_0 = J_0 \langle \mathbf{S}_0 \cdot \mathbf{S}_{d_0} \rangle , \tag{5.10}$$

$$A_i = J_i' \langle \mathbf{S}_0 \cdot \mathbf{S}_{d_i'} \rangle + 2J_i'' \langle \mathbf{S}_0 \cdot \mathbf{S}_{d_i''} \rangle , \; i = 1, 2, 4, \tag{5.11}$$

$$A_3 = J_3' \langle \mathbf{S}_0 \cdot \mathbf{S}_{d_3'} \rangle + J_3'' \langle \mathbf{S}_0 \cdot \mathbf{S}_{d_3''} \rangle + J_3''' \langle \mathbf{S}_0 \cdot \mathbf{S}_{d_3'''} \rangle , \tag{5.12}$$

The expression for the form factor is:

$$|f_{Cr^{5+}}(|Q|)|^2 = \left| Ae^{-as^2} + Be^{-bs^2} + Ce^{-cs^2} + D \right|^2 , \tag{5.13}$$

where $s = |Q| /4\pi$. The constants for the form factor of Cr^{5+} could not be found in the literature, therefore they were estimated by extrapolation from the known form factors of Cr^{3+}, Cr^{4+} and V^{4+}, as can be seen in Figure 5.11(left) obtaining: $A = -0.2602$, $a = 0.03958$, $B = 0.33655$, $b = 15.24915$, $C = 0.90596$, $c = 3.2568$ and $D = 0.0159$.

The data collected with $E_i = 13.06$ meV was multiplied by energy transfer and integrated over an energy range of 4.16 meV $<$ E < 7.07 meV to give the first moment, this is shown in Fig. 5.11(right) as a function of wavevector. The theoretical expression (Equation 5.9) was then used to fit the data by varying the quantities A_0 and A_i. The best fit is shown in the figure by the green line, corresponding to the fit values of $A_0 = 402(3)$, $A_1 = -24(5)$, $A_2 = -24(4)$, $A_3 = -45(4)$. The goodness of fit was $R^2 = 0.9301$.

The results reveal that the dominant exchange constant of $Sr_3Cr_2O_8$ which is responsible
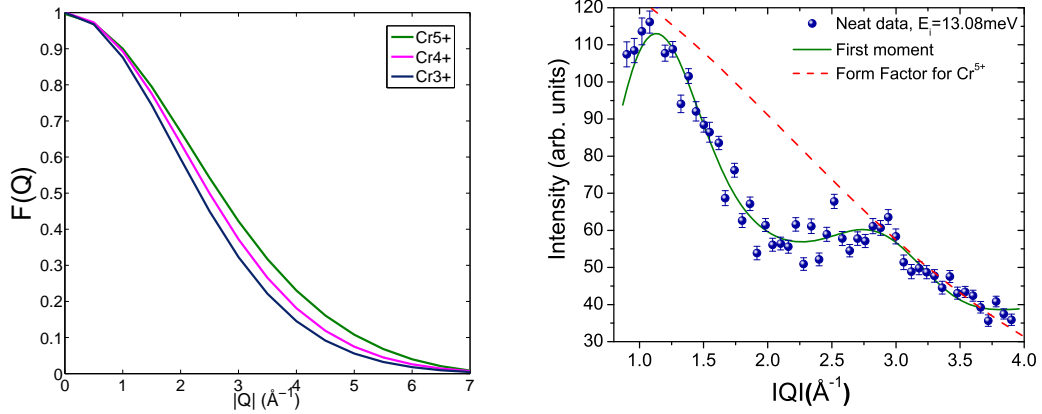
Figure 5.11: (left) Magnetic form factor for different Cr ions. (right) The data (blue circles) from Fig. 5.8, multiplied by energy transfer integrated over energy and plotted as a function of wavevector. The green line gives the fit to the first moment sum rule, Eqn 5.9.

for coupling the spins into dimers is the intrabilayer interaction, J_0 although this result had been assumed it had not been experimentally verified until now. Indeed the size of A_0 is more than one order of magnitude greater than the other A_i values, clearly identifying it as the main interaction. Unfortunately it is not possible to obtain the absolute values of the exchange constants using this method as the fit quantities also depend on the spin correlation functions. Nevertheless it is clear that there are significant interdimer interactions and that $Sr_3Cr_2O_8$ can be viewed as a network of dimers coupled both along the c_h axis and within the distorted 'hexagonal' plane.

In order to gain more information about the exchange paths in $Sr_3Cr_2O_8$ it is necessary to measure the magnon dispersions along specific directions in reciprocal space, since only in this way can the set of interactions J_i' and J_i'' (J_i''') be distinguished from each other and their values accurately determined. This information can be obtained by doing single crystal inelastic neutron scattering measurements, as shown in the next section.

5.5 Single Crystal Inelastic Neutron Scattering

Single crystal inelastic neutron scattering experiments have been performed on two instruments, the V2-Flex triple axis spectrometer at HZB and the Merlin time of flight spectrometer at ISIS. These two experiments allowed the dispersion relation of the magnons within the excitation band detected on NEAT to be acquired. The analysis of the results and the fitting of the dispersion along key directions using a RPA model that will be explained later allowed the exchange couplings in $Sr_3Cr_2O_8$ to be extracted.

For simplicity, the single crystal data were analyzed in terms of the hexagonal reciprocal space instead of the three monoclinic reciprocal spaces.

5.5.0.1 V2-Flex

In order to make an accurate determination of the exchange constants, high resolution single crystal inelastic neutron scattering experiments were performed using V2-Flex at $2\,\mathrm{K}$. The excitation spectrum was mapped out by scanning the energy transfer at constant wavevector in the $(h_h, 0_h, \ell_h)$ and (h_h, h_h, ℓ_h) planes. A total of 70 scans were performed mapping the excitations along c_h^*: $(0_h, 0_h, \ell_h)$, $(1_h, 0_h, \ell_h)$, $(0.5_h, 0_h, \ell_h)$ and in the hexagonal plane: $(h_h, 0_h, 1.5_h)$, $(h_h, 0_h, 3_h)$, $(h_h, 0_h, 4.5_h)$, $(h_h, h_h, 3_h)$. Some of these scans are shown in Figure 5.12. The inset in Figure 5.12(a) illustrates the hexagonal reciprocal space (red) while the green and blue lines show the wavevectors that were scanned. There are regions where only one mode was detected along c_h^* (Fig. 5.12a) and others where three peaks were observed (Fig. 5.12b). These three excitation branches confirm the Jahn-Teller distortion and the twinning described earlier. This structural phase transition gives rise to three monoclinic twins, each of which produces a separate mode. The twins are rotated by $60°$ with respect to each other in the hexagonal plane but coincide along the c_h axis. As a result the three twins are degenerate in reciprocal space along (h_h, k_h, ℓ_h) for h_h, k_h integer but are non-degenerate at other wavevectors (Fig. 5.12(a). Similar dispersion relations have been measured in Ba$_3$Cr$_2$O$_8$ by M. Kofu *et al.* [62], showing that this compound undergoes the same structural distortion found in Sr$_3$Cr$_2$O$_8$. Kofu *et al.* measured inelastic neutron scattering on the compound and by applying a magnetic field proved that the three modes are all triply degenerate. This confirms that the three magnetic modes are triplons or magnons coming from the three twin domains.

The scans were combined to make colormaps of the dispersions along specific directions. Figure 5.13 shows two colorplots for the directions $(0_h, 0_h, \ell_h)$ and $(h_h, 0_h, 3_h)$. The excitations disperse in all directions showing that the interdimer couplings are three-dimensional. The branches are degenerate for the directions $(0_h, 0_h, \ell_h)$ and $(1_h, 0_h, \ell_h)$, so along the c_h^* for h_h and k_h integer. They are non-degenerate when h_h and k_h are non-integer.

As can be clearly seen in Figure 5.13(a) the scattered intensity is strongly modulated, especially along the direction $(0_h, 0_h, \ell_h)$. This is true for dimerized systems such as Sr$_3$Cr$_2$O$_8$ as the intensity of the excitations is dominated by the dimer structure factor.
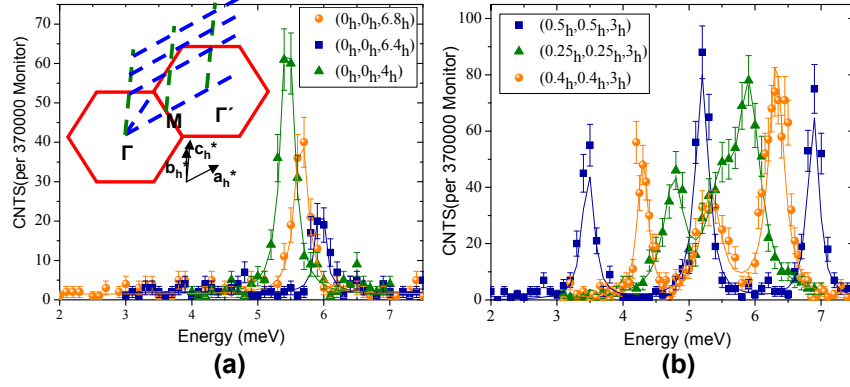
Figure 5.12: Constant-wavevector scans in the (a)$(0_h, 0_h, \ell_h)$ and (b)$(h_h, h_h, 3_h)$ directions measured at $2\,\mathrm{K}$ on Flex. The solid lines are fits to Lorentzian functions. The inset shows the wavevectors scanned in these experiments.
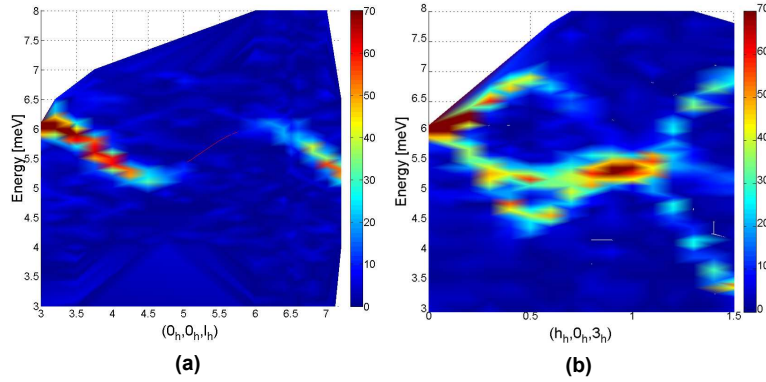
Figure 5.13: Constant-wavevector scans in the (a)$(0_h, 0_h, \ell_h)$ and (b)$(h_h, 0_h, 3_h)$ directions have been interpolated in order to display the dispersion relation. The color gives the scattered intensity in arbitrary units.

According to Furrer and Güdel, the structure factor can be written as [80]:

$$|f_{\mathrm{Cr}^{5+}}(|\boldsymbol{Q}|)|^2 \left(1 - cos(\boldsymbol{Q} \cdot \boldsymbol{d})\right) = |f_{\mathrm{Cr}^{5+}}(|Q|)|^2 \left(1 - cos(2\pi\ell_h d_0/c_h)\right). \tag{5.14}$$

Since the dimer separation d_0 is parallel to the c_h-axis, an intensity modulation as a function of wavevector transfer along ℓ_h is expected. The individual scans were fitted to a Lorentzian function and the intensities were extracted. The colored symbols in Fig. 5.14 show the intensity of the excitation in the $(0_h, 0_h, \ell_h)$ direction. The intensity is found to modulate with a distinctive minimum at $\ell_h = 5.5\,\mathrm{r.l.u.}$; a comparison to the theoretical expression in Equation 5.14 (orange line) suggests that the dimer separation is $c_h/5.5 = 3.67\,\text{Å}$ which is close to the nearest neighbor Cr^{5+}-Cr^{5+} distance of $d_0 =$

3.7140(4) Å. This modulation therefore provides yet further evidence that the dimers in $Sr_3Cr_2O_8$ are formed by the nearest neighbor intrabilayer coupling which is parallel to c_h.
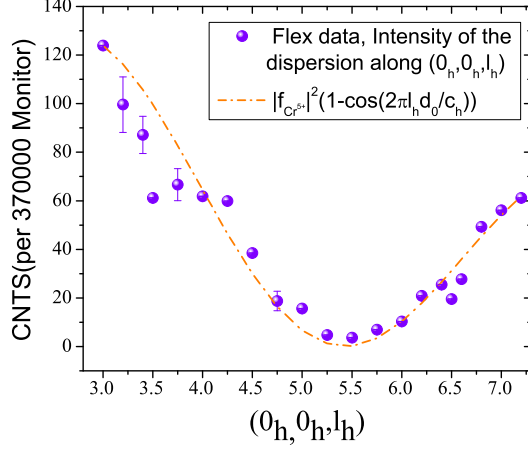
Figure 5.14: Fitted intensity of the magnon in the $(0_h, 0_h, \ell_h)$ direction, solid line represent the structure factor for a dimer system according to Equation 5.14.

The triple axis measurements clearly provide detailed high resolution information about the dispersion of the magnons along key high symmetry directions in reciprocal space. Nevertheless the dimers are coupled 3-dimensionally and the magnetic modes are expected to disperse along all directions in reciprocal space. In order to fully understand the dispersion, it is necessary to have information at all wavevectors. This information can be obtained in a more effective way using a time of flight spectrometer and doing ω scans.

5.5.0.2 Merlin

Single crystal inelastic neutron scattering experiments were performed at 6 K on the Merlin ToF spectrometer to measure the magnetic excitations over a large region of reciprocal space (h_h, k_h, ℓ_h) using the technique described in the experimental details section. The software package Horace [73] was used to combine all the individual scans and for data visualization. Figure 5.15 shows the full extent of the dispersion in the $a_h^* b_h^*$-plane summed over the perpendicular direction c_h^* in the range $-3 < \ell_h < 0$. A complicated excitation spectrum is revealed, and is in agreement with the powder data, having a gap of 3.4 meV and a maximum energy of ≈ 7 meV.

Figure 5.16 shows two slices for constant h_h and k_h as a function of ℓ_h and energy transfer. The left figure shows a single dispersion curve along $(0_h, 1_h, \ell_h)$ whereas the
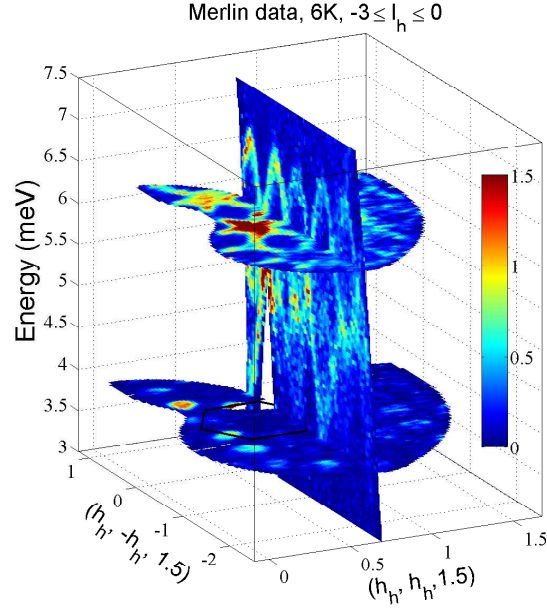
Figure 5.15: The Merlin data set displaying the dispersion as a function of energy and wavevector in the hexagonal (a_h^*, b_h^*)-plane and integrated over c_h^*, from -3 to 0 r.l.u. The solid black hexagon indicates the hexagonal Brillouin Zone. The intensity is in arbitrary units.

right figure shows three magnon modes dispersing along $(-0.5_h, 1.5_h, \ell_h)$. These results are in agreement with the Flex results.
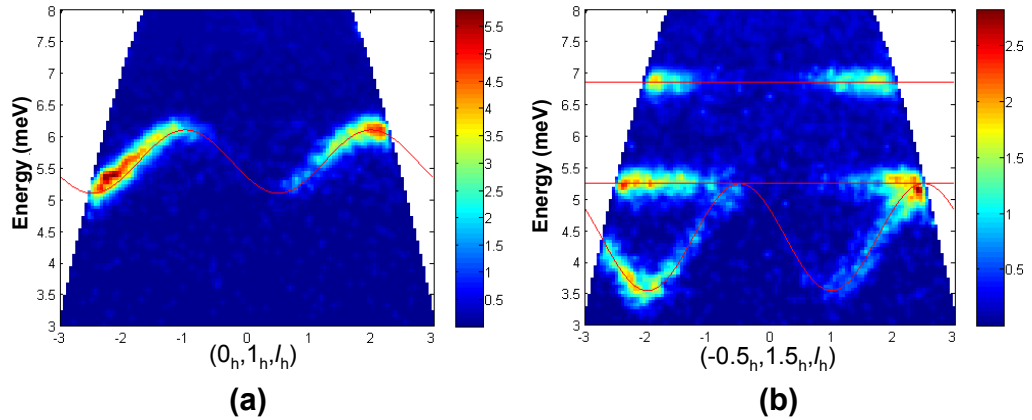
Figure 5.16: Slices through the Merlin data plotted as a function of energy transfer and wavevector along $(0_h, 1_h, \ell_h)$ (left) and $(-0.5_h, 1.5_h, \ell_h)$ (right). The intensity is in arbitrary units. The sinusoidal and flat lines are a guide to the eye for the dispersion relation.

Figure 5.17 shows two slices at constant energy transfer plotted as a function of two

wavevector directions in the 'hexagonal' plane and the data were integrated over c_h^*. Figure 5.17(a) is at the low energy dispersion edge of 3.5 meV. The minima of the dispersion occur at the midpoints of the faces of the hexagonal Brillouin zone, equivalent to $(1/2_h, 1/2_h, 0_h)$, which correspond to the corners and center of the three monoclinic Brillouin zones. Figure 5.17(b) shows the dispersion at a constant energy transfer of 6 meV. All the modes merge together at h_h and k_h integer, which is in the center of the Brillouin zone (Γ).

(a)   **(b)**
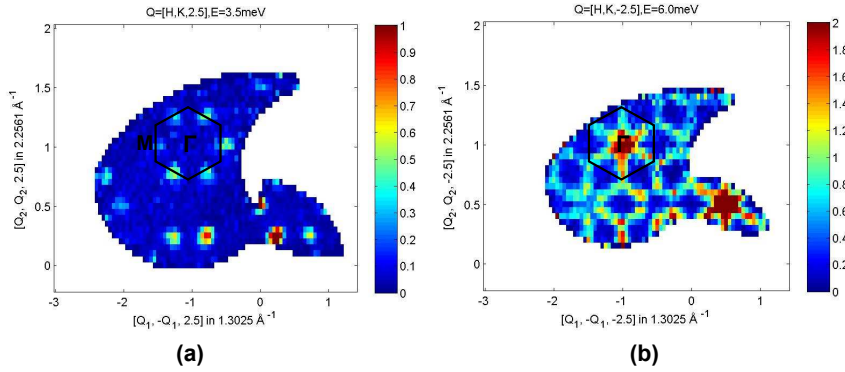
**Figure 5.17:** Slice showing the scattering for energy transfer 3.5 meV (a) and 6meV (b) as a function of wavevector in the hexagonal (a_h^*, b_h^*)-plane, integrated over c_h^*, from -3 to 0 r.l.u. The solid black hexagon indicates the hexagonal Brillouin Zone. The intensity is in arbitrary units.

In addition to the observed one-magnon scattering, two-magnon scattering is also expected where the neutron creates two magnons simultaneously. At large separation the magnons do not interact but behave as free particles, but when they come closer they can interfere and scatter off each other. Ignoring magnon-magnon interactions the energy of this new state, ω_{2mag} is equal to the sum of the energies of the 2 single magnons $\omega_{1mag}(p) + \omega_{1mag}(q)$, and has total wavevector $\boldsymbol{k} = \boldsymbol{p} + \boldsymbol{q}$. Since the energy and wavevector transfer of the neutron is shared between two magnons there are many ways in which the scattering condition can be achieved and this results in the formation of a continuum as shown in Figure 5.18 for the case of 1-dimensional dimer magnet [81].

The two magnon cross-section is expected to be considerably weaker than the one-magnon cross-section, but nevertheless observable thanks to the new generation of time of flight spectrometers that have a high flux and low background.

Figure 5.19(a) shows Merlin data collected at 6 K with an incident energy of 25 meV as a function of wavevector and energy transfer. These data were measured on a single crystal for only one crystal orientation ω. All the data were averaged to obtain a pseudo powder spectrum as a function of $|\boldsymbol{Q}|$. The two-magnon scattering is weak and barely visible in this slice. there is a phonon component that increases above 3 Å^{-1} and the
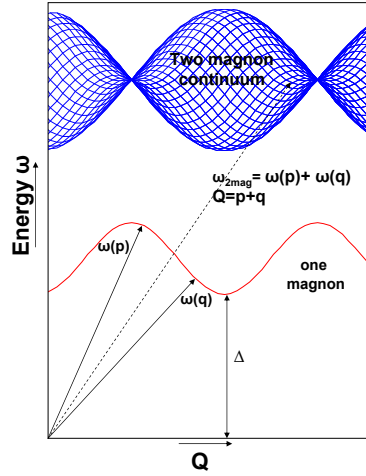
Figure 5.18: One-magnon and two-magnon scattering on a 1-dimensional dimer magnet [81] as a function of energy and wavevector transfer. For a 3-dimensional magnet as $Sr_3Cr_2O_8$ the two magnon continuum has no nodes.

strong feature at $5.5\,\text{Å}^{-1}$ is an acoustic phonon.

The structure factor for the two-magnon process is in antiphase to the structure factor of the one-magnon. This implies that the two-magnon continuum would be more intense in the regions where the one-magnon intensity is low. The structure factor has the form:

$$|f_{\text{Cr}^{5+}}(|Q|)|^2 \left(1 + cos(2\pi\ell_h d_0/c_h)\right). \tag{5.15}$$

The two-magnon component is much clearer when a 1d cut is done through the single crystal data as shown in fig 5.19(b). The cut was performed along $-0.2 < h_h < 0.2$, $-1 < k_h < 1$, $-1 < \ell_h < 1$ where the one-magnon intensity is weakest and the two-magnon is maximized.

As expected the two-magnon continuum was detected at twice the one-magnon energy and with a bandwidth that is the same as the one-magnon bandwidth (8.7-12.1 meV). Both one- and two-magnon signal show some structure because of the limited integration range of the data.

5.6 Random Phase Approximation

The *Random Phase Approximation* (RPA) provides a powerful description of the effects of interactions between individual or groups of magnetic ions for example magnetic excitons in rare earth systems [3, 82] and the effects of weak coupling between spin chains and molecular magnets. RPA also provides a way to describe the dispersion
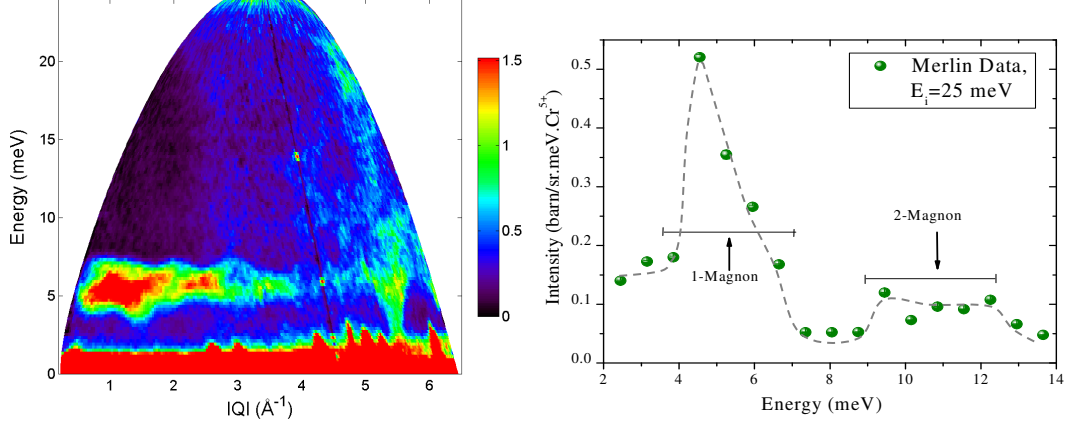
Figure 5.19: (left) Merlin data collected at 6K with an incident energy of 25meV as a function of wavevector and energy transfer. These data were measured on a single crystal at a single angle ω but have been plotted as a powder average, the two-magnon scattering can not be seen clearly. Phonon contribution increases above 3 Å^{-1}. (right) 1$-$ and 2$-$magnon scattering measured at $T = 6$ K with incident neutrons of energy 25 meV pointing in the $(h_h, h_h, 0_h)$ direction. The data are integrated over the wavevector ranges $-0.2 < h_h < 0.2$, $-1 < k_h < 1$, $-1 < \ell_h < 1$. Lines are guides to the eye.

relations of magnons in dimer systems. The model is based on a Heisenberg Hamiltonian that is rewritten in terms of dimer spin operators and pseudo dimer spin operators. Second quantization is performed by writing the Hamiltonian in terms of standard basis operators. The equation of motion is then decoupled by the RPA. In this approximation, the expectation value of the spin operator S_i^z is considered close to its saturation value. In this limit S_i^z must be nearly independent of time, $S_i^z \approx \langle S_i^z \rangle$. This approximation holds for the low temperature regime, where the fluctuations do not play an important role. RPA has been used to describe weakly coupled dimer systems such as CsCr$_2$Br$_9$ [83] and the compounds Ba$_3$Cr$_2$O$_8$ [62] and Ba$_3$Mn$_2$O$_8$ [61] which are isostructural to Sr$_3$Cr$_2$O$_8$ where it has been successful in describing INS data at low temperatures and zero field. In this section, the RPA is explained and applied to Sr$_3$Cr$_2$O$_8$ by means of fitting the TAS data. This approximation makes it possible to extract the exchange couplings in this compound.

The Heisenberg Hamiltonian explained in Chapter 2 given in Equation 2.9 is adequate to describe the magnetic interactions in Sr$_3$Cr$_2$O$_8$, and can be written in absence of a magnetic field as:

$$\mathcal{H} = -\frac{1}{2} \sum_{i,j,\mu,\nu} \mathcal{J}_{i\mu,j\nu} s_{i\mu} \cdot s_{j\nu}, \tag{5.16}$$

where i, j designate the dimer and $\mu = 1, 2$, $\nu = 1, 2$ for the individual Cr^{5+} ions on

dimers i and j respectively. The intradimer exchange is $J_0 = -J_{i1,i2}$, where $(i1, i2)$ are the nearest neighbor Cr^{5+} pairs. Due to the different interdimer interactions, it is necessary to rewrite the Hamiltonian in terms of a singlet-triplet basis by introducing the total dimer spin $K_i = s_{i,1} + s_{i,2}$ and the Néel dimer spin or pseudodimer spin operator $L_i = s_{i,1} - s_{i,2}$. This makes it possible to separate the Hamiltonian in three terms:

$$\mathcal{H} = \mathcal{H}_0 + \mathcal{H}_K + \mathcal{H}_L, \tag{5.17}$$

where

$$\mathcal{H}_0 = -\frac{1}{4} J_0 \sum_i (K_i \cdot K_i - L_i \cdot L_i),$$

$$\mathcal{H}_K = -\frac{1}{4} \sum_{i,j} J_{ij} K_i \cdot K_j, \tag{5.18}$$

$$\mathcal{H}_L = -\frac{1}{4} \sum_{i,j} J_{ij} L_i \cdot L_j.$$

$\mathcal{H}_0$ is the dimer Hamiltonian which was explained in Chapter 2. It gives the biggest contribution to the Hamiltonian and therefore it defines the singlet ground state. $\mathcal{H}_K$ has the form of a normal Heisenberg Hamiltonian, but the interacting spins are dimer spins rather than single-ion spins. $\mathcal{H}_L$ represents the interaction between the pseudodimer spins. K_i is diagonal in the singlet-triplet dimer spin space, meaning that it has only non-zero matrix elements between the three excited $S = 1$ states, whereas L_i is completely off-diagonal. The term that produces the dispersion of the singlet-triplet excitation is therefore $\mathcal{H}_L$ while $\mathcal{H}_K$ can be neglected for low temperatures where the population of the excited states is small, since then the dynamical effects due to K_i are negligible [83]. In order to use the RPA to decouple the equation of motion, the Hamiltonian must be written in terms of the standard basis operators defined by the basis $|S, S_z\rangle$ as:

$$a^i_{mn} = (|m\rangle \langle n|)_i, \ m, n = 0, 1, 2, 3, \tag{5.19}$$

where m and n number the dimer states. For the singlet $n = 0$ $|0, 0\rangle = |0\rangle$ while for the triplet states: $n = 1, 2, 3$ $|1, +1\rangle = |1\rangle$, $|1, 0\rangle = |2\rangle$ and $|1, -1\rangle = |3\rangle$. The pseudodimer

spin operator can be written in terms of the standard basis operators:

$$L_{jx} = \frac{1}{\sqrt{2}}[a_{30}^j - a_{10}^j + a_{03}^j - a_{01}^j],$$
$$L_{jy} = \frac{1}{\sqrt{2}}[a_{30}^j + a_{10}^j - a_{03}^j - a_{01}^j], \tag{5.20}$$
$$L_{jz} = a_{20}^j + a_{02}^j.$$

The Hamiltonian becomes:

$$\mathcal{H} = J_0 \sum_i [a_{11}^i + a_{22}^i + a_{33}^i] - \sum_{ij} J_{ij}[a_{01}^i a_{10}^j + a_{03}^i a_{30}^j - a_{01}^i a_{03}^j - a_{10}^i a_{30}^j$$
$$+ a_{02}^i a_{20}^j + \frac{1}{2}(a_{20}^i a_{20}^j + a_{02}^i a_{02}^j)], \tag{5.21}$$

Next a 6×6 matrix of time and temperature dependent Green's functions is defined and a Fourier transformation in space and time is done, as describe in references [3, 84], the equation of motion for the Green's functions can be written as:

$$\hbar\omega \left\langle\left\langle a_i; a_j^\dagger \right\rangle\right\rangle - \left\langle\left\langle [a_i, \mathcal{H}]; a_j^\dagger \right\rangle\right\rangle = \left\langle [a_i, a_j^\dagger] \right\rangle, \tag{5.22}$$

where a_i is a vector operator of site i with components: $a_i = (a_{01}^i, a_{10}^i, a_{02}^i, a_{20}^i, a_{03}^i, a_{30}^i)$. The RPA is used now to decouple the higher-order Green's functions by making the approximation $a_{mn}^i a_{m'n'}^j \approx a_{mn}^i \left\langle a_{m'n'}^i \right\rangle + \left\langle a_{mn}^i \right\rangle a_{m'n'}^i$. With this approximation the fluctuations in time have been neglected, this means the effects of the surrounding ions are accounted for by a time-independent molecular field. This decouples the 6×6 matrix equations into three 2×2 matrix equations; see reference J. Jensen *et al.* [84]. The equations can be solved to give the dispersion relation:

$$\hbar\omega \cong \sqrt{J_0^2 + J_0 R(T) J(\mathbf{q})}, \tag{5.23}$$

where $J(\boldsymbol{q})$ is the Fourier transform of the interdimer exchange couplings and is given by

$$\mathbf{J}(\boldsymbol{q}) = \sum_{ij} J(\mathbf{R_{ij}}) e^{-i\boldsymbol{q}\cdot(\mathbf{R_i}-\mathbf{R_j})}. \tag{5.24}$$

$R(T)$ denotes the difference in thermal populations of the ground and excited states, or
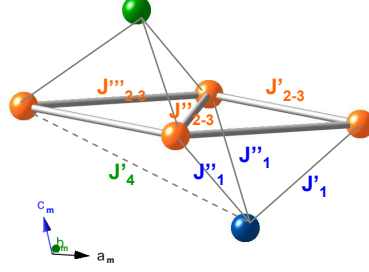
Figure 5.20: Crystal structure of $Sr_3Cr_2O_8$ showing only the dimers represented by spheres. The gray lines illustrate the interdimer exchange couplings.

in other terms, the singlet-triplet transition matrix element, and is given by [62, 82, 85]:

$$R(T) = \frac{1 - e^{(-J_0/K_B T)}}{1 + 3e^{(-J_0/K_B T)}},\tag{5.25}$$

which at low temperatures ($2\,\mathrm{K}$) is equal to 1 for $Sr_3Cr_2O_8$. The RPA is only valid for low temperatures and it is more accurate for 3-dimensional systems with long range interactions because a large number of nearest neighbors reduces fluctuations [3]. In order to develop a better understanding of the exchange interactions in $Sr_3Cr_2O_8$ the extracted experimental dispersion relations were fitted to the expression above. In the RPA approach the basic unit is the dimer and all other exchange interactions are considered as interdimer couplings. In the case of $Sr_3Cr_2O_8$ the interdimer interactions can be understood according to Figure 5.20, where the colored spheres represent dimers rather than magnetic ions and the gray lines represent interdimer bonds. The Fourier transform of the interdimer coupling, $J(\boldsymbol{q})$ for Twin 1 is:

$$J(h_h, k_h, \ell_h)_{Twin1} = 2J_1' cos\left(\frac{2}{3}\pi(2h_h + k_h + \ell_h)\right) + 2J_1'' cos\left(\frac{2}{3}\pi(-h_h + k_h + \ell_h)\right)$$

$$+2J_1'' cos\left(\frac{2}{3}\pi(-h_h - 2k_h + \ell_h)\right) + 2(J_2' - J_3')cos(2\pi h_h) + 2(J_2'' - J_3'')cos(2\pi k_h)$$

$$+2(J_2'' - J_3''')cos(2\pi(h_h + k_h)) + 2J_4' cos\left(\frac{2}{3}\pi(2h_h + 4k_h + \ell_h)\right)$$

$$+2J_4'' cos\left(\frac{2}{3}\pi(2h_h - 2k_h + \ell_h)\right) + 2J_4'' cos\left(\frac{2}{3}\pi(-4h_h - 2k_h + \ell_h)\right),$$
$$\tag{5.26}$$

where the set of 4th order interactions J_4', J_4'' have been included, these were found to be significant in the analysis of $Ba_3Mn_2O_8$. Note that in this model it is not possible to distinguish between the sets J_2', J_2'' and J_3', J_3'', J_3''' and only the difference between these

exchange parameters matters i.e. $J_2' - J_3'$ etc. Also note that the minus sign expresses the fact that J_2' and J_3' compete if they have the same sign (e.g. both antiferromagnetic) but reinforce each other if they have different signs. $J(\boldsymbol{q})$ for the other twins can be generated from that of Twin 1 by permuting the exchange constants as follows

$$\left\{ J_{1,2-3,4}', J_{1,2-3,4}'', J_{2-3}''' \right\}_{\text{Twin1}}$$

$$\rightarrow \left\{ J_{1,2-3,4}'', J_{2-3}''', J_{1,2-3,4}' \right\}_{\text{Twin2}}$$

$$\rightarrow \left\{ J_{2-3}''', J_{1,2-3,4}', J_{1,2-3,4}'' \right\}_{\text{Twin3}}.$$

In this way the magnetic excitations for all three twins can be calculated. The 70 constant-wavevector, energy scans measured on Flex were fitted to Lorentzian functions to obtain the peak positions and thus map out the dispersion relations of the three twinned domains as a function of energy and wavevector. In these experiments the excitations were measured in two planes the $(h_h, 0_h, \ell_h)$ and (h_h, h_h, ℓ_h) and for these specific planes Equation 5.26 reduces to:

$$J(h_h, 0_h, \ell_h)_{Twin1} = 2J_1' cos\left(\frac{2}{3}\pi(2h_h + \ell_h)\right) + (4J_1'')cos\left(\frac{2}{3}\pi(-h_h + \ell_h)\right)$$

$$+(2(J_2' - J_3') + 2(J_2'' - J_3'''))cos(2\pi h_h) + 2(J_2'' - J_3'')$$

$$+(2J_4' + 2J_4'')cos\left(\frac{2}{3}\pi(2h_h + \ell_h)\right) + 2J_4'' cos\left(\frac{2}{3}\pi(-4h_h + \ell_h)\right) \qquad (5.27)$$

and

$$J(h_h, h_h, \ell_h)_{Twin1} = 2J_1' cos\left(\frac{2}{3}\pi(3h_h + \ell_h)\right) + 2J_1'' cos\left(\frac{2}{3}\pi(\ell_h)\right)$$

$$+2J_1'' cos\left(\frac{2}{3}\pi(-3h_h + \ell_h)\right) + 2((J_2' - J_3') + 2(J_2'' - J_3''))cos(2\pi h_h)$$

$$+2(J_2'' - J_3''')cos(4\pi h_h) + 2J_4' cos\left(\frac{2}{3}\pi(6h_h + \ell_h)\right) + 2J_4'' cos\left(\frac{2}{3}\pi\ell_h\right)$$

$$+2J_4'' cos\left(\frac{2}{3}\pi(-6h_h + \ell_h)\right). \qquad (5.28)$$

These equations can be simplified further if scans along key directions are considered, e.g. for directions where h_h and k_h are integers and ℓ_h varies, the set of interactions $J_2' - J_3'$, $J_2'' - J_3''$, $J_2'' - J_3'''$ do not modulate the structure but only give an overall constant, thus allowing us to obtain the interactions J_0, J_1', J_1'' and J_4', J_4''. The directions with h_h and k_h half-integer were then used to get the values of $J_2' - J_3'$, $J_2'' - J_3''$ $J_2'' - J_3'''$. The full data set was fitted to Equation 5.23, and a set of exchange constants were extracted that

could accurately model the data with a goodness of fit of $R^2 = 0.7$. Figure 5.21 shows the fit dispersion relations along some of the key directions and a direct comparison with Flex data.
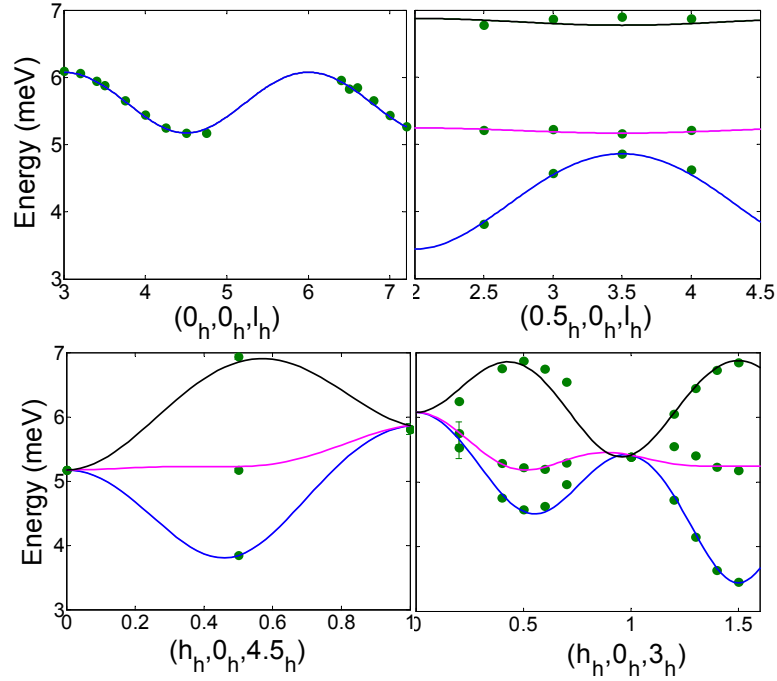
Figure 5.21: Dispersion relation for the directions $(0_h, 0_h, \ell_h)$, $(0.5_h, 0_h, \ell_h)$, $(h_h, 0_h, 4.5_h)$ and $(h_h, 0_h, 3_h)$. The blue, magenta and black lines correspond to the fit dispersion relations of the three monoclinic twins. The green points are the fit peak positions measured on Flex. The wavevectors on the x-axis are labeled using the hexagonal notation.

The fit exchange constants are listed in Table 5.3 and the resulting dispersion relations for the three monoclinic twins are illustrated in Figure 5.22. The green circles give the excitation energies extracted from each scan and the lines are fits to the RPA model. The three lines (magenta, black and blue) represent the three twins which are rotated by $60°$ with respect to each other about the c_h^*-axis. The dispersion of Twin 1 (blue line) is the same as that of Twin 2 (magenta line) $60°$ away in reciprocal space and the same as that of Twin 3 (black line) $120°$ away.

The neutron scattering cross-section from these modes can also be calculated as explained in Chapter 3 and is given by

$$\frac{d^2\sigma(\boldsymbol{Q}, E)}{d\Omega dE} \approx \frac{|f_{\mathrm{Cr}^{5+}}(|Q|)|^2 \, (1 - cos(\frac{2\pi\ell_h d_0}{c_h})) e^{(-(E-\hbar\omega)^2/\Delta E^2)}}{\hbar\omega(1 - e^{E/k_B T})}, \tag{5.29}$$
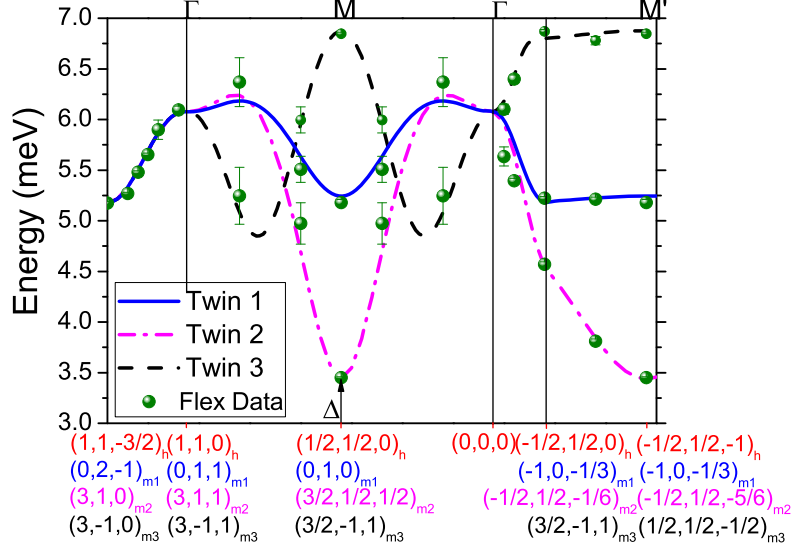
Figure 5.22: Dispersion relation. The blue, magenta and black lines correspond to the fit dispersion relations of the three monoclinic twins. The green points are the fit peaks positions measured on Flex. The wavevectors in red on the x-axis are labeled given the hexagonal notation, and the corresponding monoclinic notations are in blue, magenta and black.

Table 5.3: The exchange constants in units of meV extracted from the RPA model, compared to the values for Ba$_3$Cr$_2$O$_8$ and Ba$_3$Mn$_2$O$_8$. Antiferromagnetic interactions are positive while ferromagnetic interactions are negative. J' is the sum of the interdimer couplings and is given by $J' = |J_1'| + 2|J_1''| + |J_4'| + 2|J_4''| + 2(|J_2' - J_3'|) + 2(|J_2'' - J_3''|) + 2(|J_2'' - J_3'''|)$.

Exchange Constants	Sr$_3$Cr$_2$O$_8$	Ba$_3$Cr$_2$O$_8$ [62]	Ba$_3$Mn$_2$O$_8$[61]
J_0	5.551(9)	2.38	1.642
J_1'	-0.04(1)	-0.15	-0.118
J_1''	0.25(1)	0.08	$= J_1'$
J_1'''	$= J_1''$	0.10	$= J_1'$
$J_2' - J_3'$	0.751(9)	0.10	0.256-0.142
$J_2'' - J_3''$	-0.543(9)	-0.52	$= J_2' - J_3'$
$J_2''' - J_3'''$	-0.120(9)	0.07	$= J_2' - J_3'$
J_4'	0.06(2)	0.10	-0.037
J_4''	-0.05(1)	0.04	$= J_4'$
J_4'''	$= J_4''$	0.09	$= J_4'$
J'	3.5(1)	1.94	1.147
J'/J_0	0.6374	0.8151	0.6983

where E is the energy transfer, ΔE is the energy resolution of the instrument which is assumed to be Gaussian and T is the temperature. The cosine term comes from the

structure factor of a single dimer. Using the fit values of the exchange constants (from Table 5.3), a simulation was performed of the Merlin experiment. Figure 5.23 shows good agreement between the data and the simulation for various slices.
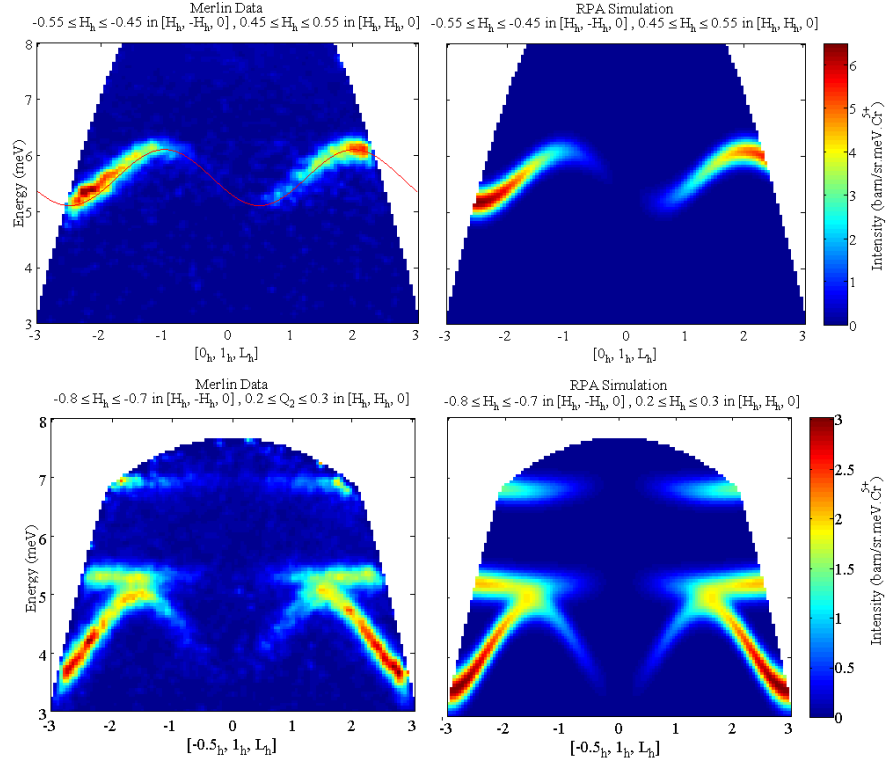
Figure 5.23: Slices of the Merlin Data (left panels) and the RPA simulation (right panels) for the directions $(0_h, 1_h, \ell_h)$ (top panels) and $(-0.5_h, 1_h, \ell_h)$ (bottom panels), with $E_i = 10$ meV and $T = 6$ K. The intensity is in arbitrary units. The solid red line is the calculated RPA dispersion relation along $(0_h, 1_h, \ell_h)$.

The RPA model along with the fit exchange constants were also used to reproduce the data from the inelastic powder measurement performed on V3-NEAT. In order to calculate the powder average, the intensity was calculated using the RPA model with the exchange values in Table 5.3 for the measured range of $|Q|$. $|Q|$ was defined as a sphere with two angles 2θ and ϕ. Where $\theta = 2\pi u$ and $\phi = cos^{-1}(2v - 1)$ and u, v are random numbers. 100 points were selected randomly on the surface of the sphere, and for each point (h_h, k_h, l_h) was calculated, the neutron scattering cross section was then calculated using Equation 5.29 for each point and the intensity was summed and normalized by the number of points. This procedure was repeated for each $|Q|$ value. The powder average is shown in Figure 5.24.

Cuts were made through the RPA powder simulation as a function of energy and wavevec-
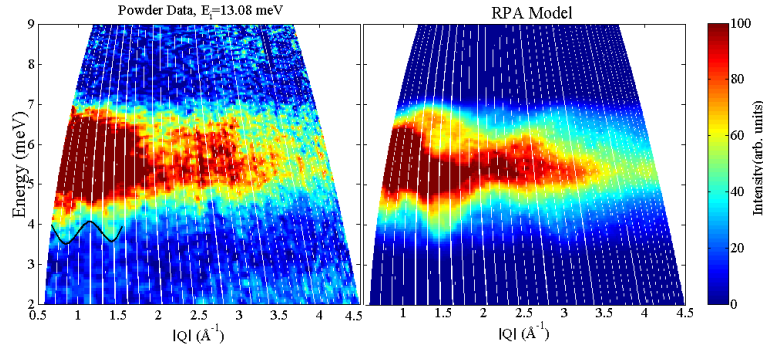
Figure 5.24: The left panel shows the inelastic neutron scattering data measured on a powder sample. The data were collected on NEAT at 2 K and the incident energy was 13.08 meV. The figure on the right is powder average of the dispersion relation obtained using RPA. The intensity is in arbitrary units. The solid black line is a guide to the eye for the measured minima of the powder spectrum.

tor and compared with the Neat data as shown in Fig. 5.25, the agreement with the powder data is good and can describe the data as accurately as the first moment sum rule.
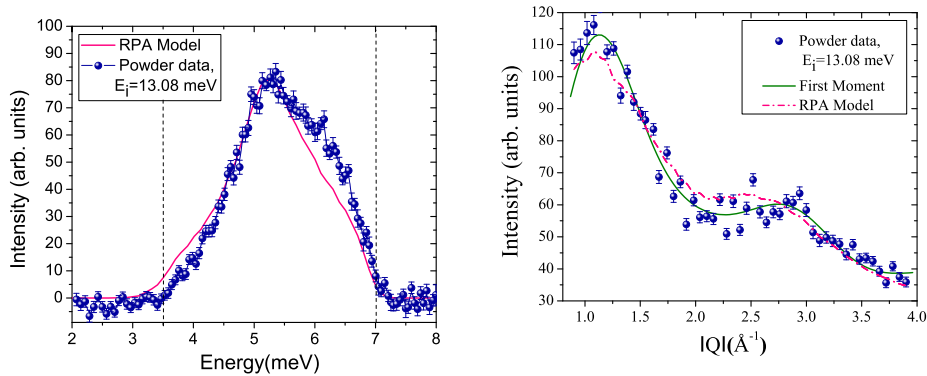
Figure 5.25: (left)The data (blue circles) and RPA simulation (magenta line) from Fig. 5.24, integrated over the wavevector range $1.5\,\text{Å}^{-1} < |Q| < 3.5\,\text{Å}^{-1}$ and plotted as a function of energy. The dashed vertical lines indicate the bandwidth of the excitations. (right) The data (blue circles) and RPA simulation (magenta line) from Fig. 5.24, multiplied by energy transfer and integrated over the energy range 4.16-7.07 meV. The green line gives the fit to the first moment sum rule, Eq. 5.9.

Finally, the fit interactions were used to calculate the effective field experienced by each dimer, defined as the sum of the interdimer interactions: $J' = |J'_1| + 2\,|J''_1| + |J'_4| + 2\,|J''_4| + 2(|J'_2 - J'_3|) + 2(|J''_2 - J''_3|) + 2(|J''_2 - J'''_3|)$ of $J' = 3.5(1)\,$meV (see Table 5.3). This was
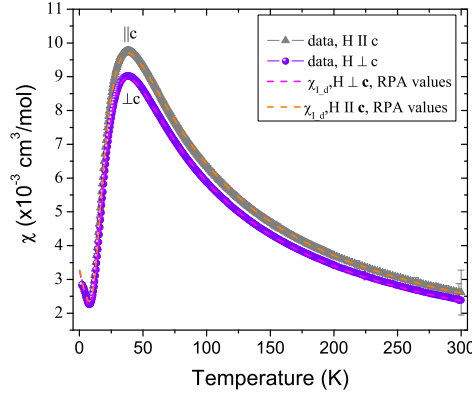
Figure 5.26: Static susceptibility data measured using the SQUID magnetometer for field applied both parallel and perpendicular to c_h displayed along with the fit interacting dimer model given by Eq. 4.2 using the exchange coupling values obtain from the fitting of the INS data to the RPA model.

used along with the fit value of J_0 to simulate the susceptibility data. This calculation is shown in Figure 5.26 and is consistent with the data.

5.7 Temperature Dependence

The temperature dependence of the magnon dispersion was investigated. Measurements were performed on two different instruments, the ToF spectrometer IN5 and the TAS, V2/Flex at different temperatures. Specific regions in reciprocal space were explored in these measurements, of particular interest was the thermal evolution of the minimum and maximum of the dispersion for the positions where the twins' dispersion was either degenerate, Γ point, and non-degenerate, M point.

Figure 5.27 shows four slices of the IN5 data at different temperatures for the direction (h_h, h_h, ℓ_h), with $-3.4 < \ell_h < -2.6$. The modes are not so well resolved due to the integration along c_h^*, but the two important wavevectors are visible, $(-1_h, -1_h, -3_h)$ (Γ) and $(-1/2_h, -1/2_h, -3_h)$ (M). When the temperature is increased, the bandwidth of the dispersion is renormalized, the intensity drops and the linewidth increases. The dispersion has a continuum-like behavior centered about the intradimer energy J_0, at very high temperatures and it is difficult to detect for temperatures greater than T= 75 K. The solid lines in the figure, are the calculated RPA dispersions (Eq. 5.23) for the three different twins, the singlet-triplet transition matrix element was calculated for each temperature according to Equation 5.25 where the occupation of the singlet and triplet states was taken into account. The RPA approach appears to follow the

renormalization. This renormalization occurs because as temperature is increased the dimers become thermally excited and interfere with the intersite interactions, thus, the dispersion is suppressed and the gap is renormalized. This renormalization has been reported previously for other dimer compounds, such as: BaCuSi$_2$O$_6$, KCuCl$_3$ and Pr$_3$Tl [43, 86, 82].
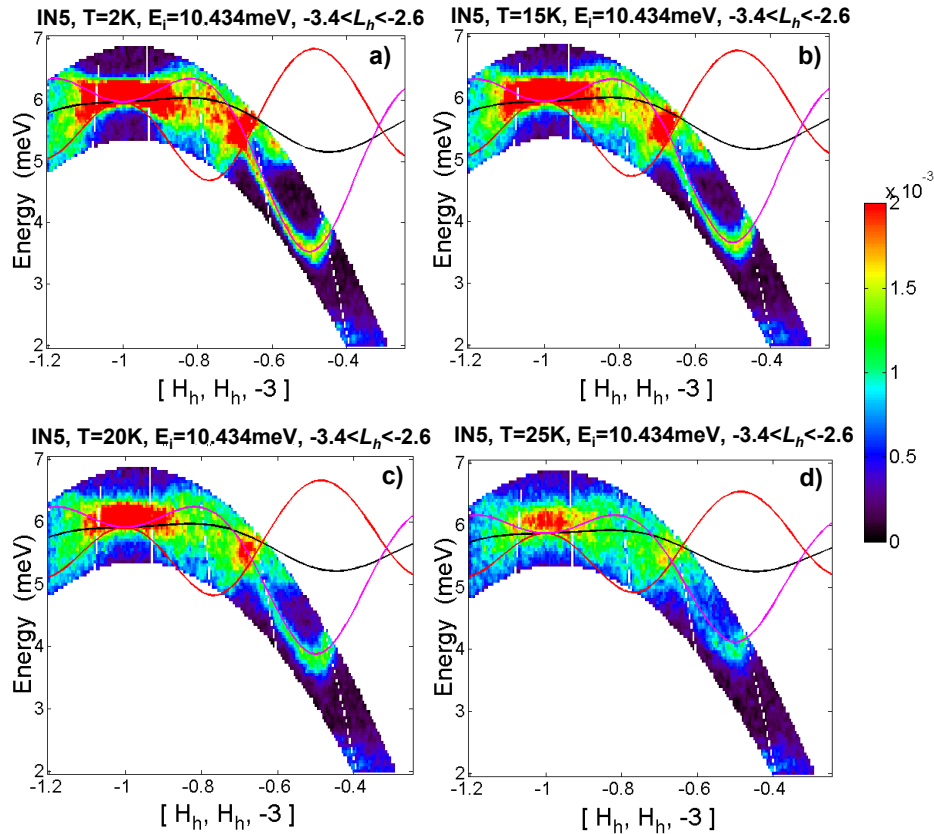
Figure 5.27: Inelastic neutron scattering data acquired on a single crystal on IN5. The different slices show the thermal evolution of the dispersion along $(H_h, H_h, -3_h)$. The solid lines are the calculated RPA dispersions for the three different twins.

High resolution energy scans were performed on V2/Flex for constant wavevectors, $(0_h, 0_h, 3_h)$ and $(1/2_h, 1/2_h, 3_h)$, at different temperatures. The results are shown together in the colorplots in Figure 5.28 as a function of energy transfer and temperature, the intensity is in arbitrary units. The points in these colorplots are the center of the peaks obtained by fitting the individual scans to a Lorentzian function as explained in the previous section. The peaks broadened and the intensity decreases with temperature in agreement with the IN5 results. The dashed and solid lines in Figure 5.28 give the en-

ergy renormalization predicted by the RPA dimer model for the three monoclinic twins. The model appears to follow the center of the excitations up to $40\,\mathrm{K}$ for $(0_h, 0_h, 3_h)$ and up to $25\,\mathrm{K}$ for the lowest and middle modes at $(1/2_h, 1/2_h, 3_h)$. The higher mode is not followed with high accuracy. It is important to note that there are no free parameters. The strong decrease in integrated intensity of the mode at $(0_h, 0_h, 3_h)$ is shown in Figure 5.29, along with the corresponding expectation values according to the RPA.
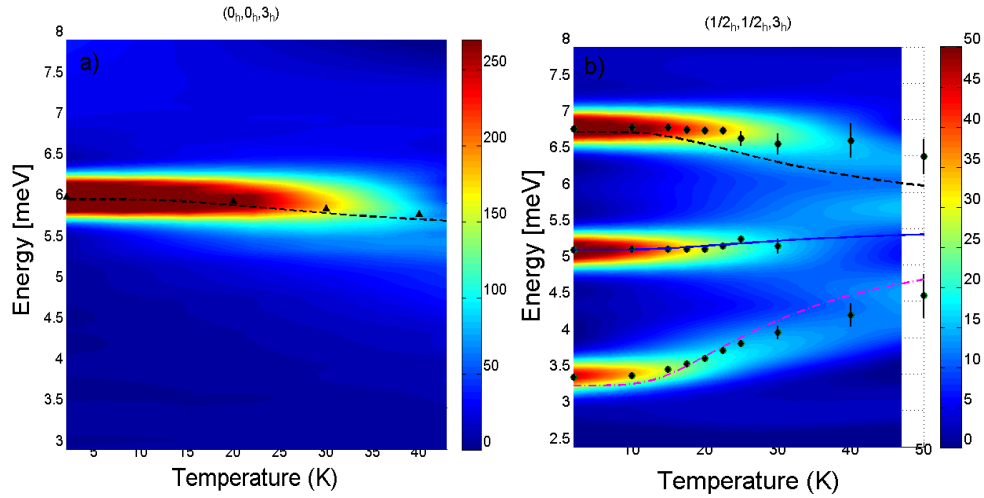
Figure 5.28: Constant-wavevector scans measured on Flex at the points $(0_h, 0_h, 3_h)$ and $(1/2_h, 1/2_h, 3_h)$. The scans acquired at different temperatures were interpolated in order to display the thermal evolution of the magnons at those two points. The color gives the scattered intensity in arbitrary units.

A careful analysis of the lineshapes of the excitation modes has been done. Special attention was paid to the lineshape evolution of the excitation at the maximum of the dispersion of the degenerate twins which occurs at $(0_h, 0_h, 3_h)$. Figure 5.30 shows the constant wavevector scans performed on V2/Flex for different temperatures, the mode occurs at an energy of $6\,\mathrm{meV}$ which is close to the upper edge of the excitation bandwidth of $7.1\,\mathrm{meV}$. The $2\,\mathrm{K}$ scan presents a Gaussian lineshape but when the temperature is increased the peak becomes asymmetric with a tail extending towards lower energies. This is a marked departure from existing theoretical predictions that give a Lorentzian profile. The lineshapes of the peaks shown in Figure 5.30 have been parameterized by fitting them to a step function equal to the low temperature excitation bandwidth ($3.5\,\mathrm{meV} < E < 7.1\,\mathrm{meV}$) multiplied by a Lorentzian peak with two different widths on the lower and upper energy sides (Γ_1 and Γ_2), as shown in the inset in Figure 5.31. The $2\,\mathrm{K}$ scan has been used to model the resolution by fitting it to a Gaussian function, this resolution function was then convolved with the Lorentzian and step function, according
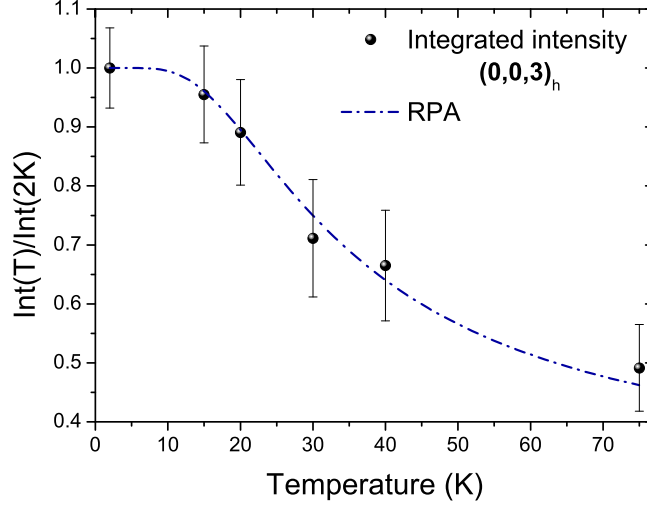
Figure 5.29: Integrated intensity for the excitation at $(0_h, 0_h, 3_h)$ measured on Flex at different temperatures. The intensity of the magnon mode decreases significantly. The blue line refers to the corresponding expectation values according to the RPA.

to the equation:

$$
I(\boldsymbol{Q}, \omega) \quad \propto \quad \int_{-\infty}^{\infty} d\omega' \sqrt{\frac{1}{2\pi\sigma^2}} e^{-\frac{(\omega-\omega')^2}{2\sigma^2}} \frac{\Gamma_s/2}{(\omega'-\omega_p) + (\Gamma_s/2)} \Theta(\omega' - \omega_l)\Theta(\omega_u - \omega')
$$

$$
\Gamma_s \quad = \quad \begin{cases} \Gamma_1, & \text{if } \omega \geq \omega_p \\ \Gamma_2, & \text{if } \omega < \omega_p \end{cases} \tag{5.30}
$$

where σ is the width of the 2 K excitation (0.14 meV) and ω_p is the maximum of the excitation peak. The fit was performed for each temperature by fixing the background to that of the 2 K scan. The extracted widths are plotted in Figure 5.31 and the fits are shown by the red solid lines in Figure 5.30, the goodness of the fits are listed in the caption of Figure 5.31. Γ_2 is close to the Γ_1 value for temperatures lower than 20 K, but it grows more rapidly with temperature giving rise to an increasingly asymmetric peak that is broader on the high energy side.

This parametrization was also done to the modes at $(1/2_h, 1/2_h, 3_h)$, but the three branches merge rapidly together and a good fit was difficult to perform. Nevertheless, in Figure 5.32, two scans are shown, at T= 2 K and T= 25 K, the resolution of the lowest energy peak was fixed to the 2 K Gaussian width and the fitting process was performed. The lowest energy peak is also found to be asymmetric with a tail that extends towards higher energies, in this case, the Γ_1 value (0.30(8) meV) is bigger than the Γ_2 value of
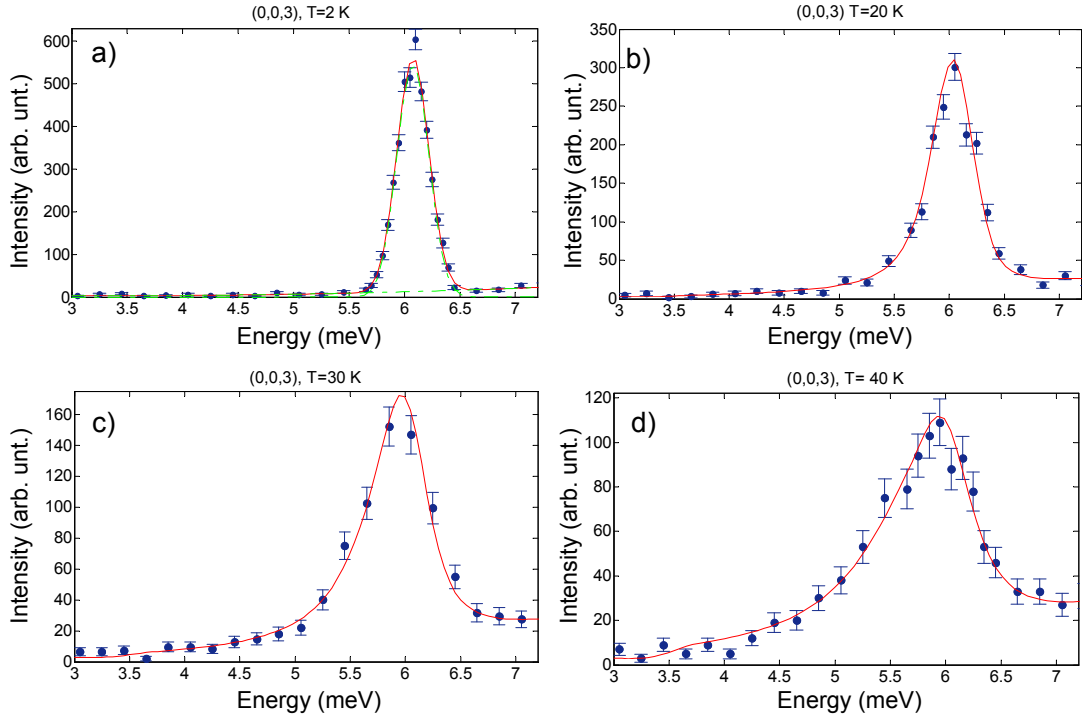
Figure 5.30: Constant-wavevector scans measured on Flex at the Γ point $(0_h, 0_h, 3_h)$ at different temperatures. The 2 K scan was fitted to a Gaussian function with sloping background, the width of the peak was 0.14 meV, the goodness of the fit is $R^2 = 0.9798$. The higher temperature scans were fitted to the Equation 5.30, the Gaussian profile of the 2 K data has been taken as the instrument resolution, the sloping background was also fix for all temperatures. The goodness of the fits are: T=20 K, $R^2 = 0.9784$. T=30 K, $R^2 = 0.9392$. T=40 K, $R^2 = 0.9322$. T=75 K, $R^2 = 0.6844$.

0.002(2) meV.

The linewidth of the excitations is related to their lifetime, which decreases when the temperature is increased, which is the well-known damping effect. The leading mechanism for the damping is the decoherence due to the random fluctuations of occupation numbers at each dimer. The RPA dimer model that described perfectly the low temperature magnetic excitations in $Sr_3Cr_2O_8$ is unable to describe the temperature dependence, as it predicts infinite lifetimes for the excitations at all temperatures. However, modifications to the RPA could be used, such as self consistent RPA that includes a damping effect and predicts symmetric Lorentzian broadening for temperatures below the gap value, at higher temperatures the lineshape is expected to be completely distorted [87, 86]. In this approximation, the excitations of $Sr_3Cr_2O_8$ would have a Lorentzian lineshape for temperatures T$< \Delta/k_B$ (T< 40 K) in contrast to the experi-
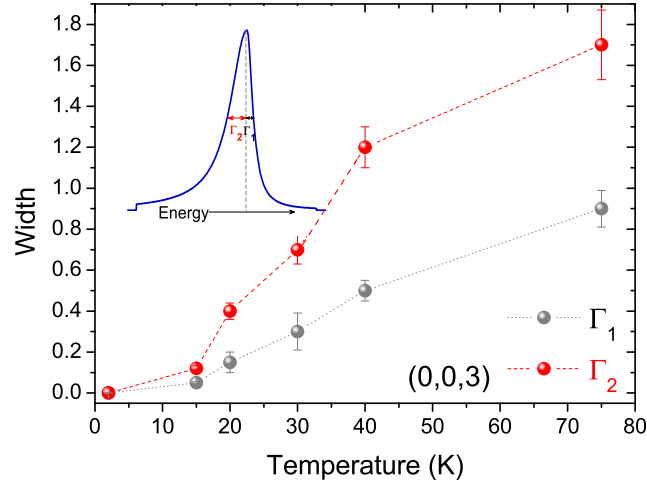
Figure 5.31: Fitted widths of the data shown in Figure 5.30. The inset shows the parametriza-tion function before convolution with the Gaussian (instrumental resolution). This function is a Lorentzian with two widths Γ_1 and Γ_2. The fit Γ_s values have been plotted. An additional fit has been done to the constant-wavevector scan measured at 70 K, nevertheless the intensity of this peak is very low and the goodness of the fit was worse than for the other temperatures ($R^2 = 0.6844$).
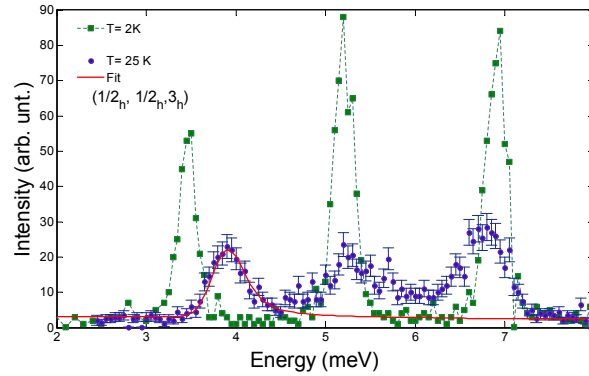
Figure 5.32: Constant-wavevector scans measured on Flex at the M point $(1/2_h, 1/2_h, 3_h)$ at two temperatures, 2 K and 25 K. The 2 K scan was fitted to a Gaussian function (with a width of 0.106 meV). This fit was taken as the instrument resolution. The lowest energy mode measured at 25 K was fitted to the Equation 5.30, the Γ_s values are: $\Gamma_1 = 0.30(8)$, $\Gamma_2 = 0.002(2)$. The goodness of the fit is $R^2 = 0.737$. The three modes at this position merge rapidly which makes difficult the fitting process.

mental results where the lineshape becomes asymmetric for temperatures above 20 K. In the scattering process a neutron polarizes an unoccupied dimer by exciting it to the triplet state, the created quasiparticle is a boson, but it is necessary to exclude states with more than one quasiparticle per dimer, therefore a hard-core constraint is included

which can be interpreted as a strong short-range repulsion between the magnons. When the temperature is increased and a magnon is created by a neutron scattering process, the excited magnon has to interact with the already thermally excited magnons, this interaction changes the dispersion relation and the lifetime of the excitation. Magnon-magnon interactions have not been well studied but their full understanding would reveal the interplay of single site fluctuations (quantum fluctuations) and thermal fluctuations. Typically, the measured and expected lineshapes of magnons or spinwaves are a symmetric Lorentzian [88, 86, 89, 90, 91]. But, recent theory and experimental measurements for the one-dimensional dimer Heisenberg chain compound $(Cu(NO_3)_2)$ show that the thermal broadening is asymmetric, therefore the effects of temperature are not simple decoherence but promote the interaction between the quasiparticles [75, 92]. These results for $Sr_3Cr_2O_8$ show for the first time that asymmetric lineshape broadening is not confined to one-dimensional dimer systems, but that a strongly correlated gas of hardcore bosons can also be realized in three dimensions.

5.8 Discussion and Conclusions

All the results shown here and in the previous chapter provided a consistent picture of $Sr_3Cr_2O_8$ as a dimerized spin-1/2 antiferromagnet. The first moment extracted from powder INS and the modulation in intensity of the dispersion along the c_h^* axis, confirm that the intradimer exchange constant is the nearest neighbor intrabilayer interaction J_0. This dimerization gives rise to a singlet ground state and gapped one-magnon excitations. There are in addition significant interdimer interactions that allow the dimer excitations to hop and develop a dispersion. The dispersion of the one-magnon mode produces a bandwidth extending between the gap energy of 3.5 meV and the maximum value of 7.0 meV as found by inelastic neutron scattering. The low background, high flux and sensitivity of the detectors on Merlin made it possible to detect a second band due to two-magnon excitations centered at 10.5 meV.

Powder INS results are in good agreement with the values obtained from the high field magnetization measurements shown in the previous chapter and confirm the picture of interacting dimers giving rise to gapped and dispersive magnon excitations. These results can be compared to the inelastic neutron scattering measurements of Chapon *et al.* [50] which were performed on a powder sample. A gapped band of excitations was observed centered at an energy of 5.46 meV in agreement with our data. The FWHM of this band was found to be 2.1 meV although values of the gap and upper boundary were not obtained due to the poorer energy resolution of their measurement.

The three measured dispersion branches are in agreement with the monoclinic structure and crystal twining. This distortion would produce spatially anisotropic exchange interactions and result in three twinned domains of equal volume below the phase transition.

The single crystal INS results were fitted and compared to a RPA model based on the dimer unit and the intradimer and interdimer interactions were determined. The intradimer exchange is calculated to be $J_0 = 5.551(9)\,$meV and the effective interdimer exchange is $J' = 3.5(1)\,$meV. These values reproduce all data, DC susceptibility, magnetization, powder INS and single crystal INS. RPA was also used to successfully describe the low temperature zero field excitations in $Ba_3Cr_2O_8$ [62] and $Ba_3Mn_2O_8$ [61]. However, this model is not expected to work near the quantum critical point and in the AFM field-induced phase. For the ordered phase other models can be used such as bosonic theories, bond-operator model, self consistent RPA and $1/z$ expansion. The bosonic theories consider the dimerized systems as interacting bosons using model Hamiltonians for massive non-relativistic bosons with short range interactions. Rewriting the Hamiltonian in terms of bosonic operators that create or anhilate magnons, allows the Hamiltonian to be separated into a chemical potential term or hopping term and a repulsive magnon interaction term. These theories have been applied to systems like $TlCuCl_3$ [42] and $BaCuSi_2O_4$ [93]. But, they suffer from inconsistencies as they neglect the highest level of the triplet from participating in the magnon condensation above the QCP. Nevertheless these models describe the critical properties much better than mean field theories. The bond operators model considers a system of interacting bosons by introducing an infinite on-site repulsion between local triplet excitations. This model is an improvement from the bosonic theories as it takes into account the higher triplet modes in the condensate, retaining all four states of each dimer. This model has been used to describe the condensate in $TlCuCl_3$ [94]. Self consistent RPA (scRPA) handles the problem of the double occupancy of the local dimer levels by decoupling the equations of motion in the next order beyond RPA. It has been used for describing $TlCuCl_3$ [84]. The $1/z$ expansion includes effects due to fluctuations by utilizing high-density $1/z$ expansion, where z is the coordination number of interacting neighbors. It includes, to first order the effects of fluctuations at each site. It has been used for describing $TlCuCl_3$, Pr, HoF_3, $LiHoF_4$ [95, 3, 96, 97, 98]. Both RPA and scRPA coincide with $1/z$ for low temperatures at zero field, but they all fail at the critical point, scRPA also reproduces well the experimental results in the AFM phase [84].

Band structure calculations have been performed for $Sr_3Cr_2O_8$ and were used to determine the exchange interactions. Chapon $et\,al.$ used the Extended Hückel Tight Binding Model [50] and found a value of the ratio J'/J_0 to be 0.11, which is much smaller than

our experimentally determined value of 0.6455. Radtke *et al.* performed density functional theory calculations and predict an antiferromagnetic interaction $J_0 = 6.24\,\text{meV}$ within the dimer and that all the remaining interactions J' are an order of magnitude weaker, such that the magnetic ground state is a spin-singlet [51].

$Sr_3Cr_2O_8$ can be compared to the related compounds $Ba_3Mn_2O_8$ and $Ba_3Cr_2O_8$. The magnetic ion Mn^{5+} has spin-1 compared to spin-1/2 for Cr^{5+}, and is not Jahn-Teller active. As a result $Ba_3Mn_2O_8$ retains hexagonal symmetry down to low temperatures and the interactions remain frustrated. A single one-magnon excitation branch is observed with minima at $(1/3_h, 2/3_h, 1/2_h)$ and equivalent positions [61]. In contrast $Ba_3Cr_2O_8$ like $Sr_3Cr_2O_8$ undergoes a Jahn-Teller distortion to monoclinc symmetry leading to spatially anisotropic exchange interactions and three excitation branches arising from the three twinned domains with minima at the $(1/2_h, 1_h, 0_h)$ and symmetry equivalent positions.

The values of intradimer interaction J_0 are smaller in the Ba compounds being $1.64\,\text{meV}$ for $Ba_3Mn_2O_8$ [61] and $2.38\,\text{meV}$ for $Ba_3Cr_2O_8$ [62]. This may simply be due to the intradimer distance which is greater for $Ba_3Cr_2O_8$ ($3.934\,\text{Å}$) and $Ba_3Mn_2O_8$ ($3.984\,\text{Å}$) than for $Sr_3Cr_2O_8$ ($3.842\,\text{Å}$) allowing for better overlap of orbitals. The sizes of the interdimer exchange constants are also on average smaller in these compounds although the ratio of the intradimer to interdimer couplings is larger. In $Ba_3Cr_2O_8$ $J' = 1.94\,\text{meV}$, and $J'/J_0 = 0.8151$ while for $Ba_3Mn_2O_8$ $J'/J_0 = 0.6983$ showing that the ratio of excitation bandwidth to the average mode energy is greater than in $Sr_3Cr_2O_8$ where $J'/J_0 = 0.6455$. Finally the spin gap of $Sr_3Cr_2O_8$ is $3.5\,\text{meV}$ and is thus significantly larger than that of $Ba_3Mn_2O_8$ ($1.08\,\text{meV}$) and $Ba_3Cr_2O_8$ ($1.38\,\text{meV}$).

In order to learn more about the magnetic excitations in $Sr_3Cr_2O_8$, optical measurements were performed. Small single crystal samples were oriented cut and polished and sent to the research groups of Peter Lemmens (TU Branschweig) and Joachim Deisenhofer (University of Augsburg). Raman scattering published by D. Wulferding *et al.* [63] revealed two modes at around 45 and $90\,cm^{-1}$ ($5.58\,\text{meV}$ and $11.2\,\text{meV}$), both modes have a broad linewidth. The one at $90\,cm^{-1}$ is prominent at low temperatures, while the one at $45\,cm^{-1}$ develops a finite intensity at temperatures from $10\,\text{K}$ to $75\,\text{K}$. The temperature dependence of the intensity was fitted to the Bose Einstein factor associated with a thermal population of the singlet ground state and excited triplet state. A value for the energy gap of $40\,\text{K}$ ($3.45\,\text{meV}$) was obtain which is in total agreement with the data shown here. This spectrum was taken using different light polarizations and the presence of a magnetic component in the horizontal plane suggests the pres-

ence of interdimer interactions in that plane. The high energy mode is ascribed to a two-magnon process involving the simultaneous creation of two dimer excitations [99]. The low energy mode is associated with a three-magnon process occurring via a transition from one singlet and one excited triplet state to two neighboring triplet states. It only occurs at a finite temperature because a thermally excited triplet is involved. THz transmission experiments were performed by Z. Wang *et al.* [74], and revealed at least 4 absorption peaks that correspond to acoustic and optical excitations from the singlet ground state to the excited triplet states Zeeman split by the external magnetic field as well as intra-triplet excitations. The linear Zeeman splitting follows $h\nu = h\nu_0 \pm g\mu_B H$ with $h\nu_0 = 5.13$ meV for the optic mode and the effective g-factor 1.92(3). For the acoustic mode $h\nu_0 = 6.08$ meV which coincides with the magnetic excitation observed with INS at the Γ point. The energies of all the absorption peaks could be modeled by using the exchange couplings described in this chapter. The fact that the singlet-triplet transitions were observed implies the presence of an additional small anisotropic contribution (e.g. DM) to the spin Hamiltonian, which mixes the singlet and the triple states and allows these otherwise forbidden excitations.

Further investigation of Sr$_3$Cr$_2$O$_8$ is planned in the future focusing on the temperature dependence of the linewidth of the magnon mode. In this chapter, ToF and TAS data acquired at different temperatures have been shown. The results conclude that there is a reduction of the magnon lifetimes which is evidenced by a damping of the excitations and there is a renormalization of the magnon energies. The reduction of the integrated intensity and the energy renormalization can be described by RPA. The RPA follows the energy normalization for temperatures below 25 K but it is not a good approximation to the behavior of the higher energy mode. The RPA model described here predicts sharp excitations at all temperatures as it ignores correlations between the magnons and breaks down if the quasiparicles are highly mobile. In contrast the measurements reveal a lineshape for Sr$_3$Cr$_2$O$_8$ that not only broadens with temperature but does so asymmetrically. This behavior which was recently predicted for and observed in a one-dimensional dimer system is due to the hardcore constraint which acts as an effective interaction between dimers. New theories must be developed and used to describe the asymmetrical broadening of the magnon excitations in Sr$_3$Cr$_2$O$_8$ such as scRPA, $1/z$ and low-temperature expansions [84, 95, 100, 101]. The results shown here reveal that in Sr$_3$Cr$_2$O$_8$ there are strong correlations between magnons. Other experiments could be performed on Sr$_3$Cr$_2$O$_8$, to investigate the lineshape by employing a resolution decoupled method, such as spin-echo triple axis spectrometry [102, 88], this would lead to a more

accurate parameterization of the asymmetry.

6 Nuclear and Magnetic Structure of the Frustrated Magnet SrYb$_2$O$_4$

6.1 Introduction

In the previous chapters the magnetic behavior of the quantum dimer magnet Sr$_3$Cr$_2$O$_8$ was discussed. In that case, the magnetic ion (Cr^{5+}) is a transition metal, where the spin orbit coupling is weak and the orbital moment is quenched. In that compound, the crystal field is strong and gives rise to a non degenerate orbital level and orbital ordering. In this chapter a completely different approach to magnetism will be discussed, where the system is strongly correlated so that the independent electron picture breaks down completely. The spin orbit coupling is so strong that it plays an important role, while the crystal field is weak and the orbital moment is unquenched therefore the Hund's rules are well satisfied. This is the case for SrYb$_2$O$_4$ where the magnetic ion is the rare earth (RE) Yb^{3+}, the physics involved is different due to the intrinsic properties of the RE ion. The low temperature magnetic behavior associated with the RE ion depends on the properties of the CF ground state and on the origin, size, and sign of the interionic interactions. The magnetic interactions in this kind of compound are competing and lift the degeneracy of the crystal field ground state. The anisotropy favors a set of crystallographic directions related by a rotational symmetry operator along which moments tend to align themselves. This anisotropy could require fields up to hundreds of Tesla to overcome. The anisotropy influences the long range magnetic order in this compounds and the variation of temperature and field thus reveals a rich variety of intermediate phase transitions to different structures. The magnetic exchange in these compounds can be of different origins. In the case of metallic compounds the conduction electrons mediate the exchange. But for lanthanides in insulating materials the strongest magnetic coupling is due to direct exchange, nearest neighbor antiferromagnetic (AFM) coupling and also the weaker anisotropic dipole-dipole interaction. When the effects of dipole-dipole interactions are included the internal degrees of freedom are fixed and the spins are able to minimize their energy by ordering in a non collinear planar configuration which satisfies

some AFM constraints. The arrangement of the lanthanides is the relevant part of the structure to consider when interpreting magnetic properties. In some cases the nuclear structures have geometric frustrated motifs and the magnetic moments are unable to minimize their classical ground state by minimizing the 2-body magnetic exchange interactions. The phenomena of magnetic frustration can lead to quantum fluctuations that dominate the physics at lowest temperatures [103, 3, 104, 105].

Some examples of frustrated and insulating magnetic $4f$ materials are the pyrochlores such as R$_2$Ti$_2$O$_7$ and R$_2$Sn$_2$O$_7$. In the case of R= Ho and Dy a strong Ising anisotropy gives rise to spin ice. The rare earth ion carries a large magnetic moment between five and ten Bohr magnetons and the dipolar interactions between the nearest neighbor make a sizable contribution to the total magnetic interaction. It has been shown that it is the dipolar interactions which compete with the Ising anisotropy and cause the spin ice phenomenology [106, 107, 108, 109]. In Yb$_2$Ti$_2$O$_7$, a sharp first order transition is observed in specific heat measurements [110], and long range AFM order develops with an ordering wavevector $\boldsymbol{k} = (0, 0, 0)$ [111]. The Tb$_2$Ti$_2$O$_7$ antiferromagnet is particularly interesting since it appears to be an excellent candidate for collective paramagnetism or spin liquid behavior, as it fails to develop long range order, the dipolar interactions play a very important role in frustrating the nearest neighbor exchange interactions and are significant players in the formation of a possible spin liquid state [105, 112].

Another example of a RE frustrated insulator is Gd$_3$Ga$_5$O$_{12}$, it consists of corner sharing triangles. In this material, experimental evidence of a magnetic field induced spin liquid arising from the nearest neighbor exchange interaction has been found, as well as a re-entrance from a long range ordered magnetic state to a spin liquid upon cooling [113].

This chapter describes the properties of the insulating frustrated rare earth antiferromagnet SrYb$_2$O$_4$. SrYb$_2$O$_4$ is a member of the SrL$_2$O$_4$ family that has been investigated in the 1960's because it is isostructural to the post-spinel compound CaFe$_2$O$_4$ which is a key material for geology and crystallography [114]. However, the magnetic properties of these compounds have not been well investigated until now. Only two papers could be found describing their magnetic structure and magnetic susceptibility. The magnetic susceptibility and room temperature powder neutron diffraction of SrL$_2$O$_4$ with L=Dy,Ho,Tm and Yb were published by Karunadasa *et al.* [104]. SrDy$_2$O$_4$ shows magnetic scattering at low temperatures (T=20 K-40 K) due to short range correlations while the Ho compound exhibits long-range two dimensional order. SrEr$_2$O$_4$ has been investigated in detail by Petrenko *et al.* [115], they report long range AFM order below T=0.75 K.

Magnetic phenomena are also expected in $SrYb_2O_4$. Here the magnetic Yb^{3+} ion is characterized by an angular momentum $S = 1/2$, $L = 3$, $J = 7/2$ and a Landé g-factor $g_J = 8/7$. However, the magnetic properties of $SrYb_2O_4$ have not been investigated so far. Karunadasa *et al.* did not detect magnetic order in $SrYb_2O_4$. A series of diffraction papers can be found in the literature from the 1960's and 1970's where the nuclear structure of $SrYb_2O_4$ was investigated using X-ray diffraction at room temperature. These papers ascribe the structure to be orthorhombic with space group *Pnam* (62) and with all atoms at Wyckoff site $4c$ $(x, y, 1/4)$ [116, 117, 118, 119, 120, 121]. A. Antony *et al.* [118] published the nuclear structure of $SrYb_2O_4$ in 2001. Their refinement gives the unit cell parameters $a = 9.9941$ Å, $b = 11.764$ Å, $c = 3.3596$ Å. (Their a and b lattice parameters are actually swapped relative to ours). The crystal structure consists of nonmagnetic Sr atoms filling the columnar cavities of a network of edge and corner shared YbO_6 octahedra. These octahedra form the walls of a honeycomb-like structure, running perpendicular to the *a-b* plane, see Figure 6.1(a). The Yb^{3+} ions are arranged in 'zig-zags' chains running parallel to the *c*-axis (Figure 6.1(b)). Each chain contains only one of the two crystallographically independent Yb^{3+} ions.
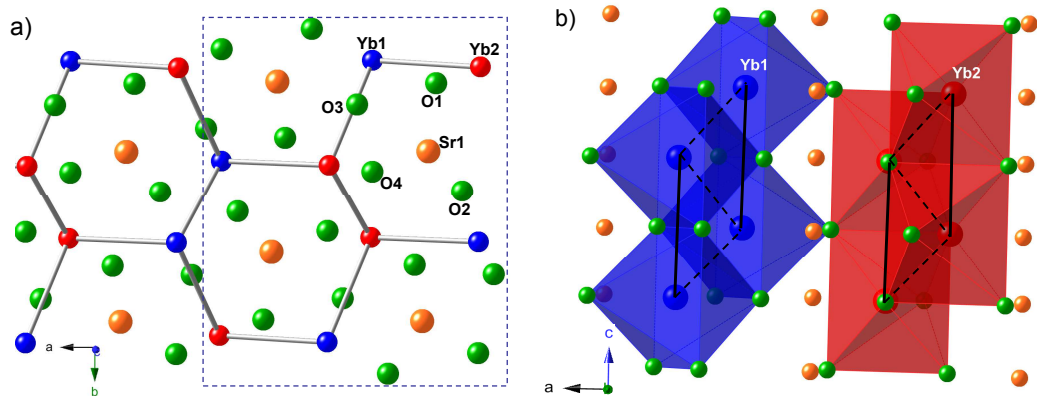
Figure 6.1: a) Crystal structure of $SrYb_2O_4$ showing one unit cell. Blue lines connect the two inequivalent Yb atoms (Yb1 in red and Yb2 in blue). Oxygen atoms are green and Strontium orange. b) 'Zig-zags' chains running along the c-axis, oxygen atoms form different octahedra around Yb ions, Sr ions fill the columnar cavities. The black dashed lines connect the first neighbors and they will be referred as to 'zig-zags' in the text. The solid black lines connect the second neighbors and they will be called as the 'legs' of the 'zig-zag' chain. The atomic positions are obtained from the refinement of E9 data at T=10 K, explained later in this chapter.

In 2005, Karunadasa *et al.* [104] published room temperature powder neutron diffraction data of $SrYb_2O_4$ and related compounds; they found the atomic positions shown in Table 6.1. They did not find any magnetic transition down to T=2 K, although the presence of low temperature short range magnetic correlations was suggested based on

susceptibility measurements. The interesting aspect of this nuclear structure is the geometric frustration along the zig-zag chains where the similarity in the first and second neighbor Yb-Yb distance suggest the possibility of competing first and second neighbor exchange interactions. Furthermore, the honeycomb structure in the *ab*-plane has a low coordination number. Both features are well known to cause quantum fluctuations which could prevent materials with strong 3D interactions from establishing long range order either reducing the Néel temperature or suppressing the magnetic order completely [122].

Table 6.1: Atomic positions of SrYb$_2$O$_4$ according to Karunadasa [104] at room Temperature. The space group is Pnam and all the atoms occupy Wyckoff site $4c$ $(x, y, 1/4)$.

Atom	x	y	B(Å^2)
Sr	0.7528	0.6503	0.81
Yb1	0.4217	0.1090	0.59
Yb2	0.4253	0.6123	0.59
O1	0.2102	0.1716	0.65
O2	0.1234	0.4802	0.91
O3	0.5176	0.7839	0.82
O4	0.4247	0.4239	0.79
$a = 9.9941$ Å,	$b = 11.764$ Å,	$c = 3.3596$ Å	

The diffraction investigations published previously are based on powder sample results and took place at room temperature. In contrast, we have grown the first bulk single crystal of this compound, and this, along with the possibility of cooling the sample to millikelvin temperatures in a dilution fridge opens up the opportunity of thoroughly investigating the magnetic properties of this compound for the first time.

Heat capacity has been measured on a single crystal at different magnetic fields down to 30 mK, see Figure 6.2. A second order transition has been detected at $T = 0.92$ K, in zero field. The transition occurs at lower temperatures when applying a magnetic field suggesting that it is a transition to a 3D long-range magnetically ordered state. The absence of finite magnetization at low temperatures implies that the order is antiferromagnetic.

In order to understand the crystal and low temperature magnetic structure of SrYb$_2$O$_4$ a total of five diffraction experiments have been done using neutrons and X-rays on powder and single crystal samples. The results will be described in this chapter. Additionally, heat capacity and magnetocaloric effect (MCE) data are presented here and reveal a rich phase diagram as a function of magnetic field and temperature.
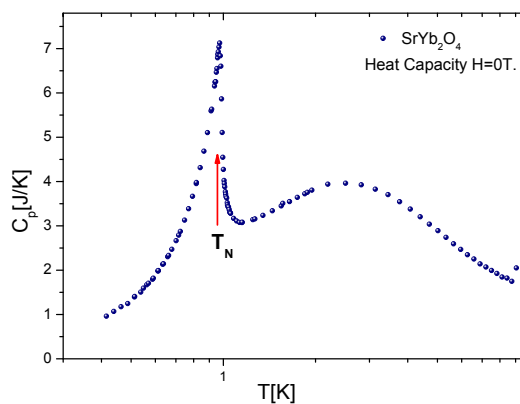
Figure 6.2: Heat capacity in zero field. The lambda anomaly at T=0.92 K indicates a second order transition to long-range antiferromagnetic order.

6.2 Experimental Details

Powder samples of $SrYb_2O_4$ were synthesized through a solid state reaction. Stoichiometric amounts of $SrCO_3$ (99.994% purity, Alfa Aesar) and Yb_2O_3 were mixed thoroughly, pressed into a pellet and heated three times for periods of 38 hours at 1200°C with intermediate grindings to achieve a single phase powder of $SrYb_2O_4$. Single crystals were grown from the melt by N. Islam and A. Niazi at HZB. First the powder was pressed into a feed rod using a cold isostatic press (EPSI). The growth was performed by the floating zone technique, using a high temperature optical floating zone furnace (Crystal Systems Inc. Model FZ-T$-$10000$-$H-VI-VPO). The feed rods were prepared as mentioned in Chapter 4. Four 300 W tungsten halide lamps focused by four ellipsoidal mirrors are used to melt the tip of the feed rod which is then recrystallized on a seed crystal to achieve single phase growth, the molten zone is then moved along the feed rod at a rate 1mm/hour to obtain a large single crystal. The growth was performed in air at ambient pressure. The resulting samples were typically transparent and cylindrical with a diameter of ≈ 5 mm and length 20 mm (see Figure 6.3). In general all rare earth based compounds have a very high melting temperature, this is also the case for $SrYb_2O_4$. Therefore the single crystal growth is challenging as it is difficult to maintain a molten zone throughout the growth, a furnace allowing higher temperatures would have made the growth easier. In order to investigate the crystal and magnetic structure of $SrYb_2O_4$ different neutron diffractometers were used. These are the high resolution powder diffractometer, E9, the focusing powder diffractometer E6 and the single crystal diffractometer (E4) all of which are installed in the reactor Hall (E$-$hall) at the BERII reactor at the Helmholtz Zentrum Berlin. In addition, the D7 diffractometer at ILL
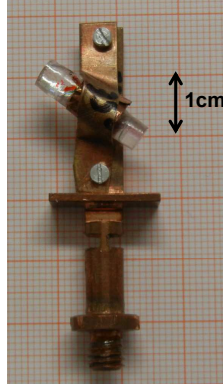
Figure 6.3: SrYb$_2$O$_4$ single crystal used for the E4 and D7 diffraction experiments and IRIS, IN5 inelastic experiments. The crystal is mounted in a Cu holder that ensures thermal conductivity.

which can perform **XYZ** polarization analysis was used to measure both single crystal and powder samples.

The E6 diffractometer provides low resolution, high intensity powder patterns at small wavevector transfers making it ideal for magnetic structure determination. It is equipped with a horizontally and vertically curved monochromator made from Pyrolytic Graphite reflecting from the $(0, 0, 2)$ Bragg peak (PG002). A fan collimator imitating a vertical slit with varying distance from the monochromator allows a relatively high flux while reducing background (see Fig. 6.4). By varying the horizontal focusing of the monochromator and the fan opening of the collimator, a correlation between the direction of the incoming neutrons and their wavelength can be achieved. Thus the orientation of the resolution ellipsoid can be changed with respect to the scattering wavevector **Q**.

In the focusing configuration the resolution ellipsoid is oriented with its long axis perpendicular to the wavevector transfer so that the resolution parallel to **Q** is maximized. An incident wavelength of $\lambda_0 = 2.4\,\text{Å}$ was used which gives the highest flux. The powder sample (mass of $14\,\text{g}$) was placed inside an annular aluminum sample can, which held it in the form of a cylindrical shell of thickness $2\,\text{mm}$, height $3.4\,\text{cm}$, outer diameter $2.2\,\text{cm}$ and inner diameter $2\,\text{cm}$. The lid was made of Cu to provide good thermal contact. The can was sealed under a ^{4}He atmosphere and filled with ^{3}He to ensure good thermal conductivity. Unfortunately the can was designed for inelastic neutron scattering rather than diffraction, and provided a large sample diameter which broadened the Bragg peaks so that the effective resolution was worse than expected ($\Delta 2\theta = 1.4°$ whereas the nominal value is $0.5°$). Using a dilution stick inserted into an orange cryostat to cool the sample, diffraction patterns were collected at $40\,\text{mK}$, $200\,\text{mK}$, $400\,\text{mK}$, $600\,\text{mK}$, $800\,\text{mK}$ and $1000\,\text{mK}$. The diffracted neutrons were measured using a position sensitive detector

$(300 \times 300 \, \text{mm}^2)$. Each scan consisted of 21 steps of the detector angle to cover a 2θ range of $136°$. For better statistics the scans at base temperature and $1\,\text{K}$ were repeated several times. The difference between the high ($1\,\text{K}$) and low ($30\,\text{mK}$) temperature patterns was taken to extract the magnetic intensity for magnetic structure refinement.

In order to study the nuclear structure of $SrYb_2O_4$ the high resolution powder diffrac-
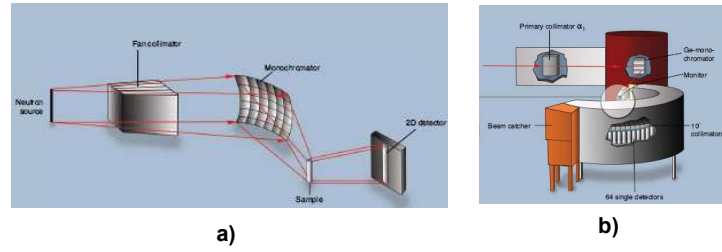
Figure 6.4: Diagram of E6 (a) and E9 (b). Taken from reference [76].

tometer E9 was used (see Figure 6.4). This instrument is ideal for nuclear structure determination as it can access high diffraction angles and small wavelengths and is able to measure a large number of peaks with high resolution. An incident wavelength of 1.798 Å was selected using the $(5, 1, 1)$ reflection of a Ge monochromator. A sapphire single crystal filter in the primary beam is used to reduce the number of epithermal neutrons. The detector bank consists of 64 ^{3}He single detector tubes each with a $10'$ collimator placed in front to improve the resolution. The angular distance between two detectors is nominally $2.5°$. By scanning this interval in steps of $0.0769°$ we obtained a diffraction pattern covering a total range of $160°$ in 2θ. The effective height of each detector tube is $150\,\text{mm}$. The resulting vertical detector aperture is about $7°$. The highest possible resolution provides a FWHM of about $0.28°$ in 2θ for the sharpest reflections, in our case the resolution was $0.31°$. We used a hollow cylindrical Cu sample can ($1.5\,\text{cm}$ of diameter) which was filled to a height of $1\,\text{cm}$ with $6\,\text{g}$ of $SrYb_2O_4$ powder. A mixture of deuterated ethanol and methanol was added to ensure thermal contact, the can was then attached to a dilution insert. Nevertheless, the diffraction pattern showed a bump of incoherent scattering around $|\boldsymbol{Q}| = 1.75\,\text{Å}^{-1}$ ($\approx 30°$ in 2θ) due to the alcohol mixture as is shown in the inset in Figure 6.9, this unfortunately coincided with crucial peaks. Data were collected at two temperatures $T = 0.03\,\text{K}$ and $10\,\text{K}$, with a counting time of 72 hours each.

E4 is a two-axis diffractometer designed to measure single crystal samples inside heavy sample environments which cannot be tilted out of the horizontal scattering plane (see Fig. 6.5). It was necessary to use E4 to measure $SrYb_2O_4$ rather than a conventional four-circle diffractometer because the dilution stick which was required to cool the sample
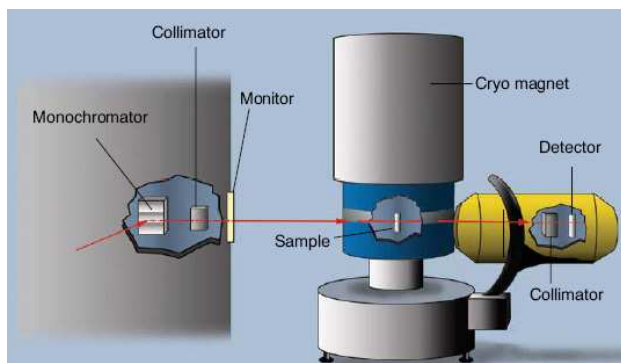
Figure 6.5: Diagram of the two axis spectrometer E4. Taken from reference [76].

below its transition temperature could not be tilted. The vertically focusing monochromator (PG002) was used to select an incident wavelength of 2.43 Å. Our single crystal sample, grown in an optical floating zone furnace, had a cylindrical shape (length of 1.5 cm, diameter of 5 mm) and mass of 3.2 g. It was mounted on a copper holder for good thermal contact (see Fig. 6.3). Two different horizontal scattering planes were chosen, firstly $(0, K, L)$ and secondly $(H, K, 0)$. A total of 101 reflections (48 unique) were measured at 30 mK, 10 K and 300 K. In addition, the temperature dependence of the 4 reflections $((0, 0, 1), (1, 1, 0), (0, 2, 0)$ and $(0, 1, 0))$ was followed between $T = 0.03$ K, and 1.07 K. The scattered intensity was detected in a ^{3}He 2D-position sensitive detector of size, 200×200 mm^2, which had an efficiency at $\lambda = \approx 2.43$ Åof about 85% . Each Bragg reflection was measured by performing an omega scan with fixed 2θ over about $4°$ in steps of $0.08°$. The two dimensional Bragg peaks were integrated over the x and y axes of the detector and plotted as a function of omega using the Lamp data analysis package. The one dimensional peaks were then fitted using a Pseudo-Voigt function plus linear background. This was done for both temperatures, T=30 mK and 10 K individually. To extract the magnetic intensities, the difference between the high and low temperature detector images was taken for every point in the scan and the resulting two dimensional peak was integrated and fitted as mentioned above. It was not always possible to obtain accurate intensities due to powder lines from the crystal holder, peaks that were too broad, large extinction effects or extra peaks coming from a smaller crystallite, see Figure 6.6. Beside this, intensity was found at every reflection, even on the positions forbidden by the Pnam space group. We believe this extra intensity is due to contamination from higher order scattering. This contamination was present even though two PG filters (4 cm) were placed before the sample.
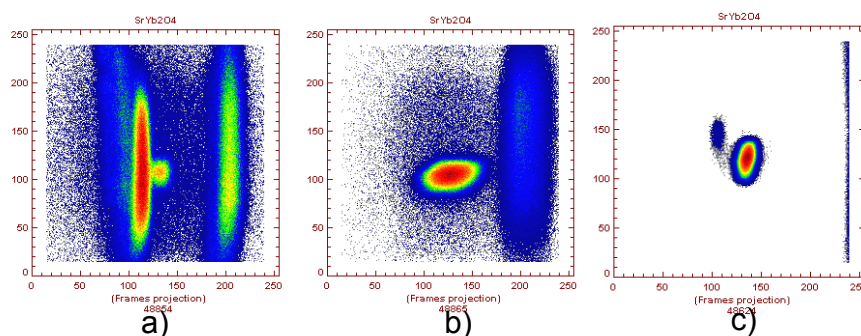
Figure 6.6: Detector image of E4 showing problematic reflections due to powder lines, broad peaks and multiple crystallites. a) $(0, 4, 1)$ powder lines, b) $(0, 7, 1)$ too broad peaks. c)$(3, -2, 0)$ peaks from smaller crystallites.
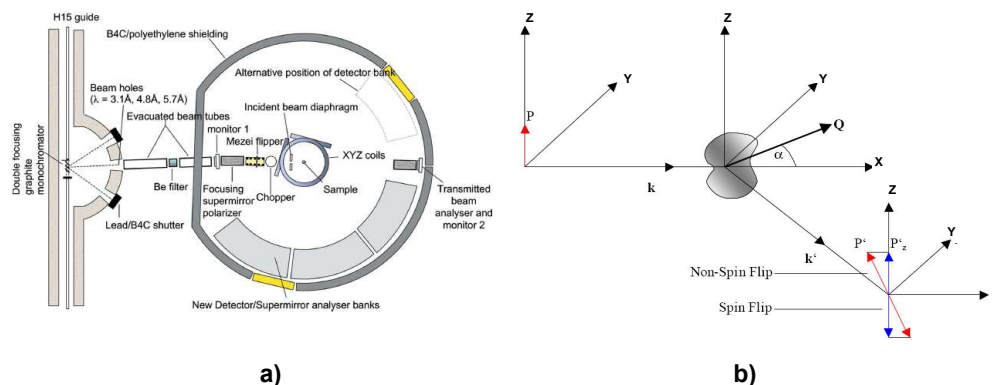
Figure 6.7: (a) Diagram of the D7 setup for diffraction.(b)Orientation of the **XYZ** polarization analysis coordinate system, with initial polarization along the z-axis. Taken from reference [123].

The last experiment was performed on D7 at the ILL (see Fig. 6.7). This instrument is a cold neutron multidetector diffractometer with full **XYZ**-polarization analysis. This allows the unambiguous separation of nuclear, magnetic, nuclear-spin-incoherent and isotope incoherent contributions to the scattering function simultaneously over a large range of scattering vector **Q**. The instrument consists of a horizontally and vertically focusing monochromator (PG002) and a cold Be filter is used to suppress higher order contamination. The beam is polarized using a supermirror bender which provides high polarization efficiency over a wide wavelength band. It has a Mezei flipper, which consist of a coil producing a well defined horizontal magnetic field with a sharp transition at the coil surface ($\pi-$coil with a Brookhaven correction coil). The instrument has a set of three orthogonal coils around the sample position producing magnetic fields in the **X**, **Y** and **Z** directions. This allows the incident neutron spin direction to be defined. The

instrument uses supermirror benders as polarization analyzers, installed in front of the
^{3}He detector tubes. These polarizers−detector blocks are in three sets which can move
around covering a large range in 2θ, see Figure 6.7(a). We have used D7 to measure both
powder patterns and single crystal Bragg reflections of SrYb$_2$O$_4$. For both measurements
the sample was cooled in a dilution fridge to a minimum temperature of T=29 mK and
the incident wavelength was $\lambda_0 = 4.84$ Å. The polarization was calibrated using quartz,
and the polarization ratio was found to be 0.944. The energy resolution, determined
by the width of the incoherent elastic line was 0.16 meV. In the case of the powder
measurements, we used a 11.408 g sample, in an annular Cu can. The can had an inner
diameter of 1.15 cm, an external diameter of 1.6 cm and the sample height was 4.2 cm. To
get a fine 2θ dataset at T=29 mK, 11 detector positions were used and for each position
6 polarization channels were measured, **XX**$_{nsf}$, **YY**$_{nsf}$, **ZZ**$_{nsf}$, **XX'**$_{sf}$, **YY'**$_{sf}$ and
ZZ'$_{sf}$ (where the subscripts nsf and sf refer to the non-spin-flip and spin-flip channel).
The procedure was repeated for 36 hours to acquire good statistics. In addition to the
quartz calibration, a vanadium and an empty can calibration were done. The vanadium
calibration corrects the efficiency of the detectors and gives the intensity in absolute
units. For the single crystal measurements, the same crystal as for the E4 experiment
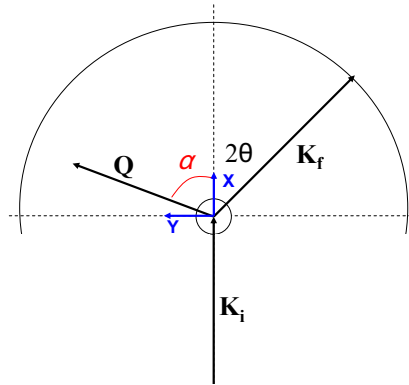
Figure 6.8: Sketch of the wavevector transfer **Q** along with the initial and final neutron wavevec-
tors k_i and k_f. The directions of the **X** and **Y** polarizations and the Schärpf angle are also shown.

was used, it was again mounted on a Cu holder with $(H, K, 0)$ as the scattering plane.
We measured 11 Bragg peaks at 29 mK, each with 6 different polarizations. For these
measurements 5 different detector positions were used around the nominal 2θ for each
Bragg peak, and for each of these positions omega scans of 30° (step size 0.15°) were
performed and counted for 8 seconds at every position and polarization channel. For the
polarization analysis, the **X**, **Y** and **Z** polarization directions are fixed with respect to the

instrument rather than being parallel and perpendicular to the wavevector transfer as in the case of the commonly used Blume-Maleev coordinate system [124, 125]. The angle between the **X** polarization axis and **Q** is called the Schärpf angle, α (see the Figure 6.8). For powder samples of paramagnets or collinear antiferromagnets, the polarization of the scattered beam has the direction of the scattering vector[126, 123, 127]. Therefore, the Schärpf angle can be calculated from a calibration with a static diffuse magnetic scatterer; the compound used for that was $MnSiO_4$ and the angle was calculated to be approx 90°. Using this assumption for the powder patterns, it is possible to separate magnetic, from nuclear and spin-incoherent components of the scattering function. In the case of the single crystal the Schärpf angle can be written in terms of 2θ for a specific Bragg peak as $\alpha = \frac{\pi}{2} - \theta$. The cross-sections for the **X**, **Y** and **Z** polarizations can be expressed in terms of α. They are given by[123]:

$$
\begin{aligned}
\left(\frac{\partial^2\sigma}{\partial\Omega\partial E}\right)^z_{SF} &= \frac{2}{3}\left(\frac{\partial^2\sigma}{\partial\Omega\partial E}\right)_{SI} + \frac{1}{2}\left(\frac{\partial^2\sigma}{\partial\Omega\partial E}\right)_{MAG}, \\
\left(\frac{\partial^2\sigma}{\partial\Omega\partial E}\right)^z_{NSF} &= \frac{1}{3}\left(\frac{\partial^2\sigma}{\partial\Omega\partial E}\right)_{SI} + \frac{1}{2}\left(\frac{\partial^2\sigma}{\partial\Omega\partial E}\right)_{MAG} + \left(\frac{\partial^2\sigma}{\partial\Omega\partial E}\right)_{NUC} + \left(\frac{\partial^2\sigma}{\partial\Omega\partial E}\right)_{II}, \\
\left(\frac{\partial^2\sigma}{\partial\Omega\partial E}\right)^y_{SF} &= \frac{2}{3}\left(\frac{\partial^2\sigma}{\partial\Omega\partial E}\right)_{SI} + (1+sin^2\alpha)\frac{1}{2}\left(\frac{\partial^2\sigma}{\partial\Omega\partial E}\right)_{MAG}, \\
\left(\frac{\partial^2\sigma}{\partial\Omega\partial E}\right)^y_{NSF} &= \frac{1}{3}\left(\frac{\partial^2\sigma}{\partial\Omega\partial E}\right)_{SI} + (cos^2\alpha)\frac{1}{2}\left(\frac{\partial^2\sigma}{\partial\Omega\partial E}\right)_{MAG} + \left(\frac{\partial^2\sigma}{\partial\Omega\partial E}\right)_{NUC} + \left(\frac{\partial^2\sigma}{\partial\Omega\partial E}\right)_{II}, \\
\left(\frac{\partial^2\sigma}{\partial\Omega\partial E}\right)^x_{SF} &= \frac{2}{3}\left(\frac{\partial^2\sigma}{\partial\Omega\partial E}\right)_{SI} + (1+cos^2\alpha)\frac{1}{2}\left(\frac{\partial^2\sigma}{\partial\Omega\partial E}\right)_{MAG}, \\
\left(\frac{\partial^2\sigma}{\partial\Omega\partial E}\right)^x_{NSF} &= \frac{1}{3}\left(\frac{\partial^2\sigma}{\partial\Omega\partial E}\right)_{SI} + (sin^2\alpha)\frac{1}{2}\left(\frac{\partial^2\sigma}{\partial\Omega\partial E}\right)_{MAG} + \left(\frac{\partial^2\sigma}{\partial\Omega\partial E}\right)_{NUC} + \left(\frac{\partial^2\sigma}{\partial\Omega\partial E}\right)_{II},
\end{aligned}
\tag{6.1}
$$

where the subscripts *MAG*, *SI*, *NUC*, *II* refer to the magnetic, spin incoherent, nuclear coherent and isotope incoherent components of the scattering cross section. Using these equations it is possible to separate the nuclear, magnetic and isotope incoherent scattering.

Besides these experiments some additional test measurements were also performed. They were used to determine whether the forbidden peaks observed in the E4 measurement were real or due to an artifact, e.g. $\lambda/2$ contamination. One check was a powder diffraction measurement using synchrotron X-rays at the MAGS beam time at BESSY, HZB. An initial wavelength of 1.55 Å was used. The sample was a tiny single crystal of $SrYb_2O_4$ which was crushed and ground to fine powder. This powder was mounted in

a capillary. Since there was no facility to rotate the powder during the measurement, the intensities were unreliable and it was not possible to refine the data. Nevertheless, with strong intensity and an excellent 2θ resolution of $0.0367°$ ($\Delta d = 0.00549$ Å, $\Delta Q = 0.00248$ Å^{-1}) it is good enough to detect peak splitting, additional reflections or other signs of lower symmetry. All the data were collected at room temperature. Further tests were performed on the single crystal sample using the V2/FLEX triple axis spectrometer. The crystal was mounted with $(0, K, L)$ in the horizontal scattering plane and was cooled to 10 K. The vertically focusing monochromator and flat analyzer (both PG002) were set to scatter a wavelength of 5.6 Å. A Be Filter was placed in the scattered beam. Measurements of forbidden and allowed peaks were performed with and without the Be filter to determine whether the peaks are really present or simply due to higher order contamination.

Heat capacity and magnetocaloric effect (MCE) measurements on single crystal samples were performed to map out the magnetic phase diagram of SrYb$_2$O$_4$. These measurements were done using a home made calorimeter CM14.5T [26], the oriented samples were mounted in a copper base of a ^{3}He sorption cryostat inserted in a H=14.5 T cryomagnet. The samples used were single crystal pieces of mass 3.07 mg oriented along the a and c axes as well as a 1.87 mg single crystal aligned along the b-axis. The heat capacity was measured in the temperature range 0.28 K$< T <$1.1 K for the samples aligned along the a and b axes and for 0.28 K$< T <$9 K for the sample aligned along the c-axis. Constant magnetic fields (initial:step:final; 0 T:0.1 T:1 T, 1 T:0.2 T:2 T, 2 T:0.5 T:4.5 T, 6 T:3 T:12 T) were applied along the c-axis (0 T:0.25 T:5 T, along the a-axis and 0 T:0.25 T:12 T, along the b-axis). The same samples and same equipment were used to measure the magnetocaloric effect (MCE). Constant temperatures were set (T=0.3 K and 1 K for the field parallel to the a-axis, T=0.3 K:0.1 K:1.1 K with the magnetic field along the b-axis and T=0.3 K:0.1 K:1 K with the field parallel to the c-axis) and the magnetic field was ramped up and down from 0 T to 12 T with a sweep rate of 0.075 T/min. The magnetic moment was measured using a Quantum Design Physical Property Measurement System (PPMS) with a Vibrating Sample Magnetometer [25] at the Laboratory for Magnetic Measurements, HZB. The single crystal was oriented using the X-ray Laue technique, cut and installed in a brass sample holder; the magnetic moment was measured at 2 K and a magnetic field from 0 T to 14 T was applied along the three different crystallographic directions.

6.3 Results and Discussion

6.3.1 Nuclear Structure

As mentioned before, the nuclear structure of $SrYb_2O_4$ consists of two inequivalent types of YbO_6 octahedra. The Yb^{3+} ions form zig-zag chains along the **c** axis and honeycombs in the *ab*-plane (see Fig. 6.1). The space group at room temperature is *Pnam* (62), and all atoms are at the Wyckoff position 4c $(x, y, 1/4)$. Bulk properties measurements suggest the absence of any structural phase transitions between room temperature and T=30 mK. The crystal structure of $SrYb_2O_4$ was refined within the *Pnam* space group at 10 K from the E9 data, using the atomic positions at T=300 K published by Kuranadasa *et al.* [104], as starting parameters (Table 6.1).

The E9 data along with the best refinement are shown in Figure 6.9. 330 reflections were fitted using the Rietveld method in Fullprof [128]. As the sample can was made of Cu, the pattern was contaminated by a few Cu Bragg peaks which were removed before the refinement. The profile used for the peaks was a pseudo−Voigt function convolved with an axial divergence asymmetry function. An excellent refinement was achieved ($R_p = 2.48$, $R_{wp} = 3.17$, $R_{exp} = 1.31$, $\chi^2 = 5.89$) confirming the *Pnam* space group, and the lattice parameters and atomic positions at T=10 K are listed in table 6.2. The low temperature (T=40 mK) E9 data were also refined, the crystal and magnetic structure (explained in the next section) were fitted simultaneously, this refinement reveals that there is no a significant structural change accompanying the magnetic transition (see Table 6.2).
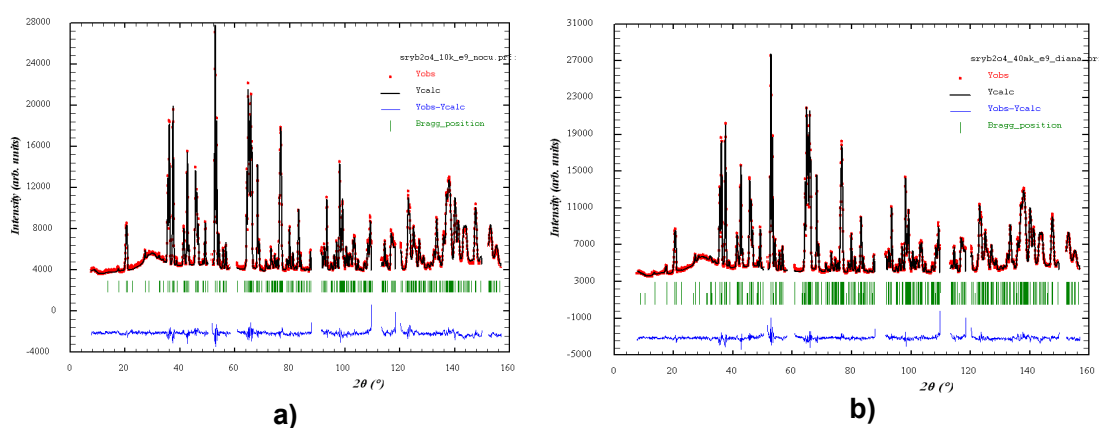
**Figure 6.9:** Rietveld refinement of the E9 data collected at (a)T=10 K and (b)T=40 mK. The regions contaminated by Cu powder lines from the sample holder have been removed. The red dots indicate the measured data, the black line indicates the calculated data, the blue line represents the difference of both and the green bars indicate the (h, k, l) positions.

Table 6.2: Crystal structure from the refinement of the E9 data at T=10 K and T=40 mK. All atoms are in the Wyckoff site $4c$ $(x, y, 1/4)$.

Atom	x (T=10 K)	y (T=10 K)	x (T=40 mK)	y (T=40 mK)
Sr	0.7544(3)	0.6514(3)	0.7546(3)	0.6512(3)
Yb1	0.4221(2)	0.1091(1)	0.4217(2)	0.1090(1)
Yb2	0.4260(2)	0.6124(2)	0.4264(2)	0.6123(2)
O1	0.2106(4)	0.1736(3)	0.2108(4)	0.1725(3)
O2	0.1236(4)	0.4798(4)	0.1246(4)	0.4800(3)
O3	0.5183(4)	0.7835(3)	0.5179(4)	0.7833(3)
O4	0.4217(5)	0.4230(3)	0.4219(4)	0.4229(3)
10 K	$a = 9.97595(7)$ Å,	$b = 11.75488(7)$ Å	$c = 3.35265(2)$ Å	
40 mK	$a = 9.97576(7)$ Å,	$b = 11.75466(8)$ Å	$c = 3.35260(3)$ Å	

The E4- single crystal diffraction experiment, found intensity at all reciprocal lattice vectors and all temperatures $(10\,\text{K}-300\,\text{K})$, even at positions forbidden by the crystal symmetry. The reflection conditions for the *Pnam* space group are: $0kl : k+l = 2n$, $h0l : h = 2n$, $h00 : h = 2n$, $0k0 : k = 2n$, $00l : l = 2n$, however, intensity was found at room temperature on forbidden reflections like $(1,0,0)$, $(0,1,0)$, $(0,0,1)$. Initially a lowering in symmetry was suspected, e.g. a monoclinic distortion to $(P2/m)$, but this could be unambiguously ruled out by performing tests on other instruments, firstly on the neutron triple axis V2/Flex$-$HZB, where a Be filter was used to eliminate higher order scattering and secondly on the MAGS high resolution synchrotron X-ray diffractometer. Using V2/FLEX, wavevector scans were made through specific Bragg reflections. The scans were done with and without a Be filter in order to determine the contribution due to $\lambda/2$ contamination. First of all the efficiency of the filter was checked by measuring $(0, 0.5, 0.5)$. With the Be filter the count rate was 1 count per second whereas without the filter it was 445 per second. In comparison the allowed $(0,1,1)$ peak, has 1024 counts per second with Be filter and 1495 counts without, see Figure 6.10. Therefore the Be filter is highly efficient and removes all $\lambda/2$ contamination. Similar scans were then performed through specific forbidden peaks, as shown in Figure 6.10. The results confirm the complete absence of intensity for $(0,1,0)$, $(0,3,0)$, $(0,0,1)$ when the filtered beam is used, in agreement with the reflection conditions of the *Pnam* space group. In addition synchrotron X-ray powder diffraction was used to search for splitting or forbidden reflections that could imply a monoclinic distortion at room temperature, since the high instrumental resolution allows a d-space splitting of 0.00549 Å to be observed. The pattern could still be indexed in the space group *Pnam*, with no additional reflections or splitting. Therefore it can be concluded that there is no structural distortion and
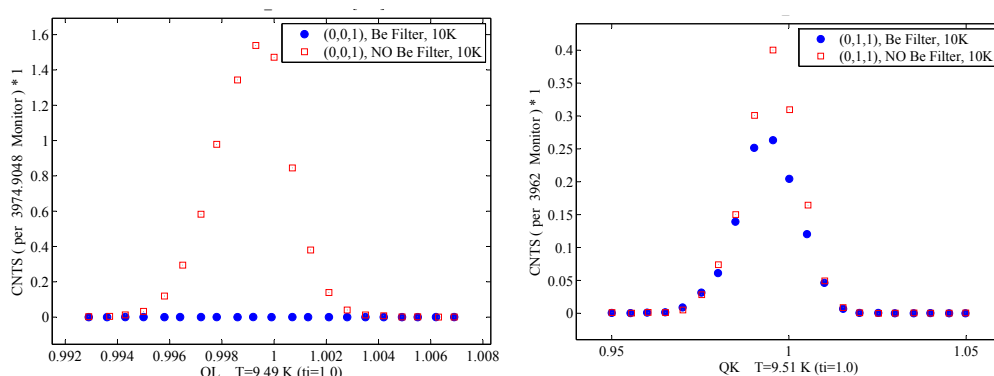
Figure 6.10: Comparison of scans with and without the Be filter. (left): The $(0,0,1)$ peak forbidden in Pnam is 100% $\lambda/2$. (right) The $(0,1,1)$ allowed structural peak is 35% $\lambda/2$.

the space group of $SrYb_2O_4$ is *Pnam* down to T=30 mK. The forbidden reflections observed in the E4 data must therefore be due to substantial contaminated by higher order scattering. Although this X-ray diffraction pattern could not be used to refine the atomic positions since the intensities were unreliable because the sample was not rotated during the measurement, it could be used to obtain accurate values of the lattice parameters. By performing the profile matching option of Fullprof (see Figure 6.11) the values of the lattice parameters were found to be $a = 9.99805(82)$ Å, $b = 11.78752(104)$ Å, $c = 3.36164(32)$ Å at room temperature. These values can be compared to the low
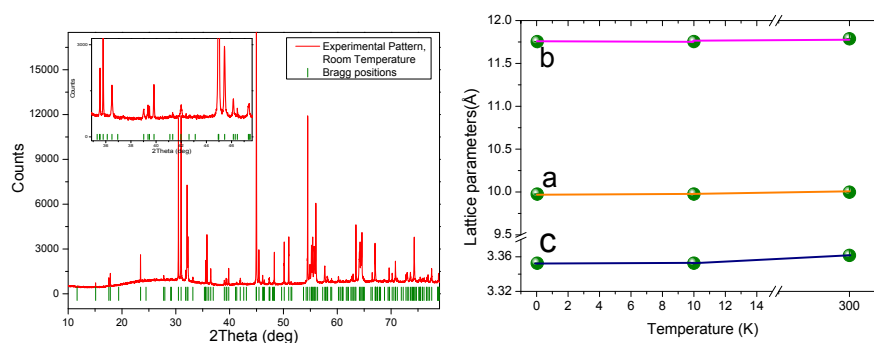
Figure 6.11: Left: X-ray diffraction pattern of $SrYb_2O_4$ measured at 300 K. Right: Lattice parameters at three different temperatures. The 40 mK and 10 K points were obtained from E9 refinement. Room temperature parameters were obtained by profile matching of the x−ray pattern.

temperature lattice parameters obtained from the E9 measurement (see Figure 6.11). No significant change in the lattice parameters is observed in the measured temperature range (40 mK−300 K).

The crystal structure extracted from the E9 data is shown in Figure 6.12. As found by Karunadasa *et al*. [104], the two inequivalent Yb^{3+} ions form zig-zag chains along the *c*-axis and make a distorted honeycomb arrangement in the *ab*-plane. Figure 6.13 shows the YbO$_6$ octahedra for both Yb ions. The distances between the Yb ions and oxygens are listed. The octahedra are distorted, and have monoclinic site symmetry. Since the Yb^{3+}-Yb^{3+} distances are short we can expect magnetic interactions between them giving rise to long-range magnetic order as will be discussed in the next section.
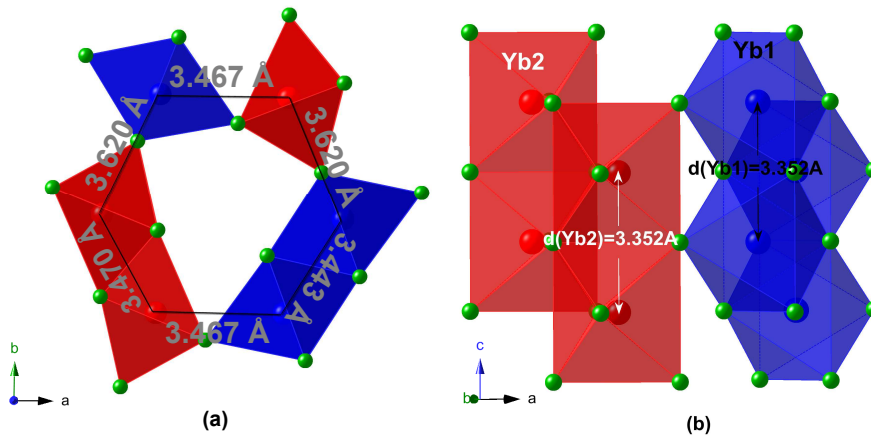
Figure 6.12: Crystal structure of SrYb$_2$O$_4$ projected onto the (a) *ab*-plane, (b) *ac*-plane. The O^{2-} are represented by green circles. The Yb^{3+} lie inside the octahedra, Yb1 in the blue octahedra and Yb2 in the red octahedra. Sr^{2+} ions are not shown but would be in the gaps between the octahedra. The Yb^{3+}-Yb^{3+} distances are obtained from the E9 refinement at T=10 K.
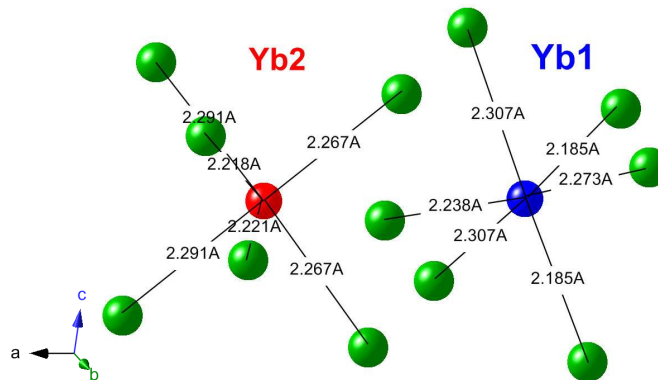
Figure 6.13: Crystal structure of SrYb$_2$O$_4$, showing distances between the Yb^{3+} ions (red and blue) and the oxygens (green) that form the surrounding octahedra. These values come from the E9 refinement at T=10 K.

6.3.2 Magnetic Structure

As mentioned before, according to heat capacity $SrYb_2O_4$ undergoes a phase transition to long-range antiferromagnetic order around $T = 0.92$ K. A series of powder diffraction patterns were measured on E6 as a function of temperature from 1 K to 30 mK to investigate this transition. These patterns are shown for $20° < 2\theta < 30°$ by the colorplot in Figure 6.14. There is a clear increase in the intensity of the $(0, 2, 0)$ reflection with decreasing temperature indicating additional magnetic intensity at the nuclear peak position. The $(2, 0, 0)$ reflection is a strong nuclear peak and its change with temperature is difficult to observe. In Figure 6.15 high $(1\,K)$ and low $(30\,mK)$ temperature patterns are shown; no additional peaks appear below the Néel temperature and all the peaks could be indexed with integer indexes implying that the ordering wavevector $\mathbf{k} = (0, 0, 0)$. E4 data were used to follow the temperature dependence of specific reflections measured
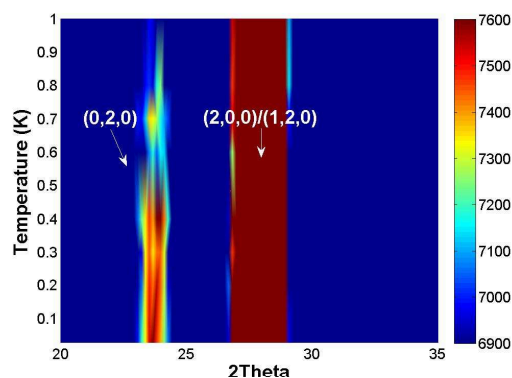
Figure 6.14: Colorplot showing the powder patterns measured on E6 as a function of 2θ versus temperature. Intensity scale gives counts per 100000 monitor. A notable change is obvious in the (0,2,0) reflection.

on the single crystal. There are significant changes for the $(0, 2, 0)$ and $(0, 0, 1)$ reflections. $(0, 1, 0)$ is forbidden and as explained earlier, the observed intensity corresponds to pure $\lambda/2$ contamination. $(1, 1, 0)$ appears to have no magnetic component, see Figure 6.15.

In order to understand the possible types of magnetic structure in $SrYb_2O_4$, a representation analysis was performed using the BasIreps program implemented in the Fullprof suite [129]. There are two inequivalent Yb^{3+} sites lying at Wyckoff position $4c$, each of which generates four Yb^{3+} ions in the unit cell at fractional coordinates $(x, y, 1/4)$, $(-x, -y, 3/4)$ and $(x + 1/2, -y + 1/2, 1/4)$, $(-x + 1/2, y + 1/2, 3/4)$. These Yb positions along with the space group $Pnam$ and the propagation vector $\boldsymbol{k} = (0, 0, 0)$ allow four possible types of magnetic order within the a-b plane given by the irreducible repre-
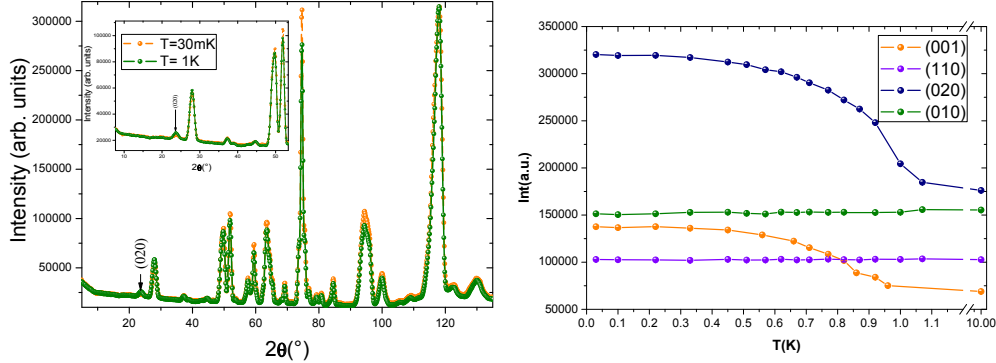
Figure 6.15: (left):1 K (red) and 30 mK (blue) powder patterns from E6. (right): Temperature dependence of the intensity of four reflections measured on E4. Two of them are pure nuclear reflections $(1, 1, 0)$ and $(0, 1, 0)$. The other two have both magnetic and nuclear components, and reveal the onset of magnetic order around $T = 0.9$ K

sentations $\Gamma_1(C_xF_y)$, $\Gamma_2(F_xC_y)$, $\Gamma_3(G_xA_y)$ and $\Gamma_4(A_xG_y)$, while along the $c-$axis the ordering follows $\Gamma_5(C_z)$, $\Gamma_6(F_z)$, $\Gamma_7(G_z)$ or $\Gamma_8(A_z)$. Here x, y and z refer to modes along the a, b and c directions. It is also possible to have magnetic components along all three crystallographic directions, e.g. the combinations $\Gamma_1 \oplus \Gamma_5$, $\Gamma_2 \oplus \Gamma_6$, $\Gamma_3 \oplus \Gamma_7$ or $\Gamma_4 \oplus \Gamma_8$. The irreducible representations refer to the modes $F(++++)$, $C(++--)$, $G(+--+)$ and $A(+-+-)$ where the symbols in brackets give the relative spin direction (either up $'+'$ or down $'-'$) of the sequence of four Yb ions generated for each Yb site listed above. Since the structure is antiferromagnetic we do not consider the ferromagnetic F mode, which rules out Γ_1, Γ_2 and Γ_6; and leaves Γ_3, Γ_4, Γ_7 and Γ_1.

In order to determine which of the remaining irreducible representations describes best SrYb$_2$O$_4$ the relative intensities for various Bragg peaks for the x, y and z components of the **A**, **G** and **C** modes were simulated using Fullprof (see Table 6.3). Two cases are considered, first when the moment on the two Yb sites are equal $(\mu(Yb1) = \mu(Yb2))$ and second when only one Yb site carries magnetic moment $(\mu(Yb1) \neq 0, \mu(Yb2) = 0)$. Each case produces different Bragg peak intensities. The table also includes the experimental values for the intensities of these Bragg peaks measured on the single crystal using the E4 diffractometer for comparison. Although the intensities from E4 are not sufficiently accurate to perform a magnetic structure refinement they provide valuable information about the peak intensity. By comparing the experimental and theoretical values it should be possible to determine which type of magnetic structure occurs in SrYb$_2$O$_4$ and whether the ordered moments on the two Yb sites are similar or different.

The E4 results provide the follow information:

Table 6.3: Simulated relative intensities of various Bragg peaks for the possible magnetic modes of $SrYb_2O_4$ for the cases when $\mu(Yb1) = \mu(Yb2)$ (upper table) and $\mu(Yb1) \neq 0$ $\mu(Yb2) = 0$ (lower table). The experimental intensities of these peaks obtained from E4 are also shown. *E4nucl* lists the nuclear intensity of these reflections at 1 K and *E4mag* shows the result of subtracting the high temperature (1 K) intensities from the low temperature (30 mK) intensities, giving the magnetic component.

$\mu(Yb1)$	$= \mu(Yb2)$										
(h,k,l)	*E4nucl*	*E4mag*	*Gx*	*Gy*	*Gz*	*Ax*	*Ay*	*Az*	*Cx*	*Cy*	*Cz*
$(0,1,0)$	55.6	3.4	0.2	0	2	0	0	0	471	0	0.1
$(1,0,0)$	100.9	1.1	0	0	0	0	481	481	0	1769	1770
$(1,1,0)$	158.53	74.5	0.1	0.2	0.3	0.1	0.1	0.3	1	0.1	0.1
$(0,2,0)$	635.19	615.4	0	0	0	690	0	696	0	0	0
$(1,2,0)$	2093.5	8.1	470	200	770	5	1.8	7	19	6	26
$(2,0,0)$	3467.5	82.8	0	330	330	0	0	0	0	0	0
$(2,1,0)$	85.87	24.3	0.1	0.2	0.2	0.1	0.1	0.2	0.1	0.1	0.1
$(0,3,0)$	60.18	5.36	0.1	0	0.1	0	0	0	0.2	0	0.2
$(2,2,0)$	1557.17	37.64	2.5	6	10	66	92	58	136	188	324
$(1,3,0)$	342.21	198.6	0.1	0.1	1	0.1	0.1	0.1	0.1	0.1	0.1
$(0,0,1)$	70.42	826.0	172	175	0	0	0	0	0.1	0	0
$(3,0,0)$	244.42	3.6	0	0	0	0	168	171	0	3	3
$(0,1,1)$	870.13	173.62	0	0	0	0.1	0.1	0	0	0	0
$\mu(Yb1)$	$\neq 0$	$\mu(Yb2)$	$= 0$								
$(0,1,0)$	55.6	3.4	314	0	314	0	0	0.2	0	0	471
$(1,0,0)$	100.9	1.1	0	0	0	0	126	126	0	437	437
$(1,1,0)$	158.53	74.5	35	50	85	43	115	198	24	32	56
$(0,2,0)$	635.19	615.4	0	0	0	173	0	73	0	0	0
$(1,2,0)$	2093.5	8.1	141	49	190	17	0.5	2.2	6	2	8
$(2,0,0)$	3467.5	82.8	0	85	85	0	0	0	0	0	0
$(2,1,0)$	85.87	24.3	4	21	24	12	71	84	6	31	37
$(0,3,0)$	60.18	5.36	53	0	53	0	0	0	15	0	15
$(2,2,0)$	1557.17	37.64	1.4	2	3.5	15	21	36	34	48	83
$(1,3,0)$	342.21	198.6	2.5	0.7	5	60	9	68	16	2.6	20
$(0,0,1)$	70.42	826.0	44	44	0	0	0	0	0	0	0
$(3,0,0)$	244.42	3.6	0	0	0	0	42	42	0	0.4	0.4
$(0,1,1)$	870.13	173.62	0	0	0	46	42	3.5	0	0	0

- The $(0,1,0)$ reflection has no intensity or is very weak. By comparison to the simulated intensities it is clear that if only one Yb site is ordered, the modes *Gx*, *Gz*, *Cx* and *Cz* which give strong intensity in the simulation must be absent, and only *Gy*, *Ax*, *Ay*, *Az* and *Cy* are possible. However, if the two Yb ions have similar

moments we can not exclude any mode since none of them produce intensity at $(0, 1, 0)$.

- $(1, 0, 0)$ has none or very little intensity, therefore the modes *Ay*, *Az*, *Cy* and *Cz* which give strong intensity in the simulation for both models must be absent.

- $(1, 1, 0)$ has some intensity. This peak is expected to be very small for all modes if both Yb sites have the same ordered moment, while it is expected to be fairly strong for all modes if only one Yb site orders. We conclude that in SrYb$_2$O$_4$ both Yb sites order but they do not have the same moment.

- $(0, 2, 0)$ is a strong magnetic peak indicating that the modes *Ax* and/or *Az* are present.

- $(1, 2, 0)$ has a strong nuclear component, the magnetic component has been calculated from the subtraction of the high and low temperature datasets, therefore the magnetic component is unreliable for this peak and cannot be used to draw conclusions about the magnetic structure.

- $(2, 0, 0)$ has very strong nuclear component and therefore the magnetic component is unreliable. Nevertheless it seems to indicate that the modes *Gy* and/or *Gz* are present.

- $(0, 3, 0)$ is very weak, therefore *Gx* and *Gz* can be excluded if only one Yb site is ordered. Alternatively, if one or both of these modes are present it indicates that the two Ybs have similar moment sizes.

- $(1, 3, 0)$ has substantial intensity indicating that the two Yb sites have unequal moment and that *Ax* and/or *Az* are present.

- $(0, 0, 1)$ is very strong indicating that *Gx* and/or *Gy* are present.

- $(3, 0, 0)$ has no intensity excluding the *Ay* and *Az* modes.

- $(0, 1, 1)$ has intensity, indicating that the two Yb have different moment sizes and the *Ax* and/or *Ay* modes are present.

In conclusion, SrYb$_2$O$_4$ has a magnetic structure where the two Yb sites have different moment sizes but neither are zero. Many of the modes could be excluded, and the remaining modes which are *Gy* and *Ax*, show that the order follows the $\Gamma_4(A_xG_y)$, representation with the magnetic moments predominantly in the *a-b* plane. It is not possible

to exclude the *Gz* mode because a small amount of intensity was found on $(1, 2, 0)$ and $(0, 3, 0)$ which might indicate a weak *Gz* order. As $\boldsymbol{k} = (0, 0, 0)$ for $SrYb_2O_4$, the magnetic peaks coincide with the nuclear Bragg peaks making the separation of the magnetic intensity from the much stronger nuclear intensity difficult and unreliable. Therefore, in order to learn more about the structure and in particular about the order along the *z* direction we remeasured some of the Bragg peaks with the D7 instrument using **XYZ** linear polarization analysis. This technique allows the nuclear and magnetic components to be separated. Inspection of the single crystal peak intensity in the different polarization channels provides a lot of information. The most important information is given by the spin flip components, which do not contain any nuclear intensity, but are purely magnetic and spin incoherent. Thus it is possible to identify whether a reflection is purely nuclear or purely magnetic or a mixture. It should be noted that the **X**,**Y**, **Z** coordinate system for the polarization is different from *a*,*b*,*c* or *xyz* coordinate system of the crystal. The **X** and **Y** polarization directions lie in the horizontal scattering plane but do not coincide with the crystal axes. The **Z** polarization direction is vertical and can provide important information. By orienting the $SrYb_2O_4$ crystal so that the *c*-axis coincides with the vertical **z** axis for the polarization, only magnetic components along the *c* axis (and nuclear intensity), are observed in the *NSF* channel of **Z** polarization, allowing us to establish whether the *Gz* mode exists. Tables (6.4 and 6.5) list the intensities for several peaks observed in the various polarization channels.

Figure 6.16 shows an example of one Bragg reflection measured on D7. The results indicate that the $(2, 2, 0)$ reflection has strong nuclear intensity and a weak magnetic contribution. According to Table 6.3, this situation happens when the two Ybs carry different moment and when the modes *Cx*, *Cy*, *Cz* are absent. The conclusions deduced from the D7 measurement are listed in the last column of Tables 6.4 and 6.5. They are consistent with the E4 measurement and provide useful additional information. The $(0, 1, 0)$ and $(0, 3, 0)$ reflections are particularly useful, they have no nuclear intensity as revealed by zero counts in some or all of the NSF channels. The *Gz* mode is expected to contribute to these peaks and would appear in the **Z**'nsf channel. The fact that there is no intensity in this channel proves that the *Gz* is absent. The strong SF intensities of the $(0, 2, 0)$ peak suggests that the *Ax* mode is present, whilst the weak SF intensities of the $(0, 0, 1)$ peak suggests that the *Ay*, *Az* modes are absent . We therefore exclude the *Gz* mode and conclude that only *Gy* and *Ax* exist: $G(+ - -+)$, $A(+ - +-)$. Altogether these results show that the magnetic moments line mostly in the *ab*-plane and the two inequivalent Yb ions carry different sized moments. Using the results of the

Table 6.4: Polarization analysis of specific Bragg peaks performed on D7. The maximum and integrated intensity is listed for six polarization channels (**Z**sf, **Z'**nsf, **X**nsf, **X'**sf, **Y**nsf, **Y'**sf). Note that the (**XYZ**) coordinate system used for the polarization (described in the experimental details section) is not the same as (xyz) the mode or crystal coordinate system. **Z** is the only axis shared by both coordinate systems.

Bragg Peak	Pol.	Max. Inten	Integrated Intensity	Remarks
$(1,0,0)$	**Z** nsf	0.4	0.1587(498)	nuclear
$\alpha = 76$	**Z'** sf	0.25	0.1128(372)	magnetic
	X nsf	0.38	0.1866(445)	$Ay = 0$
	X' sf	0.25	0.1364(372)	$Az = 0$
	Y nsf	0.55	0.2381(569)	$Cy = 0$
	Y' sf	0.15	0.0406(276)	$Cz = 0$
$(2,1,0)$	**Z** nsf	0	0.0000(19)	no nuclear
$\alpha = 58$	**Z'** sf	1.5	2.3644(1105)	weak magnetic
	X nsf	1.1	2.0463(1122)	$Gz = 0$
	X' sf	0.2	0.4477(641)	2 Ybs have different
	Y nsf	0.2	0.4805(687)	moments
	Y' sf	1.0	1.9315(1072)	
$(1,4,0)$	**Z** nsf	11.5	46.0703(8763)	strong nuclear
$\alpha = 31$	**Z'** sf	7	29.9375(5944)	magnetic
	X nsf	14	56.7690(1.0544)	
	X' sf	4	19.6355(4272)	
	Y nsf	15	67.1332(1.2407)	
	Y' sf	3	8.7767(2561)	
$(1,3,0)$	**Z** nsf	12	34.4146(5951)	strong nuclear
$\alpha = 48$	**Z'** sf	9	26.2212(4629)	magnetic
	X nsf	16	51.1223(8503)	2 Ybs have different
	X' sf	3	9.1084(2204)	moments
	Y nsf	15	44.5538(7437)	Ax and/or $Az \neq 0$
	Y'sf	5	16.3145(3242)	
$(0,2,0)$	**Z** nsf	12	19.8527(1.0952)	strong nuclear
$\alpha = 66$	**Z'** sf	20	31.0206(1.6531)	strong magnetic
	X nsf	30	47.4367(2.5034)	Ax and/or $Az \neq 0$
	X' sf	4	3.2059(2644)	
	Y nsf	15	23.7249(1.2982)	
	Y' sf	15	26.5902(1.4325)	

representation analysis done above, it is possible to start the detailed refinement of the powder-diffraction data. The subtraction of the high and low temperature E9 patterns did not give enough statistics to define and refine the magnetic structure. Nevertheless by fitting the low temperature pattern to both phases (nuclear and magnetic), the

Table 6.5: (Continuation Table 6.4). Polarization analysis of specific Bragg peaks performed on D7. The maximum and integrated intensity is listed for six polarization channels (**Z**sf, **Z**'nsf, **X**nsf,**X**'sf, **Y**nsf, **Y**'sf). Note that the **XYZ** coordinate system used for the polarization (described in the experimental details section) is not the same as the (xyz) mode or crystal coordinate system. **Z** is the only axis shared by both coordinate systems.

Bragg Peak	Pol.	Max. Inten	Integrated Intensity	Remarks
$(0,1,0)$	**Z** nsf	0	0.0000(7398)	No nuclear
$\alpha = 78$	**Z**' sf	0.25	0.2131(1601)	small magnetic
	X nsf	0	0.0000(7581)	$Gz \approx 0$
	X' sf	0.29	0.1983(1297)	
	Y nsf	0.31	0.2091(7711)	
	Y' sf	0	0.0000(1149)	
$(0,3,0)$	**Z** nsf	0	0	No nuclear
$\alpha =$	**Z**' sf	0	0	
	X nsf	0	0	$Gx = 0$
	X' sf	0	0	$Gz = 0$
	Y nsf	0	0	
	Y' sf	0	0	
$(1,1,0)$	**Z** nsf	1.5	0.1649(255)	weak nuclear
$\alpha = 71$	**Z**' sf	6.5	9.7837(2157)	magnetic
	X nsf	8	9.7516(2182)	Gy
	X' sf	1.7	0.4118(597)	Ax
	Y nsf	2	0.8143(646)	2 Ybs have different
	Y' sf	7.5	9.1746(2087)	moments
$(2,2,0)$	**Z** nsf	62	91.0183(1.8952)	Strong nuclear
$\alpha = 51$	**Z**' sf	3	4.7479(1996)	magnetic
	X nsf	62	95.3523(1.9822)	
	X' sf	3	1.3870(1822)	
	Y nsf	62	93.4717(1.9322)	
	Y' sf	2	3.3504(1933)	

data were refined to give the magnetic structure presented in Table 6.6. The free ion magnetic moment for Yb^{3+} is $4\mu_B$ ($g_J\mu_B J$), whereas the refinement of the magnetic structure shows that the ordered moment is reduced from this value giving $3.31\mu_B$ for Yb1 and $1.85\mu_B$ for Yb2. The fit is rather good, giving a R$-$factor of 3.16, RF$-$factor of 2.60 and χ^2 of 4.47 (see Figure 6.9). The D7 powder diffraction data can be also fitted. It is possible to separate magnetic, nuclear and incoherent components by setting the Schärpf angle $\alpha = 90°$ and using Equations 6.2. See Figure 6.17. The D7 30 mK nuclear pattern was fitted to the crystal structure model and a total of 24 reflections were refined. The powder pattern and the results of the refinement are shown in Figure 6.18.
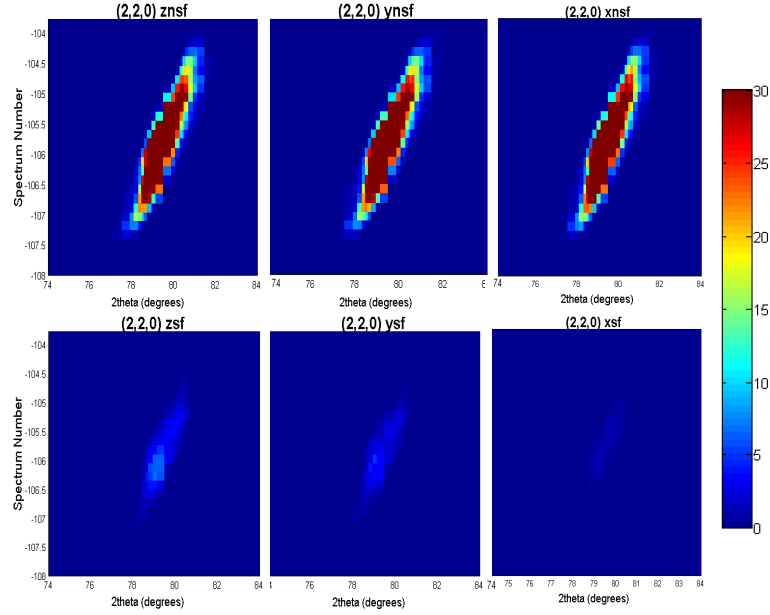
Figure 6.16: $(2,2,0)$, D7, single crystal diffraction for six polarization channels. The results indicate that the $(2,2,0)$ reflection has strong nuclear intensity and a weak magnetic contribution.
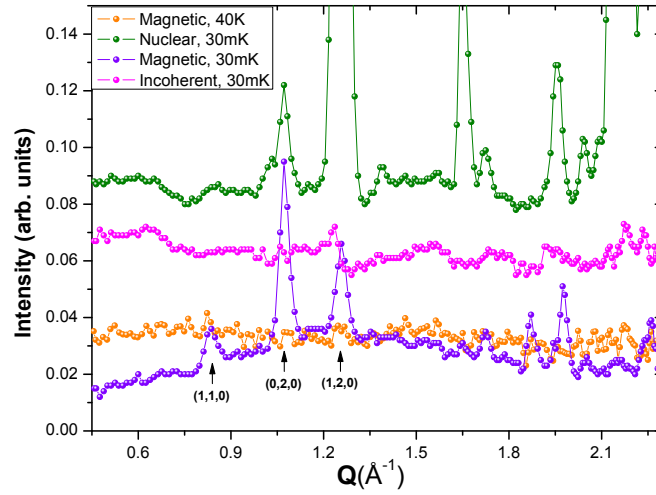
Figure 6.17: Powder diffraction patterns measured on D7 using different polarizations. The nuclear, magnetic and incoherent components have been separated using Equations 6.2.

A pseudo−Voigt peak profile was used and only the parameters from the instrument were fitted. The atomic positions and lattice parameters were fixed to the E9 values. The fitted half-width parameters of the peak profile were: $U = 3.0(7)$, $V = -4.0(9)$, $W = 4.4(7)$. The best refinement was: $R_p = 5.25$, $R_{wp} = 7.03$, $R_{exp} = 6.48$, $\chi^2 = 1.18$

Table 6.6: Results of crystal and magnetic structure refinement of E9 data at T=40 mK. For the magnetic structure $\Gamma_4(AxGy)$ was assumed and $\mu_z = 0$.

Name	x	y	B (Å^2)
Sr	0.7547(3)	0.6512(3)	0.67(5)
Yb1	0.4218(2)	0.1090(1)	0.54(3)
Yb2	0.4265(2)	0.6123(1)	0.53(3)
O1	0.2107(4)	0.1725(3)	0.46(6)
O2	0.1246(4)	0.4800(3)	0.83(6)
O3	0.5180(4)	0.7833(3)	0.65(6)
O4	0.4220(4)	0.4229(3)	0.84(6)
Cell parameters :	$a = 9.97576(7)$ Å,	$b = 11.75466(7)$ Å,	$c = 3.35259(2)$ Å
Name	$\mu_x(\mu_B)$	$\mu_y(\mu_B)$	$\mu(\mu_B)$
Yb11	3.0(2)	−1.4(4)	3.3(3)
Yb12	−3.0(2)	1.4(4)	3.3(3)
Yb13	−3.0(2)	−1.4(4)	3.3(3)
Yb14	3.0(2)	1.4(4)	3.3(3)
Yb21	0.5(2)	−1.8(4)	1.8(4)
Yb22	−0.5(2)	1.8(4)	1.8(4)
Yb23	−0.5(2)	−1.8(4)	1.8(4)
Yb24	0.5(2)	1.8(4)	1.8(4)
R:3.16, RF:2.6	$\chi^2 : 4.47$		

(see Figure 6.18a). The magnetic component of the D7 powder pattern was then fitted
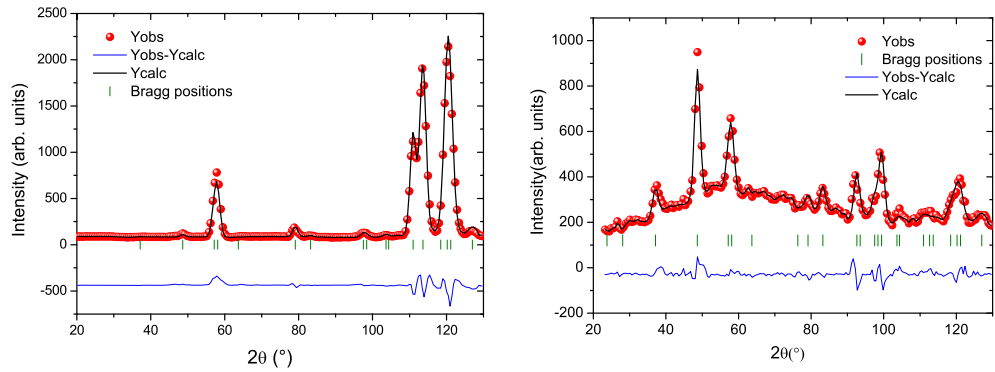
Figure 6.18: (left): Rietveld refinement of the nuclear component of the D7 powder pattern at 30 mK. (right): Refinement of the magnetic component.

assuming the $\Gamma_4(AxGy)$ irreducible representation. The atomic positions were fixed to the E9 values while the lattice parameters and peak profile were fixed to the values from the fit of the D7 nuclear component. The resulting magnetic refinement is given in

Table 6.7: Results of the magnetic structure refinement assuming $\Gamma_4(AxGy)$ of the magnetic component of the D7 diffraction pattern, μ_z=0.

Name	$\mu_x(\mu_B)$	$\mu_y(\mu_B)$	$\mu(\mu_B)$
Yb11	3.37(5)	−1.9(1)	3.90(8)
Yb12	−3.37(5)	1.9(1)	3.90(8)
Yb13	−3.37(5)	−1.9(1)	3.90(8)
Yb14	3.37(5)	1.9(1)	3.90(8)
Yb21	0.81(5)	−2.0(1)	2.2(1)
Yb22	−0.81(5)	2.0(1)	2.2(1)
Yb23	−0.81(5)	−2.0(1)	2.2(1)
Yb24	0.81(5)	2.0(1)	2.2(1)
$R_p = 3.53$,	R_{exp}=5.18,	R_{exp}=5.76	
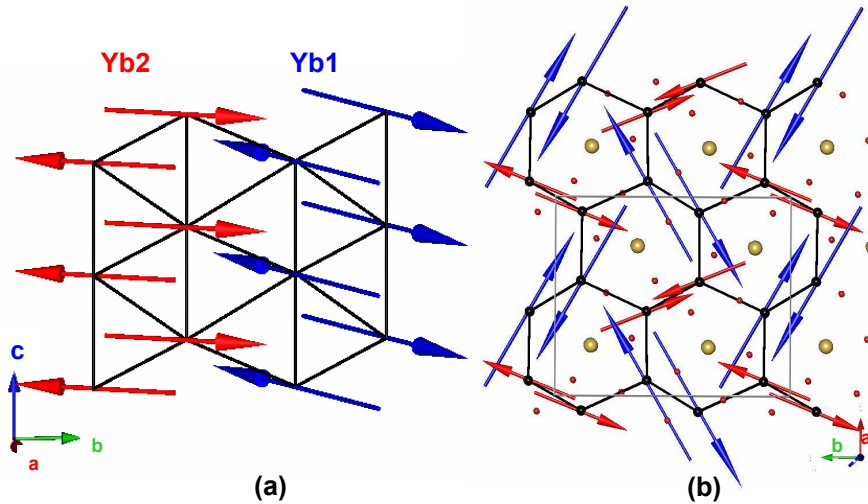
Figure 6.19: Sketch of magnetic structure, showing the two Yb ions (Yb1 blue, Yb2 red). (a)zig-zag chains of Yb1 and Yb2. (b) projection onto the a-b plane.

Table 6.7 and the fitted powder pattern is shown in Fig. 6.18(right). An excellent fit is achieved. The magnetic moments of the two Yb ions are quite different in the a direction but are similar along b. The component moment along the z axis was set to be zero. The total ordered moment for the two Ybs are different, 3.90(8)μ_B for Yb1 and 2.2(1)μ_B for Yb2. They are both reduced from the fully ordered value of $4\mu_B$, that could be due to the single ion anisotropy. The R-factors are: $R_p = 3.53$, R_{exp}=5.18 and R_{exp}=5.76. Figure 6.19 shows the sketch of the magnetic structure of SrYb$_2$O$_4$. The spins within each chain are collinear, aligning ferromagnetically along the 'legs' and antiferromagnetically along the 'zig-zags'. While the spins of different chains are canted with respect to each

other in an angle close to 90°. It is possible to swap the moment's sites, exchanging Yb1 with Yb2 in the refinement parameters, this calculates less intensity for some reflections like $(2, 1, 0)$ and $(1, 1, 0)$. Using the moment values listed in Table 6.7, gives the best refinement with the R-factors: R_p =3.78, R_{wp}=5.47 and R_{exp}=24.4 (see Figure 6.20). The magnetic structure determined from D7 data was used to simulate the diffraction
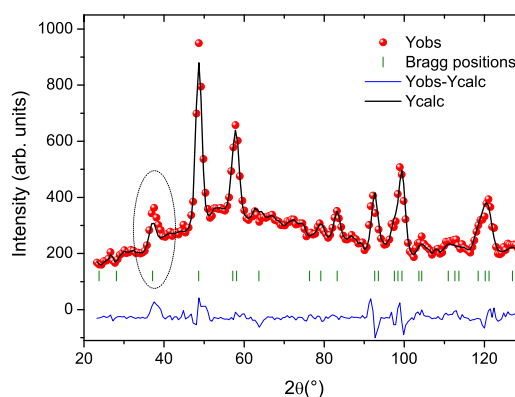
Figure 6.20: D7 pattern and refinement, 30 mK with Yb1 and Yb2 swapped. The Yb moment value of Table 6.7 are used. There is a noticeable difference for $(1, 1, 0)$ reflection.

patterns obtained on E9, E6 and E4. As can be seen in Figure 6.21, the D7 parameters
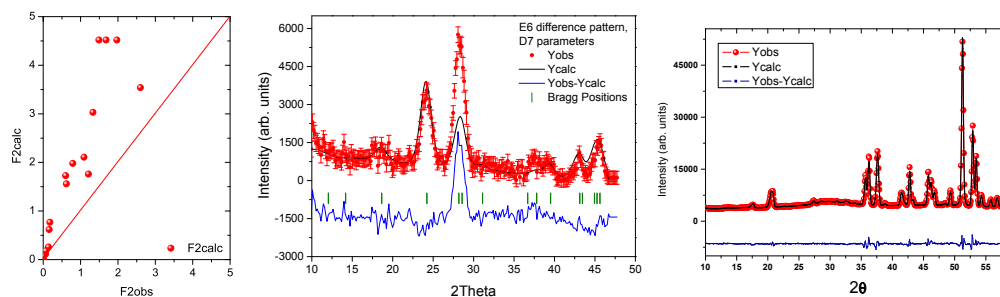
Figure 6.21: (left) Observed vs. calculated integrated magnetic intensity of $SrYb_2O_4$ for E4 data at T=40 mK fitted with D7 parameters. RF2−factor:124, RF2w−factor:133. RF−factor:55.2, χ^2(Intens):0.336 × 10^5. (middle) E6 difference pattern fitted using D7 model. The magnetic R-factor was 32.9. (right) E9 pattern, 40 mK, fitted using D7 parameters. R−Bragg= 11.52.

do not fit the E6 and E4 data perfectly. The E4 data are highly contaminated with higher order $(\lambda/2)$ scattering, as well as the extinction and multiple scattering leading to inaccurate intensities (Fig. 6.21(left)). The E6 data were collected on a powder and therefore did not suffer from extinction or multiple scattering effects. Nevertheless the E6 difference pattern does not give correct magnetic intensities for reflections that have

a big nuclear contribution, such as $(2, 0, 0)$ $(2\theta{=}28.17^\circ)$, see Figure 6.21(middle). The fit of the E9 low temperature data was satisfactory, the result of the refinement of both the nuclear and magnetic phases can be seen in Figure 6.21(right). However the E9 data which cover a large wavevector range emphasize the nuclear peaks while the counting statistics on the magnetic peaks is poor. Therefore we consider the magnetic structure obtained by the refinement of D7 powder data as the most accurate since there was: (1) no $\lambda/2$ contamination, (2) no extinction problems as it was a powder and (3) the nuclear component was separated from the magnetic signal by the polarization analysis.

6.4 Phase Diagram

A set of heat capacity and magnetocaloric effect measurements as a function of temperature and magnetic field, respectively have been performed on SrYb$_2$O$_4$ in order to map out the phase diagram of this compound. The magnetic field was applied along the three crystallographic directions. Heat capacity at low temperatures shows two anomalies, the lowest temperature one is a lambda-like transition, related to the onset of AFM order. This anomaly is shifted towards lower temperatures when applying a magnetic field, see Figure 6.22(left). The second anomaly is Schottky-type and appears around 2.5 K in zero field. It moves towards higher temperatures when applying a magnetic field, see Figures 6.22, 6.25. This anomaly is related to short range magnetic correlations, due to a splitting of the ground state doublet and it will be discussed further in the next chapter. The derivative of the magnetization with respect to temperature was determined using
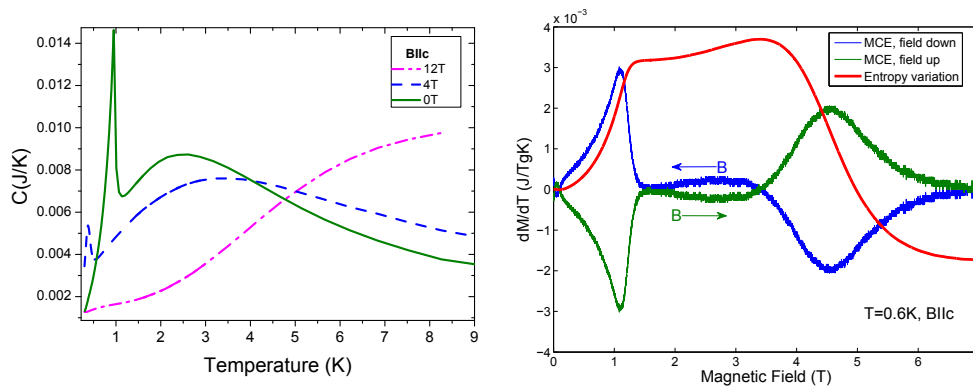
Figure 6.22: (left) Heat capacity for various fields applied along the c-axis. (right) Magneto caloric effect at T=0.6 K for field applied along the c-axis. The relative change in entropy is overplotted and given in arbitrary units.

the relation $(\delta Q/\delta B)/T = -(\partial M/\partial T)|_B$, where δQ is the amount of heat generated or

absorbed by the sample for a field change δB due to the magnetocaloric effect. Figure 6.22(right) shows the magnetocaloric effect for a temperature of T=0.6 K. The magnetocaloric effect is the heating or cooling of the material when there is a magnetic field variation. It is characterized by the temperature change in an adiabatic process and by the entropy change in an isothermal process [130, 131]. The MCE is most suitable to extract phase boundaries at constant magnetic field, while the heat capacity is the ideal choice to detect phase transitions at constant temperatures. AFM transitions are associated with an inverse magnetocaloric effect for positive magnetic field changes. Figure 6.22(right) shows the adiabatic temperature changes for both increasing and decreasing magnetic field. At T=0.6 K two transitions are observed, the first at $\approx$ 1.1T is a second order transition while the second at $\approx$ 4.5T is broader and could be defined as a crossover. The crossover might be linked to close proximity in phase space to a critical point that can be reached only by the application of some other external parameter such as pressure. The integral of $(\partial M/\partial T)|_B$ over field gives entropy, this is plotted in Fig. 6.22(right) in red. For the lower field transition, there is an abrupt change of the slope of the entropy with field. This suggests a second order transition from a more ordered state to a less order one, in this case from the 3D AFM ordered phase to the paramagnetic phase. The higher field anomaly has smoother entropy change and since the entropy decreases, it could be associated with an increase in order, e.g. the magnetic moments start to cant along the field direction. Figure 6.23 shows the variation of temperature when changing the magnetic field along the three different crystallographic directions. Along the c-axis two critical fields can be seen below 7 T. The lowest critical field indicates the transition from an ordered state to a more disordered one, while, the second represents an increase of order, as explained in Figure 6.22(right). For the a-axis the low field transition is absent but it has a transition at 4.5 T that is similar to the transition found for the c-axis. Another crossover happens around 8 T, which also implies a change to a more ordered state. Along the b-axis the features are different, two critical fields at $\approx 1.5\,T$ and $\approx 6\,T$ are detected: where the one at lower fields indicates a transition from an ordered state to a more disordered one.

Magnetization measurements can also be used to map out the phase diagram. Figure 6.24 shows the magnetization at 2 K along the three crystallographic axis. At 14 T the magnetic field has not saturated the sample to its full magnetization value of $M_s = g_J \mu_B J = 4\mu_B$ along any of the axes. The magnetization for $B \parallel c$ is much greater than for $B \parallel a$ or b indicating that c is the easy axis at 2 K. The magnetization along c appears to reach a half magnetization plateau of $2.0\mu_B \approx M_s/2$ at a field
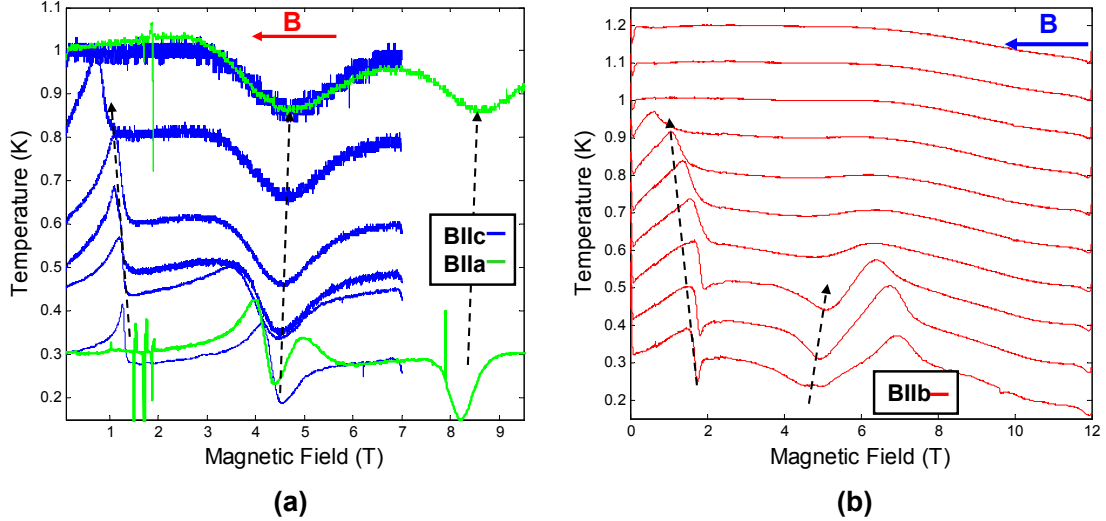
Figure 6.23: (a)Overplot of the magnetocaloric effect for different temperatures with the field applied along the *c*-axis (blue) and the *a*-axis (green), the y-axis indicates the temperature. Each scan has a different initial temperature and its temperature variation with decreasing field is shown. (b)Overplot of MCE for different temperatures with the field applied along the *b*-axis.

of H=10 T. The magnetization along all directions is highly non-linear and has multiple crossing points. The derivative of the magnetization along the *c*-axis is shown as an inset in Figure 6.24 at least 3 changes in the magnetization slope can be detected. These changes occur at magnetizations of $M_s/10$, $M_s/4$, $3M_s/8$ and $M_s/2$ and fields of 1.5 T, 4 T, 8.2 T and 11 T respectively. This is in agreement with the MCE which shows a phase transition around H=1 T and a crossover point around H=4 T. It is expected that these crossovers and transitions will appear sharper in the magnetization at lower temperatures. Such changes in the magnetization slope have been reported before for SrL$_2$O$_4$ with L=Ho, Dy and Er. Karunadasa *et al.* [104] ascribed this behavior to the presence of metamagnetism. The term metamagnetism can be applied to qualitatively different physical phenomena. It can describe changes from ordered antiferromagnetic states at low field to ferromagnetically polarized states at high field via spin-flip or spin-flop processes [132]. Metamagnetic behavior is common in highly anisotropic magnetic systems such as DyPO$_4$, FeCO$_3$, DyAl$_5$O$_{12}$ and Sr$_3$Ru$_2$O$_7$ [133, 132]. In Figure 6.25, the phase diagram as a function of temperature and magnetic field applied along the *c*-axis is shown. The color scale corresponds to the heat capacity in units of J/K. The vertical solid arrow represents the MCE measurement at T=0.6 K, shown in Figure 6.22. The red dots represent the critical fields extracted from this measurement. MCE scans with the magnetic field along the *c*-axis were performed at a total of 7 temperatures. A
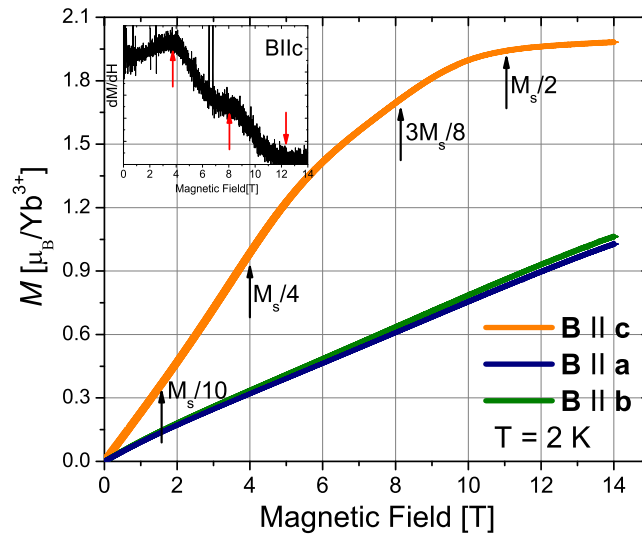
Figure 6.24: Magnetization as a function of magnetic field applied along the three different crystallographic directions measured in the PPMS at 2 K. The inset shows the derivative of the magnetization along the *c*-axis, many crossover regions were found.
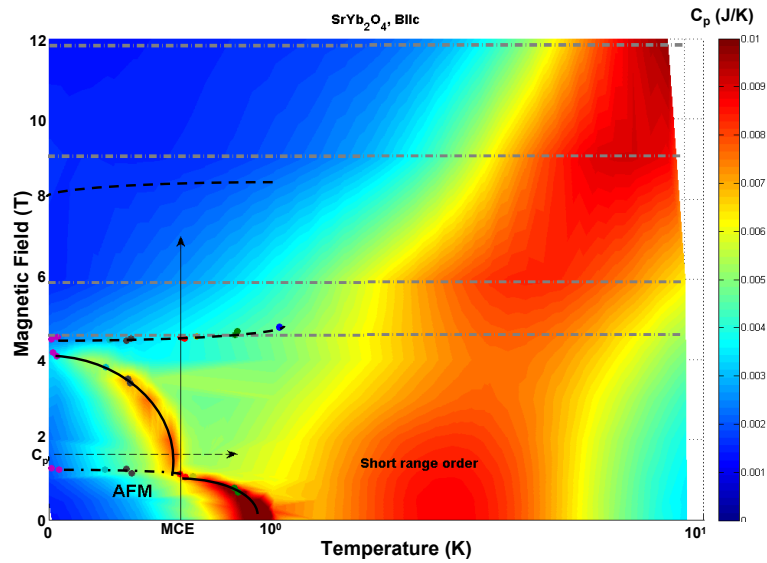
Figure 6.25: Phase diagram with magnetic field along the *c*-axis. The colors indicate the heat capacity in units of J/T. The points indicate the critical fields extracted from magnetocaloric effect measurements. Black solid lines show second order phase transitions. Dash-dot black lines indicate the transition from the AFM phase to a less ordered one. Dashed black lines show metamagnetic crossovers. Above H=4.5 T there are just three heat capacity scans at: H= 6 T, 9 T and 12 T, the colors between them result from the interpolation of the data. Below H=4.5 T the data were collected every H=0.2 T. The temperature axis is in logarithmic scale.

similar procedure has been carried out for magnetic field along the *a* and *b* directions. The horizontal dashed arrow in Figure 6.25 represents the heat capacity measurement at 1.7 T. The magnetic phase diagram of SrYb$_2$O$_4$ is very rich and complex as shown
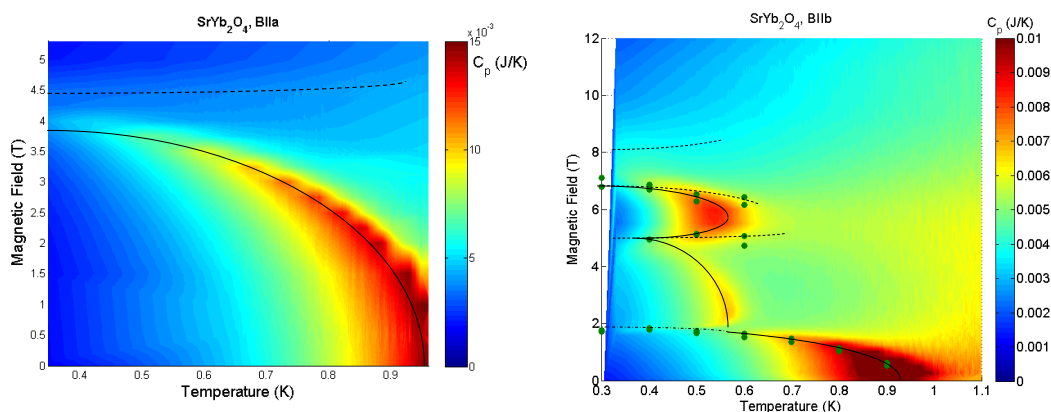
Figure 6.26: Phase diagram with magnetic field along *a*-axis (left) and *b*-axis (right). The colors indicate the heat capacity in units of J/T. The points are the critical fields extracted from the MCE. Black solid lines represent second order transitions detected using heat capacity measurements and dashed black lines represent metamagnetic crossovers.

in Figures 6.25 and 6.26. The phase diagram is clearly different along the *a*, *b* and *c* directions suggesting that the magnetic moments are very anisotropic. At low temperatures a total of 4 magnetic phases were detected with the field along the *a*-axis, 5 along the *b*-axis and 4 along the *c*-axis. In Figures 6.25, 6.26 black solid lines show the phase boundaries of the second order transitions. Dash-dot black lines show the second order transition from the AFM phase to a less ordered one. Dashed black lines show metamagnetic crossovers. An exhaustive neutron diffraction study at different fields and temperatures will be necessary to understand the magnetic behavior in these phases.

6.5 Conclusions

The first single crystals of the insulating and frustrated rare earth antiferromagnet SrYb$_2$O$_4$ have been grown and have been used to perform a thorough investigation of the crystal and magnetic structure of this compound and the magnetic phase diagram as a function of field and temperature. A series of powder and single crystal diffraction experiments were performed. Several issues made the analysis of the data challenging, such as higher order scattering and extinction. In the case of the unpolarized-single crystal measurements on E4, substantial higher order scattering was present, which gave intensity to forbidden reflections. For this reason the refinement of E4 data was not suc-

cessful. The possibility of a structural distortion to a lower symmetry space group was ruled out because these reflections vanished when using a highly efficient Be filter on the V2-flex cold triple axis spectrometer. A further test experiment on the high resolution X-ray diffractometer MAGS at BESSY reveal no peak splitting which indicates that no lowering of the symmetry, such as to monoclinic or triclinic occurs. Therefore, all the data were analyzed assuming the *Pnam* space group. All atoms are in the Wyckoff position $4c$ $(x, y, 1/4)$. The lattice parameters do not change significantly when changing temperature. At base temperature ($40\,\mathrm{mK}$) the lattice parameters are: $a = 9.97576(7)\,\text{Å}$, $b = 11.75466(7)\,\text{Å}$, $c = 3.35259(2)\,\text{Å}$. The E9 results give the most accurate values of the atomic positions due to the large wavevector transfer range. The positions were listed in table 6.2.

The discovery of long-range magnetic order on $SrYb_2O_4$ at T=0.92 K was made here by heat capacity and neutron diffraction. The magnetic structure is antiferromagnetic with ordering wavevector $\mathbf{k} = (0, 0, 0)$, meaning that the magnetic peaks coincide with the nuclear ones. This makes it difficult to separate nuclear and magnetic components. Because of this, additional polarized single crystal and powder diffraction measurements were performed on D7, which allowed the magnetic and nuclear components to be separated. The magnetic component of the D7 powder data was then refined assuming a magnetic structure model obtained by representation analysis. The best solution is shown in table 6.7. The magnetic moments of both Yb ions lie in the *ab*-plane, while the component along the *c*-axis is negligible. The two inequivalent Yb ions have different moment sizes and directions. The moment along *a* of Yb2 is smaller than the component for Yb1, but along *b* they are almost equal. The total ordered moment for Yb1 is $3.88(8)\mu_B$ and for Yb2: $2.2(1)\mu_B$. Both moments are reduced from the fully ordered moment of Yb^{3+} $(4\mu_B)$, which may be a consequence of the crystal field or magnetic frustration. The spins within each chain are collinear, aligning ferromagnetically along the 'legs' and antiferromagnetically along the 'zig-zags'. While the spins of different chains are canted with respect to each other in an angle close to $90°$.

The magnetic structure of $SrYb_2O_4$ is different from the magnetic structure of the isostructural compound $SrEr_2O_4$ [115]. In that case, the moments point along the *c*-axis, but only one of the two Er sites carries a sizable magnetic moment. Two types of magnetic ordering co-exist in $SrEr_2O_4$: one is a fully ordered 3D AFM phase, which appears below a distinct transition temperature, the other is short range ordered displaying a 2D character, with no sharp transition. T. Hayes *et al.* [134] suggests that only one of the Er ions is contributing to each phase and the interaction between the two sites is expected to be very small. For $SrDy_2O_4$ a 2D short range ordered phase was

observed analogous to the SrEr$_2$O$_4$ with field induced phase transitions [134].

A rich magnetic phase diagram was discovered for SrYb$_2$O$_4$ as a function of magnetic field and temperature; a number of transitions and crossovers were found implying a series of metamagnetic phases and showing how anisotropic the material is. These results inspire a deeper study. Neutron diffraction experiments could be performed in the future to explore the different magnetic phases by applying magnetic fields along the three different crystallographic directions and varying temperature. Diffuse magnetic scattering was measured using D7 and it was present in all measurements below T=40 K. This indicates the presence of short-range magnetic order, and it is also visible as a broad peak around 2.5 K in the heat capacity (Figure 6.2). Diffuse scattering was also observed at low temperature in SrDy$_2$O$_4$ and SrEr$_2$O$_4$ near the $(0, 2, 0)$ reflection, which disappears above T=5 K for SrDy$_2$O$_4$ and 20 K for SrEr$_2$O$_4$. In the case of SrHo$_2$O$_4$ two magnetic transitions were found, below T=40 K a broad peak appears due to short-range magnetic ordering [104]. The nature of the collective magnetic excitations in SrYb$_2$O$_4$ as well as the higher energy crystal field levels will be the subject of the next chapter.

7 Magnetic Excitations of SrYb$_2$O$_4$

7.1 Introduction

In the previous chapter the crystal and magnetic structure that arises due to interactions between the Yb^{3+} ions in SrYb$_2$O$_4$ were investigated. In this chapter the effect of the local crystal field on the Yb^{3+} ions and its magnetic properties will be studied. Yb^{3+} is a rare earth ion with 13 electrons and has the electronic configuration: $[Xe]4f^{13}6s^2$, with a total spin of $S = 1/2$ and orbital angular momentum $L = 3$. The large nuclear charge acting on the inner unfilled $4f$ shell of electrons in rare earth ions enhances the spin orbit coupling that competes with the crystal field (CF) splitting. This competition determines the degree of quenching and the magnitude of the magnetic anisotropy. Yb^{3+} is largely unquenched because the crystal field is weak and the large spin-orbit coupling ensures that the $4f$ cloud is rigidly coupled to the spin resulting in a total angular momentum J [2, 135]. Yb^{3+} has an odd number of electrons, so according to the Kramer's theorem all the energy states must have even degeneracy. The effect of a low symmetry crystal field is to reduce the degeneracy to doublets. The doublet degeneracy can be lifted by applying a magnetic field. The magnetic character of the lowest doublet determines the magnetic character of the ion [135]. The starting point in this chapter is to consider that the magnetic Yb^{3+} ions are essentially free except for the interaction with the surrounding atoms through the crystalline electric field. This field is due to the surrounding ions which in this case form a distorted oxygen octahedron (see Fig 7.1). The ground manifold degeneracy is partly lifted by the operation of the Stark effect of the crystalline electric field. Hund's rules hold for the ground manifold, therefore $J = S + L = 7/2$ and since the system has a single hole the configuration of Russell-Saunders coupling is a good approximation. The result is that L, S, and J will be good quantum numbers. The spin-orbit interaction gives a large energy difference between the two lowest energy manifolds, giving a ground state with $J = 7/2$, and an excited state with $J = 5/2$ separated by about $1\,\text{eV}$ [136]. The effect of the CF is to split the $(2J + 1)$-fold degeneracy of the ground state [137]. The levels consist of $(J + 1/2)$ doublets $((7/2 + 1/2) = 4$ doublets). The wavefunctions of the Kramer's doublets are

linear combinations of states $|\pm m_J\rangle$ that make up the J-manifold. The actual energy levels and relative admixtures of the states depend of course on the size of the various parameters of the crystal field [138]. The monoclinic site symmetry splits the quartet Γ8 [139] into two doublets (see Figure 7.1). The crystal field Hamiltonian as explained
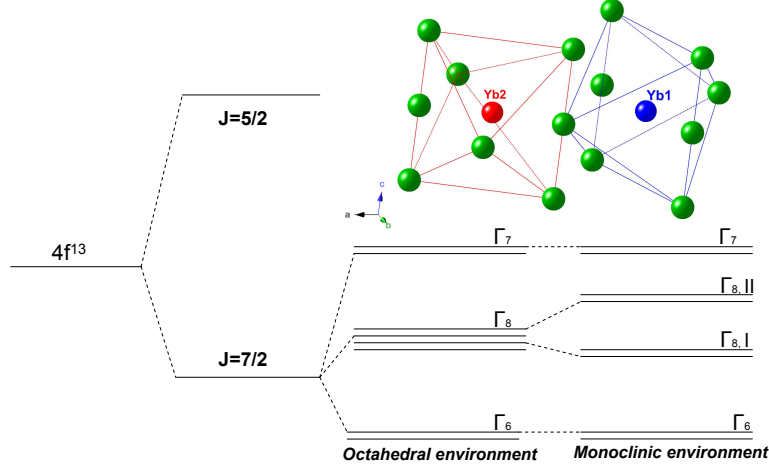
Figure 7.1: Level scheme for Yb^{3+} in Octahedral and monoclinic site symmetry. YbO$_6$ octahedra are also shown, the circles in green represent the oxygens, the blue circle is Yb1 and the red is Yb2.

in Chapter 2 can be written in terms of the extended Stevens operators,

$$\mathcal{H}_{CF} = \sum_{kq} B_k^q O_k^q (J_x, J_y, J_z), \tag{7.1}$$

where B_k^q are the CF parameters and O_k^q the operator equivalents. As explained in the previous chapter the site symmetry for both inequivalent Yb ions is monoclinic, C$_{1h}$, and is characterized by a single mirror plane perpendicular to the c-axis. This local environment allows parameters B_k^q with $q = \pm 0, \pm 2, \pm 3, \pm 4, \pm 6$. In total 19 orientation dependent parameters (real and imaginary/negative q) would be needed to express the single ion Hamiltonian. These variables can be obtained by fitting experimental data such as inelastic neutron scattering. While the two Yb^{3+} ions in this compound share the monoclinic c-axis the size and orientation in the $a - b$ plane of the distortion that they experience is potentially different. This in turn makes it difficult to select a single axis system and therefore to obtain a set of CF parameters that determine the single ion anisotropy for both sites. This makes the understanding of the magnetic properties of the system and the analysis of single crystal data especially difficult. The principal experimental method for investigating CF is inelastic neutron scattering (INS). In this

chapter we show the INS data of $SrYb_2O_4$ are shown and different models that fit them are discussed. DC susceptibility and heat capacity data will also be shown and compared with the different models. In order to analyze the data shown here a main question arises: what is the crystal field experienced by the Yb ions in this material and how does it split the $J = 7/2$ ground state manifold? It is not possible to fit 19 CF parameters without reliable starting parameters, this is why two different ways of obtaining the starting parameters were used. The first one is the point charge calculation and the second is a simulated annealing algorithm. In the follow sections both will be explained. Different parameters have been found and in order to compare them and determine whether they are equivalent within a rotation, rotational invariants will be calculated [140, 141]:

$$(S_k)^2 = \frac{1}{2k+1} \sum_q |B_k^q|^2 \,. \tag{7.2}$$

The quantities S_k measure the strength of the CF terms and are independent of the coordinate system used, making it a perfect tool for a systematic comparison between different CF parameters sets. This is necessary because solutions obtained from powder samples cannot determine the coordinate system.

In the literature it is common to find works since 1960's that analyze the CF of Yb^{3+} embedded in different host materials, such as doped optical inorganic materials and salts. Different site symmetries and host materials were tested and different applications for these materials were discovered such as infrared lasers, scintillator materials for neutron detection [142], and lately optical refrigeration [143]. The potential of Yb^{3+} for applications comes from the simple electronic structure that prevents the existence of several relaxation processes that influence the dynamics of populations of the energy levels.

Knowledge of the ground state multiplet of the Yb ions will help in the understanding of the magnetic correlations in this material and the magnetic interactions of Yb^{3+} ions with their neighbors. The magnetic interactions in insulators can be due to the very weak and anisotropic dipole-dipole interaction, which for $SrYb_2O_4$ is expected to be about $0.02\,\mathrm{meV}$ and/or superexchange interactions via intermediate O^{2-} ions. There are two situations, the first where the CF is strong as compared with the magnetic interactions and the second when the magnetic interactions dominate the CF splitting energies. Interesting interplays take place between both interactions which results in bands of magnetic excitations and one or more magnetic phases [144, 105]. Yb^{3+} has almost fully occupied orbitals, because the $4f$ shell is full except for one electron. The CF is much stronger than the magnetic interactions. The low energy excitation mode

has only a small dispersion providing evidence of that, as will be shown later in this chapter.

In this chapter static magnetic susceptibility, specific heat and inelastic neutron scattering data will be shown. In order to understand the crystal field in SrYb$_2$O$_4$, powder inelastic neutron scattering data are fitted using programs as FOCUS [145] and CF_fit_Yb [146]. The initial parameters for the fits have been found in two ways; firstly by calculating the point charge using the software package McPhase [147] and secondly by a simulated annealing algorithm [77]. A few models will be proposed and a comparison to the data will be shown.

7.2 Experimental Details

In this chapter both powder and single crystal data are shown and analyzed with the aim of finding the CF parameters that describe the single ion magnetism in this compound. The paramagnetic susceptibility was measured using a Quantum Design Physical Property Measurement System (PPMS) with a Vibrating Sample Magnetometer [25] at the Laboratory for Magnetic Measurements, HZB. The single crystal samples were grown as described in the previous chapter, oriented using the x-ray Laue technique and cut into pieces of $3 \, \text{mm}^3$ size. The data were collected in a magnetic field of 1T applied parallel to the a, b and c axes. These measurements were performed over two temperature ranges of T= 2 K-300 K and T= 310-980 K. For the low temperature measurements the sample was glued on a brass sample holder using GE varnish glue. For the high temperature measurements (T= 310 K-980 K) an oven set-up was utilized, the crystal was fixed on a zirconia sample stick using cement glue and wrapped in copper foil to minimize heat leaks. In order to account for the diamagnetic background produced by the sample holders and the glue, the temperature dependence of the empty sample stick was measured and subtracted from the data. Heat capacity measurements were done using two different instruments. The first was the PPMS and the second CM14.5T both at the laboratory for magnetic measurements at HZB. CM14.5T is a home made calorimeter [26] mounted on the copper base of a ^{3}He sorption cryostat inserted in a 14.5 T cryomagnet. The temperature can be regulated from $T = 0.28 \, \text{K}$ to 30 K. Single crystal samples of mass 3.07 mg oriented along the a and c axes and 1.87 mg aligned along the b-axis were used to measure the heat capacity at different magnetic fields (H= 0 T, 2 T, 4 T, 8 T, 10 T and 13 T). Higher temperature measurements were done on SrYb$_2$O$_4$ from T= 2 K to 400 K at zero field using the heat capacity option on the PPMS [25]. A strong lattice contribution sets in at $T = 12 \, \text{K}$. High energy inelastic neutron scattering was

performed using the Merlin time of flight spectrometer at ISIS. For this an Al container filled with 6.8667 g of $SrYb_2O_4$ powder was used as sample. Different incident energies were used (60.4 meV, 88.58 meV, 110 meV and 170 meV). Data were acquired at different temperatures: T= 8 K, 100 K, 240 K and 290 K using a closed cycle cryostat. Each data set was measured for 200 $\mu Ahrs$. This measurement was performed twice and the second time the sample absorbed humidity which unfortunately gave rise to additional hydrogen modes e.g. at 80 meV. The incident energies, chopper speeds and resolution at different energy transfers are given in Table 7.1.

Table 7.1: Incident energies, chopper speeds and expected resolution values at different transfer energies on Merlin experiment.

E_i (meV)	Chopper speed (Hz)	Resolution at E_t=0 meV	Resolution at E_t=32 meV	Resolution at E_t=70 meV
60.4	300	1.83	1.2	
88	250	3.51	2.40	1.61
110	250	4.63	3.43	2.35
170	350	6.83	5.61	4.47

When analyzing these data the background was subtracted by making cuts at constant wave vector and extrapolating the regions without magnetic signal. It is important to note that there is a large phonon contribution at low energies which merges with the quasielastic signal due to the cryostat. This makes it very difficult to analyze the low energy region (E< 10 meV) even after a background subtraction. Merlin data were converted to absolute intensity units by the standard Vanadium calibration. The IN5 time of flight spectrometer at ILL was used to investigate low energy transfer ranges, on 11.4 g of powder in a Cu can. Measurements were done at two temperatures, 0.1 K and 1 K which were achieved using a dilution fridge. The incident neutrons had wavelengths (energies) of 5 Å(3.27 meV), 5.5 Å(2.70 meV) and 6 Å(2.27 meV). Each data set was measured for 30 min at least twice. For all wavelengths, the choppers were spinning at 12000 rpm. The resolution was about 100 μeV at the elastic line. Vanadium normalization was carried out to obtain absolute intensity units. Single crystal neutron scattering was also performed using the IN5 spectrometer. A single crystal of mass 3.2 g was mounted on a copper sample stick and inserted inside a dilution fridge in order to reach low temperatures. The $(0, K, L)$ plane was in the horizontal scattering plane and data were collected along all directions (H, K, L) using the position sensitive detectors. The crystal was rotated about a vertical axis and a range of 100° was scanned in 1° steps

. The spectrum was measured at each angle for 40 min (370000 monitor counts) at a base temperature of T= 0.06 K and initial wavelength of $\lambda_0 = 5.5$ Å(2.70 meV), the chopper speed was 12000 rpm and the resolution at the elastic line was 75 μeV. Higher temperature scans were done in a similar way for wavelengths of 5 Å(3.27 meV) with a chopper speed of 6666 rpm and resolution of 100 μeV and 3 Å(9.09 meV) with a chopper speed of 8000 rpm giving a resolution at the elastic line of 500 μeV. Datasets at T= 1.6 K, 2 K, 20 K and 40 K were acquired. The datasets were combined using the Horace software to make a 4D dataset in $HKLE$, as discussed in Chapter 5 for the Sr$_3$Cr$_2$O$_8$ measurement on Merlin. Cuts and slices of specific directions and planes could then be extracted. Single crystal neutron scattering was also done using the IRIS indirect geometry chopper spectrometer at ISIS, in order to investigate the wavelength and energy dependence of the low energy magnetic dispersion. A single crystal of SrYb$_2$O$_4$ of mass 3.197 g was aligned with $(H, K, 0)$ in the horizontal scattering plane. The crystal was rotated about a vertical axis over a range of 98° with 2° steps and for some regions 1° steps. The spectrum was measured at each angle for 300 μAmps using a fixed final energy of 1.843 meV (6.662 Å) which provided energy transfers up to 1.9 meV. All spectra were measured in the AFM ordered phase at 50 mK. To reach this temperature a dilution fridge was used. These datasets were also recombined using the software Horace to make a 3D dataset in H, K, E.

7.3 Magnetic Susceptibility, Specific Heat and Magnetic Entropy

Figure 7.2 shows the DC susceptibility measured in the PPMS with a magnetic field of 1T applied along the three crystallographic axis a,b and c. In the low temperature region there is a gradual change in slope that suggests an onset of short range order (see Figure 7.2(left)). The susceptibility starts to curve downwards most visibly for the c direction, around T= 2.5 K. No sharp transition is observed as the AFM phase below T$_N = 0.9$ K as found in the previous chapter, while this measurement only went down to T= 2 K. The inverse susceptibility for a range of temperature from T= 2 K-970 K is shown in Figure 7.2(right). The temperature dependence of the inverse susceptibility in a magnetic field shows Curie behavior above T= 700 K. The results along the three crystallographic directions were fitted to the Curie-Weiss law, given in Chapter 4, and repeated here for convenience:

$$\chi_{obs} = \frac{C}{T - \theta}, \tag{7.3}$$
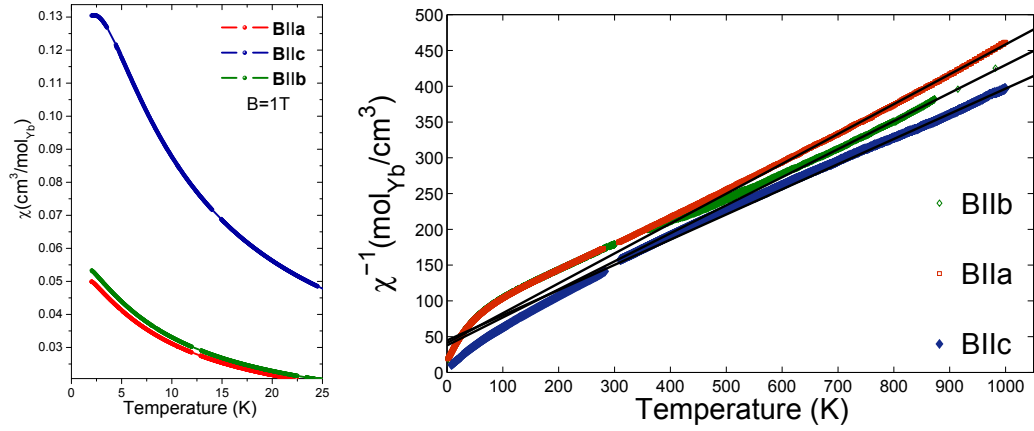
Figure 7.2: (left) DC Susceptibility measured with an applied magnetic field of $H = 1\,\text{T}$ along the three principle crystallographic directions. (right) Inverse susceptibility of $SrYb_2O_4$, the three black solid lines represent the fitting to the Curie-Weiss law for each direction.

where C is the Curie constant and θ is the Curie-Weiss temperature. In computing the susceptibility, the Van Vleck contribution due to the quantum mixing of excited CF states by the Zeeman interaction can be neglected as this is very small in the rare earth compounds [148, 3]. The results of the fitting are shown in Table 7.2 and as black lines in Figure 7.2(right).

Table 7.2: Results of the fit of the high temperature inverse susceptibility (temperature range 700-970 K) to the Curie-Weiss law. R^2 is the correlation coefficient for the fit. The powder inverse susceptibility was obtained by averaging the components along the three different directions.

B $\parallel$	$\theta(K)$	C(cm^3K/mol)	μ_{eff} (μ_B)	R^2
a	$-98(1)$	2.396(3)	4.17	0.998
b	$-96(1)$	2.550(4)	4.30	0.995
c	$-127(2)$	2.841(6)	4.50	0.995
Powder	$-110(1)$	2.592(3)	4.31	0.997

The effective moment is calculated from the magnetic static susceptibility as: $\mu_{eff} = (3k_B/\mu_0 N_A \mu_B^2)^{1/2}\sqrt{\chi T}$ for large T, whereas the theoretical effective moment is:

$$\mu_{eff} = g_j \mu_B \sqrt{J(J+1)} = 4.5356\mu_B. \tag{7.4}$$

μ_{eff} obtained from the powder average susceptibility value at T= 1000 K is $4.31\mu_B$ which is reduced from the theoretical value, this is probably because the four doubly

degenerate levels of the $J = 7/2$ multiplet are not fully populated even at $1000\,\mathrm{K}$ so that the full moment is not achieved. The Curie-Weiss temperatures are negative and are much bigger than the Néel temperature of $\mathrm{T}_N = 0.92\,\mathrm{K}$. The values shown for the powder were calculated by fitting the susceptibility data obtained from the average of all three directions. The Curie-Weiss temperature values are in agreement with the value obtained by Karunadasa *et al.* [104] for a powder sample of $-99.4\,\mathrm{K}$. The goodness of the fits are shown in the last column of Table 7.2. The B_2^0 crystal field parameter can be obtained from the Curie-Weiss temperatures. The paramagnetic curie temperatures can be used to determined by the lowest rank interactions (B_2^0) assuming that the two ion coupling is isotropic Heisenberg exchange. If the *c*-axis (or quantization axis) is a three fold or six fold symmetry axis and the basal-plane components of the susceptibility are equal, the high temperature expansion in the mean field approximation predicts [3]:

$$B_2^0 = -\frac{5}{6}k_B \frac{\theta_{||} - \theta_{\perp}}{(J - 1/2)(J + 3/2)}, \tag{7.5}$$

where $\theta_{||}$ is the Curie-Weiss temperature obtained when the field is parallel to the quantization axis ($\theta_{||} = -127\,\mathrm{K}$) and $\theta_{\perp}$ is the Curie-Weiss temperature obtained when the field is perpendicular to the quantization axis, in this case the *ab*-plane ($\theta_{\perp} = -97\,\mathrm{K}$). k_B is the Boltzmann constant and J is the total angular moment $7/2$. The symmetry conditions do not hold for SrYb$_2$O$_4$ since there is no rotational axis and only a mirror plane. Nevertheless, Equation 7.5 could give a good estimate of B_2^0 when the B_2^2 parameter is small and when the curie temperatures in the basal plane are equal, as is shown in Table 7.2. Using this equation a value of $0.1431\,\mathrm{meV}$ is obtained for B_2^0. This value is used later as a starting parameter in the CF fitting. The susceptibility is a second rank tensor and can not therefore vary under rotation heat capacity is shown in Figure 7.3. The figure on the left shows the low temperature heat capacity and entropy measured in CM14.5T at zero magnetic field. A broad anomaly appears centered around $2.5\,\mathrm{K}$ at zero field, that could be due to short range correlations. The entropy for a formula unit mol (2Yb^{3+} ions) sums up to $2R\ln2$ (at $\approx 10\,\mathrm{K}$), suggesting the presence of a doublet ground state expected for a Kramer's ion and no other excited state below $10\,\mathrm{K}$ ($0.86\,\mathrm{meV}$). Figure 7.3(right) shows the heat capacity for a bigger range of temperatures (0.3-$300\,\mathrm{K}$). A large phonon contribution appears at about $12\,\mathrm{K}$. The heat capacity should approach the Dulong-Petit law above $300\,\mathrm{K}$, reaching a value of $C = 3nR = 174.0\,\mathrm{K}$, with $n = 7$ the number of vibrating atoms per formula unit. The phonon heat capacity was calculated

using the Einstein equation given by,

$$C_p = \sum_\epsilon 3nR(\frac{\epsilon}{k_B T})^2 \frac{e^{\epsilon/K_B T}}{(e^{\epsilon/k_B T} - 1)^2},$$
(7.6)

where ϵ is the Einstein temperature. For the model shown here, these temperatures are: 135 K, 470 K, 395 K, with factors of $1/4 : 1/2 : 1/4$. The phonon contribution to the specific heat is ≈ 10 times larger than the magnetic contribution therefore the magnetic specific heat cannot be obtained by subtracting the Einstein specific heat since the subtraction would be within the error of the measurement and would lead to systematic errors. Heat capacity data for different magnetic fields are shown in Figure 7.4. Two
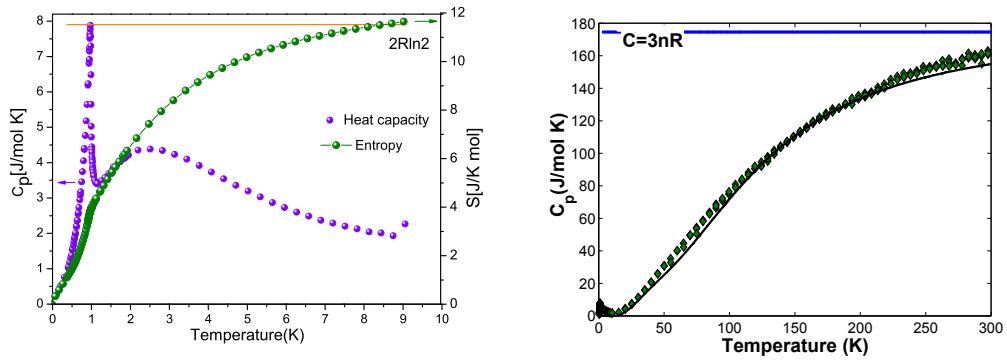
Figure 7.3: Heat capacity and magnetic entropy for $SrYb_2O_4$ in zero field. (left) Low temperature heat capacity (purple), the green data corresponds to total entropy which below 10 K is only the magnetic component. The entropy sums up to $2Rln2$ per two Yb (red line) below 10 K, suggesting that there are no excited CF levels at low energies (0.9 meV). The heat capacity has been extrapolated to zero for the calculation of the entropy. (right) Heat capacity from 0.2-300 K, it converges to the Dulong-Petit law above 300 K (blue line). The black line is the Einstein model of the phonon contribution to the heat capacity.

datasets (PPMS, CM14.5T) have been combined to obtain a range of temperatures from T= 0.3 K to 35 K. The magnetic field was applied along the c-axis. The black dashed line is the phonon model mentioned earlier. The broad anomaly decreases and moves towards higher temperatures with increasing field. A change occurs above H= 4 T where the shoulder gets broader and its heat capacity increases. As the phonon contribution is small below 15 K, heat capacity at different fields could be a good way to test for plausible CF models.
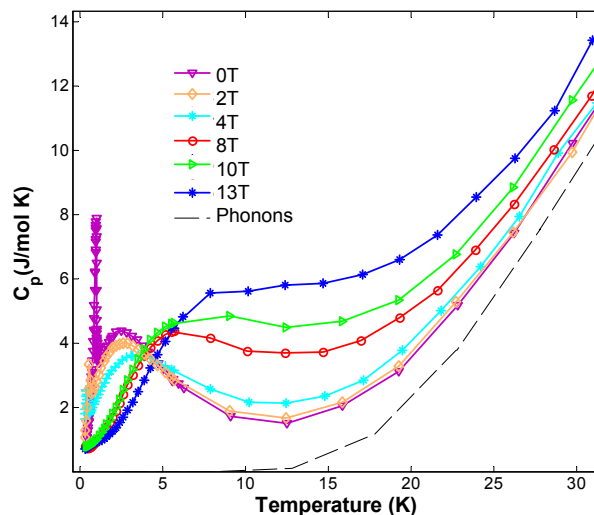
Figure 7.4: Heat capacity for different magnetic fields applied along the *c*-axis, the data were acquired using two techniques: CM14.5T and PPMS. The phonon contribution (dashed line) starts increasing above T= 13 K.

7.4 Inelastic Neutron Scattering Data

A study on inelastic neutron scattering on SrYb$_2$O$_4$ is presented here. Different experiments were done on three different time of flight spectrometers. These three different instruments let us investigate the magnetic scattering over different energy ranges and temperatures for single crystal and polycrystalline samples. Figure 7.5 shows powder inelastic neutron scattering (INS) data as a function of wavevector transfer, energy transfer and intensity in absolute units acquired on Merlin under different conditions. The Figure 7.5(left) was collected at T= 8 K, using an incident energy of 110 meV. Four inelastic modes can be seen in addition to the phonon contribution that increases in intensity at high wavevector transfer. These modes are centered at 32.5 meV, 52.6 meV, 70.27 meV and 80 meV. The dataset on the right was collected at T= 239 K using an incident beam of energy 88.58 meV. Two strong modes can be seen at 32.5 meV and 70.27 meV. The mode at 52.6 meV is very weak and the mode at 80 meV is not present at all in this second dataset. The datasets were obtained using different experimental setups, and the background is different. For the data set on the left the presence of condensed water was detected in the sample, so the mode at 80 meV is attributed to a hydrogen mode. Cuts at constant energy were made for the dataset on the left, these cuts are presented in Figure 7.6 and show the wavevector transfer dependence of the intensity. The solid line is the magnetic from factor for Yb^{3+}. The mode at 80 meV does not follow the
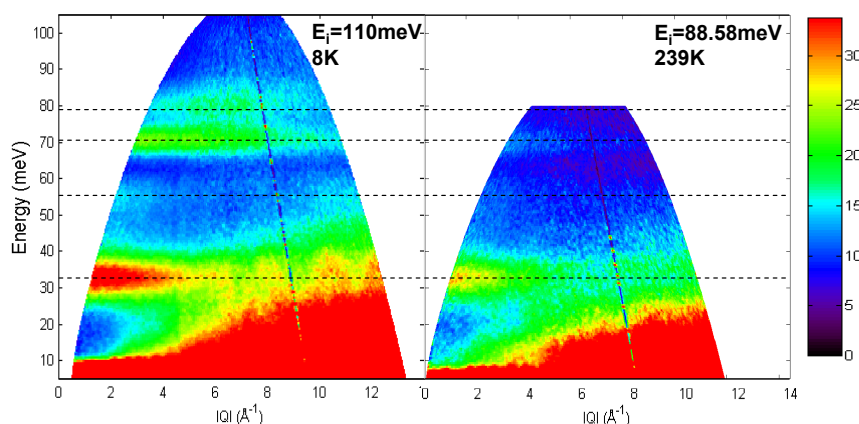
Figure 7.5: Inelastic neutron scattering data acquired on Merlin. The color scale gives the intensity in units of $mb/sr.meV.f.u.$ The data were acquired at T= 8 K and incident energy of $E_i = 110$ meV (left) and T= 238 K and $E_i = 88.58$ meV (right). The dashed lines indicate the inelastic modes energies found in these data.

magnetic magnetic form factor as its intensity increases around $6.5 \, \text{Å}^{-1}$ which makes clear that it does not have a magnetic origin and confirming that it is a hydrogen mode due to water contaminations on the sample space. The mode centered at 32.5 meV follows the magnetic form factor, at T= 8 K it has a width of 4 meV which is equal to the instrument resolution and it starts showing a phonon contribution at $6 \, \text{Å}^{-1}$. The mode centered at 52.6 meV is weak and follows the magnetic form factor until $6.5 \, \text{Å}^{-1}$ where the phonon contribution starts being stronger. The mode at 70.27 meV, has a width of 3.4 meV which is wider than the instrument resolution of 2.6 meV. Its intensity decreases with increasing temperature suggesting that it is magnetic but it does not appear to follow the form factor because it is contaminated by the hydrogen mode that increases the background at $4 \, \text{Å}^{-1}$. Figure 7.7 shows the temperature dependence of the INS data. Constant wavevector cuts ($3.8 \, \text{Å}^{-1} < |Q| < 4.8 \, \text{Å}^{-1}$) have been made from datasets obtained on Merlin at different temperatures using the same incident energy of 110 meV. The intensity of the modes at 32.5 meV and 70.27 meV drops considerably between 100 K and 290 K. This reduction is too large to be explained by the Boltzmann factor if the mode at 32.5 meV is the first excited state. This could suggest the existence of a lower energy mode not observable by neutron scattering that becomes thermally populated thus reducing the population of the ground state and hence the intensity of the excitations from the ground state. The mode at 52.6 meV is very weak at 290 K and it is not possible to distinguish it from the background. Figure 7.8 is a cut at constant wavevector ($3.8 \, \text{Å}^{-1} < |Q| < 4.8 \, \text{Å}^{-1}$) from the dataset acquired with an incident energy
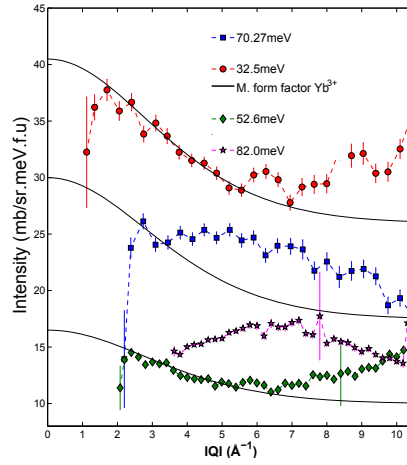
Figure 7.6: Cuts at constant energy transfer to the INS dataset acquired on Merlin at 8 K and E$_i$ = 110 meV. It shows cuts at 32.5 meV, 52.6 meV, 70.27 meV and 82 meV. The solid line represents the magnetic form factor. The modes at 32.5 meV, 52.6 meV and 70.27 meV have a magnetic origin whereas the mode at 82 meV is a hydrogen mode.
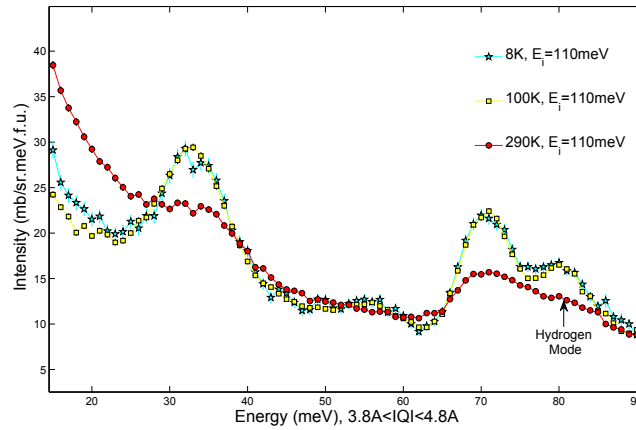
Figure 7.7: Cuts at constant wavevector of the datasets acquire on Merlin at different temperatures (8 K,100 K,290 K) with E$_i$ = 110 meV. There is a substantial drop in the intensity of the modes above 100 K.

of 60.4 meV at 240 K. The mode at 30.2 meV is much wider than the resolution which is 1.2 meV as is depicted in the figure by the horizontal blue line. The mode can not be described as a Gaussian function as it has some wings on either side, that could be due to excitations from levels that are thermally populated at this temperature. Apart from the CF levels, SrYb$_2$O$_4$ presents low energy magnetic excitations below 2 meV. To access those energy transfers two ToF spectrometers were used, IN5 and IRIS, and both powder and single crystal samples were investigated. Figure 7.9(left) shows low energy
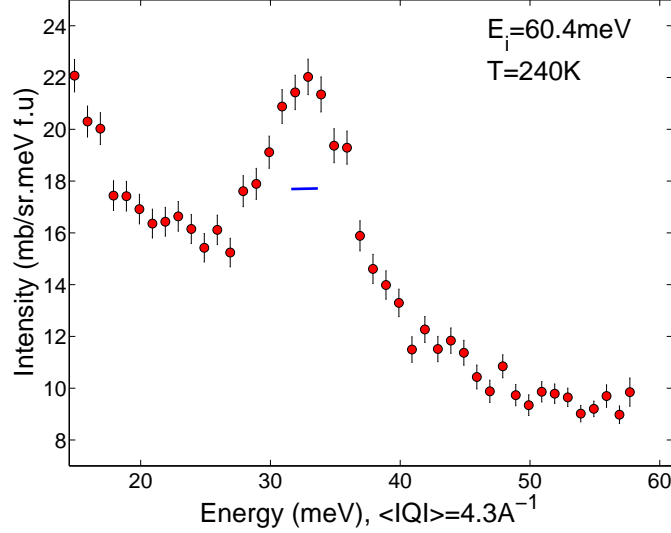
Figure 7.8: Cut at constant wavevector ($3.8\,\text{Å}^{-1} < |Q| < 4.8\,\text{Å}^{-1}$) of the dataset acquired on Merlin at 240 K with an incident energy of 60.4 meV. There is a mode at 32 meV which is much wider than the instrument resolution for that energy transfer. The horizontal blue line gives the size of the energy resolution.

powder INS data obtained on IN5 at 0.1 K as a function of scattering angle and energy transfer. The incident energy was 3.27 meV ($\lambda_0 = 5\,\text{Å}$). There is a low energy excitation with a complicated wavevector dependence and modulated intensity which has a bandwidth of 1 meV and a gap of 0.2 meV in the AFM phase. The maximum of the intensity of this low energy excitation is around $1.12\,\text{Å}^{-1}$, that coincides with $(0, 2, 0)$ which is a strong magnetic Bragg peak in the ordered phase, as explained in the previous chapter. Figure 7.9(right) shows the temperature dependence of the low energy mode, constant scattering angle (52.8°) cuts were made from two datasets. The first one obtained at 0.1 K and with incident wavelength 5 Å and the second at 1 K with incident wavelength 6 Å. The intensity has a maximum at about 0.4 meV and decreases when the temperature increases although it does not disappear completely in the paramagnetic phase. The Q dependence of the intensity of the low energy modes indicates short range spin correlations above T_N. This low energy excitation has also been measured on a single crystal using the ToF spectrometers IRIS and IN5. The IRIS measurement investigates the low energy magnetic excitation in the $(H, K, 0)$ plane at T=50 mK whereas the IN5 experiment investigates the dispersion along all directions in reciprocal space at two temperatures, in the AFM phase at T=70 mK and above the Néel temperature, 1.6 K. These magnetic excitations arise from interactions between the Yb^{3+} ions. Taking into
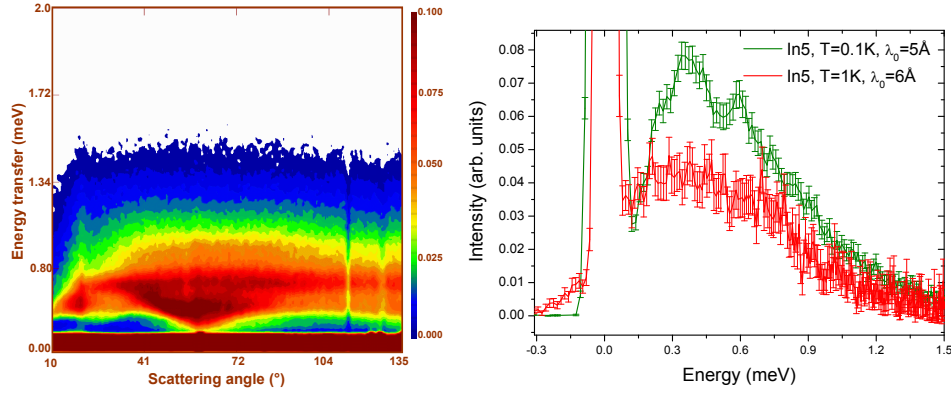
Figure 7.9: Low energy powder inelastic neutron scattering (IN5-ILL). (left) Colorplot, temperature: $0.1\,\mathrm{K}$, incident wavelength: $5\,\text{Å}$. Intensity is maximum at about $2\theta = 52.8°$ ($Q = 1.12\,\text{Å}^{-1}$). (right) Cuts at constant scattering angle ($62°$), green: temperature: $0.1\,\mathrm{K}$, incident wavelength: $5\,\text{Å}$, red: temperature: $1\,\mathrm{K}$, incident wavelength: $6\,\text{Å}$.

account the number of magnetic ions per unit cell, a maximum of 8 modes are expected although some may be degenerate.

Figure 7.10 shows some cuts through the IRIS data. These data were collected at $50\,\mathrm{mK}$ (below the magnetic transition) and show at least two clear modes plus diffuse scattering. The minima of the excitations are found to be in the Γ points for $(H, K, 0)$ with $H = N + 2M$ and $K = 2N$, where M and N are integer. There is a strong intensity modulation, especially along the b^* axis. The modes are wider than the instrument resolution. Figure 7.11 shows four colorplots as a function of wavevector and energy transfer
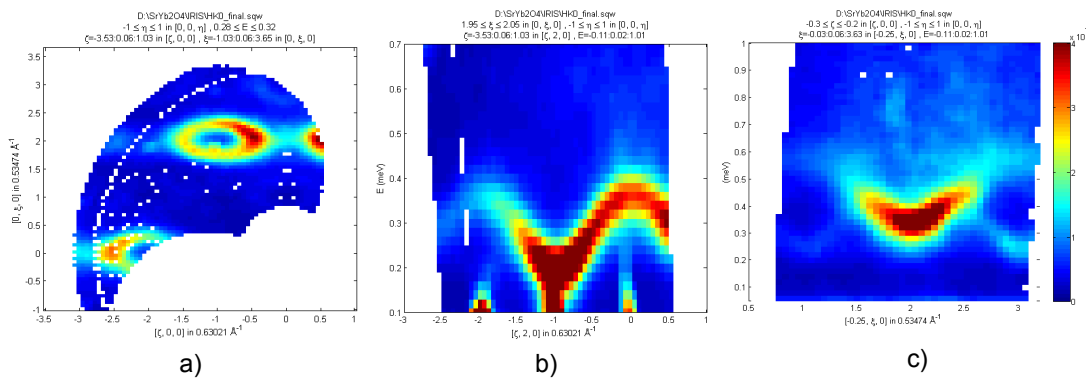
Figure 7.10: Single crystal inelastic neutron scattering (IRIS-ISIS) at T= $50\,\mathrm{mK}$ shows low energy dispersive modes. a) constant energy colorplot at $0.3\,\mathrm{meV}$ showing the $(H, K, 0)$ dispersion. b) constant K cut $(H, 2, 0)$ showing a minimum at $(-1, 2, 0)$. c) constant H cut $(-0.25, K, 0)$ showing two branches and diffuse scattering that goes up to $1\,\mathrm{meV}$.

and the colors give the neutron scattering intensity in arbitrary units measured on IN5. Three of them were acquired at T=70 mK with an incident energy of $E_i = 2.704$ meV. The fourth shows a slice through the data acquired at T=1.6 K with an incident energy of $E_i = 3.27$ meV. Below T_N some of the modes are wider than the instrumental resolution and diffuse magnetic scattering is detected up to 2 meV along all crystallographic directions, specially along the c^* axis. In the paramagnetic phase the modes are not well defined, but there is diffuse magnetic scattering well above the T_N. For both planes, $(H, K, 0)$ and $(0, K, L)$, the intensity is modulated, being more intense near the Γ points, and with energy minima at $(H, K, 0)$, $H = N + 2M$ and $K = N$ and for $(0, K, L)$, $H + K = N$. The minima in $(H, K, 0)$ with $K = N$ were detected with IN5 and not with IRIS probably because better signal/background ratio on IN5. It is important to note that the data acquired along c^* has only a small range in L due to the small c lattice constant and the low incident energy. Above the Néel temperature, the diffuse magnetic scattering remains, showing a strong intensity at $(0, K, L)$ with $K = 2N$. Heat capacity measurements (Figure 7.3(left)) showed that the magnetic entropy below 10 K sums up to $Rln2$ per Yb, therefore the low energy magnetic excitations are not an excited crystal field level but are due to excitations within the ground state doublet. They arise from the single ion anisotropy, dipolar interactions and/or an internal mean field due to Yb^{3+}-Yb^{3+} magnetic exchange interactions which lifts the degeneracy of the ground state doublet and makes the spin excitations gapped and dispersive.

Low energy magnetic excitations have also been observed in the isostructural compound $SrEr_2O_4$ by T. Hayes $et\,al.$ [149]. They investigated these excitations using the D7 diffractometer at ILL, no energy analysis was done, therefore they studied the INS and diffuse magnetic scattering integrated over an energy transfer range from the elastic line up to 8.5 meV. Rods of scattering are observed in the $(0, K, L)$ plane close to the half integer positions $(0, K, \pm 1/2)$ and $(0, K, \pm 3/2)$ suggesting strong antiferromagnetic correlations along the c axis but only weak correlations in the $a - b$ plane. The diffuse scattering therefore appears to be independent of the magnetic structure which is characterized by $\boldsymbol{k} = (0, 0, 0)$. Furthermore the diffuse scattering sharpens only gradually with decreasing temperature and shows no anomaly at T_N. In $SrEr_2O_4$ only one of the two inequivalent Er ions order according to Petrenko $et\,al.$ [115], therefore they suspect that the diffuse magnetic scattering is predominantly due to the Er that remains paramagnetic. Such behavior is called cooperative paramagnetism, in which the magnetic correlations are short ranged and the magnetic system undergoes fluctuations. This behavior is thought to arise from the strong geometric frustration in these systems. The INS measured in $SrEr_2O_4$ suggest that the magnetic interactions may have
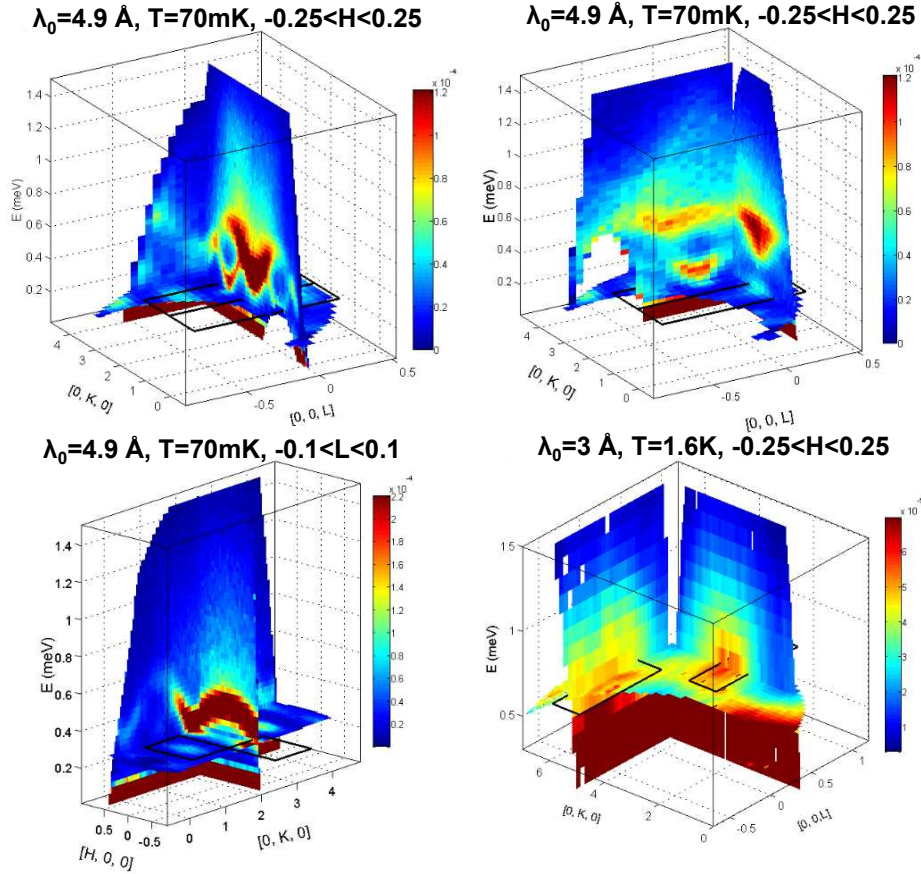
Figure 7.11: Single crystal INS data (IN5-ILL). The two top and the left bottom colorplots show data acquired at T= 70 mK with E$_i$ =2.704 meV. The fourth colorplot shows data acquired at T= 1.6 K with an incident energy of 3.27 meV.

1 or 2-dimensional behavior. This in contrast with our findings for SrYb$_2$O$_4$, where the magnetic neutron scattering intensity is dispersive along all crystallographic directions, therefore the nature of the magnetic correlations is 3-dimensional.

As a first attempt to understand the magnetic correlations in SrYb$_2$O$_4$ it is possible to use the first moment sum rule to identify the dominant exchange interactions in the system, as it was performed for Sr$_3$Cr$_2$O$_8$ in Chapter 5. Following Equation 5.8 and taking as references works on TbTi$_2$O$_7$ where diffuse magnetic scattering has been measured due to cooperative paramagnetism in this system [150, 112]; the intensity of

powder INS can be modeled with the expression,

$$I(|\boldsymbol{Q}|) \propto A_i\,|f_{\mathrm{Yb}^{3+}}(|Q|)|^2 \left(1 - \frac{sin(|Q|\,|d_i|)}{|Q|\,|d_i|}\right),\tag{7.7}$$

where $A_i = \boldsymbol{J}_i\langle \boldsymbol{J}_0, \boldsymbol{J}_i\rangle$, d_i is the distance between one Yb and another at site i, $\boldsymbol{J}_i$ is the exchange constant coupling them, and $f_{Yb^{3+}}(|Q|)$ is the magnetic form factor for Yb^{3+} [151]. This expression was used to analyze the magnetic background of the low temperature (T= 30 mK) magnetic component of the D7 powder pattern, where polarization analysis was used to separate the magnetic from the nuclear scattering, see Figure 7.13. For this measurement an incident neutron beam with wavelength $\lambda_0 = 4.84\,\text{Å}$ was used and no energy analysis is done. The data is equivalent to the integration over an energy transfer range from -3.49 meV to 3.49 meV, therefore, the magnetic Bragg peaks and the low energy magnetic excitations have been sum up. These data have then been fitted with the expression 7.7 for each individual Yb^{3+}-Yb^{3+} distance, according to the values listed in Figure 7.12. A_i was the only parameter which was fitted. The results are compared in Figure 7.13. The distances along the 'zig-zag' chains and in the honeycomb

J_i	$d_i(\text{Å})$	$Q(\text{Å}^{-1})$
J_1	3.35	1.407
J_2	3.44	1.370
J_3	3.47	1.358
J_4	3.47	1.358
J_5	3.62	1.302
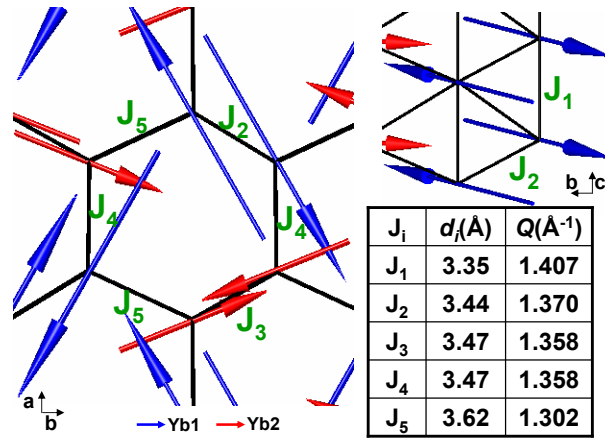
Figure 7.12: Distances between Yb^{3+} ions in $\mathrm{SrYb_2O_4}$, and corresponding magnetic exchanges. The arrows represent the directions of the magnetic moments found by the refinement of the magnetic structure explained in the previous chapter. The wavevector positions of the maximum in intensity expected for each interaction in the first sum rule are also listed.

are very similar, and the fitting is good for all of these values, making it impossible to distinguish between exchange paths. Nevertheless, it is clear from Figure 7.13 that the broad peak in the magnetic component of the D7 powder pattern is due to the magnetic exchange coupling between the Yb^{3+} ions.
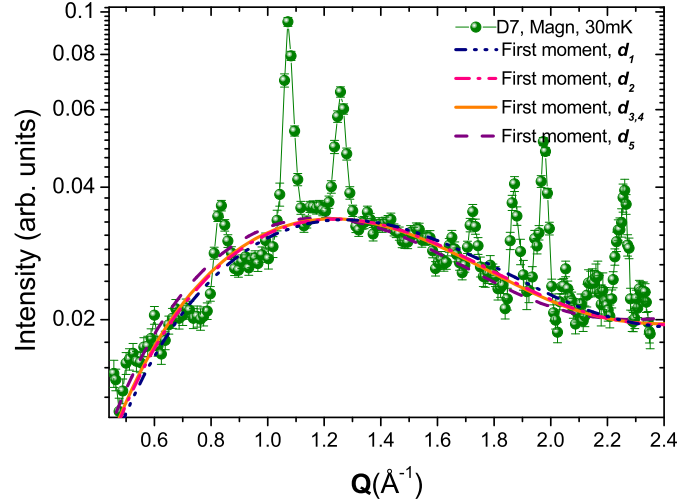
Figure 7.13: Magnetic component of the D7 powder pattern, acquired at a temperature of T= 30 mK, together to the fits to the first moment sum rule according to the text.

A random phase approximation model similar to that used for Sr$_3$Cr$_2$O$_8$ in Chapter 5 could be used to model the low energy magnetic excitations in SrYb$_2$O$_4$[3, 152]. But in this case more terms must be added to the Hamiltonian, such as the CF terms and possibly dipolar interactions. Therefore is imperative to know the CF parameters and ground state of SrYb$_2$O$_4$. The following sections will focus on the fitting of higher energy powder INS with the aim of finding the CF parameters and therefore defining the CF Hamiltonian and ground state for this compound. The study of the CF is a prerequisite to any understanding of the low temperature magnetic properties.

7.5 The Crystal Field

In the next subsections two different approaches are going to be used with the aim of find the CF parameters of SrYb$_2$O$_4$. The first one is the classical point charge model and the second uses randomly generated parameters which are compatible with the excitations observed in the INS data.

7.5.1 Point Charge Model

The point charge model is the simplest form of an electrostatic model. The electrostatic potential at a magnetic ion is obtained by summing the contributions of all the other ions in the lattice. For lanthanide compounds, the free ion interactions are dominated by the electrostatic interactions between electrons within the ion and the spin-orbit interaction between the spin and orbital angular momenta of these electrons. In the cases where the electrostatic interactions are stronger than the spin orbit coupling and these are both stronger than the crystal field, the crystal field interactions may be modeled as a perturbation which splits a degenerate spin-orbit coupled ground state. The electrostatic potential, external to any spherically symmetric charge distribution, can be shown to be the same as that generated by the same net charge concentrated at a point at the center of that distribution. An inherent approximation in the point charge model is that the unfilled shell of electrons on the magnetic ion lie outside the charge distributions on the neighboring ions [3, 13, 2].

This approximation is poor and gives inaccurate quantitative predictions of the strength of the crystal field splitting. In the case of the lanthanide ions, the point charge model over(under)estimate the rank 2(6) contributions by a factor of 10 [2]. The crystal field parameters were calculated using the point charge model for both Yb ions in $SrYb_2O_4$. This calculation was done using the software package McPhase [147] making use of the programs *makenn* and *pointc* and using the structural parameters obtained from the previous chapter. The following results were obtained, see Table 7.3. The CF scheme is shown in Figure 7.14 together with the orbitals for both Ybs in the distorted octahedral environment. Towards the heavier end of the lanthanide series the electrons are more tightly bound and so it takes a much larger CF to deviate from spherical symmetry. Even though the $4f$ charge cloud is almost spherically symmetric for Yb^{3+}, and the CF interactions are weak, the diffraction results of the previous chapter show that there is a residual magnetic anisotropy which causes the moments to point preferentially in the ab-plane below T_N.

 Figure 7.15(a) shows a cut at constant scattering angle ($2\theta = 22.67°$) from the powder INS dataset acquired on Merlin at $8\,K$ with an incident energy of $110\,meV$. The background has been subtracted as well as the hydrogen mode at $80\,meV$. The solid lines represent the calculated neutron cross section for a CF Hamiltonian with the parameters shown in Table 7.3. The blue line gives the model for Yb1 and the red line the one for Yb2. The point charge model is similar to the experimental data assuming that the modes at $32.5\,meV$ and $70.2\,meV$ belong to the CF scheme for Yb1, the mode at $52.6\,meV$ belongs to Yb2. However, the intensities and exact positions of the modes

Table 7.3: Solution of CF using the point charge model for Yb1 and Yb2. The rotational invariants for Yb1 are: $S_2 = 1.681$, $S_4 = 0.0016$, $S_6 = 4.3 \times 10^{-7}$. And for Yb2: $S_2 = 5.379$, $S_4 = 0.0017$, $S_6 = 1 \times 10^{-8}$.

Yb1							
$k\backslash q$	-6	-4	-2	0	2	4	6
2			-2.972	2.866	0.4361		
4		0.1072	-0.115	0.0062	0.1181	0.0021	
6	-0.0005	-0.0006	8×10^{-5}	-0.0001	-8×10^{-5}	0.0001	-0.0007
Yb2							
$k\backslash q$	-6	-4	-2	0	2	4	6
2			-3.7350	0.8557	-5.1151		
4		0.0757	0.0927	0.0054	-0.11751	-0.0379	
6	0.0003	-0.0007	-1×10^{-5}	-0.0001	-0.0002	-0.0002	-0.0002
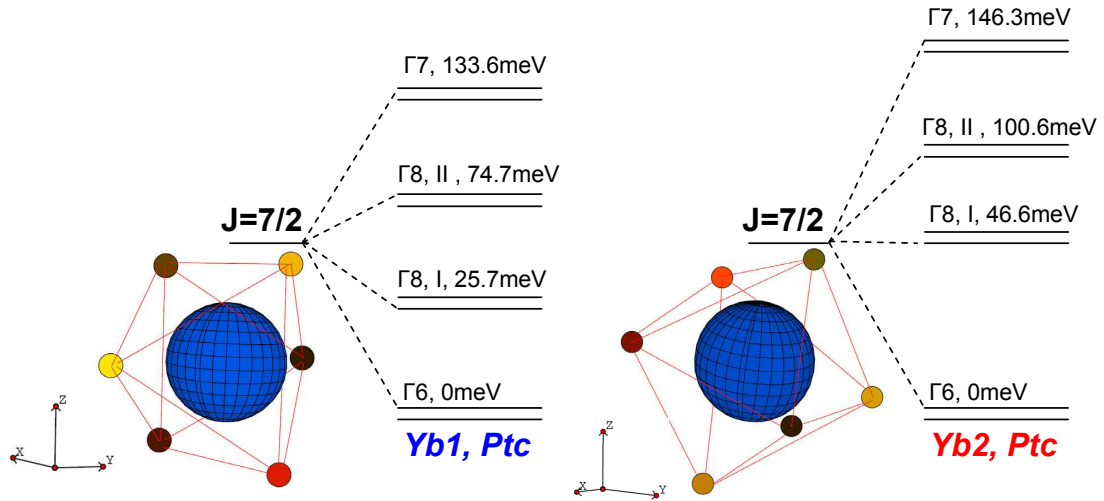
Figure 7.14: Orbitals and CF scheme from the point charge model for the two sites Calculated according to Table 7.3 for Yb1 (left) and orbital of Yb2 (right).

are not reproduced. Using the CF parameters, the wavefunctions of the Yb ions were found and the inverse susceptibility was calculated using the Equation 3.1, which for this specific case is:

$$M(H,T) = \frac{g\mu_B}{Z} \sum_i \langle i | J \cdot \hat{H} | i \rangle e^{-E_i/k_B T}, \qquad (7.8)$$

$|i\rangle$ are the eigenstates of the total Hamiltonian, $\mathcal{H} = \mathcal{H}_{CF} + \mathcal{H}_z$, where the Zeeman term is given by $\mathcal{H}_z = -g\mu_B J \cdot \hat{H}$, H is the applied magnetic field and E_i is the energy

(a) INS, PC model, T = 8 K

(b) Inverse susceptibility, PC model

(c) Heat Capacity, PC model
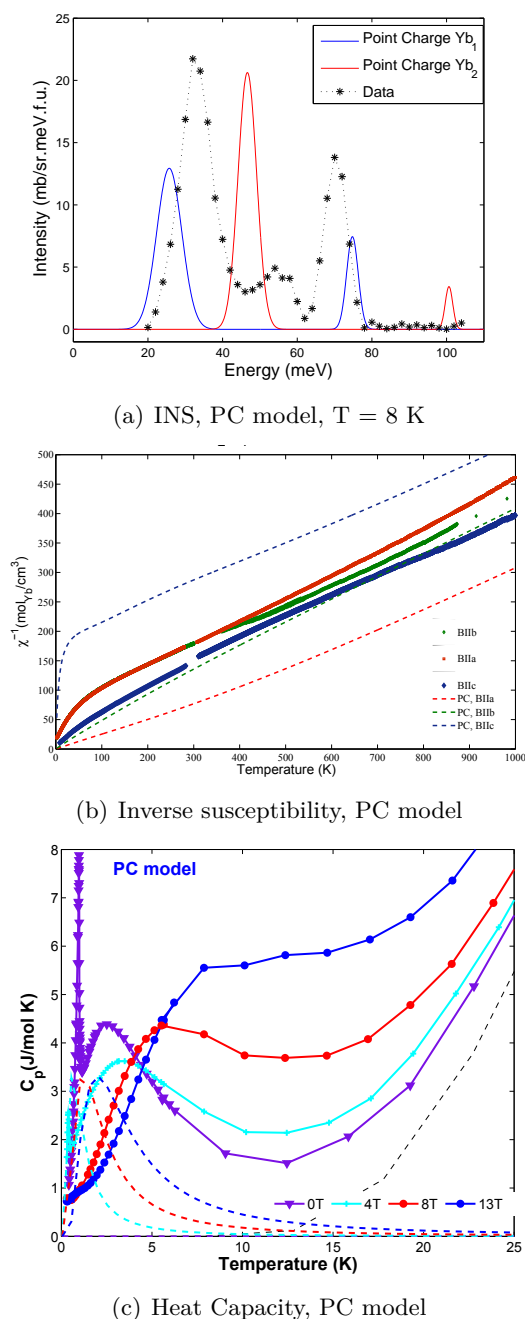
Figure 7.15: (a)Cut at constant scattering angle ($2\theta = 22.67°$) of the powder INS data acquired on Merlin at 8 K with an incident energy of 110 meV. The background has been subtracted. The solid lines represent the neutron cross section calculated using the CF parameters obtained using the point charge model. The blue line is the calculation for Yb1 and the red line is the calculation for Yb2. (b) Inverse susceptibility data for a field of 1 T applied along all three different crystallographic directions. The dashes lines correspond to the calculation of the inverse susceptibility using the point charge model and averaging the contributions for both Ybs. (c)Heat capacity for different magnetic fields applied along the *c*-axis. The dashed lines correspond to the calculation of the heat capacity using the CF parameters obtained with the point charge model. The contribution from both ions has been averaged.

of the ith level. To calculate the inverse susceptibility a constant magnetic field of 1T was set and the magnetization was calculated for the temperature range T= 2 K to 1000 K. This calculation was performed for Yb1 and Yb2 separately, the average of the susceptibility was then taken and is shown in Figure 7.15(b) along with the data. The inverse susceptibility does not reproduce the anisotropy and does not coincide with the experimental data. The effective moment is however predicted to be $4.5\mu_B$ which is close to the experimental value of $4.3\mu_B$. The heat capacity has been calculated as well using Equations 3.4 and 3.5 for different fields applied along the quantization axis c and compared to the experimental values for this field direction (see Figure 7.15(c)). As for the susceptibility the contributions of each Yb ion have been averaged. Altogether it is clear that the CF parameters obtained from the point charge model do not reproduce the experimental data. Taking the CF parameters shown in Table 7.3 as initial parameters, the inelastic neutron data were fitted using the program FOCUS [145]. FOCUS is a fitting package for crystal electric field parameter determination of rare earth containing materials. FOCUS uses the interactive program shell of MULTI-FRILLS and runs on the ISISE-Network at the ISIS Facility of the Rutherford Appleton Laboratory. It uses a GENIE environment. The fits were done independently for two temperatures, T= 8 K and 290 K, using datasets collected with incident energy of 170 meV and 110 meV. The input for the program was a cut along the energy axis at low scattering angle, integrated over a narrow angular range.

The fitted crystal field parameters for both Ybs are shown in Table 7.4. Figures 7.16(a)

Table 7.4: Solution of fit of INS data taken at 8 K and 110 meV on Merlin using FOCUS with the point charge model as starting parameter for Yb1 and Yb2. The rotational invariants for Yb1 are: $S_2 = 2.5625$, $S_4 = 0.0016$, $S_6 = 4.3 \times 10^{-7}$, and for Yb2: $S_2 = 4.7758$, $S_4 = 0.0032$, $S_6 = 1.08 \times 10^{-8}$. The goodness of the fits were $\chi^2 = 5.25$ for Yb1 and $\chi^2 = 14.849$ for Yb2.

$Yb1$							
$k\backslash q$	-6	-4	-2	0	2	4	6
2			-0.81325	-0.37015	3.5603		
4		0.1059	-0.27456	0.01899	-0.04913	0.1079	
6	-0.0005	-0.0021	8×10^{-5}	-0.00056	-0.0016	-0.0014	-0.0007
$Yb2$							
$k\backslash q$	-6	-4	-2	0	2	4	6
2			-1.2597	1.6545	-4.598		
4		0.07575	0.09276	-0.07814	-0.14519	-0.03790	
6	0.00029	-0.00067	-1.5×10^{-5}	-0.00012	-0.00022	-0.00022	-0.0002

and 7.16(b) show the fit and data for high and low temperature. The temperature dependence of the intensity is not well followed by the model. The figure on the left shows Merlin data at 8 K with an incident energy of 110 meV. The goodness of the fits were: for Yb1, 8 K, $\chi^2 = 5.25$ and for Yb2, 8 K, $\chi^2 = 14.849$. The fit is good for Yb1 but the calculated intensity for the mode at 52 meV of Yb2 is much greater than the experimental intensity. The figure on the right shows the data at 290 K. The model does not follow the temperature dependence. The heat capacity at different fields and inverse susceptibility have also been calculated for the parameters in Table 7.4 (see Figures 7.16(c), 7.16(d)). The large drop in the intensity of the excitations at 32 and 70 meV with temperature may be due to the presence of a lower energy mode (≈ 6 meV) with zero or very low intensity in neutron data. Such a mode would rapidly become populated with increasing temperature thus reducing the population of the ground state and the intensity of excitations from the ground state as is observed experimentally. In order to search for this mode, the crystals were oriented, cut and polished and then sent to the research group of Joachim Deisenhofer (University of Augsburg) to measure optical absorption. The spectra shown in Figure 7.17 were taken at room temperature and at 4 K. There is a bump around 6.98 meV that sharpens up with decreasing temperature, which could be of magnetic origin. There are also peaks around 9.2 and 10.14 meV which are ascribed to phonons. These peaks were observed in the neutron data to have a form factor that increases with wave-vector suggest a non-magnetic origin, the mode at ≈ 6 meV has however not been observed with neutrons.

7.5.2 Model using Simulated Annealing

The second method for finding the initial crystal field parameters is a simulated annealing algorithm. The algorithm needs a set of initial parameters to calculate an initial set of wavefunctions. The calculated eigenvalues are compared with the experimental CF levels. If the comparison is not satisfactory, it randomly looks for a new set of CF parameters and it repeats the process iteratively until the energies generated are close to the desired values [77]. An additional algorithm was used that calculates the neutron cross section for each new set of wavefunctions and compares them to the experimental values for different temperatures. After a thousand iterations the best solutions were saved.

Different models with different permutations of the experimentally observed crystal field levels among the two Yb ions have being tested. The best solutions were selected and over 100 solutions per model were used as initial parameters for the fitting of the neutron data. Two programs have been used for this propose. The first was FOCUS, which ac-

(a) INS, PC model in FOCUS, T = 8 K

(b) INS, PC model in FOCUS, T = 290 K

(c) Inverse susceptibility, PC model in Focus

(d) Heat Capacity, PC model in Focus
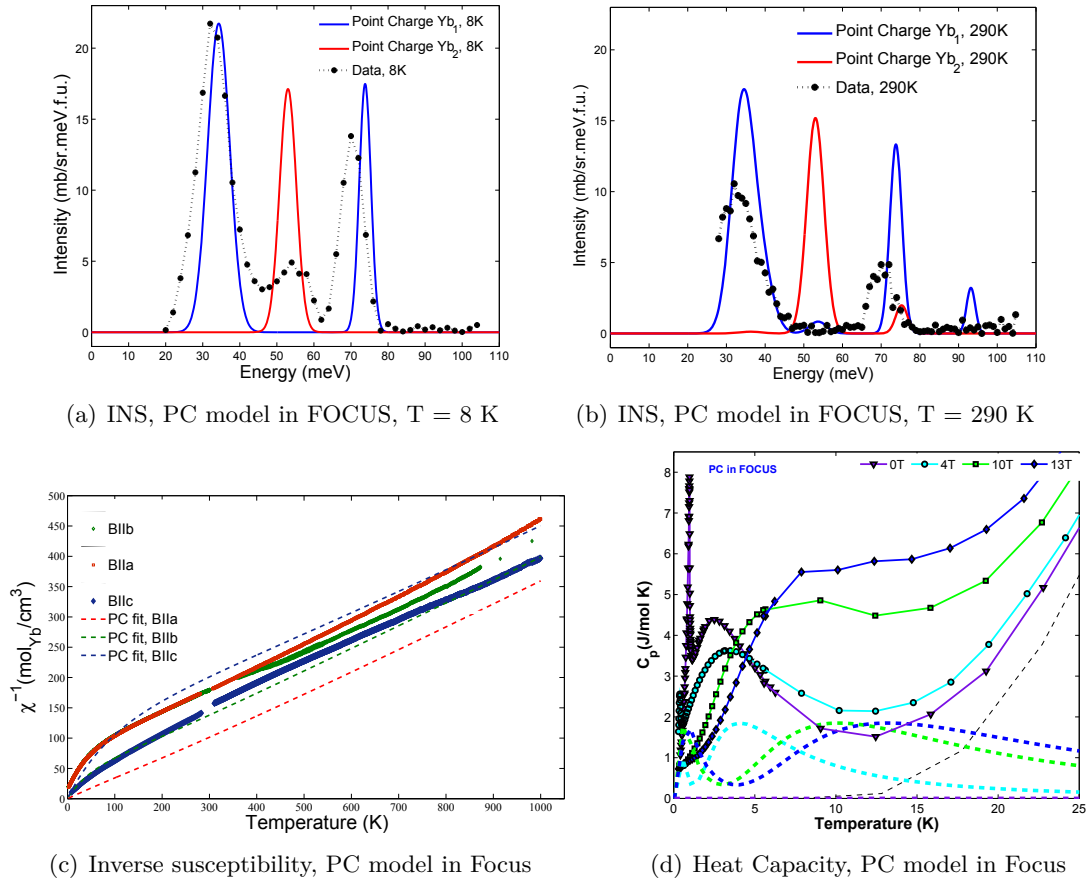
Figure 7.16: (a-b)Powder INS data acquired on Merlin together with the cross section calculated from the CF parameters obtained from the fitting of the INS data, where the PC CF parameters were used as starting parameters. The data cuts are at constant scattering angle ($2\theta = 22.67°$) and have been background subtracted. (a) Data and calculation at 8 K for both Ybs and (b) Data and calculation at 290 K. (c) Inverse susceptibility data for a field of 1 T applied along all three different crystallographic directions. The dashed lines correspond to the calculation of the inverse susceptibility using the fitted point charge model parameters and averaging the contributions for both Ybs. (d)Heat capacity for different magnetic fields applied along the c-axis. The dashed lines correspond to the calculation of the heat capacity using the CF parameters obtained with the fitting of the INS data using the PC CF parameters as starting parameters. The contribution from both ions have been summed up.
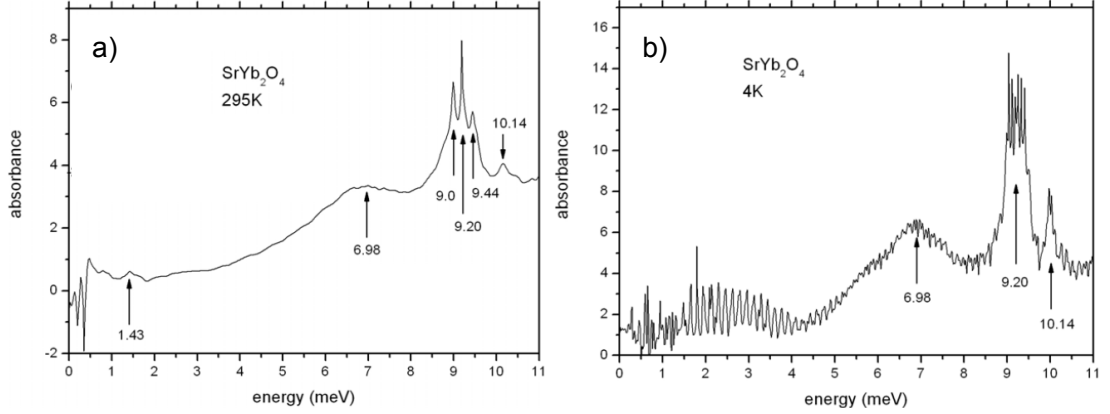
**Figure 7.17:** Optical excitation spectrum obtained at room temperature (a) and 4 K (b). A broad peak is measured centered at 6.98 meV and it is ascribed to a CF excitation. The sharp peaks around 10 meV are phonons.

cepts only one data set as input. The second is called *CF_fit_Yb* [146], which accepts as input a maximum of 6 datasets allowing different incident energies and temperatures to be fitted simultaneously to get more accurate results. This program also uses the interactive program shell of *MULTI-FRILLS* and convolutes the neutron intensities with the instrument resolution by using input instrument parameters such as distances between monochromator and sample, sample and detectors, etc.

The local symmetry used as input for both programs was monoclinic C_2. The actual point symmetry group can be approximated by a higher symmetry group C_{1h}, hence the CF parameters with negative q vanish [153] leaving the following parameters to be fitted: B_k^q with $q = 0, 2, 3, 4, 6$. This approximation was used in the CF_fit_Yb. The parameter B_2^0 is initially fixed to the value obtained from the anisotropy of the paramagnetic Curie-Weiss temperatures as mentioned before ($B_2^0 = 0.1431$).

In the first attempt, different CF schemes have been ascribed to the two different Yb. Figure 7.18 shows two examples. The first one, called here **m1** assigns the excitations as follows, Yb1: 6 meV, 35.6 meV, 70.3 meV and for Yb2: 9.6 meV, 52 meV and 112 meV. The logic behind this model was to consider the three excitations observed with neutrons at ≈ 30 meV, ≈ 50 meV and ≈ 70 meV as CF excitations plus the mode at 6 meV observed by optical absorption. Only by including this low energy mode is it possible to model the large drop in intensity of the excitations at 290 K. The CF parameters for this model are shown in Table 7.5.

This model however does not reproduce the data, in fact it overestimates the strength of the ≈ 50 meV level. The only way this model could be close to the experimental results

Table 7.5: Solution of the fit of INS data using CF_fit_Yb. Model: **m1**. The levels are calculated for Yb1 are at 6.0382 meV, 32.5665 meV and 70.2724 meV and for Yb2 at 9.6082 meV, 52.4447 meV, and 112.9943 meV. The rotational invariants are $S_2 = 0.2904$, $S_4 = 0.0041$, $S_6 = 1.7 \times 10^{-6}$ for Yb1 and $S_2 = 0.1272$, $S_4 = 0.0013$, $S_6 = 1.9 \times 10^{-5}$ for Yb2. The goodness of the fit is $\chi^2 = 60$.

$Yb1$					
$k\backslash q$	0	2	3	4	6
2	0.28177	-1.1715			
4	-0.00077	-0.18307	-0.1606	-0.0587	
6	0.00142	0.00036	0.0101	0.0045	-0.0001
$Yb2$					
$k\backslash q$	0	2	3	4	6
2	0.24250	-0.7596			
4	-0.0758	0.0753	0	-0.0055	
6	-0.0008	0.0149	-0.0012	0.0045	0.0052

Table 7.6: Solution of the fit of INS data using CF_fit_Yb. Model: **m2**. The levels calculated for Yb1 are at 8.6202 meV, 33.1221 meV and 47.9613 meV and for Yb2 at 4.0209 meV, 70.1432 meV, and 112.6870 meV. The rotational invariants are $S_2 = 0.2205$, $S_4 = 2.57 \times 10^{-4}$, $S_6 = 6.07 \times 10^{-9}$ for Yb1 and $S_2 = 0.2768$, $S_4 = 0.0035$, $S_6 = 7.3 \times 10^{-6}$ for Yb2. The goodness of the fit is $\chi^2 = 60$.

$Yb1$					
$k\backslash q$	0	2	3	4	6
2	0.10363	-1.0448			
4	-0.03160	-0.02383	0	0.02737	
6	0.00026	0.00005	0	-0.00001	-0.0001
$Yb2$					
$k\backslash q$	0	2	3	4	6
2	0.24886	1.1499			
4	-0.07916	0.15688	0	-0.02422	
6	-0.00023	0.00015	0	-0.00268	-0.0094

is by introducing a scale factor of 0.3 for the intensity of Yb2 levels, which is completely unphysical (see Figure 7.19(a)).

The next model is called **m2**. Here Yb1 has levels at 8.6 meV, 33.1 meV and 47.9 meV while Yb2 has levels at 4 meV, 70.1 meV and 112.7 meV. Again the intensities are wrong and an unphysical scaling factor of 0.7 must be used for the intensities of Yb2 CF (Figure 7.19(a)). Using these two models **m1** and **m2**, the inverse susceptibility and heat capacity at different fields have been calculated however the results do not reproduce
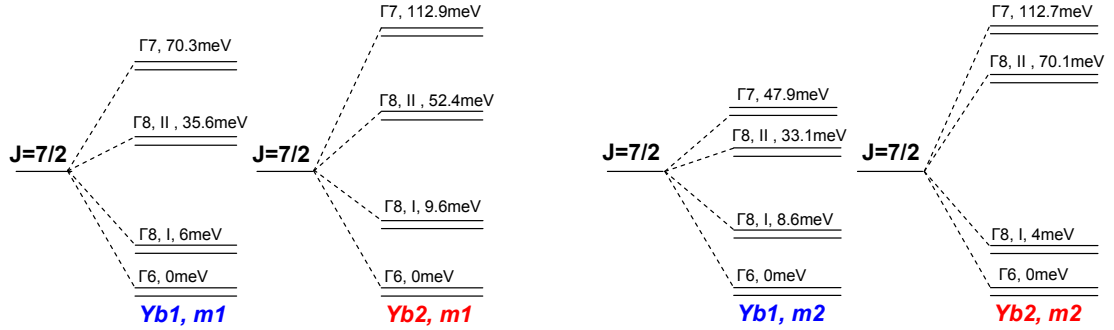
Figure 7.18: CF schemes of **m1** and **m2** for both Yb.

the experimental data (see Figures 7.19). For the specific heat, C_p, **m1** gives a fairly good approximation of the change of C_p with different fields below 12 K where the phonon contribution starts.

Finally two models have been considered where both Ybs are assumed to have the same CF scheme, they are called **Model1** and **Model2** (Figure 7.20).

In **Model1** both Ybs have energy levels at 6 meV, 32.5 meV and 70.27 meV and the mode at ≈ 50 meV which is very weak in neutron scattering is ignored. Figures 7.21(a) and 7.21(b) show the fitting of two data sets at temperatures T= 8 K and 240 K. In total 5 data sets were fitted simultaneously (E_i =110 meV at 8 K, 20 K and 290 K, E_i =65 meV at 240 K and E_i =2.27 meV at 1 K). The scalar factor for the intensity has been fixed to 1 for all datasets. The fit describes the data well ($\chi^2 = 19$) and all parameters are listed in Table 7.7.

The second model considered here is **Model2** where the three doublets are at 32.57 meV, 52.6 meV and 70.27 meV. The goodness of this fit was $\chi^2 = 37$ for five datasets. The temperature dependence of the intensity could not be modeled successfully, see Figures 7.21(a) and 7.21(b). The CF parameters are listed in Table 7.7.

The powder quasielastic scattering that was explored in detail in section 7.4 was also fitted, as shown in Figures 7.21(c) and 7.21(d). Figure 7.21(c) gives the fit when using a width for the quasielastic scattering equal to zero at zero field while for the figure on the right a molecular field of 4 T is applied along the quantization axis z. The molecular field models the effect of the magnetic interactions between neighboring Yb^{3+} ions which have so far been ignored. The effect of these interactions is greatest at low energies and temperatures and gives rise to the splitting of the ground state doublet which is visible as the broad peak at 2.5 K in the zero field heat capacity and as a shift in the quasi-elastic
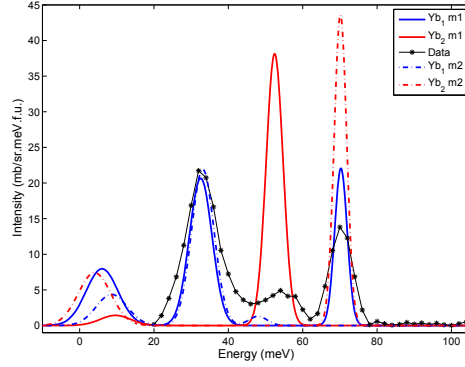
(a) INS,**m1** and **m2** , T=8 K
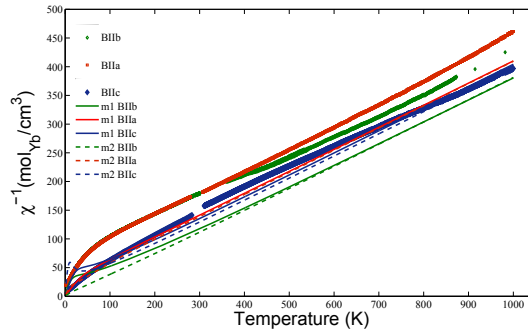
(b) Inverse Susceptibility **m1** and **m2**
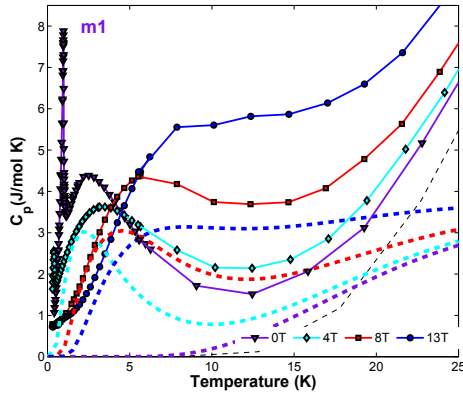
(c) Heat Capacity, **m1**
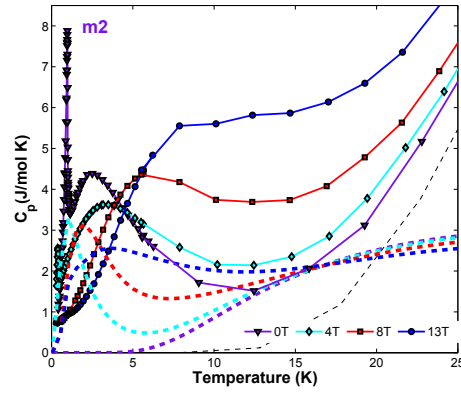
(d) Heat Capacity, **m2**

Figure 7.19: (a)Cut at constant scattering angle ($2\theta = 22.67°$) through the powder INS data acquired on Merlin together at 8 K with an incident energy of 110 meV along with the cross section calculated from the CF parameters of models **m1** (solid lines) and **m2** (dashed lines). The blue spectrums are the calculation for the CF of Yb1 and the red for Yb2. (b) Single crystal inverse susceptibility for a magnetic field of 1T. The lines are the calculations using the contribution of both Yb ions from models **m1** and **m2**. (c-d)Heat capacity at different magnetic fields applied along the *c*-axis and calculation for models **m1**(c) and **m2** (d).
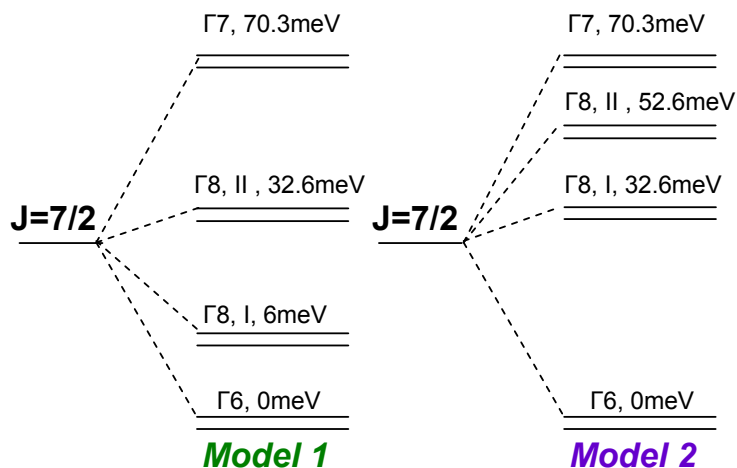
Figure 7.20: CF schemes for Yb^{3+}, for **Model1** and **Model2**. In both cases Yb1 and Yb2 are assumed to have the same energy levels.

Table 7.7: Model1 considers three modes at 6.04 meV, 32.57 meV and 70.27 meV. The rotational invariants are $S_2 = 0.2904$, $S_4 = 0.0041$, $S_6 = 1.7 \times 10^{-6}$. **Model2** considers three modes at 32.57 meV, 52.6 meV and 70.27 meV. The rotational invariants are $S_2 = 0.1570$, $S_4 = 0.0058$, $S_6 = 5.5 \times 10^{-6}$. The goodness of the fit of 5 datasets is $\chi^2 = 19$ for **Model1** and $\chi^2 = 37$ for **Model2**.

Model1					
$k\backslash q$	0	2	3	4	6
2	0.28177	-1.1715			
4	-0.0007731	-0.18307	-0.16063	-0.058728	
6	0.001425	0.00036055	0.010121	0.0045	-0.0001
Model2					
$k\backslash q$	0	2	3	4	6
2	0.44733	-0.76468			
4	-0.002493	0.060133	0	0.22069	
6	-0.001513	-0.001931	0	-0.0061233	0.005302

scattering to higher energies. **Model1** reproduces the low energy INS with a molecular field of 4 T very well while for **Model2** the fit is not as good.

Using the above parameters for **Model1** and **Model2**, the inverse susceptibility and heat capacity at different fields was calculated. Figure 7.22(a) compares the inverse susceptibility of the models with the data. The simulated high temperature inverse susceptibility diverges from the experimental results. Therefore neither **Model1** nor

(a) INS,**Model1** and **Model2** , T=240 K, E$_i$ = 60 meV

(b) INS,**Model1** and **Model2** , T=8 K, E$_i$ = 110 meV

(c) Heat Capacity, **m1**

(d) Heat Capacity, **m2**
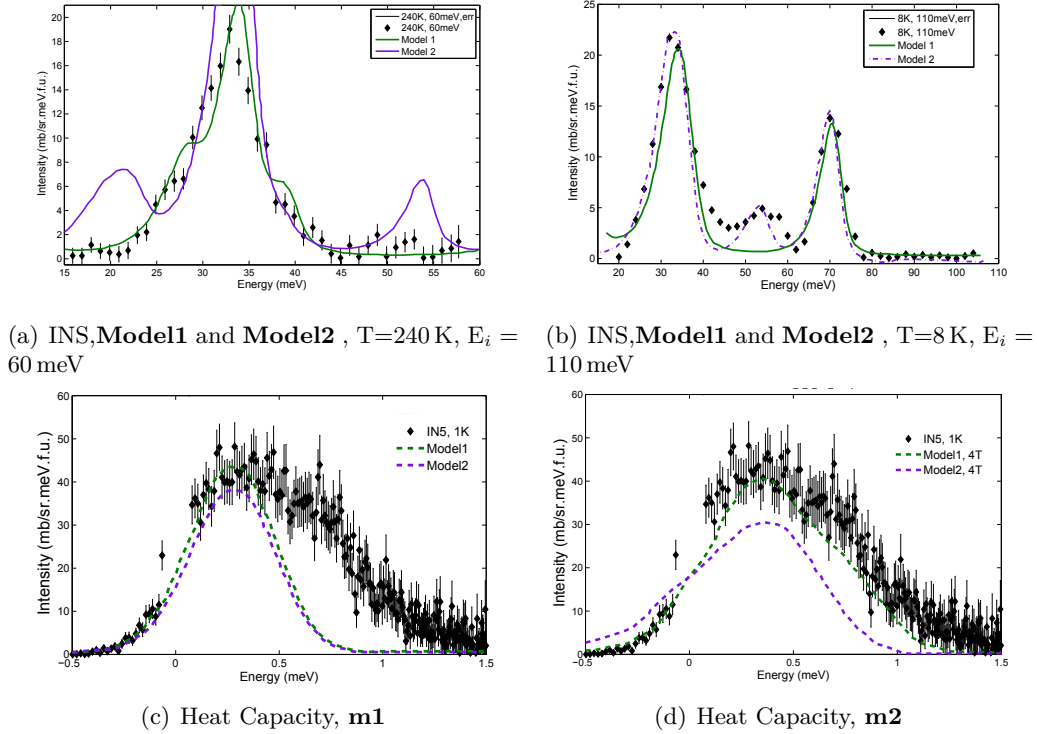
Figure 7.21: Powder INS data together with the cross section calculated from the CF parameters obtained by the fitting of the INS data with **Model1** (green) and **Model2** (purple). (a-b) data collected on Merlin, the cuts are at constant scattering angle ($2\theta = 22.67°$ for E$_i$ = 110 meV dataset and $2\theta = 25.2°$ for the E$_i$ = 60.4 meV dataset) and have been background subtracted. The figure (a) shows the data and calculations at 240 K with an incident energy of 60.4 meV. The figure (b) shows the data and calculation at 8 K with an incident energy of 110 meV. Neutron data were fitted using CF_fit_Yb, considering modes at 6.04 meV, 32.57 meV and 70.27 meV for **Model1** and at 32.57 meV, 52.6 meV and 70.27 meV for **Model2**. (c-d) Cut at constant scattering angle ($2\theta = 62°$) through the powder INS data acquired in IN5-ILL at 1 K with an incident wavelength of 6 Å(2.27 meV). Figure (c) shows the QES calculated for both models (**Model1**-green and **Model2**-purple) for zero magnetic field and figure(d) for a molecular field of 4 T (0.264 meV) along the quantization axis z.
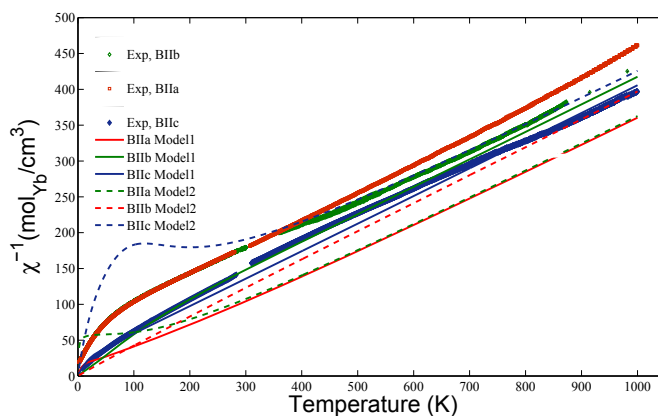
(a) Inverse Susceptibility, **Model1** and **Model2**
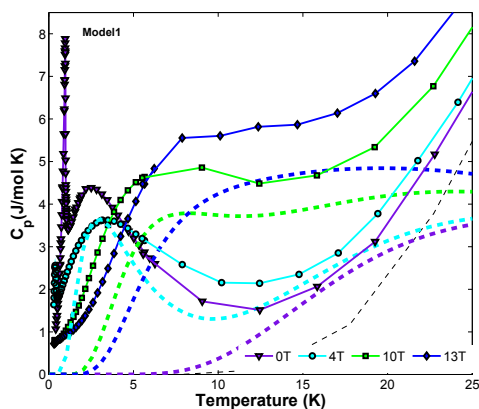
(b) Heat Capacity, **Model1**
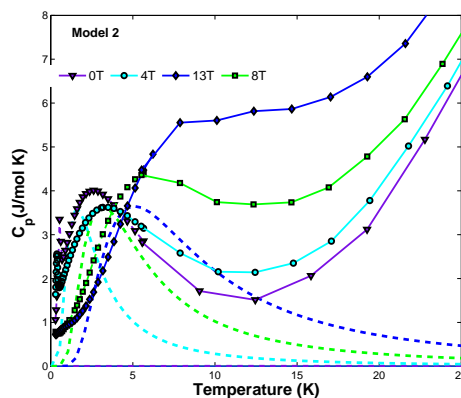
(c) Heat Capacity, **Model2**

Figure 7.22: (a)Single crystal inverse susceptibility for a magnetic field of H= 1 T. The lines are the calculations for models **Model1** (solid lines) and **Model2**(dashed lines). (b)Heat capacity for different magnetic fields applied along the c-axis. The dashed lines correspond to the calculation of the heat capacity using the CF parameters from **Model1**. (c)Heat capacity for different magnetic fields applied along the c-axis. The dashed lines correspond to the calculation of the heat capacity using the CF parameters from **Model2**.

Model2 reproduce the anisotropy of this compound.

Finally the heat capacity for different fields is shown in Figures 7.22(b) and 7.22(c) for each model. **Model1** gives a fair approximation of the heat capacity below T= 12 K while **Model2** cannot reproduce the data.

Altogether **Model1** gives the best agreement with the experimental data of all the models considered. It reproduces both the high and low energy INS at all temperatures and it also agrees with the heat capacity data. The agreement with the susceptibility is poor, this may be because the coordinate system of the crystal field parameters is incorrect since it cannot be determined by fitting powder data. This means the crystal field parameters are only correct within a rotation. The wavefunctions for **Model1** were calculated and are shown in Table 7.8. The total moment for the ground state would be $\langle J^2 \rangle = 2.68 \mu_B$ with the quantization axis along c. The next multiplet ($J = 5/2$) should be at 1.27 eV, as calculated in Mcphase, where the strength of the spin-orbit interaction has been set to 350 meV, following reference [136].

7.6 Discussion and Conclusions

A series of INS experiments have been performed to clarify the magnetic behavior of SrYb$_2$O$_4$. Other measurements were also done such as DC susceptibility and heat capacity. More than 100 CF parameters sets were tested by calculating the neutron cross section, susceptibility and heat capacity, and comparing to the experimental data. Two approaches have been taken to obtain the initial parameters for the fitting. Firstly, parameters from a point charge model were selected and secondly, randomly generating CF parameters were used which were compatible with the energies and intensities of the excitations observed with neutrons as well as the value of B_2^0 (obtained from the anisotropy of the Curie-Weiss temperatures).

The best models were selected and are shown here. The point charge model suggests that the crystal field splitting of the two Yb ions are different, however this model reproduces neither the INS data, nor the susceptibility. The temperature dependence of the INS data suggests the presence of a weak mode at low energy (≈ 6 meV) and optical absorption measurements show magnetic signal around those energies. When this mode is taken into account the agreement with the heat capacity as well as the INS datasets improves. The models discussed subsequently include this low energy mode.

Models **m1** and **m2** have completely different CF for each Yb ion as suggested by the PC model, whereas **Model1** and **Model2** assume the same CF for both Ybs. A

Table 7.8: Wavefunctions for **Model1** of the ground state multiplet $^2F_{7/2}$ and excited multiplet $^2F_{5/2}$ calculated with Mcphase.

Energy(meV)	Wavefunctions(J, m_J)
0	$-0.560967\|7/2, 1/2> +0.530897\|7/2, -5/2> ..$ $+0.435018\|7/2, -1/2> +0.346095\|7/2, -3/2>$
2.25e-13	$-0.560967\|7/2, -1/2> -0.530897\|7/2, 5/2> ..$ $-0.435018\|7/2, 1/2> +0.346095\|7/2, 3/2>$
6.43552	$-0.601268\|7/2, -7/2> -0.551743\|7/2, -3/2> ..$ $+0.38003\|7/2, -5/2> +0.373582\|7/2, -1/2>$
6.43552	$0.601268\|7/2, 7/2> +0.551743\|7/2, 3/2> ..$ $+0.38003\|7/2, 5/2> +0.373582\|7/2, 1/2>$
32.1087	$0.722135\|7/2, 5/2> -0.428305\|7/2, 1/2> ..$ $-0.394069\|7/2, -1/2> -0.356433\|7/2, -7/2>$
32.1087	$-0.722135\|7/2, -5/2> +0.428305\|7/2, -1/2> ..$ $-0.394069\|7/2, 1/2> +0.356433\|7/2, 7/2>$
70.1408	$-0.74354\|7/2, 3/2> +0.631999\|7/2, 7/2> ..$ $+0.170391\|7/2, -5/2> -0.129169\|7/2, -1/2>$
70.1408	$0.74354\|7/2, -3/2> -0.631999\|7/2, -7/2> ..$ $-0.170391\|7/2, 5/2> +0.129169\|7/2, 1/2>$
1272.08	$0.580825\|5/2, -1/2> +0.571069\|5/2, -5/2> ..$ $-0.493625\|5/2, 1/2> -0.302928\|5/2, 5/2>$
1272.08	$-0.580825\|5/2, 1/2> -0.571069\|5/2, 5/2> ..$ $-0.493625\|5/2, -1/2> -0.302928\|5/2, -5/2>$
1296.66	$0.965669\|5/2, 3/2> +0.204563\|5/2, -5/2> ..$ $-0.149709\|5/2, -1/2> +0.0361664\|5/2, 1/2>$
1296.66	$-0.965669\|5/2, -3/2> -0.204563\|5/2, 5/2> ..$ $+0.149709\|5/2, 1/2> +0.0361664\|5/2, -1/2>$
1328.64	$-0.701379\|5/2, 5/2> +0.625187\|5/2, 1/2> ..$ $+0.250229\|5/2, -3/2> +0.216563\|5/2, -5/2>$
1328.64	$0.701379\|5/2, -5/2> -0.625187\|5/2, -1/2> ..$ $-0.250229\|5/2, 3/2> +0.216563\|5/2, 5/2>$

comparison of the rotational invariants for the different models is shown Table 7.9. In this table is important to note that the PC model indeed overestimates the parameters with rank 2 and underestimates the parameters with rank 6, when comparing to the fitted parameters. S_2 is one order of magnitude bigger for the PC models than all other models. However the PC approximation is known to give poor agreement with data even for insulating samples. It does not take account of the shape of the oxygen orbitals and their overlap with the $4f$ rare earth orbitals. A set of CF parameters has been found that successfully fits the directionally independent data such as powder

Table 7.9: Comparison of the rotational invariants for each model shown here.

		S$_2$	S$_4$	S$_6$	χ^2
PC	Yb1	1.681	0.0016	4×10^{-7}	
PC	Yb2	5.379	0.0017	1×10^{-8}	
PC focus	Yb1	2.562	0.0016	4×10^{-7}	5.25 (1 dataset)
PC focus	Yb2	4.776	0.0032	1×10^{-8}	14.85(1 dataset)
m1	Yb1	0.290	0.0041	1×10^{-6}	60
m1	Yb2	0.127	0.0013	1×10^{-5}	
m2	Yb1	0.221	0.0002	6×10^{-9}	60
m2	Yb2	0.277	0.0035	7×10^{-6}	
Model1	Yb	0.290	0.0041	1×10^{-6}	19 (4 dataset)
Model2	Yb	0.157	0.0058	5×10^{-6}	37 (4 dataset)

inelastic neutron at all temperatures and incident energies and it is also able to reproduce the specific heat. This model is **Model1**. This model is not fully satisfactory since the coordinate system cannot be obtained and therefore it does not reproduce single crystal susceptibility which is highly dependent on the crystallographic direction and anisotropy in the compound. Given that there are two different Yb ions in SrYb$_2$O$_4$ it appears very difficult to accurately determine their presumably different coordinate systems from the available data. There are only a few cases in the literature describing the CF for compounds with two non-equivalent Yb^{3+} ions. Ytterbium hypophosphite and doped salts are examples [139]. In the case of Yb(H$_2$PO$_2$)$_3$, the site symmetry for both Yb ions is C_{2h}, Tanner *et al.* observed double bands of excitations which are split by about 0.75 meV using infrared spectroscopy which is only resolved for the lowest energy transitions. They attribute this splitting to the slightly different crystal fields experienced by the two Yb ions. They found bands at 21 meV and 42.3 meV. Such a splitting would be impossible to resolved at these energies with INS.

There are also other rare earth oxides that are isostructural to SrYb$_2$O$_4$ like SrEr$_2$O$_4$, SrHo$_2$O$_4$ and SrDy$_2$O$_4$ which have the same nuclear structure but different magnetic ions implying different magnetic behavior. In the case of the Er compound, the ground multiplet $^4I_{15/2}$ of Er^{3+} is split into eight Kramer's doublets for low point symmetry. Experimental reports of INS experiments to investigate the CF excitations have been published for these materials but as yet no explanation of the CF scheme or values for the CF parameters have been published [154, 115].

Finally it should be noted that there are interactions between the Yb ions. These interactions give rise to a molecular field that splits the ground state doublet to give low energy

excitations observed as a broad anomaly at T= 2.5 K in the specific heat and as a broad low energy mode in the INS. This quasi-elastic scattering was successfully simulated by **Model1** using a molecular field of 4 T. The broad peak in the D7 magnetic component powder pattern is consistent with all the exchange paths along the 'zig-zag' legs and in the honeycomb. The Yb^{3+}-Yb^{3+} distances in $SrYb_2O_4$ are very similar making it impossible to distinguish between exchange paths by using the first moment sum rule, in contrast to $Sr_3Cr_2O_8$ where a main magnetic interaction is evident. The exchange paths in the related compound $SrEr_2O_4$ are not as similar and Monte Carlo simulations performed by Hayes *et al.* [149] predict the magnetic constants to be $J_1/J_3 \approx 5$, indicating that the dominant interaction is along the *c*-axis.

The solution of the CF Hamiltonian is the first step in understanding the rich and complex magnetic behavior of $SrYb_2O_4$. Knowing the ground state and assuming that the magnetic properties of the system are well described at low temperatures in terms of the ground state doublet alone, the next step would be to model the low energy dispersive modes and diffuse magnetic scattering described in section 7.4. These excitations could be modeled using a Random Phase Approximation as it was used for $Sr_3Cr_2O_8$, but in the case of $SrYb_2O_4$ more terms must be added to the Hamiltonian like the CF terms. This approximation has been useful to describe inelastic and diffuse magnetic scattering in RE systems such as $Yb_2Ti_2O_7$ [152, 3, 155]. This model would allow the magnetic exchange interaction between the Yb^{3+} ions to be determined and provide an understanding of the complex competition between magnetic interactions and anisotropy that gives rise to the large number of potentially unusual magnetic states observed in the phase diagram as a function of field and temperature shown in the previous chapter.

8 Conclusions and Perspectives

In this thesis the results of thorough experimental investigations of two different types of frustrated magnetic insulators have been given. These results emphasize the difference between the magnetic behavior of a metal oxide system with quantum spin, $s = 1/2$, and quenched orbital moment and a rare earth system with a classical total momentum. Different mechanisms such as single ion anisotropy, frustration, structural distortions and orbital ordering, compete in these magnets to minimized the total energy of the systems. The energy minimization is constrained by the properties of the magnetic ions, the nature of their local environment and their interactions with each other.

The powder samples and single crystals used for these investigations have been prepared in the Crystal Laboratory at the Helmholtz Zentrum Berlin. The crystal growth processes represented a challenge in both cases, as single crystals of these compounds had never been grown in the past.

The main probe used here has been neutron scattering; its flexibility, simplicity and direct connection to theoretical models makes it the ideal probe for exploring magnetic phenomena. A wide variety of neutron techniques and instruments were employed. A new generation of time of flight neutron chopper spectrometers with position sensitive detectors, made it possible to follow excitations along all directions in reciprocal space, and to explore the sometimes complex dispersion relations in these materials. The high resolution that can be achieved with a triple axis spectrometer allowed specific points in reciprocal space to be studied and the lifetime of magnetic excitations to be investigated. Polarized neutron techniques enabled the unambiguous separation of nuclear and magnetic components. Neutron scattering techniques continue to improve and a new generation of instruments and neutron sources are currently under development, and will be able to explore magnetic phenomena in greater depth.

Alongside the neutron scattering experiments, measurements of the physical bulk properties of these compounds have been performed at the HZB and at the Hoch-Feld-Institute, HZDR. Advances in instrumentation allowed the physical properties under extreme conditions, like high magnetic field and dilution fridge temperatures to be explored. These conditions made it possible to access unknown and exotic magnetic phases, e.g. canted

structures.

The first part of the thesis focuses on the magnetic properties of $Sr_3Cr_2O_8$. This compound consists of hexagonal bilayers of magnetic Cr^{5+} ions. DC susceptibility, high field magnetization, powder and single crystal neutron scattering provide a picture of $Sr_3Cr_2O_8$ as an interacting dimerized spin-1/2 antiferromagnet. This dimerization gives rise to a non-magnetic, singlet ground state and gapped one-magnon excitations where interdimer interactions allow the excitations to hop and develop a dispersion. The dispersion of the one-magnon mode produces a bandwidth extending between the gap energy of 3.5 meV and upper boundary of 7.0 meV. The first moment extracted from powder INS confirms the intradimer exchange constant as the intrabilayer interaction J_0 along the c_h-axis. The single crystal INS results were fitted and compared to a random phase approximation based on the dimer unit and the intradimer and interdimer interactions were determined. The intradimer exchange is calculated to be $J_0 = 5.551(9)$ meV and the interdimer interactions sum to $J' = 3.5(1)$ meV. These values reproduce all data, DC susceptibility, magnetization, powder INS and single crystal INS. The 2-magnon continuum was also observed. The new experimental method of performing ω scans on a pixelated time-of-flight neutron spectrometer, which are then recombined to make a four-dimensional data set (Q_h, Q_k, Q_l, E), allowed the magnon dispersion in the whole Brillouin zone to be measured. The magnons disperse along all directions and the system is three-dimensional.

Three magnon branches were found in the single crystal inelastic neutron scattering experiments due to crystal twinning in the low temperature monoclinic structure. The specific heat measurements shown here reveal that there is a Jahn-Teller distortion resulting in orbital order at $T_{JT} = 285$ K. At low temperature, the crystal structure changes from hexagonal to monoclinic lifting the frustration, producing spatially anisotropic exchange interactions and enhancing the intradimer coupling. The structural distortion also gives rise to the observed twinning with three twinned domains of equal volume rotated by 60° with respect to each other. ESR and Raman spectroscopy measurements performed by D. Wulferding *et al.* and Z. Wang *et al.* [63, 58] conclude that in $Sr_3Cr_2O_8$ there are strong lattice and orbital fluctuations that are brought about by the Jahn-Teller distortion and compete with the system's new structural phase down to temperatures well below the structural transition. Further powder and single crystal inelastic neutron experiments are planned for the investigation of both, the CF scheme for $Sr_3Cr_2O_8$ and the phonon spectra as a function of temperature with the aim of shedding light on these fluctuations.

The lineshape of the triplet excitations was also investigated as a function of temperature.

At low temperatures, the magnon population is very small, they do not interact and as a result have an infinite lifetime. At higher temperatures the lifetimes are modified by the interactions between them. The existing theories predict a symmetric broadening of the peaks with temperature, in contrast, our findings reveal an asymmetric lineshape. New theories must then be developed to describe the asymmetrical broadening of the magnon excitations in three-dimensional dimerized magnets. Other experiments could be performed on $Sr_3Cr_2O_8$, to investigate the lineshape in a resolution decoupled method, such as spin-echo triple axis spectrometry, this would lead to a more accurate parametrization of the lineshapes.

$Sr_3Cr_2O_8$ is a candidate compound for BEC, where an applied magnetic field of $H_c = 30.9(4)\,T$ is required to close the spin gap and start condensing magnons into the ground state, while full saturation is achieved at a field of $H_s = 61.9(3)\,T$. The extracted critical exponent for the transition at H_c is consistent with the theoretical predictions for Bose-Einstein condensation of magnons [59]. The necessary fields to close the gap are just below the limit of new extreme sample environments for neutron scattering (HZB will have an instrument supporting a magnet with maximum field of 25-34T by 2012). The ordering wavevector is expected to be $(1/2_h, 1/2_h, 0_h)$. A high field neutron scattering experiment will be proposed in the near future with the aim of studying this unusual state of matter.

Chemical substitutions of the magnetic and A-site ions can be performed, with the purpose of finding the conditions for a crystal structure which does not distort and therefore remains frustrated at low temperatures. The substitution would also change the strength of magnetic interactions and therefore the gap size, a lower gap would make the investigation of the field induced critical phase and quantum critical point much easier. A substitution with a Jahn-Teller inactive ion would allow the role of the orbital ordering on the exchange interactions and dimerization to be explored.

The second compound investigated in this thesis, is the frustrated rare earth insulator $SrYb_2O_4$. An investigation on the nuclear and magnetic structure and magnetic properties has been done. The refinement of neutron diffraction data was used to determine that the low temperature nuclear structure of $SrYb_2O_4$, is *Pnam*. Heat capacity and neutron diffraction measurements performed at dilution fridge temperatures allowed the discovery of long-range magnetic order on $SrYb_2O_4$ at $0.92\,K$. The refinement of neutron diffraction data revealed an antiferromagnetic structure with ordering wavevector $\boldsymbol{k} = (0, 0, 0)$. The magnetic moments of both Yb ions lie in the *ab*-plane, while the component along the *c*-axis is negligible. The two inequivalent Yb ions have different

moment sizes and directions. The moments within each chain are collinear, aligning ferromagnetically along the 'legs' and antiferromagnetically along the 'zig-zags', while the moments of different chains are canted with respect to each other in an angle close to 90°. The moment along the a-axis of Yb2 is smaller than the component for Yb1, but along the b-axis they are almost equal. The total ordered value for Yb1 is $3.8(7)\mu_B$ and for Yb2: $2.1(1)\mu_B$. Both moments are reduced from the fully ordered moment for Yb^{3+} of $4\mu_B$. This reduction is a consequence of the single ion anisotropy which competes with the Yb^{3+}-Yb^{3+} interactions.

The magnetic phase diagram was mapped out along the three principal crystallographic directions as a function of magnetic field and temperature; a number of transitions and crossovers were found implying a series of metamagnetic phases and showing the highly anisotropic nature of the compound. These results motivate a deeper study, such as a set of neutron diffraction experiments at different temperatures and magnetic fields applied along the three different crystallographic directions.

A series of inelastic neutron scattering experiments at different incident energies and temperatures have been performed on various instruments to clarify the magnetic behavior of $SrYb_2O_4$. The work focused mainly on the crystal field excitations in order to have an insight on the nature of the ground state. The crystal field scheme was then determined by fitting the high energy inelastic neutron scattering data in a phenomenological approach. A series or approximations were necessary. The two Yb sites are assumed to have the same coordinate system, the negative (imaginary) CF constants were assumed to be zero and the weak mode at $52\,meV$ was not taken into account. According to the temperature dependence of the intensity of the high energy excitations, a lower energy weak mode at about $6\,meV$ should be present. Optical measurements confirmed magnetic intensity for those energies. Nevertheless, further INS experiments must be performed in this energy region for a long counting time to proved its existence. A set of CF parameters has been found that successfully fits the rotationally invariant data such as powder inelastic neutron data at all temperatures and incident energies. This model (**Model1**) is not completely satisfactory since it does not reproduce the single crystal susceptibility which is highly dependent on the crystallographic direction and anisotropy in the compound. Given that, there are two different Yb ions in $SrYb_2O_4$ it is impossible to independently determine their CF parameters. A way of simplifying the problem would be the substitution of one of the Yb ions by a non-magnetic ion. This would leave only one coordinate system and the CF would then be easily determined.

The interactions between the Yb ions give rise to a molecular field that splits the ground state doublet to give rise to low energy excitations which are observed as a broad anomaly

at T=2.5 K in the specific heat and as a band of low energy excitations in the INS experiments. Diffuse magnetic scattering is present at all temperatures, well above the Néel temperature. In the ordered state, well-defined modes appear with a linewidth bigger than the instrumental resolution, at least two gapped modes were detected. The gap value is about 0.2 meV and the excitations extend up to 0.7 meV, there is also diffuse magnetic scattering up to 1.2 meV. This observation indicates the presence of short-range magnetic correlations coexisting with the long range magnetic order. This low energy magnetic excitation was successfully simulated for the powder INS by the **Model1** using a molecular field of 4 T. The similarity of the Yb^{3+}-Yb^{3+} distances in the compound makes it impossible to distinguish between exchange paths by using the first moment sum rule, in contrast to $Sr_3Cr_2O_8$ where a main magnetic interaction is evident. In the near future, these excitations will be modeled using a random phase approximation as for $Sr_3Cr_2O_8$, but in the case of $SrYb_2O_4$ CF terms must be added to the Hamiltonian. This model would allow the magnetic exchange interactions between the Yb^{3+} ions to be determined and would provide an understanding of the complex competition between magnetic frustration and anisotropy that gives rise to the large number of potentially unusual magnetic states which appear as a function of field and temperature.

According to the magnetic structure, one Yb ion carries more moment than the second, the long-range magnetic order and well-defined excitation are probably mostly due to this site, while, the second site contributes mainly to the diffuse magnetic scattering, and therefore its correlations are short ranged. A substitution for a non-magnetic ion on one site might allow independent investigation of these two different spectra.

In conclusion, this thesis described a range of magnetic phenomena explored by a variety of experimental techniques. In many cases newly developed techniques were employed, which allow details or even new phenomena to be observed that were previously inaccessible. New results sometimes reveal that the approximations used in the past are not sufficient and can stimulate the development of theories. The compounds described here will continue to be investigated using the latest experimental techniques while the data will be compared to new theories as they develop.

Bibliography

[1] van Vleck, J. H. *Nobel Lecture* (1977).

[2] Skomski, R. *Simple Models of Magnetism.* Oxford University Press, (2008).

[3] Jensen, J. and Mackintosh, A. *Rare Earth Magnetism.* Clarendon Press Oxford, (1991).

[4] Blundell, S. *Magnetism in condensed matter.* Oxford University press, Oxford, (2001).

[5] Taylor, K. and Darby, M. *Physics of Rare Earth Solids.* Chapman and Hall, London, (1972).

[6] Majlis, N. *The Quantum Theory of Magnetism.* World Scientific, Singapore, (2000).

[7] Goodenough, J. B. *Magnetism and the Chemical Bond.* Interscience Publishers, (1963).

[8] Hund, F. *Linienspektren und Periodisches System der Elemente.* Julius Springer, (1927).

[9] Stevens, K. W. H. *Proc. Phys. Soc. Lond. A* **65**, 209–215 (1952).

[10] Newman, D. J. *Adv. Phys.* **20**, 197–256 (1971).

[11] Hutchings, M. T. *Solid State Physics* **16**, 227–273 (1985).

[12] Rudowicz, C. *J. Phys. C: Solid State Phys.* **18**, 1415–1430 (1985).

[13] Newman, D. and Ng, B. K. C. *Crystal Field Handbook.* (2000).

[14] Jahn, H. A. and Teller, E. *Proc. R. Soc. A* **161**, 220 (1937).

[15] Dirac, P. A. M. *Proc. Roy. Soc. A* **123**, 714 (1929).

[16] Anderson, P. W. *Phys. Rev.* **79**, 350 (1950).

[17] Néel, L. *Ann. de Physique* **17**, 64 (1932).

[18] Néel, L. *Ann. de Physique* **5**, 256 (1936).

[19] Bleaney, B. and Bowers, K. D. *Proc. Roy. Soc. Lond. A* **214**, 451–465 (1952).

[20] Lovesey, S. W. *Thermal neutron scattering from condensed matter, vol.2.* Oxford University Press, Oxford, (1984).

[21] Shirane, G., Shapiro, S. M., and Tranquada, J. M. *Neutron scattering with a triple-axis spectrometer.* Cambridge University Press, (2004).

[22] Squires, G. L. *Introduction to the theory of thermal neutron scattering.* Dover Publications, Inc., Mineola, New York, (1996).

[23] Chatterja, T., editor. *Neutron scattering from magnetic materials.* Elesevier, (2006).

[24] Furrer, A., Mesot, J., and Strásser, T. *Neutron Scattering in Condensed Matter Physics.* World Scientific, Singapore, (2009).

[25] PPMS. *User Manual, Quantum Design, San Diego* (2004).

[26] Kiefer, K. *Kalorimetrische und magnetische Untersuchungen am Spin-Peierls-System CuGeO3.* PhD thesis, Universität des Saarlandes, Saarbrücken, (2004).

[27] Zherlitsyn, S., Bianchi, A., and Herrmannsdoerfer, T. *IEEE Trans. App. Sup.* **16**, 1660–1663 (2006).

[28] Kirste, A. *Magnetization Measurements in Ultrahigh Magnetic Fields.* PhD thesis, Humboldt Universitaet Berlin, (2003).

[29] Hwang, J. S., Lin, K., and Tien, C. *Rev. Sci. Instr.* **68**, 94 (1997).

[30] http://www.isis.stfc.ac.uk/ (last visit: June 2011).

[31] http://www.ill.eu/ (last visit: June 2011).

[32] http://www.helmholtz-berlin.de (last visit: June 2011).

[33] Rietveld, H. M. *J. Appl. Crystallogr.* **2**, 65 (1969).

[34] Pieper, O. *Neutron Scattering Investigations of Zero- and One-dimensional Quantum Magnets.* PhD thesis, Technical University Berlin, (2010).

[35] Carlile, C. J. and Adams, M. A. *Physica B* **182**, 431–440 (1992).

[36] Bewley, R., Ecclestonb, R., McEwene, K., Haydend, S., Dovec, M., Benningtona, S., Treadgolda, J., and Coleman, R. *Physica B* **385**, 1029–1031 (2006).

[37] Bewley, R. I., Guidi, T., and Bennington, S. M. *Notiziario Neutroni e Luce di Sincrotrone* **14**, 22–27 (2009).

[38] http://www.ill.eu/instruments-support/instrumentsgroups/instruments/in5/ (last visit: June 2011).

[39] Giamarchi, T., Rüegg, C., and Tchernyshyov, O. *Nature Physics* **4**, 198–204 (2008).

[40] Ng, K. K. and Lee, T. K. *Phys. Rev. Lett.* **97**, 127204 (2006).

[41] Rüegg, C., Cavadini, N., Furrer, A., Güdel, H.-U., Krämer, K., Mutka, H., Wildes, A., Habicht, K., and Vorderwisch, P. *Nature* **423**, 62 (2003).

[42] Nikuni, T., Oshikawa, M., Oosawa, A., and Tanaka, H. *Phys. Rev. Lett.* **84**, 5868 (2000).

[43] Sasago, Y., Uchinokura, K., Zheludev, A., and Shirane, G. *Phys. Rev. B* **55**, 8357 (1997).

[44] Rüegg, C., McMorrow, D. F., Normand, B., Ronnow, H. M., Sebastian, S. E., Fisher, I. R., Batista, C. D., Gvasaliya, S. N., Niedermayer, C., and Stahn, J. *Phys. Rev. Lett.* **98**, 017202 (2007).

[45] Rüegg, C., Furrer, A., Sheptyakov, D., Strässle, T., Krämer, K. W., Güdel, H.-U., and Mélési, L. *Phys. Rev. Lett.* **93**, 257201 (2004).

[46] Kageyama, H., Yoshimura, K., Stern, R., Mushnikov, N. V., Onizuka, K., Kato, M., Kosuge, K. C., Slichter, P., Goto, T., and Ueda, Y. *Phys. Rev. Lett.* **82**, 3168 (1999).

[47] Chen, P., Lai, C.-Y., and Yang, M.-F. *Phys. Rev. B* **81**, 020409 (2010).

[48] Kodama, K., Takingawam, M., Horvatic, M., Berthier, C., Kageyama, H., Ueda, Y., Miyahara, S., Becca, F., and Mila, F. *Science* **298**, 395 (2002).

[49] Cuno, E. and Müller-Buschbaum, H. *Z. Anorg. Allg. Chem.* **572**, 95 (1989).

[50] Chapon, L. C., Stock, C., Radaelli, P., and Martin, C. *arXiv:0807.0877v2 [cond-mat.mtrl-sci]* (2008).

[51] Radtke, G., Sau, A., Dabkowska, H. A., Luke, G. M., and Botton, G. A. *Phys. Rev. Lett.* **105**, 036401 (2010).

[52] Koo, H.-J., Lee, K.-S., and Whangbo, M.-H. *Inorg. Chem.* **45**, 10743–10749 (2006).

[53] *American Ceramics Society database* .

[54] Islam, A. T. M. N., Quintero-Castro, D. L., Lake, B., Siemensmeyer, K., Kiefer, K., Skourski, Y., and Herrmannsdorfer, T. *Crys. Growth & Des.* **10**, 465–468 (2010).

[55] Ouladdiaf, B., Archer, J., McIntyre, G., Hewat, A., Brau, D., and York, S. *Physica B* **385–386**, 1052–1054 (2006).

[56] Zherlitsyn, S., Herrmannsdoerfer, T., Skourski, Y., Sytcheva, A., and Wosnitza, J. *J. Phys.: Conf. Ser.* **51**, 583–586 (2006).

[57] Singh, Y. and Johnston, D. C. *Phys. Rev. B* **76**, 012407 (2007).

[58] Wang, Z., Schmidt, M., Gunther, A., Schaile, S., Pascher, N., Mayr, F., Goncharov, Y., Quintero-Castro, D. L., Islam, A. T. M. N., Lake, B., Krug, H. A., von Nidda, A., Loidl, A., and Deisenhofer, J. *Phys. Rev. B* **83**, 201102(R) (2011).

[59] Aczel, A. A., Kohama, Y., Marcenat, C., Weickert, F., Jaime, M., Ayala-Valenzuela, O. E., McDonald, R. D., Selesnic, S. D., Dabkowska, H. A., and Luke, G. M. *Phys. Rev. Lett.* **103**, 207203 (2009).

[60] Johnston, D. *Physica B* **385–86**, 1029 (2006).

[61] Stone, M. B., Lumsden, M. D., Chang, S., Samulon, E. C., Batista, C. D., and Fisher, I. R. *Phys. Rev. Lett.* **100**, 237201 (2008).

[62] Kofu, M., Kim, J.-H., Ji, S., Lee, S.-H., Ueda, H., Qiu, Y., Kang, H.-J., Green, M. A., and Ueda, Y. *Phys. Rev. Lett.* **102**, 037206 (2009).

[63] Wulferding, D., Lemmens, P., Choi, K. Y., Gnezdilov, V., Quintero-Castro, D. L., Lake, B., and Islam, A. *arXiv:1105.2369v1 [cond-mat.str-el]* (2011).

[64] Samulon, E. C., Kohama, Y., McDonald, R. D., Shapiro, M. C., Al-Hassanieh, K. A., Batista, C. D., Jaime, M., and Fisher, I. R. *Phys. Rev. Lett.* **103**, 047202 (2009).

[65] Kawashima, N. *J. Phys. Soc. Jpn* **73**, 3219–3222 (2004).

[66] Suh, S., Al-Hassanieh, K. A., Samulon, E. C., Brooks, J. S., Clark, W. G., Kuhns, P. L., Lumata, L. L., Reyes, A., Fisher, I. R., Brown, S. E., and Batista, C. D. *arXiv:0905.0718v1 [cond-mat.str-el]* (2009).

[67] Jaime, M. *Netsu Sokutei* **37**, 26 (2010).

[68] Nakajima, T., Mitamura, H., and Ueda, Y. *J. Phys. Soc. Jpn.* **75**, 054706 (2006).

[69] Kofu, M., Ueda, H., Nojiri, H., Oshima, Y., Zenmoto, T., Rule, K. C., Gerischer, S., Lake, B., Batista, C. D., Ueda, Y., and Lee, S.-H. *Phys. Rev. Lett.* **102**, 177204 (2009).

[70] Aczel, A. A., Kohama, Y., Jaime, M., Ninios, K., Chan, H. B., Balicas, L., Dabkowska, H. A., and Luke, G. M. *Phys. Rev. B* **79**, 100409(R) (2009).

[71] Grenier, B. and Ziman, T. *C. R. Physique* **8**, 717–736 (2007).

[72] Hohenberg, P. C. and Brinkman, W. F. *Phys. Rev. B* **10**, 128 (1974).

[73] http://horace.isis.rl.ac.uk/ (last visit:July 2011).

[74] Wang, Y.-L. *Phys. Rev. Lett.* **35**, 5 (1971).

[75] Tennant, D., Notbohm, S., Lake, B., James, A., Essler, F., Mikeska, H.-J., Fielden, J., Kögerler, P., Canfield, P., and Telling, M. *arXiv:0907.2067v1 [cond-mat.str-el]* (2009).

[76] http://www.helmholtz-berlin.de/user/neutrons/instrumentation/neutron-instruments/ (last visit:July 2011).

[77] Le, M. D. *Magnetism and Quadrupolar Order in f-electron Systems.* PhD thesis, University of London, (2009).

[78] Stokes, H. and Hatch, D. *Isotropy Subgroups of the 230 Crystallographic Space Groups.* World Scientific, Singapore, (1988).

[79] Zaliznyak, I. A. and Lee, S. H. *Modern Techniques for Characterizing Magnetic Materials, Chapter 1.* Yimei Zhu, (2004).

[80] Furrer, A. and Gudel, H. U. *Phys. Rev. Lett.* **39**, 657 (1977).

[81] Tennant, D. A., Broholm, C., Reich, D. H., Nagler, S. E., Granroth, G. E., Barnes, T., Damle, K., Xu, G., Chen, Y., and Sales, B. C. *Phys. Rev. B* **67**, 054414 (2003).

[82] Houmann, J., Chapellier, M., Mackintosh, A., Bak, P., McMasters, O., and Gschneidner, K. *Phys. Rev. Lett.* **34**, 587–590 (1975).

[83] Leuenberger, B., Stebler, A., Güdel, H. U., Furrer, A., Feile, R., and Kjems, J. K. *Phys. Rev. B* **30**, 6300–6307 (1984).

[84] Jensen, J. and Smith, H. *Phys. Rev. B* **80**, 224419 (2009).

[85] Cavadini, N., Henggeler, W., Furrer, A., Güdel, H., Krämer, K., and Mutka, H. *Eur. Phys. J. B* **7**, 519–522 (1999).

[86] Cavadini, N., Rüegg, C., Henggeler, W., Furrer, A., Güdel, H., Krämer, K., and Mutka, H. *Eur. Phys. J. B* **18**, 565–571 (2000).

[87] Bak, P. *Phy. Rev. B.* **12**, 5203 (1975).

[88] Bayrakci, S. P., Keller, T., and Keimer, B. *Science* **312**, 5782 (2006).

[89] Damle, K. and Sachdev, S. *Phy. Rev. B.* **57**, 8307 (1998).

[90] Huberman, T., Tennant, D. A., Cowley, R. A., Coldea, R., and Forst, C. D. *J. Stat. Mech.* , 05017 (2008).

[91] Xu, G., Broholm, C., Soh, Y., Aeppli, G., Di Tusa, J. F., Chen, Y., Kenzelmann, M., Frost, C. D., Ito, T., Oka, K., and Takagi, H. *Science* **317**, 1049 (2007).

[92] James, A. J. A. *Dynamical Correlations of Low Dimensional Quantum Magnets.* PhD thesis, University of Oxford, (2008).

[93] Jaime, M., Correa, V., Harrison, N., Batista, C., Kawashima, N., Kazuma, Y., Jorge, G., Stern, R., Heinmaa, I., Zvyagin, S., Sasago, Y., and Uchinokura, K. *Phys. Rev. Lett.* **93**, 087203 (2004).

[94] Matsumoto, M., Normand, B., Rice, T. M., and Sigrist, M. *Phys. Rev. Lett.* **89**, 077203 (2002).

[95] Jensen, J. *Phys. Rev. B* **83**, 064420 (2011).

[96] Jensen, J. *J. Phys. C* **17**, 5367 (1984).

[97] Jensen, J. *J. Phys. B* **49**, 11833 (1984).

[98] Ronnow, H., Parthasarathy, R., Jensen, J., Aeppli, G., Rosenbaum, T., and Mc-Morrow, D. *Science* **308**, 389 (2005).

[99] Fleury, P. and Loudon, R. *Phys. Rev.* **166**, 514–530 (1968).

[100] James, A. J. A., Essler, F. H. L., and Konik, R. M. *Phys. Rev. B* **78**, 094411 (2008).

[101] Essler, F. H. L. *Private comunication* .

[102] Habicht, K., Keller, T., and Golub, R. *J. Appl. Cryst.* **36**, 1307–1318 (2003).

[103] Hodges, J. A., Bonville, P., Forget, A., Rams, M., Krolas, K., and Dhalenne, D. *J. Phys.: Condens. Matter* **13**, 9301–9310 (2001).

[104] Karunadasa, H., Huang, Q., Ueland, B. G., Lynn, J. W., Schiffer, P., Regan, K. A., and Cava, R. J. *Phy. Rev. B* **71**, 144414 (2005).

[105] Maestro, A. and Gingras, M. *J. Phys. Condens. Matter* **16**, 3339–3353 (2004).

[106] Chandra, P. and Coleman, P. *New Outlooks and Old Dreams in Quantum Anti-ferromagnets.* (1991).

[107] Canals, B. and Lacroix, C. *Phys. Rev. Lett.* **80**, 2933 (1998).

[108] Reimers, J. N., Berlisnky, A. J., and Shi, A. C. *Phys. Rev. B* **43**, 865–878 (1992).

[109] Ramirez, A. P., Hayashi, A., Cava, R. J., Siddharthan, R., and Shastry, B. S. *Nature* **399**, 333 (1999).

[110] Hodges, J. A., Bonville, P., Forget, A., Yaouanc, A., Dalmas de Reotier, P., Andre, G., Rams, M., Krolas, K., Ritter, C., Gubbens, P. C. M., Kaiser, C. T., King, P. J. C., and Baines, C. *Phys. Rev. Lett.* **88**, 077204 (2002).

[111] Gardner, J., Ehlers, G., Rosov, N., Erwin, R., and Petrovic, C. *Phys. Rev. B* **70**, 180404(R) (2004).

[112] Gardner, J. S., Dunsiger, S. R., Gaulin, B. D., Gingras, M. J. P., Greedan, J. E., Kiefl, R. F., Lumsden, M. D., MacFarlane, W. A., Raju, N. P., Sonier, J. E., Swainson, I., and Tun, Z. *Phys. Rev. Lett* **82**, 1012(4) (1999).

[113] Petrenko, O. A., Ritter, C., Yethiraj, M., and McK Paul, D. *Phys. Rev. Lett.* **80**, 4570 (1998).

[114] Hill, P. M., Peiser, H. S., and Rait, J. R. *Acta Crystallogr.* **9**, 981 (1956).

[115] Petrenko, O. A., Balakrishnan, G., Wilson, N. R., Brion, S., Suard, E., and Chapon, L. C. *Phy. Rev. B* **78**, 184410 (2008).

[116] Pepin, J. *J. Appl. Cryst.* **14**, 70–71 (1981).

[117] Ponader, C. and Brown, G. E. *Geochimica er cosmochimica Acta* **53**, 2893–2903 (1989).

[118] Antony, S. A., Nagaraja, K., Reddy, G., and Sreedharan, O. *Materials Letters* **51**, 414–419 (2001).

[119] Muller-Buschbaum, V. H. and Schenck, R. *ZAAC* **377**, 70 (1970).

[120] Barry, T. and Roy, R. *J. Inorg. Nucl. Chem* **29**, 1243–1248 (1976).

[121] Reid, A. F. *J. American Ceramic Society* **50**, 491 (1970).

[122] Richter, J., Schulenburg, J., and Honecker, A. *Quatum* **2**, 85–153 (2004).

[123] Stewart, J. R., Deen, P. P., Andersen, K. H., Schober, H., Barthelemy, J., Hillier, J. M., Murani, A. P., Hayes, T., and Lindenau, B. *J. Appl. Cryst.* **78**, 69–84 (2009).

[124] Blume, M. *Phy. Rev.* **130**, 1670 (1963).

[125] Brown, P. J., Forsyth, J. B., and Tasset, F. *Proc. R. Soc. Lond. A* **442**, 147 (1993).

[126] Schärpf, . and Capellmann, H. *Phys. Stat. Sol.* **135**, 359 (1993).

[127] Schärpf, . and Capellmann, H. *Z. Phys. B Cond. Matt.* **80**, 253–262 (1990).

[128] http://www.ill.eu/sites/fullprof/index.html (last visit: April 2011).

[129] http://www.ill.eu/sites/fullprof/php/programsfa7c.html?pagina=GBasireps (last visit:April 2011).

[130] Oliveira, N. A. *Phys. Reports* **489**, 89–159 (2010).

[131] Rüegg, C., Kiefer, K., Thielemann, B., McMorrow, D. F., Zapf, V., Normand, B., Zvonarev, M. B., Bouillot, P., Kollath, C., Giamarchi, T., Capponi, S., Poilblanc, D., Biner, D., and Kramer, K. *Phys. Rev. Lett.* **101**, 247202 (2008).

[132] Stryjewski, E. and Giordano, N. *Adv. in Phys.* **26**, 487–650 (1977).

[133] Perry, R. S., Galvin, L. M., Grigera, S. A., Capogna, L. A., Schofield, J., and Mackenzie, A. P. *Phys. Rev. Lett.* **86**, 2661–2664 (2001).

[134] Hayes, T., Petrenko, O., Balakrishnan, G., Lees, M., Manuel, P., Ritter, C., and Deen, P. *Poster Presentation, PHFM10* (2010).

[135] Dean, W. K. *Correlation of electron spin resonance and optical absorption spectra of Yb and Tm ions in Fluorite crystals*. PhD thesis, Texas Tech University, (1971).

[136] Carnall, W. T., Goodman, G. L., Rajnak, K., and Rana, R. S. *J. Chem. Phys.* **90**, 3443 (1989).

[137] Thornley, J. H. M. *Proc. Phys. Soc.* **88**, 325 (1966).

[138] Abragam, A. and Bleaney, B. *Electron paramagnetic resonance of transition metal ions*. Clarendon Press Oxford, (1970).

[139] Tanner, P. A., Mak, C. S. K., and Mak, T. C. *Polyhedron* **19**, 863–870 (2000).

[140] Rudowicz, C. and Qin, J. *Phys. Rev. B* **67**, 174420 (2003).

[141] Rudowicz, C. and Qin, J. *J. Alloys Comp.* **385**, 238–251 (2004).

[142] Boulon, G. *J. Alloys and Compounds* **451**, 1–11 (2008).

[143] Sheik-Bahae, M. and Epstein, R. I. *Nature Photonics* **1**, 693 (2007).

[144] Fulde, P. and Loewenhaupt, M. *Adv. Phys.* **34**, 589 (1985).

[145] Fabi, P. *Technical Report RAL-TR-* **95**, 023 (1995).

[146] Eugene, E. *Technical Report RAL-TR-* **95** (1995).

[147] http://www.mcphase.de/ (last visit: July 2011).

[148] Cao, H. B., Gukasov, A., Mirebeau, I., and Bonville, P. *J. Phys.: Condens. Matter* **21**, 492202 (2009).

[149] Hayes, T., Balakrishnan, G., Deen, P., Manuel, P., Chapon, L. C., and Petrenko, O. *arXiv:1106.0654v1 [cond-mat.str-el]* (2011).

[150] Ueland, B. G., Gardner, J. S., Williams, A. J., Dahlberg, M. L., Kim, J. G., Qiu, Y., Copley, J. R. D., Schiffer, P., and Cava, R. J. *Phys. Rev. B* **81**, 060408(R) (2010).

[151] Dianoux, A.-J. and Lander, G., editors. *Neutron data booklet.* Old City Publishing Group Science imprint, (2003).

[152] Thompson, J. D., McClarty, P. A., Ronnow, H. M., Regnault, L. P., Sorge, A., and Gingras, M. J. P. *Phys. Rev. Lett.* **106**, 187202 (2011).

[153] Rudowicz, C. *J. Chem. Phys.* **84**, 5045 (1986).

[154] Kenzelmann, M. and Hansen, B. R. *ISIS Experimental Report* **510364** (2005).

[155] Kao, Y. J., Enjalran, M., Del Maestro, A., Molavian, H., and Gingras, M. J. P. *Phys. Rev. B* **68**, 172407 (2003).